

ANALYSIS OF LOSS MECHANISMS IN SUPERCONDUCTING WINDINGS
FOR ROTATING ELECTRIC GENERATORS

by

JOSEPH VITO MINERVINI

B.S., United States Merchant Marine Academy
(1970)

S.M., Massachusetts Institute of Technology
(1974)

SUBMITTED TO THE DEPARTMENT OF
MECHANICAL ENGINEERING IN PARTIAL
FULFILLMENT OF THE REQUIREMENTS
FOR THE DEGREE OF

DOCTOR OF PHILOSOPHY

at the

MASSACHUSETTS INSTITUTE OF TECHNOLOGY

June 1981

© Massachusetts Institute of Technology 1981

Signature of Author _____

[Signature] Department of Mechanical Engineering
May 14, 1981

Certified by _____

[Signature] Joseph L. Smith, Jr.
Thesis Supervisor

Accepted by _____

Warren M. Rohsenow
Chairman, Department Committee on Graduate Students

ARCHIVES
MASSACHUSETTS INSTITUTE
OF TECHNOLOGY

JUL 31 1981

LIBRARIES

ANALYSIS OF LOSS MECHANISMS IN SUPERCONDUCTING WINDINGS
FOR ROTATING ELECTRIC GENERATORS

by

JOSEPH V. MINERVINI

Submitted to the Department of Mechanical Engineering
on May 14, 1981 in partial fulfillment of the
requirements for the Degree of Doctor of Philosophy
in Mechanical Engineering

ABSTRACT

Loss mechanisms in superconducting windings are investigated with specific emphasis on the hysteretic ac loss in the superconducting filaments. The two-dimensional current distribution is given for a superconducting filament carrying a dc transport current in a time-varying transverse magnetic field. The current distributions are calculated from the critical state model by using the mathematics of complex variables and a numerical iterative technique. Results are presented as polynomial curves that define regions of positive and negative current. The field required to fully penetrate the filament is given as a function of the transport current. Hysteresis losses are computed for both the partial penetration and full penetration regimes as a function of the transport current and the magnitude of the perturbation field. Results are given in non-dimensional form and the energy loss provided by the external magnetic field is distinguished from the energy loss provided by the transport current power supply.

The ac loss theory is applied to the design of the superconducting field winding for a 10 MVA synchronous electric generator including specification of the winding configuration and conductor. Thermal and electrical performance analyses are given. Fabrication techniques for the winding are developed and verified by the construction and testing of a prototype superconducting coil.

Thesis Supervisor: Dr. Joseph L. Smith, Jr.
Title: Professor of Mechanical Engineering

ACKNOWLEDGEMENTS

This work was supported by the U.S. Department of Energy under Contract No. EX-76-A-01-2295, Task Order No. 11.

I would like to thank the members of my thesis committee, Professors Gerald Wilson and William Unkel and Dr. John Williams and particularly my Thesis Advisor Professor Joseph L. Smith, Jr. with whom I had many useful discussions which helped focus my work. Many thanks go to Dr. Yuki Iwasa and Jim Maguire for their help with the experiments at the Francis Bitter National Magnet Laboratory.

Of course, special thanks must go to the staff and students at the Cryogenic Engineering Laboratory who, over the years, have formed a community with which I am proud to have been associated. This applies particularly to Bob Gertsen, Carl Benner, Ken Tepper, and Howard Lunn for their technical contributions to the experiments, for our friendly little lunchtime "seminars", and for our after hours, extracurricular activities which helped remove a lot of the rough edges.

Finally, but most importantly, I say thank you to Greta for her support, encouragement and love.

TABLE OF CONTENTS

	<u>PAGE</u>
ABSTRACT	2
ACKNOWLEDGEMENTS	3
LIST OF TABLES	7
LIST OF FIGURES	8
LIST OF SYMBOLS	12
CHAPTER I. INTRODUCTION	17
I.1 Background	17
I.2 Problem Statement	21
CHAPTER II. REVIEW OF SUPERCONDUCTING PHENOMENA	24
II.1 Zero Resistivity and the Meissner Effect	25
II.2 The Critical Field	31
II.3 Thermodynamic Phase Transition	32
II.4 Electrodynamics and the Penetration Depth	37
II.5 The Coherence Length	40
II.6 Type I and Type II Superconductivity	42
II.7 Flux Flow and Flux Flow Resistivity	50
II.8 The Critical State	55
II.9 Superconductors for Technical Applications	59
CHAPTER III. THEORY OF AC LOSSES IN SUPERCONDUCTORS	64
III.1 The Critical State Model Applied to AC Losses	66
III.1.1 One-Dimensional Flux Penetration	68
III.1.2 One-Dimensional Effect of Transport Current	74
III.2 Existing Loss Models	77
III.3 Mathematical Technique for Calculation of Two-Dimensional Flux Penetration	80
III.4 Partial Penetration Flux Profiles	86
III.5 Two-Dimensional AC Loss Calculation	97

	<u>PAGE</u>
III.5.1 Partial Penetration Without Transport Current	98
III.5.2 Full Penetration Without Transport Current	104
III.5.3 Partial Penetration with Transport Current	107
III.5.4 Full Penetration with Transport Current	116
III.6 Application to Multifilamentary Conductors and Experimental Evidence	129
CHAPTER IV. APPLICATION OF LOSS THEORY TO A SUPERCONDUCTING GENERATOR	134
IV.1 Superconducting Field Winding Design for a 10 MVA Generator	134
IV.2 AC Loss Calculation	144
IV.2.1 Eddy Current Loss	145
IV.2.2 Hysteresis Loss	147
IV.3 Thermal Analysis	149
IV.3.1 One-Dimensional Steady State Heat Transfer Model	151
IV.3.2 Two-Dimensional Steady State Heat Transfer Model	153
IV.3.3 Adiabatic Heating Model	157
IV.3.4 Frictional Heating	159
CHAPTER V. EXPERIMENTAL COIL	162
V.1 Winding Fabrication	166
V.2 Assembly to Structure	178
V.3 Test Configuration	183
V.4 Test Results	186
CHAPTER VI. CONCLUSIONS	195
APPENDIX A - SUMMARY OF IMPORTANT LOSS FORMULA	198
APPENDIX B - COMPUTER PROGRAMS	201
APPENDIX C - HEAT TRANSFER MODELS	218
C.1 One-Dimensional Model	218
C.2 Two-Dimensional Model	221

	<u>PAGE</u>
BIBLIOGRAPHY	225
REFERENCES	226
BIOGRAPHICAL NOTE	231

LIST OF TABLES

<u>NUMBER</u>	<u>TITLE</u>	<u>PAGE</u>
3.1	Coefficients of Polynomial Functions that Define Flux Penetration Curves	95
4.1	Characteristics of the Field Winding Modules	138
4.2	Conductor Dimensions and Operating Characteristics	141
4.3	AC Loss Parameters and Results	150
4.4	Heat Transfer Model Parameters and Maximum Temperature Rise	154
4.5	Summary of Heat Transfer Analyses	160

LIST OF FIGURES

<u>NUMBER</u>	<u>TITLE</u>	<u>PAGE</u>
2.1	Resistivity of Superconducting and Normal Conductors as a Function of Temperature	26
2.2	Magnetic Behavior of a Perfect Conductor	28
2.3	Magnetic Behavior of a Superconductor	29
2.4	Magnetization of Ideal Type I Superconductors as a Function of Applied Field	30
2.5	Temperature Dependence of the Critical Field	30
2.6	Variation of the Entropy with Temperature for the Superconducting and Normal Phases	35
2.7	Variation of the Electronic Specific Heat with Temperature Showing the Discontinuous Jump Between the Superconducting and Normal Phases	36
2.8	Flux Penetration into a Slab of Type I Superconductor Showing the London Penetration Depth λ_L	39
2.9	Magnetic Flux Density, Superelectron Density, and Free Energy for Type I and Type II Superconductors	44
2.10	Magnetization Curves for Ideal Type I and Type II Superconductors	45
2.11	Single Vortex with Normal Core and Shielding Currents	46
2.12	Diagram Showing Different Superconducting States as a Function of Magnetic Field and the Parameter κ	48
2.13	Flux Penetration into an Ideal Type II Superconductor Showing the Vortices Surrounded by the Screening Currents	49
2.14	Ideal Type II Superconductor Carrying a Transport Current in a Uniform External Field	51
2.15	Voltage-Current Characteristics for Ideal Type II Superconductor Showing: a) Effect of Impurities; b) Effect of Magnetic Field; and, c) Flux Flow Resistivity versus H for Different Temperatures	58

<u>NUMBER</u>	<u>TITLE</u>	<u>PAGE</u>
2.16	Critical Field Versus Critical Temperature for Various Superconductors at Different Current Densities in the Superconductor	62
3.1	Field and Current Distribution in a Type II Superconducting Slab of Thickness d with External Field Applied Parallel to the Slab Surface	70
3.2	Magnetization Curve for a Type II Superconducting Slab	71
3.3	Kim Model of Field and Current Distribution in a Type II Superconducting Slab of Thickness d with External Field Applied Parallel to the Surface	73
3.4	Bean Model of Field and Current Distribution in a Slab Carrying a Transport Current, $I_t/I_c = 0.5$	74
3.5	Contour C in Complex z -Plane Enclosing Region R of Constant Current Density J	82
3.6	Cylindrical Superconducting Filament in a Uniform External Field Showing Partial Penetration	87
3.7	Superposition of Contours to Enclose Regions of Net Positive and Negative Current Density	87
3.8	Position of Field Points for Evaluation of Residual Functions	93
3.9	Contours of Limits of Flux Penetration into a Circular Superconducting Filament for Different Values of External Field	96
3.10	Current Distributions in a Circular Superconducting Filament for One Cycle of External Field Change from $H_0 + \Delta H_e$ to $H_0 - \Delta H_e$	99
3.11	Magnetization Loop for Circular Superconducting Filament	103
3.12	Current Distributions in a Circular Superconducting Filament Carrying Transport Current in a Changing External Field	109
3.13	Regions of Transport Current Surrounded by Shielding Current Patterns for: a) Proposed Model, b) Carr Model	112

<u>NUMBER</u>	<u>TITLE</u>	<u>PAGE</u>
3.14	Full Penetration Field as a Function of the Fraction of Critical Current	114
3.15	Current Distributions for a Changing Transport Current in a Constant Uniform External Field	115
3.16	Full Penetration Flux Motion for Increasing and Decreasing External Field	117
3.17	Functions α , β , and γ Versus Transport Current, i	122
3.18	Shielding Loss Versus Transport Current for Different Values of External Field Change	126
3.19	Transport Loss Versus Transport Current for Different Values of External Field Change	127
3.20	Total Loss Versus Transport Current for Different Values of External Field Change	128
4.1	Cross-Section of the MIT 10 MVA Rotor	135
4.2	View of Field Winding in the Straight Section	136
4.3	Schematic Representation of Yoke Structure and Conductor Module	139
4.4	Short Sample Data for 10 MVA Generator Superconducting Wire	143
4.5	Heat Transfer Models: a) One-dimensional; b) Two-dimensional	152
5.1	Testing Coil and Structure Cross-Section	164
5.2	Detail of the Intra-module Construction	165
5.3	Winding Mandrel	167
5.4	Winding Jig Showing the Mandrel and 24 Clamps Mounted to the Base Table	167
5.5	Conductor Started in Winding Mandrel and Leading to Spool Overhead	169
5.6	Completion of First Turn Showing Phenolic Transition Piece and Phenolic Positioning Piece	169

<u>NUMBER</u>	<u>TITLE</u>	<u>PAGE</u>
5.7	Beginning of Winding of Second Turn	171
5.8	First Layer Half Complete Up to Turn Seven	171
5.9	First Layer Complete and Ready for Short Testing	172
5.10	First Layer is Prepared for Removal from Winding Jig and Curing in Oven	172
5.11	Winding Mandrel Top and Bottom Flanges have had Slots Machined for Better Placement of the Insulating Strips	174
5.12	Completed Coil Showing all Six Cured Layers Still Mounted on the Winding Mandrel	176
5.13	Top View of the Coil. The Large Cooling Channels Between the Layers are Clearly Visible	177
5.14	Yokes Loosely Fitted to the Coil and Resting on One of the Support Plates	179
5.15	The Coil is Loosely Fitted to the Structure and Prepared for Welding	180
5.16	Welding Clamp and Chill Arrangement	182
5.17	Coil and Structure Attached to Current Leads and Holder and Ready for Insertion in Test Dewar	184
5.18	Arrangement of Current Leads and Normal to Superconducting Transition in Copper Blocks. Instrumentation Connecting Strip is at Top of Picture	185
5.19	Close Up of Coil Showing Voltage Taps in Center of Picture	186
5.20	Superconducting Current Lead Transition to Copper Block. The Conductor is Doubled in this Region to Insure a Low current Density	188
5.21	Schematic of Set Up to Test the Model Coil at FBNML	189
5.22	Trace of Voltage Across Coil Terminals Versus Time During Heater Induced Quench	191
5.23	Operating Characteristics of Test Coil and Generator Field Winding	193

LIST OF SYMBOLS

A	Area
a	x-axis intercept of flux contour (Eq. 3.30)
a_n	Real coefficients of polynomial defining flux contour
B	Magnetic flux density
C	Contour for integration
C_p	Specific heat at constant pressure
CSC	Copper-to-Superconductor ratio
D_m	Magnetic diffusivity
d	Filament diameter or slab thickness
E	Electric field intensity
ΔE	Change in energy
e	Electron charge
f	Frequency
f	Fraction of cooled conductor surface (Eq. 4.7)
$f(T)$	Free energy density
$f(z)$	Complex analytic function
f_L	Lorentz force density
$g(T,H)$	Gibbs free energy density
H	Magnetic field intensity
H_0	Constant uniform external bias field
ΔH_e	Magnitude of cyclic external field change
h	Convective heat transfer coefficient
I	Current

i	Dimensionless current
J	Current density
k	Thermal conductivity
L	Conductor width
L_x	x-axis intercept of flux contour
L_y	y-axis intercept of flux contour
ℓ	Mean free path length (Chapter II)
ℓ	Length of conductor (Chapter III)
M	Magnetization
m	Mass
n	Number of flux lines per unit volume
n_s	Number of superelectrons per unit volume
P	Power loss
p	Cooled perimeter of conductor
Q	Latent heat (Chapter II)
Q	Energy transferred as heat (Chapter IV)
\dot{Q}	Rate of heat transfer
R	Filament radius
R	Region of uniform current density (Section III.3)
R_k	Residual field of point k
s	Specific entropy
T	Temperature
t	Time
t	Conductor thickness (Chapter IV)
u	Real part of analytic function $f(z)$

V	Volume
v	Imaginary part of analytic function $f(z)$
v_L	Velocity of flux lines
W	Energy loss
W_i	Internal heat generation per unit volume
X_p	Limit of flux penetration in superconducting slab
X_m	X-axis intercept of flux contour (Table 3.1)
z	Complex field point, $x + iy$
z^*	Complex conjugate of z, $x - iy$

Subscripts

c	Critical
c1	Lower critical
c2	Upper critical
e	External
f	Flux flow
f	Fluid (Chapter IV)
fpo	Full penetration without transport current
fpt	Full penetration with transport current
h	Hysteresis
in	Inside region R
m	Matrix
m	Maximum
n	Normal
out	Outside region R
P	Full penetration

p ₀	Partial penetration without transport current
p _t	Partial penetration with transport current
s	Superconducting (Chapter II)
s	Shielding (Chapter III)
t	Transport
+	Positive current
-	Negative current
	Parallel
⊥	Perpendicular

Greek Symbols

$\alpha(i)$	Shielding loss coefficient
$\beta(i)$	Transport loss coefficient
β	Dimensionless field parameter (Eq. 3.60)
β	Fin coefficient (Eq. 4.7)
$\gamma(i)$	Total loss coefficient
δ	Current coefficient (Eq. 3.27)
ζ	Variable denoting a point along contour C (Sections III.3 - III.4).
η	Viscous damping coefficient
κ	Order parameter, λ/ξ
λ	Volume fraction of superconductor
λ	Penetration depth
λ_L	London penetration depth
μ_0	Permeability of free space, $4\pi \times 10^{-7}$ Henry/meter
μ_r	Relative permeability, dimensionless

ξ	Coherence length
ρ	Electrical resistivity
σ	Electrical conductivity
τ_m	Magnetic diffusion time for superconducting filament
τ_0	Magnetic diffusion time for composite conductor
ϕ_0	Quantum of flux
ψ	Wave function

CHAPTER I
INTRODUCTION

Very often during the relatively short history of science and technology great scientific breakthroughs have developed suddenly after long years of steady but slow effort due to seemingly unrelated events. So it was in 1911 with the accidental discovery of superconductivity by H. Kammerlingh Onnes. The actual event that triggered the discovery of this exciting phenomenon occurred three years earlier in 1908 when Onnes successfully liquified helium for the first time after many years of painstaking effort by himself and other researchers. This new technology opened the door to the vast field of extremely low temperature physics and resulted not only in the discovery of superconductivity but also the discovery of superfluid helium II.

Likewise superconductivity has opened another scientific door through the benefits of very high magnetic fields and zero resistivity. The potential applications of superconductivity span the scale from very small microelectronic devices based upon quantum effects to extremely large scale energy devices [1,2,3]. The characteristics of zero resistivity are attractive for increasing the speed and reducing the power requirements of microelectronic devices. Presently speed and power dissipation are two limitations on further development of conventional electronic components. Thus a superconducting computer is a logical extension of this rapidly developing technology. Present small scale applications include superconducting quantum interference

devices, magnetometers, rf cavities, etc.

On a larger scale, the capability of superconducting magnets to create very high magnetic fields over large volumes with relatively small power requirements is being used to extend the range of conventional magnet technology and open up new engineering applications. For example, superconducting magnets are rapidly replacing conventional magnets for physics applications such as bubble chamber magnets, NMR magnets, and particularly high energy physics particle accelerators. Superconducting beamline dipole magnets are to be used on a very large scale for particle accelerators at the Fermi National Accelerator Laboratory's Energy/Doubler facility and Brookhaven National Laboratory's Isabelle Storage Ring. Other medium scale applications include magnetic separation and magnetic levitation.

The largest scale applications of superconductivity lie primarily in the technologies of power and propulsion devices. Research and development has been carried out in the late 1960's and through the 1980's on superconducting motors and generators for ship propulsion and large scale central power generation, superconducting ac and dc transmission lines and superconducting energy storage magnets for power grids and pulsed energy sources. The emerging technologies of MHD and fusion power generation will require superconducting magnets on an extremely large scale. Actually these last two technologies would not be feasible at all without the use of superconducting magnets.

The subject of this thesis was developed out of research on superconducting machines that has been carried out since the late 1960's through

joint programs of the Cryogenic Engineering Laboratory (CEL) and the Electric Power Systems Engineering Laboratory (EPSEL) at M.I.T. This work at M.I.T. was begun following early work in the field by Woodson, Stekly et al. [4,5] at Avco. The first superconducting machine built at M.I.T. demonstrated that a superconducting winding and its liquid helium cryostat could be successfully operated rotating at 3600 RPM and energized to 45 kVA [6,7].

A second major advance in superconducting machinery came with the design, construction and testing of an experimental 3 MVA generator at M.I.T. [8,9,10,11]. This machine was temporarily connected to the Cambridge Electric System as a synchronous condenser in a program supported by the Electric Power Research Institute (EPRI).

Encouraged by the great success of the M.I.T.-EPRI research programs as well as by superconducting generator research by other groups in the United States and around the world, the CEL and EPSEL laboratories at M.I.T. began another superconducting generator program in 1976 with support from the U.S. Department of Energy. The objective of the program, entitled "Demonstration of an Advanced Superconducting Generator", is to demonstrate advanced concepts in a prototype superconducting generator [12]. The research is focused on the design, construction, and testing of a prototype 10 MVA superconducting generator that will prove the feasibility of design concepts to be used in a generator of 2000 MVA rating for a central power generating station.

It is in the context of this program that the subject of this thesis was developed. One of the key problem areas uncovered by earlier work was

the problem of shielding the field winding from alternating magnetic fields. Shielding from ac fields is necessary because superconductors exhibit a hysteretic loss under the influence of changing external fields or a changing transport current. This loss of energy when deposited in the field winding at liquid helium temperatures could be potentially devastating to the stable operation of the generator. Operating stability and reliability are extremely important criteria for the selection of large central power generating plants. In addition the cost of the refrigeration plant required to handle this low temperature power dissipation must be factored into any economic feasibility analysis. Thus it is extremely important to have a clear understanding of the basic physical mechanisms that are responsible for this energy dissipation and it is equally important to have mathematical models which can accurately predict this loss. Only then can a truly optimized generator be designed that reflects all the important engineering design trade-offs. In this case the general trade-off is more shielding versus more cooling. In order to have adequate information upon which to base the design decisions it is necessary to be able to compute accurately the ac loss in the superconductor under all expected operating conditions. This information is used in a thermal analysis to determine the adequacy of the winding cooling arrangement. Of course these analyses are interrelated with electrical and structural considerations.

Existing loss models were obtained from the literature and applied to the field winding design of the generator. However, it became apparent that these loss models were not totally adequate to give confident

estimates of the ac losses for all expected operating conditions. Thus a considerable contribution to the ac loss theory could be made if the existing loss models could be improved. This would also provide a quantitative basis upon which to make design decisions for the field winding.

I.2 Problem Statement

The primary goal of this thesis is to investigate the loss mechanisms in superconductors, make improvements to the loss models where necessary and apply these results to the design of a superconducting field winding for a rotating electric generator.

During the investigation of the loss models it was determined that there was considerable area for improvement of the hysteresis loss model for superconducting filaments. This model is inadequate because it relies on one-dimensional solutions for flux penetration when two-dimensional solutions are required for accuracy. This is a particular problem whenever the filament is carrying a transport current, that is, for most cases of practical interest.

Thus the work of this thesis is concerned with four specific tasks, namely:

- 1) an investigation of all loss mechanisms in the superconducting winding and an estimate of their impact on the winding performance.

- 2) an improved analysis of one of the most important loss mechanisms, the hysteresis loss in superconductors carrying transport current. The model is improved by solving for the ac loss from two-dimensional solutions of the field and current distributions, where only one-dimensional solutions were previously used.

3) the application of tasks 1 and 2 to the design of the superconducting field winding for a 10 MVA synchronous electric generator including specification of the conductor and winding configuration and thermal and electrical performance analyses.

4) the verification of the winding concept by developing fabrication techniques and actual construction of a prototype winding for performance testing.

The presentation of the four tasks is roughly divided into four chapters. Chapter II contains a general introductory survey of superconducting phenomena that is intended to provide a background for further discussion of the hysteresis loss mechanisms. The concepts of flux flow and the critical state model are discussed in order to provide the basis for the loss model presented in Chapter III. A discussion of other superconducting phenomena such as the Meissner effect is given for general interest and to provide a context for the special physical properties of the superconducting state.

In Chapter III the ac loss theory is developed from the critical state model. A new mathematical technique is provided as a means for computing the two-dimensional distributions of current and field in the critical state. The technique uses the mathematics of complex variables and a numerical contour integration to compute the two-dimensional magnetic field components due to any given distribution of uniform current density. The actual flux penetration contours are found from an iterative solution. The results are applied directly to calculate the ac loss for partial and full penetration of the superconductor with and without transport current. It is shown how the loss provided by

by the external magnetic field is distinguished from the loss provided by the transport current. The loss expressions are given in non-dimensional form so that they are valid in any superconducting winding application and, not necessarily specific to a rotating electric generator.

The first section of Chapter IV is devoted to a discussion of the 10 MVA generator field winding design and superconductor selection. The results of Chapter III are then used to explicitly compute the ac losses in the field winding for the expected operating conditions. A thermal analysis uses different heat transfer models to ascertain the stable operation of the winding during all transient conditions.

Chapter V gives details of the fabrication techniques used to construct a small, superconducting experimental coil to simulate one module of the field winding. Test results are given of the operating performance of the coil. It is important to note that, although the field winding design appears specific to the prototype rotating electric generator, many of the design concepts would be useful in solving some of the stress distribution problems and frictional heating problems encountered in other high current density, large scale coil designs for other applications such as MHD magnets.

A bibliography of some selected books on superconductivity has been provided as a general informational source on this topic. Specific references are given where required. Together the two lists should provide a fairly comprehensive background on superconductivity for the interested reader.

CHAPTER II
REVIEW OF SUPERCONDUCTING PHENOMENA

Superconductivity is one of the most interesting phenomena known to modern science. With its discovery by Onnes in 1911 came an initial excitement over the potential to create very high magnetic fields which would hopefully lead to other advances in science and technology. However, it was soon found that the known superconducting materials could not carry very significant currents because the superconductivity was destroyed by moderate magnetic fields; fields too low to warrant any special technical interest. Thus further interest in research and development waned as superconductivity became known as a very interesting curiosity with little technical significance.

Further study proceeded at a rather low but steady level of activity. In the 1930's this study resulted in some interesting phenomenological discoveries and descriptions by scientists such as Meissner, the London brothers, Pippard and others. However, it wasn't until the 1950's that a microscopic theory of superconductivity was developed by Bardeen, Cooper, and Schrieffer which later became widely accepted as giving a true description of superconducting phenomena. The BCS theory was based upon the formation of paired electrons, Cooper pairs, in the superconducting state [13]. In the same time frame a more macroscopic theory by Ginzburg and Landau was advanced that was more useful in explaining some mixed state phenomena [14]. Since the theory was phenomenologically based, it was given little attention until Gorkov showed that it was truly a limiting case of

the microscopic theory [15]. Together with the work of Abrikosov [16] this became known as the GLAG theory of superconductivity and is most useful in explaining type II superconductivity.

The following sections of this chapter give a very brief overview of some of the most basic superconducting phenomena in layman's terms. Hopefully they will provide the reader with a simple introduction to a few of the basic concepts and terms which are necessary to gain an understanding of the ac loss mechanisms in type II superconductors. They are in no way meant to provide a complete and detailed description of the microscopic theory. A bibliography is provided along with specific references so that the reader can investigate this interesting phenomena to any depth desired.

II.1 Zero Resistivity and the Meissner Effect

It all started in 1911 in Leiden when H. Kammerlingh Onnes was using his newly developed helium liquification technique to measure the low temperature resistance of mercury. He discovered that the resistance suddenly dropped to zero at a temperature close to that of liquid helium. This sudden phase transition from the normal conducting state to a state of zero dc electrical resistance became known as superconductivity.

The resistivity of all metals decreases with temperature because the resistance due to thermal vibrations of the lattice is reduced. That is, phonon scattering of the conducting electrons decreases with decreasing temperature. However, there will always be some residual resistivity due to impurities in the metal or lattice defects. Figure 2.1 illustrates the different resistive properties of a normal conductor and a supercon-

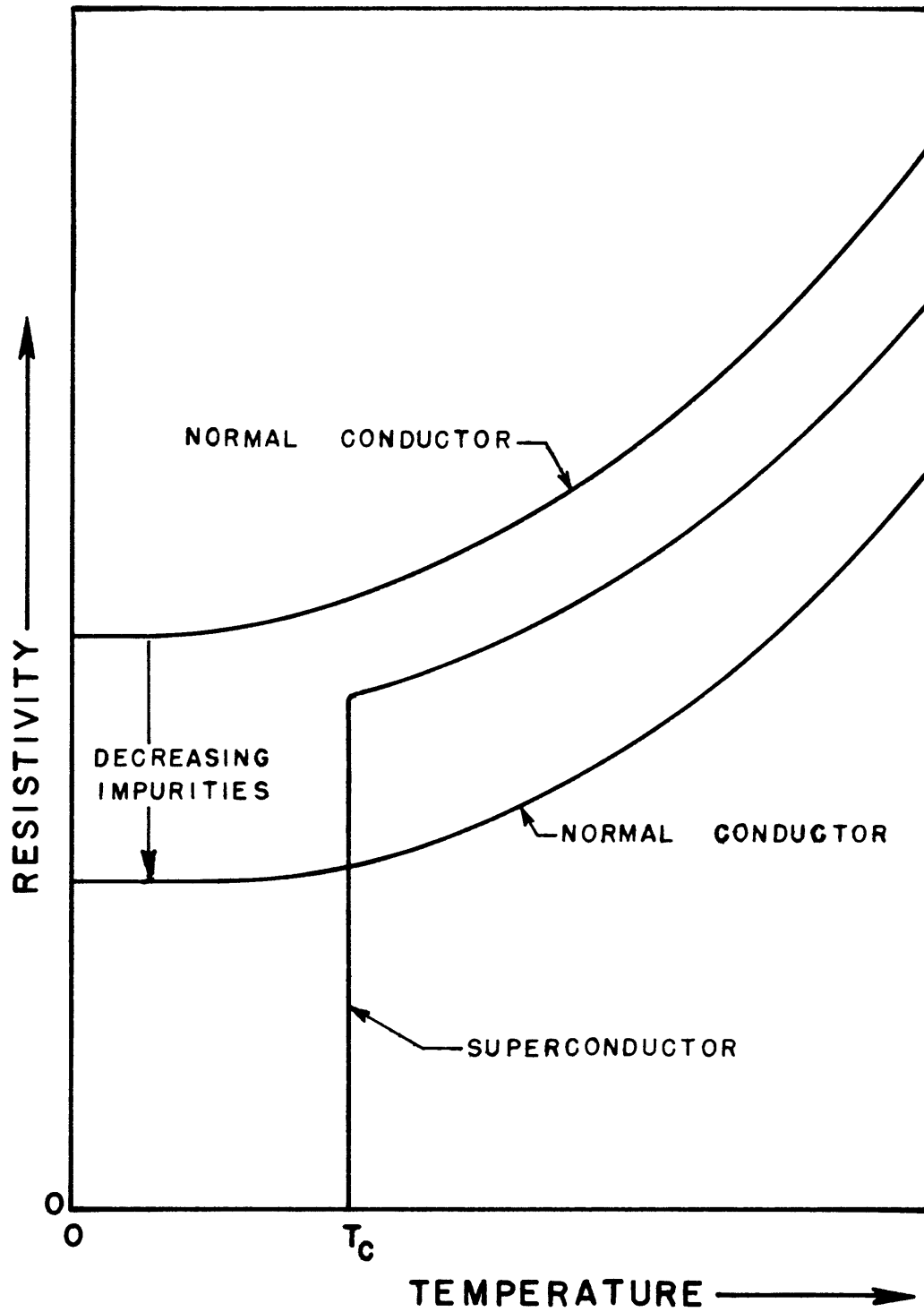


Fig. II.1. Resistivity of superconducting and normal conductors as a function of temperature.

ductor. The residual resistivity of a normal conductor can be reduced, and even made vanishingly small at $T=0$, by reducing the level of impurities and defects in the material, though it will always have a finite resistance at a finite temperature. The superconductor on the other hand exhibits a distinct and sudden transition to zero resistivity at a finite temperature.

The characteristic phenomena of zero dc electrical resistance, however, is not sufficient to explain the extraordinary magnetic behavior of materials in the superconducting state. One of the fundamental magnetic phenomena exhibited by superconductors is their ability to expel a magnetic field from the interior of the bulk superconductor when the material is cooled below the transition temperature, T_c , in a magnetic field. This was discovered by Meissner and Ochsenfeld and is referred to as the Meissner effect [17]. A superconductor never allows any magnetic flux in the interior. This is a characteristic of materials possessing perfect diamagnetism. The sequence of pictures in Figs. 2.2 and 2.3 illustrate the behavior of perfect conductance and perfect diamagnetism respectively. The Meissner effect is shown in the sequence of Figures 2.3a to 2.3g. The perfect conductor behavior is characterized by $dB/dt = 0$ everywhere in the material, while the superconductor is characterized by $B = 0$ everywhere in the material.

The bulk superconductor is perfectly diamagnetic up to the critical field, H_c when the superconducting state is destroyed by a phase change into the normal state. The magnetization of the type I superconductor as a function of applied magnetic field is shown in Fig. 2.4. The interior region of the bulk conductor is completely screened by surface super-

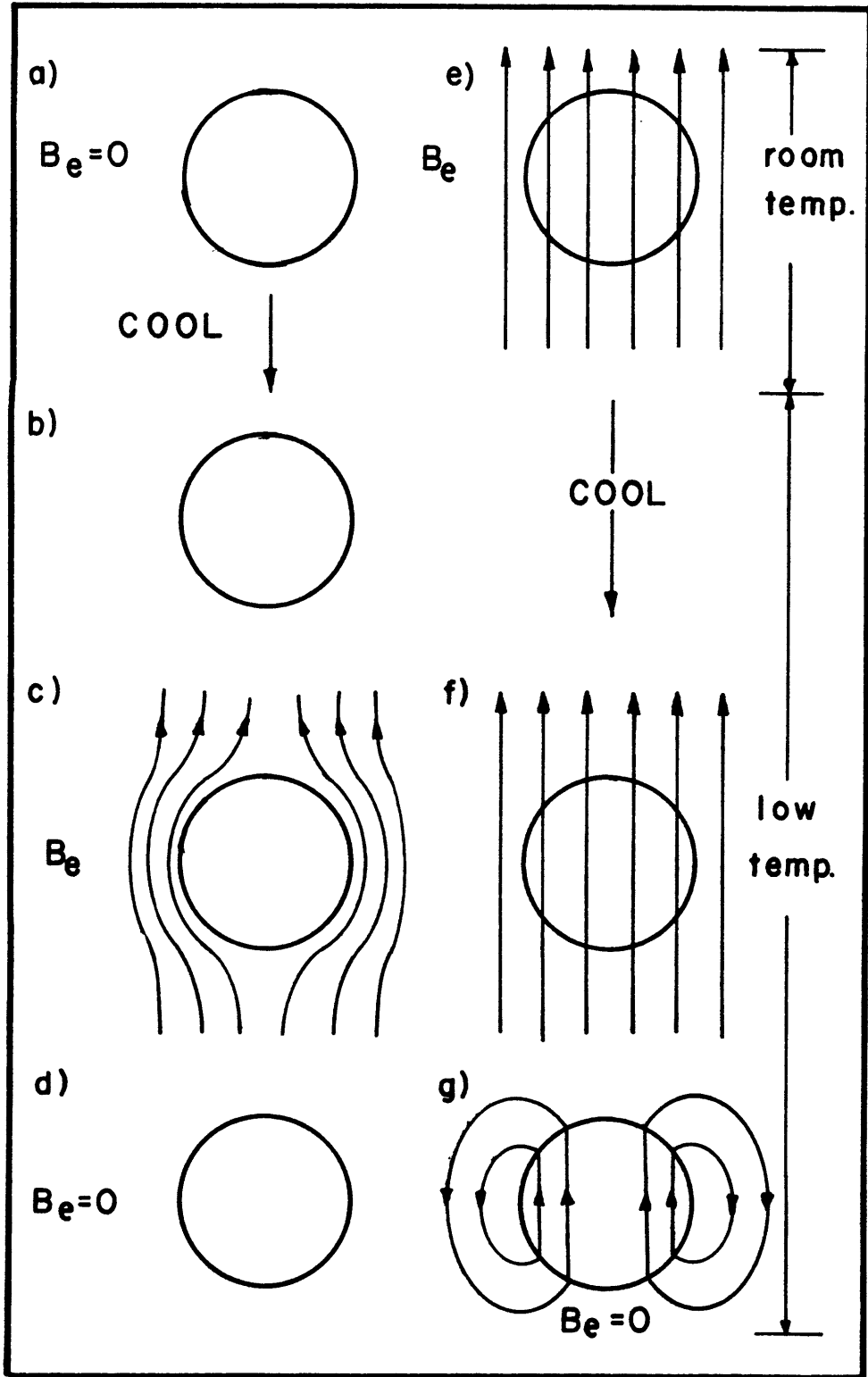


Fig. II.2. Magnetic behavior of a perfect conductor.

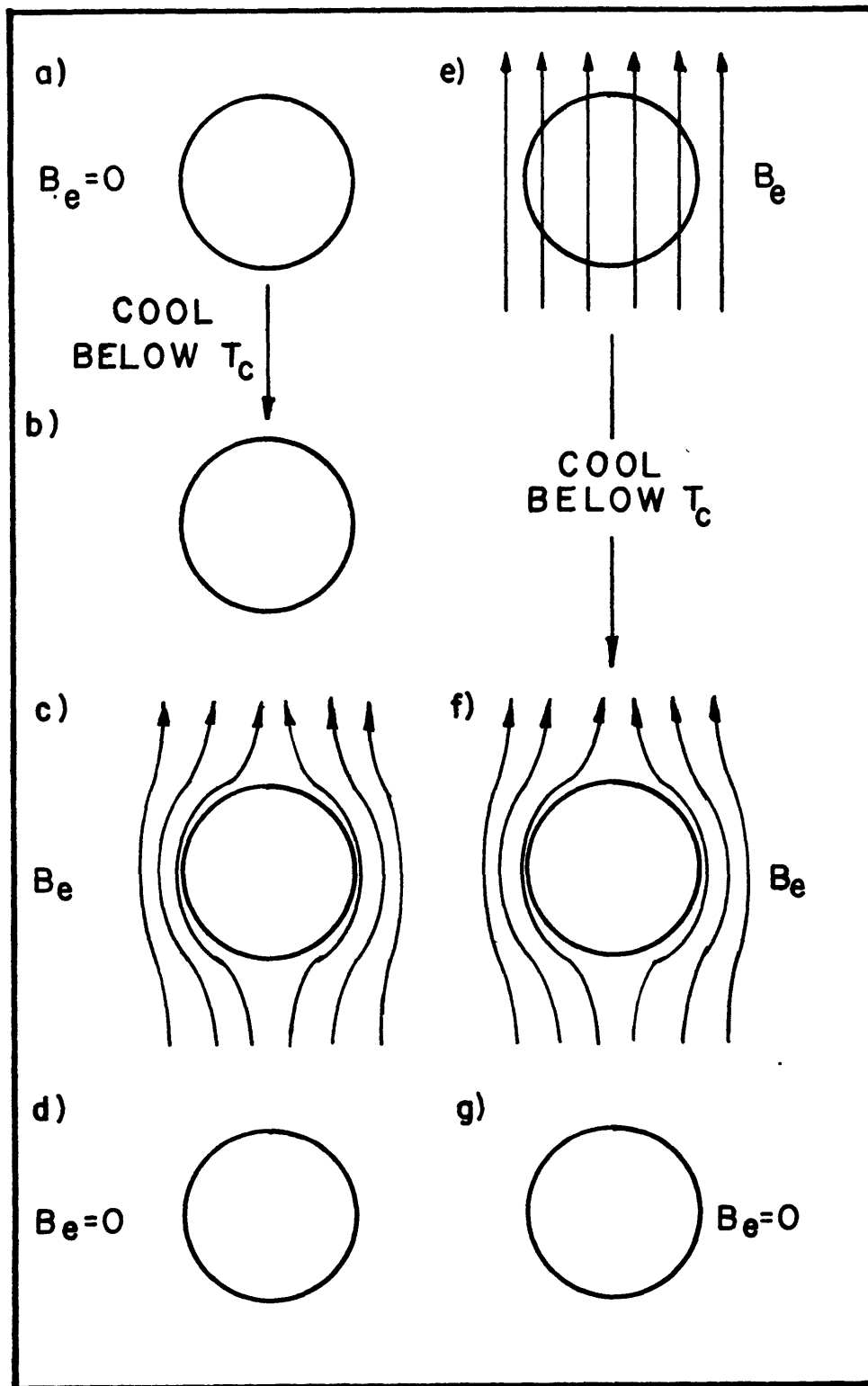


Fig. II.3. Magnetic behavior of a superconductor.

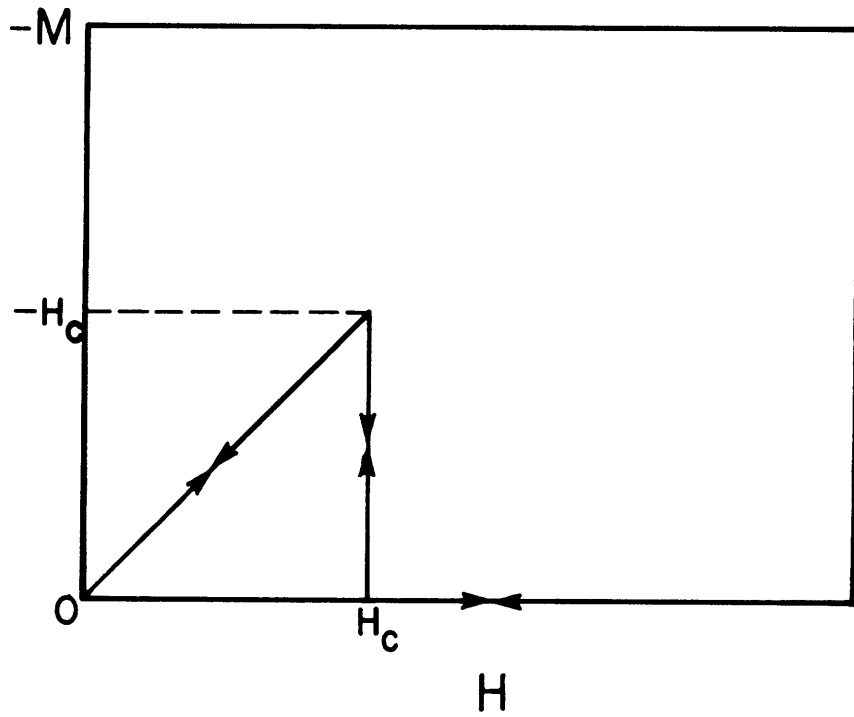


Fig. II.4. Magnetization of ideal Type I superconductor as a function of applied field.

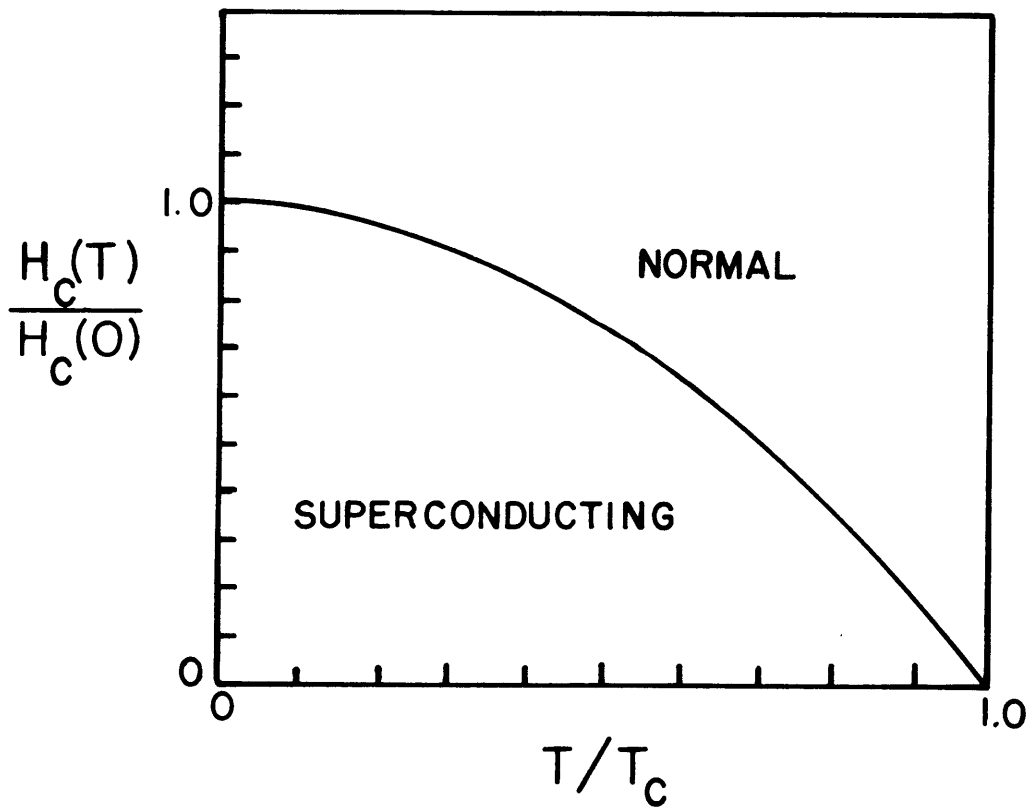


Fig. II.5. Temperature dependence of the critical field.

currents that flow in a penetration layer of depth, λ . Under steady state conditions the superconductor has zero resistance and these screening currents persist indefinitely.

II.2 The Critical Magnetic Field

Early attempts to create useful magnetic fields with superconductors by putting a current through them failed when it was discovered that a strong magnetic field would destroy superconductivity. The critical field, $H_c(T)$, is a function of temperature and decreases to zero at the critical temperature, $T = T_c$. At $T = 0$, $H_c(0)$ is a maximum.

The physical basis for the critical field derives from the energy balance between the energy associated with holding the magnetic field outside against the magnetic pressure and the difference in free energy between the superconducting and normal phases. It can be written as

$$\frac{\mu_0 H_c^2(T)}{2} = f_n(T) - f_s(T) \quad , \quad (2.1)$$

where $f_n(T)$ is the free energy density in the normal state and $f_s(T)$ is the free energy density in the superconducting state at zero field. The variation of critical magnetic field with temperature has been experimentally determined to be approximately parabolic:

$$H_c(T) \approx H_c(0) \left[1 - \left(\frac{T}{T_c} \right)^2 \right] . \quad (2.2)$$

The critical field versus temperature variation is shown in Fig. 2.5.

The critical field characteristics and the Meissner effect allow us to construct the magnetization curve for a type I superconductor. If the magnetic field is applied parallel to a specimen such that the de-

magnetizing coefficient is zero we can write

$$B = \mu_0(H + M) \quad (2.3a)$$

and inside the specimen

$$B = 0 \quad \text{so} \quad -M = H \quad (2.3b)$$

The magnetization curve (shown in Fig. 2.4) can be traced reversibly. Since the types of superconductors that exhibit this behavior are mostly pure elements, such as mercury, lead, tin, etc., they are sometimes called soft superconductors.

II.3 Thermodynamic Phase Transition

The fact that the transition between the superconducting and normal states is reversible allows the use of equilibrium thermodynamics to describe this phase transition. According to the Gibbs Phase Rule for a pure substance two intensive properties must be independently specified to fix the state of one phase of the substance. Those two properties are normally chosen to be temperature, T , and magnetic field, H since they are the variables most normally controlled. Then the specific Gibbs free energy $g(H,T)$ for either phase can be written as [18]

$$g(H,T) = f(T) + \int H dM \quad (2.4)$$

where $f(T) = g(0,T)$. For the normal phase $B = \mu_0 H$ from Eq. (2.3a) because $M = 0$ so

$$g_n(H,T) = f_n(T) - \mu_0 \frac{H^2}{2} \quad (2.5)$$

However, for the superconducting phase $B = 0$ (Eq. 2.3b) and

$$g_s(H,T) = f_s(T) \quad (2.6)$$

Now for any two phases of a pure substance in equilibrium the Gibbs free energy of each phase must be equal, thus

$$g_s(H,T) = g_n(H,T) \quad (2.7)$$

Substituting Eqs. (2.5) and (2.6) in Eq. (2.7) and noting that $H = H_c(T)$ at the phase transition we get

$$\frac{\mu_0 H_c^2(T)}{2} = f_n(T) - f_s(T) \quad (2.8)$$

which is identical to Eq. (2.1) which was written previously without proof. This energy difference is called the "condensation energy".

Some other interesting thermodynamic properties such as the latent heat and the specific heat can also be easily derived. The specific entropy s is given by

$$s = - \left(\frac{\partial f}{\partial T} \right) \quad (2.9)$$

and thus the latent heat per unit volume for a reversible transition is given by

$$Q = T(s_s - s_n) = \mu_0 T H_c \frac{d H_c}{dT} \quad (2.10)$$

For the specific heat

$$c = T \left(\frac{\partial s}{\partial T} \right)_H \quad (2.11)$$

so for the change in specific heat for the two phases we get

$$(c_n - c_s) = - \mu_0 \left[T \left(\frac{\partial H_c}{\partial T} \right)^2 + T H_c \frac{\partial^2 H_c}{\partial T^2} \right] \quad . \quad (2.12)$$

From Fig. 2.5 it can be seen that $\partial H_c / \partial T$ is always negative so Eq. (2.10) indicates that the entropy of the superconducting phase is less than the entropy of the normal phase. Thus it is not surprising that the superconducting state is usually considered a more ordered state of the material. Indeed there is a higher degree of order due to the pairing of the electrons. At $T = 0$ the entropy must be zero from the third law of thermodynamics so that the latent heat is also zero. At finite temperatures and fields the specimen releases heat during the phase transition since Eq. (2.10) is negative. At the critical temperature, T_c the critical magnetic field, $H_c = 0$ so that the latent heat is again zero. Figure 2.6 shows the variation in the entropy of the two phases as a function of temperature.

From Eq. (2.12) it can be seen that the specific heat of the two phases are equal to zero at $T = 0$. At the critical temperature, $H_c = 0$ and Eq. (2.12), reduces to

$$c_n - c_s = - \mu_0 T_c \left(\frac{\partial H_c}{\partial T} \right)^2 \quad , \quad (2.13)$$

that is, there is a discontinuity in the specific heat at this point. This is called a "second order transition". It is somewhat analogous to the jump in specific heat of liquid helium at the lambda point where it becomes superfluid helium II. At some intermediate values of T the

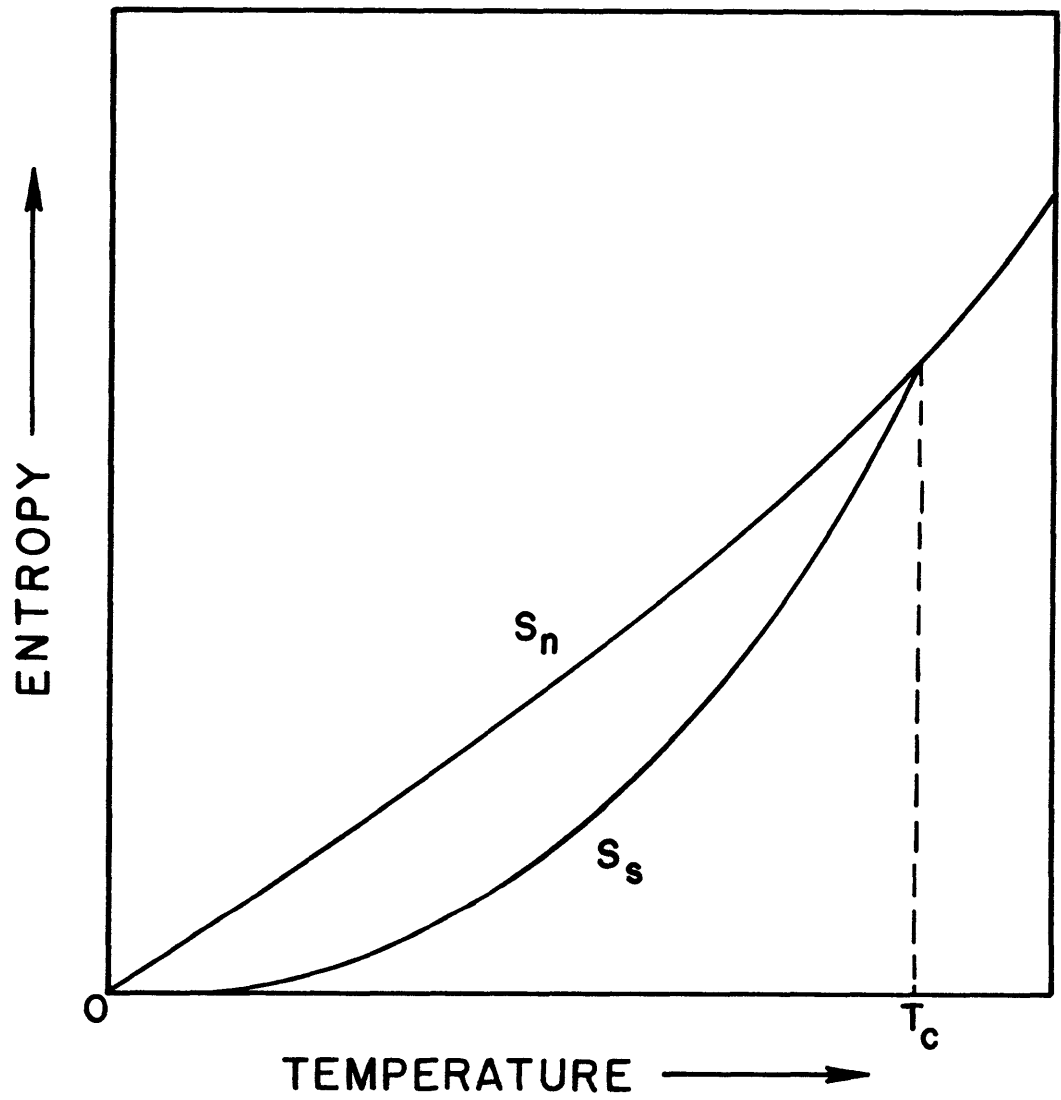


Fig. II.6. Variation of the entropy with temperature for the superconducting and normal phases.

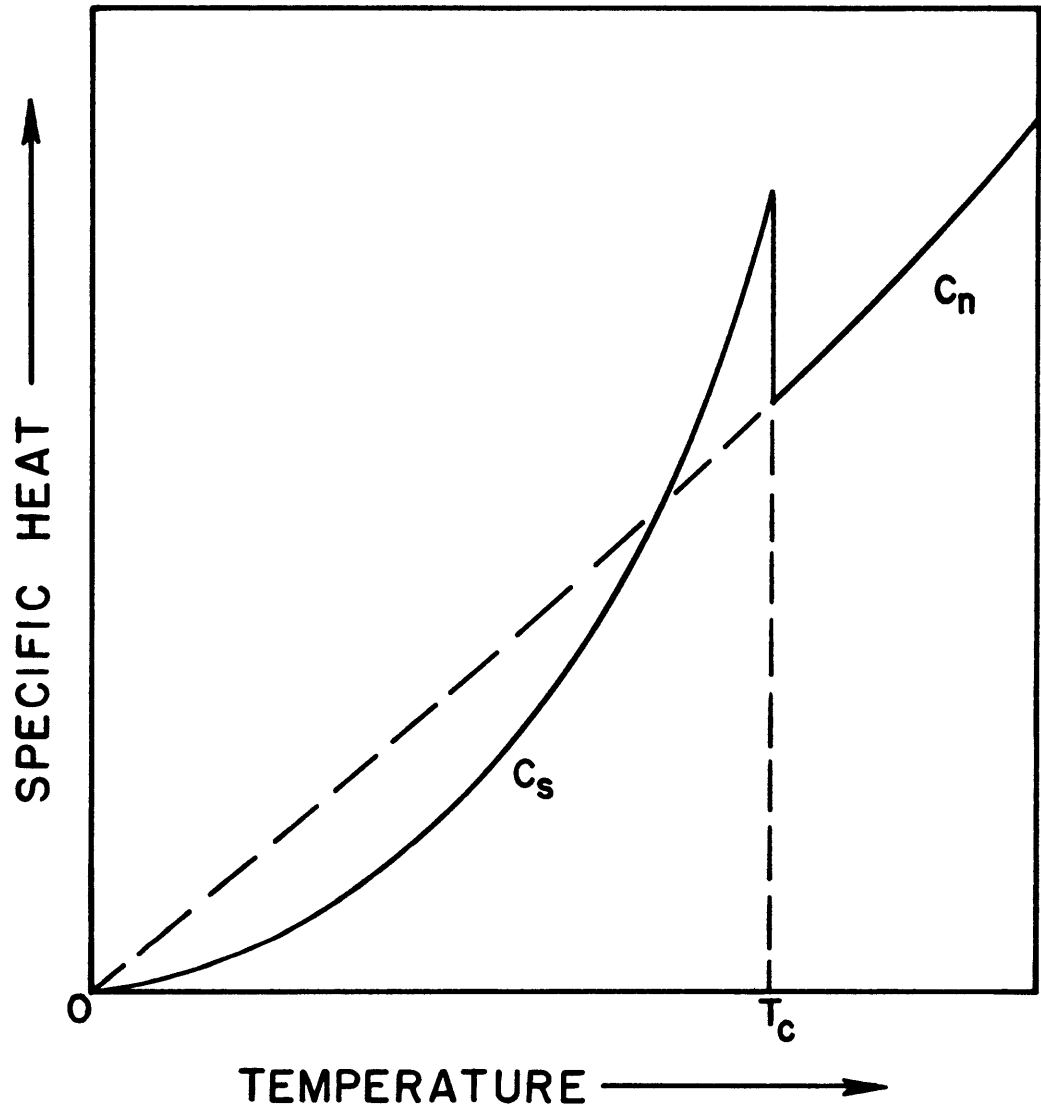


Fig. II.7. Variation of the electronic specific heat with temperature showing the discontinuous jump between the superconducting and normal phases.

change in the specific heat is positive and at other values it is negative during the phase transition. This is shown schematically in Fig. 2.7, where the specific heat for the normal and superconducting phases are plotted as a function of temperature.

All of this thermodynamic development has been based upon the phase transition being reversible. Experimental measurements of the specific heat and the critical field variation with temperatures have confirmed the reversibility of the transition.

II.4 Electrodynamics and the Penetration Depth

In 1933 the brothers F. and H. London proposed a phenomenological set of equations to describe the observed magnetic behavior of superconductors [19]. The set of equations which have become known as the London equations are:

$$\mathbf{B} = - \frac{m}{n_s e^2} \nabla \times \mathbf{J} \quad (2.14)$$

and

$$\frac{\partial \mathbf{J}}{\partial t} = \frac{n_s e^2}{m} \mathbf{E} \quad (2.15)$$

where n_s is the number of superelectrons per unit volume and m and e are their mass and electric charge, respectively. These equations supplement but do not replace the Maxwell equations. Note that from the Maxwell equation, $\nabla \times \frac{\mathbf{B}}{\mu_0} = \mathbf{J}$,

$$\mathbf{B} = - \frac{m}{n_s e^2} \nabla \times \mathbf{J} = \frac{-m}{n_s e^2} \nabla \times \left(\nabla \times \frac{\mathbf{B}}{\mu_0} \right)$$

so

$$\mathbf{B} = - \frac{m}{n_s e^2} \left[\nabla(\nabla \cdot \frac{\mathbf{B}}{\mu_0}) - \nabla^2 \frac{\mathbf{B}}{\mu_0} \right]$$

by vector identity and since $\nabla \cdot \mathbf{B} = 0$

$$\mathbf{B} = \frac{m}{\mu_0 n_s e^2} \nabla^2 \mathbf{B} .$$

This can be rewritten as

$$\nabla^2 \mathbf{B} = \frac{1}{\lambda_L^2} \mathbf{B} \quad (2.16)$$

where

$$\lambda_L = \frac{m}{\mu_0 n_s e^2}$$

is the London penetration depth. This equation agrees with the observed phenomena of the Meissner effect because it shows the interior is exponentially screened from the applied field. For example, if the above equation is applied to the geometry of a one-dimensional slab in a uniform external field (Fig. 2.8) we can write

$$\frac{\partial^2 B(x)}{\partial x^2} = \frac{1}{\lambda_L^2} B(x)$$

which has solutions of the form

$$B(x) = C_1 e^{x/\lambda_L} + C_2 e^{-x/\lambda_L} .$$

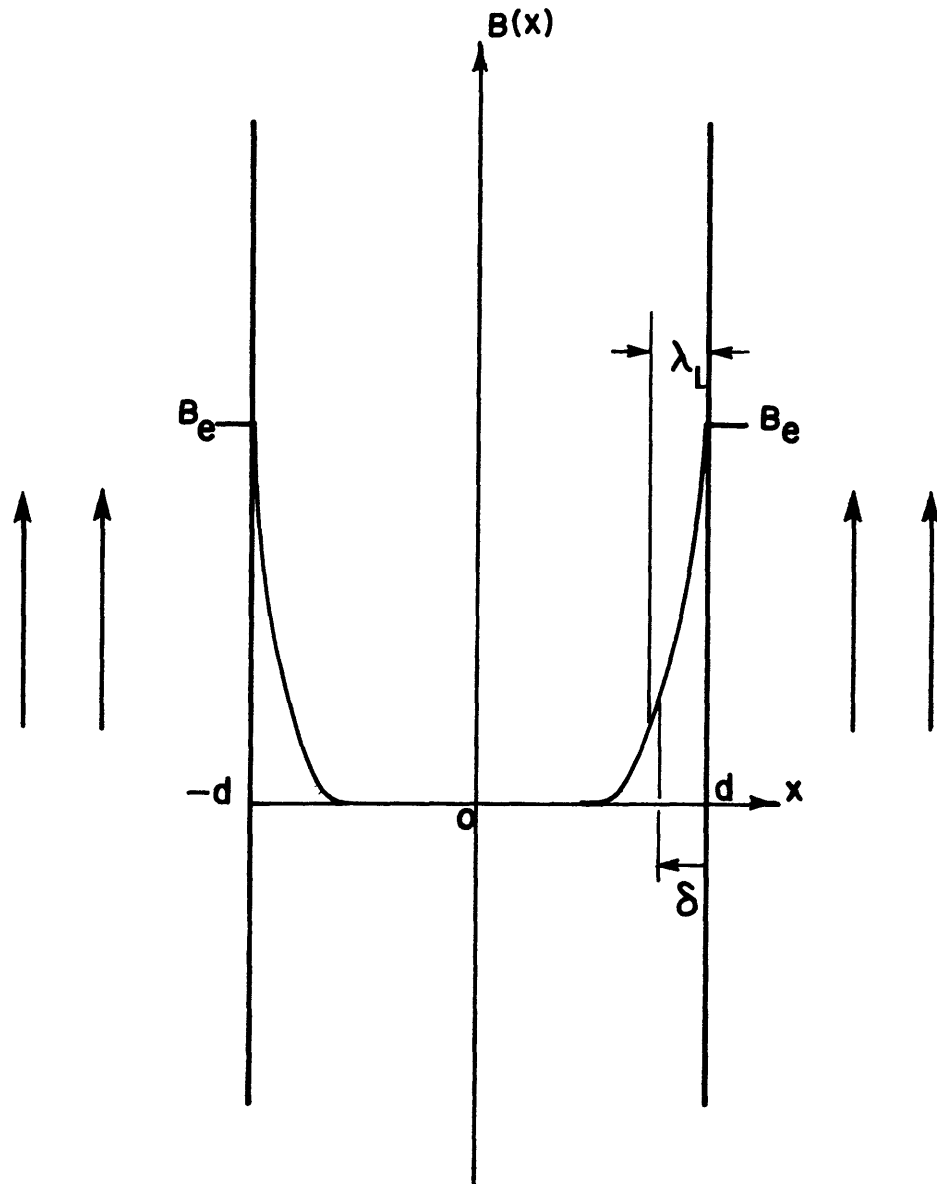


Fig. II.8. Flux penetration into a slab of Type I superconductor showing the London penetration depth λ_L .

For $B(\pm d) = B_e$ we get

$$B(x) = \frac{B_e}{\cosh(d/\lambda_L)} \cosh(x/\lambda_L) \quad .$$

Figure 2.8 shows the field profile in the slab superconductor. Near the surface

$$B(x) \approx B_e e^{-\delta/\lambda_L}$$

where

$$\delta = d - x$$

is the distance from the surface. The London penetration depth, λ_L , is based upon classical theory and thus is only qualitatively correct. The more rigorous microscopic BCS theory and the Ginzburg-Landau theory give more accurate values for λ based upon quantum effects. However, the London parameter is good to within a factor of about 2 and has a typical value of order 500 Å.

II.5 The Coherence Length

The other important parameter in superconductivity is the coherence length, ξ . It was originally introduced by Pippard [20] in 1953 but a more rigorous treatment is given by the Ginzburg-Landau theory. The concept of the coherence length stems from the electron interaction in the superconducting state.

The superconducting state is an ordered state of the conduction electrons in a metal. At room temperature the conduction electrons form a gas, but at low temperature, below T_c , they condense into a state of

lower energy in which they form loosely bound pairs. As an electron passes near the lattice ions an attractive coulomb interaction occurs which deforms the lattice. The disturbance propagates through the lattice as a phonon, which transmits the momentum lost by the first electron to a second electron, keeping the total momentum of the electron pair a constant. The total attractive interaction must be greater than the screened repulsion of the two electrons.

These two electrons are thus weakly bound and referred to as Cooper pairs. The distance over which they interact is large and so necessarily encompass many other such paired electrons. However every pair has the same constant total momentum so that nothing prohibits a pair from breaking up and reforming with any other pair through a phonon interaction. This maintains the maximum possible number of pairs at any time. If an electric field is applied the pairs behave as a single particle with two electron charges with the center of mass of all pairs having the same momentum. Each pair is locked in with the motion of every other pair. They can carry a resistanceless current because none of the paired electrons can be scattered by lattice imperfections which normally cause low temperature residual resistance. Thus they are superconducting. The thermal conductivity is less in the superconducting state than in the normal state because the heat conduction occurs by an individual electron energy exchange process.

This collective interaction of the electrons in a superconductor is somewhat similar to but not quite the same as the collective behavior of the helium atoms in superfluid liquid helium II.

Since superconductivity requires a strong coupling between the conduction electrons and the lattice, it is not surprising to find that materials with very good normal conductance do not become superconducting. The conduction electrons in these materials interact very weakly with the lattice.

The distance over which the electron pair interacts is called the coherence length. The distance is typically of the order 10^4 \AA , in pure metals, but it is reduced by impurities in the conductor. For a perfectly pure conductor the coherence length is denoted by ξ_0 . Pippard proposed that in the presence of scattering by impurities ξ vary as

$$\frac{1}{\xi} = \frac{1}{\xi_0} + \frac{1}{\ell}$$

where ℓ is the mean free path.

The true significance of ξ was shown by the Ginzburg-Landau theory. They introduced a complex pseudowave function ψ as an order parameter of the superconducting electrons such that $n_s = |\psi(x)|^2$ where n_s is, as before, the volume density of the superelectrons. This ξ is the characteristic length of the order parameter.

II.6 Type I and Type II Superconductivity

Ginzburg and Landau combined the two important parameters of penetration depth and coherence length into a single parameter by forming their ratio,

$$\kappa \equiv \frac{\lambda}{\xi} \quad (2.17)$$

In a pure type I superconductor κ is small. Abrikosov used this parameter to define the difference between type I and type II superconductors by investigating what happens if κ is made large. The effect is shown in Fig. 2.9. The values of superelectron density, n_s , magnetic field, H , and free energy density, f , are shown as a function of distance from a superconducting to normal interface for both type I and type II superconductivity. The difference between the two types is that in I the surface energy is positive at the interface whereas in II the surface energy is negative. For type I this means that it is energetically favorable for superconductivity to be destroyed rather than have normal regions coexist with superconducting regions for fields above H_c . Thus the bulk superconductor goes normal above the critical field. However, the inverse is true for type II superconductors. In this case, regions of superconductivity can coexist with the normal material above H_c . Abrikosov discovered that this does indeed occur. He determined that for values of $\kappa > 1/\sqrt{2}$ the material enters the mixed state with a continuous increase of flux penetration above $H_{c1} < H_c$ up to a second critical field $H_{c2} = \sqrt{2}\kappa H_c$. The magnetization of the two types of superconductors as a function of field strength is shown in Fig. 2.10.

In addition Abrikosov discovered that the flux is quantized and enters as a regular array of individual flux tubes or vortices each containing one flux quantum of magnitude $\phi_0 = 2.07 \times 10^{-15}$ webers. The central core of the tube which contains the flux quantum is normal and the remaining superconducting material is screened from the flux by a supercurrent ring surrounding the tube (Fig. 2.11).

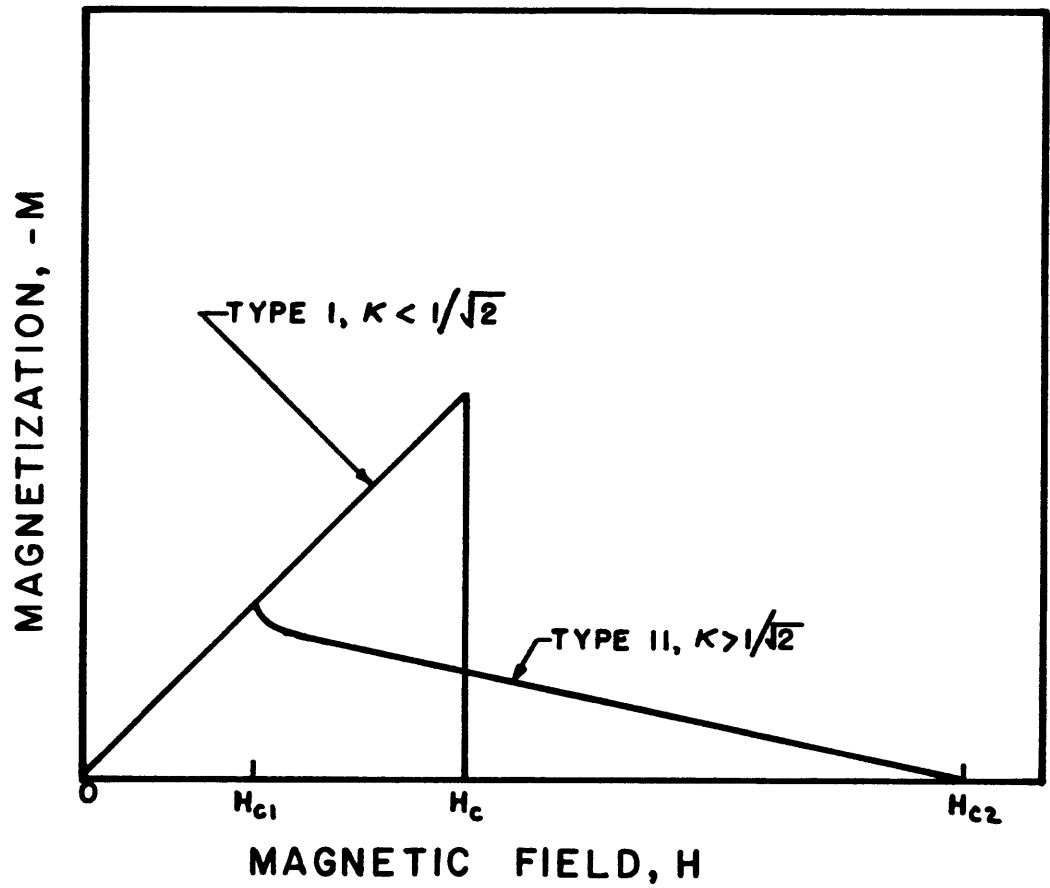
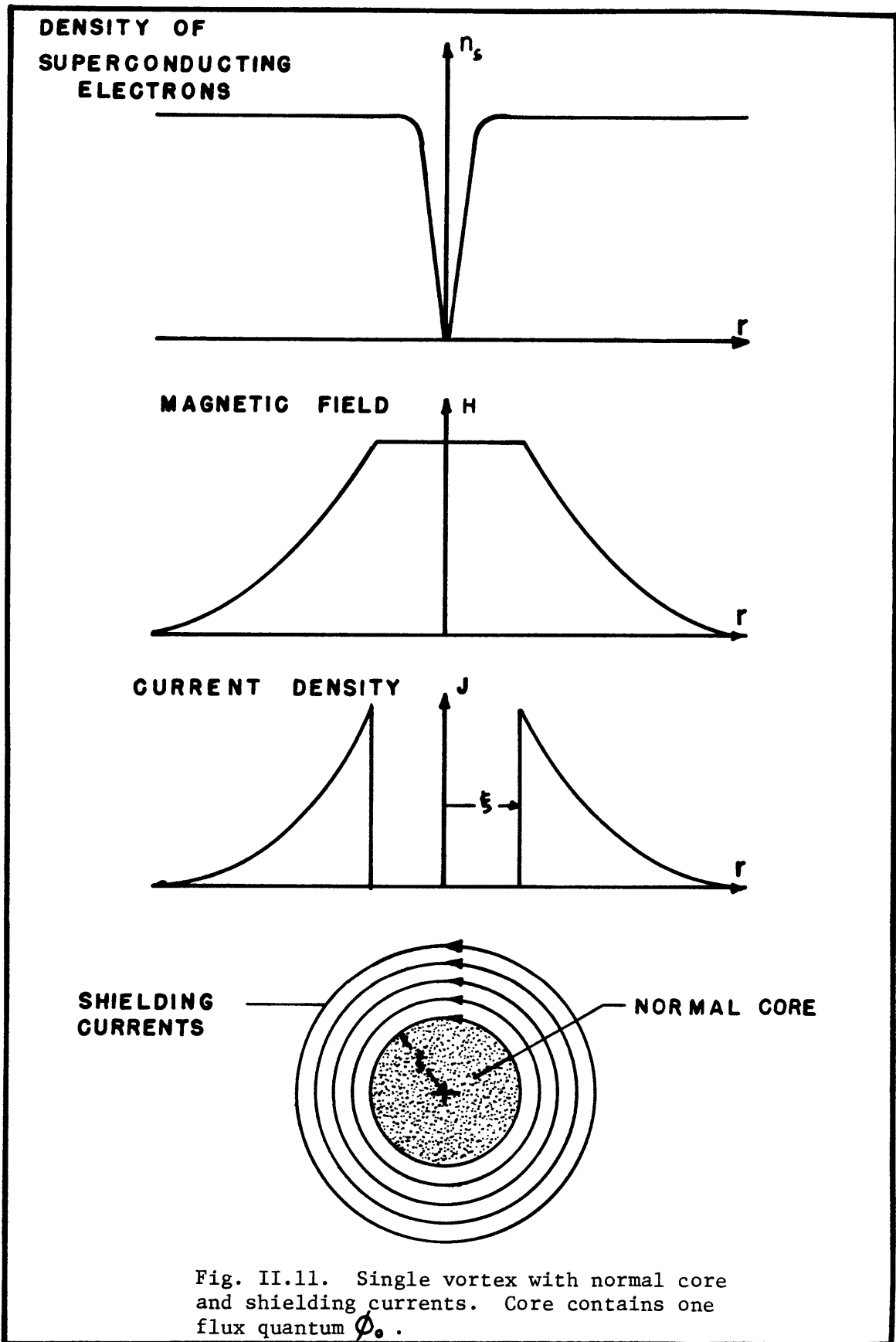


Fig. II.10. Magnetization curves for ideal type I and type II superconductors. The area under both curves is equal to the condensation energy $\mu_0 \frac{H_c^2}{2}$.



Normally for very pure or "soft" metals κ is less than $1/\sqrt{2}$ and these are type I. For impure metals or alloys, ξ is reduced, and κ is greater than $1/\sqrt{2}$ and these "hard" materials are of type II. The different types of superconducting states as a function of κ are shown in Fig. 2.12.

Since the superconductors of technological importance are the high critical field type II conductors, some time should be spent understanding the flux and current structures in the mixed state. An ideal type II superconductor will have no defects in the lattice or atom impurities to pin the flux quanta. The equilibrium flux distribution is a triangular lattice array of the vortices uniformly distributed over the cross section of the material and oriented parallel to the applied field. At low values of applied field the vortices are widely spaced. As the external field is increased the vortices get packed in tighter and tighter until just at the critical field all the normal cores of the vortices begin to overlap and the remaining superconductivity is totally destroyed. The actual vortex lattice may deviate from the ideal triangular lattice due to interactions with the crystal lattice. The basic vortex lattice of an ideal conductor is shown in Fig. 2.13.

In reality, however, there are no ideal superconductors. This is actually very fortunate since they do not have a very high value of H_{c2} or high critical current. Relatively impure type II superconductors have high values of H_{c2} due to the high value of κ . In addition the defects and impurities in the lattice create pinning sites for the flux vortices. The critical current of the superconductor increases directly

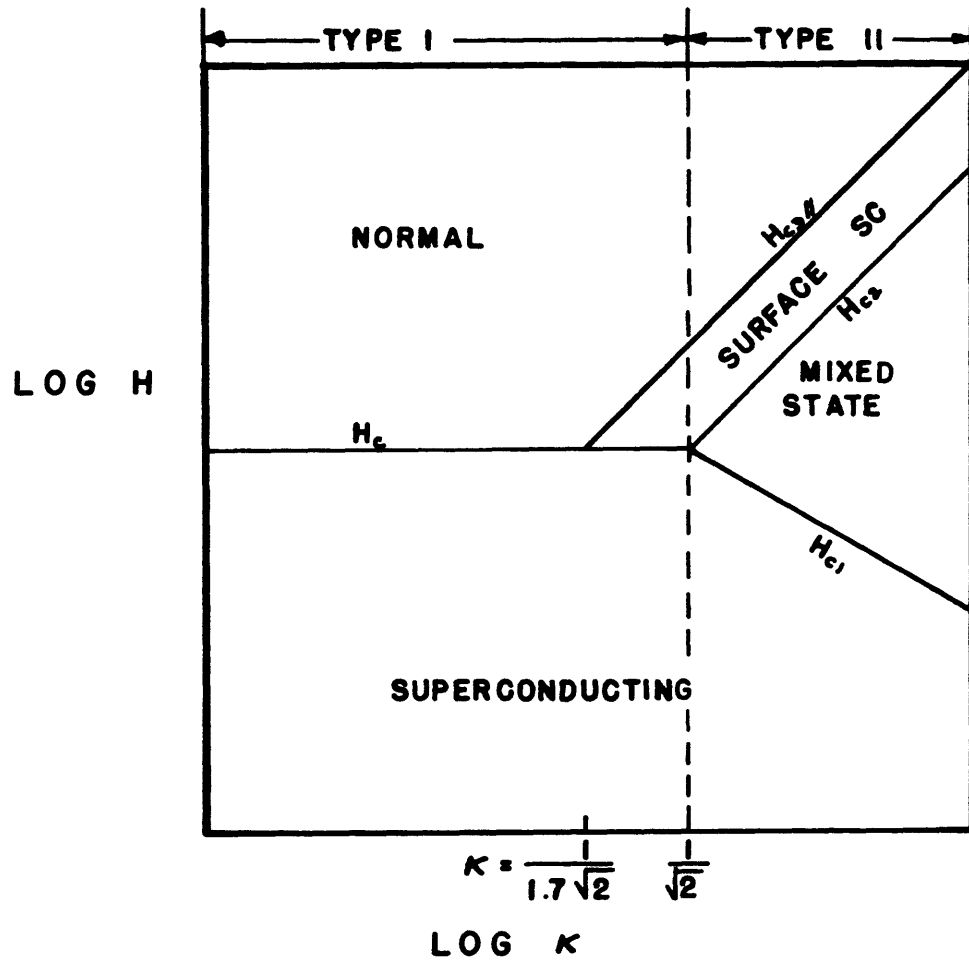


Fig. II.12. Diagram showing different superconducting states as a function of magnetic field and the parameter κ .

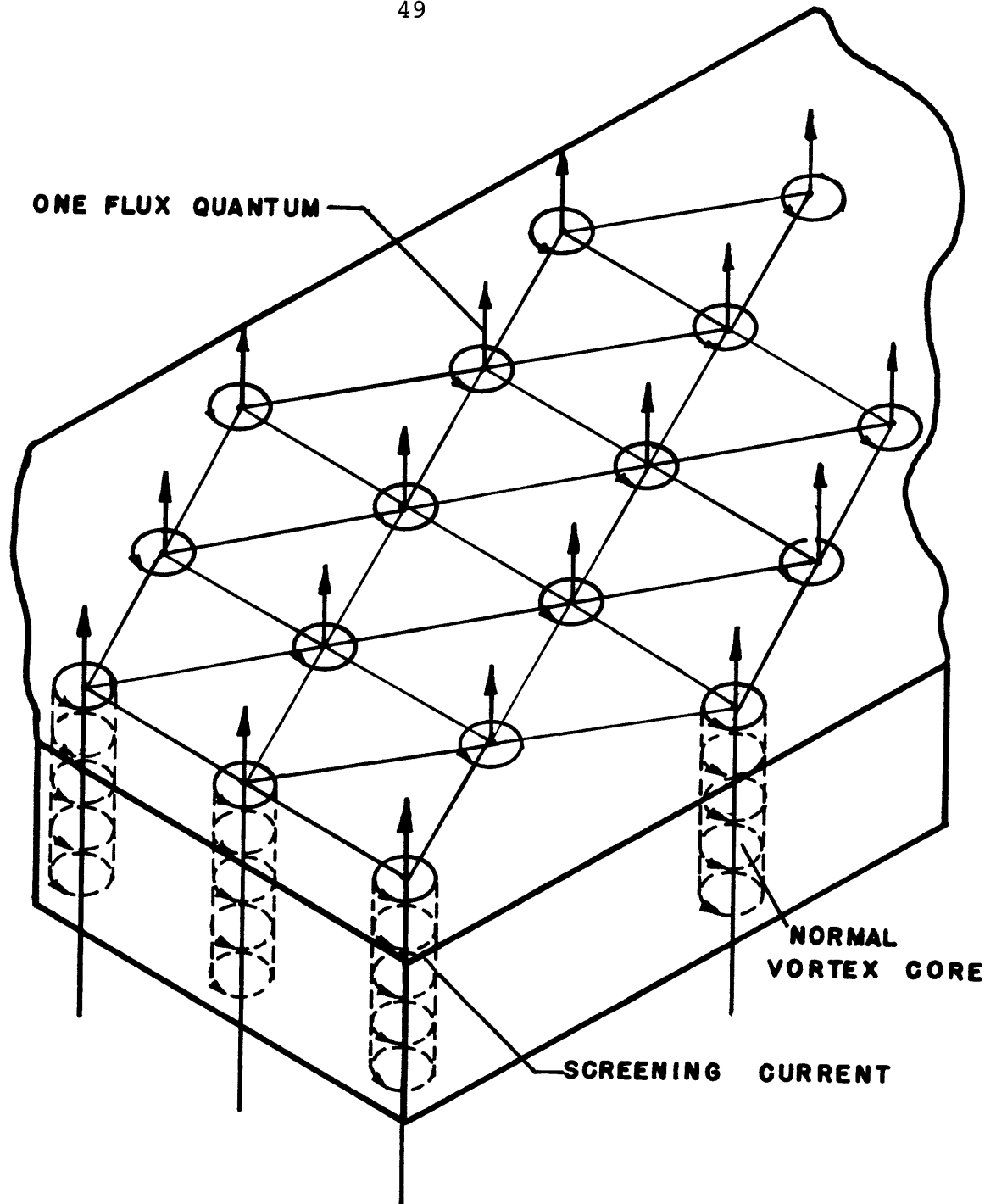


Fig. II.13. Flux penetration into an ideal type II superconductor showing the vortices surrounded by the screening currents. Each vortex contains one flux quantum. A triangular lattice pattern is formed to minimize the energy.

with the number and strength of the pinning sites. The reasons for this behavior will become clear from the explanation of flux motion and flux flow resistivity.

II.7 Flux Flow and Flux Flow Resistivity

The phenomena of flux motion and flux flow resistivity are really the heart of the dissipative mechanism in superconductors. In order to understand the phenomena it must be shown that the flux vortices do indeed move and if they move, the action is dissipative. This can be shown by considering the case of an unpinned ideal type II superconductor carrying a transport current in a uniform background field as shown in Fig. 2.14. The transport current interacts with the flux quanta to exert a Lorentz force on each flux vortex of the form $f_L = J_t \times \phi_0$. In the above expression f_L is the force per unit length on the flux vortex, J_t is the transport current density and ϕ_0 is the quantum of flux in the vortex. The moving flux vortices will induce an electric field E , given by

$$E = v_L \times B = v_L \times n\phi_0 \quad (2.18)$$

where v_L is the velocity of flux lines and n is the number of flux lines per unit area such that $B = n\phi_0$. Since there is no pinning force to balance the Lorentz force, we might assume that the flux lines accelerate and thus E would increase with time. However, the observed voltage indicates that E is constant in time implying a drag force must exist to balance the Lorentz force. This force balance was proposed by Kim [21] in the form

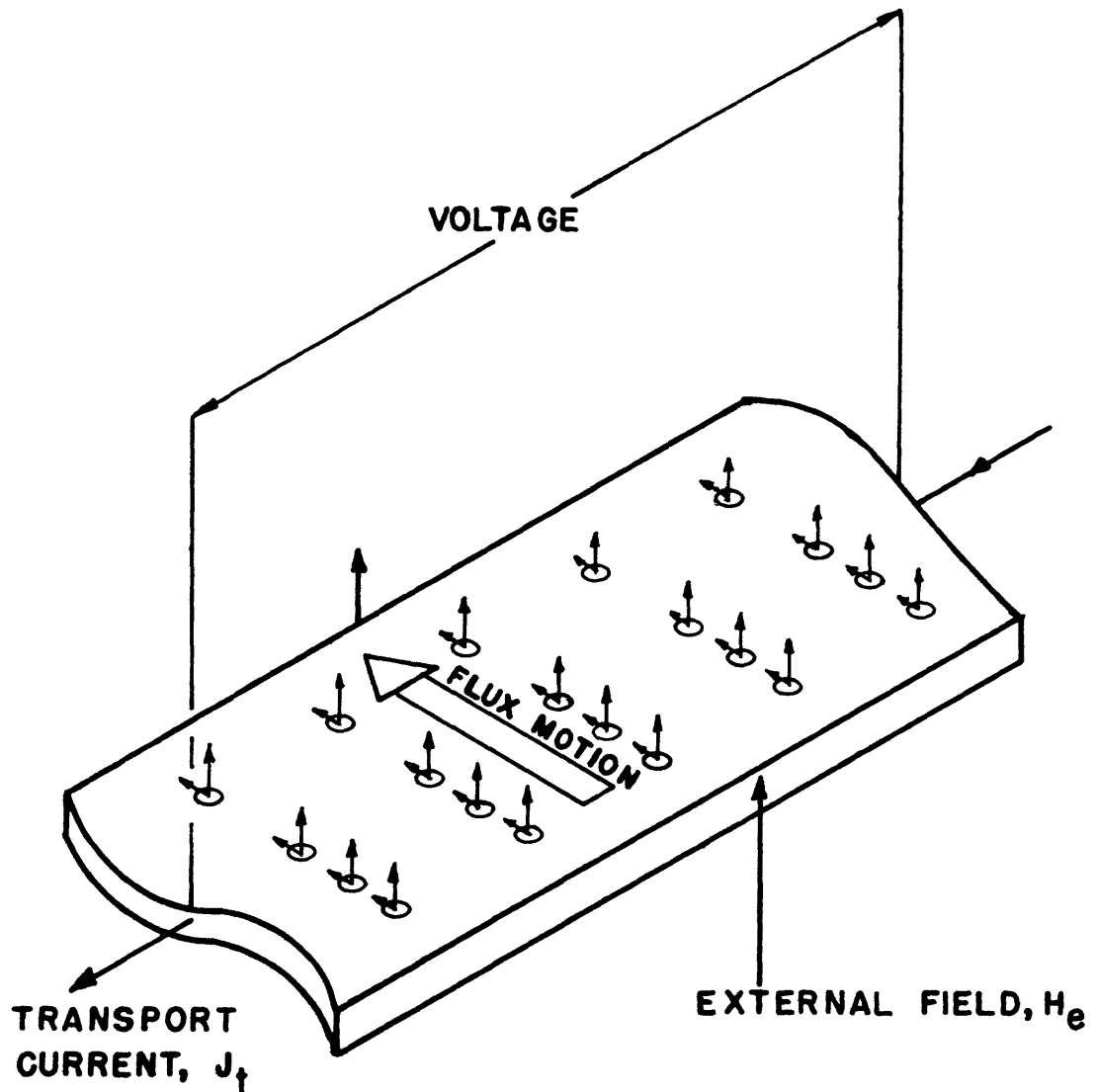


Fig. II. 14. Ideal type II superconductor carrying a transport current in a uniform external field. The Lorentz force drives the flux vortices across the specimen. The flux motion is dissipative and requires a voltage to sustain the transport current.

$$\eta v_L = f_L = J_t \times \phi_0 \quad (2.19)$$

where η is a viscous damping constant. The damping force is dissipative and thus requires a power input $P = J \cdot E$ to maintain the transport current. Equations (2.18) and (2.19) can be combined to define the "flux flow resistivity":

$$\rho_f = \frac{E}{J} = \frac{B\phi_0}{\eta} \quad (2.20)$$

Experimental measurement of ρ_f determines the viscosity coefficient η .

So far, no mention has been made of exactly what is the dissipative mechanism due to a moving vortex. Experimental measurements of ρ_f by Kim, Hempstead and Strand show that it is a function of temperature and as T goes to 0 it is well correlated by the expression

$$\rho_f = \rho_n \frac{H}{H_{c2}} \quad (2.21)$$

where ρ_n is the resistivity of the normal material [9]. The ratio H/H_{c2} is just the fraction of the normal core area. This is a very interesting result because it implies that the dissipation is due to the transport current flowing through the normal cores of the moving flux vortices.

Actually there have been several theories about the dissipative mechanism but one of the more successful and simpler models was derived by Bardeen and Stephen [22]. The model is very simple in that it assumes that all the dissipation takes place by normal resistivity in the central core of the flux vortices where the normal radius is assumed to be equal

$$\eta v_L = f_L = J_t \times \phi_0 \quad (2.19)$$

where η is a viscous damping constant. The damping force is dissipative and thus requires a power input $P = J \cdot E$ to maintain the transport current. Equations (2.18) and (2.19) can be combined to define the "flux flow resistivity":

$$\rho_f = \frac{E}{J} = \frac{B\phi_0}{\eta} \quad (2.20)$$

Experimental measurement of ρ_f determines the viscosity coefficient η .

So far, no mention has been made of exactly what is the dissipative mechanism due to a moving vortex. Experimental measurements of ρ_f by Kim, Hempstead and Strand show that it is a function of temperature and as T goes to 0 it is well correlated by the expression

$$\rho_f = \rho_n \frac{H}{H_{c2}} \quad (2.21)$$

where ρ_n is the resistivity of the normal material [9]. The ratio H/H_{c2} is just the fraction of the normal core area. This is a very interesting result because it implies that the dissipation is due to the transport current flowing through the normal cores of the moving flux vortices.

Actually there have been several theories about the dissipative mechanism but one of the more successful and simpler models was derived by Bardeen and Stephen [22]. The model is very simple in that it assumes that all the dissipation takes place by normal resistivity in the central core of the flux vortices where the normal radius is assumed to be equal

to ξ . They solve for the electric field distribution due to a flux vortex moving across the specimen and then derive the current distribution and energy dissipation due to this induced electric field. The resulting expression for the flux flow resistivity agrees with the empirically determined expression (Eq. 2.21) given by Kim.

Other more rigorous analyses of this dissipative mechanism were given by Schmid [23], Caroli and Maki [24], and Hu and Thompson [25] by using time-dependent Ginzburg-Landau theory. A different approach was taken by Clem [26] who derived the dissipation due to the irreversible entropy generation at the trailing and leading edges of the moving flux vortex where the normal-superconducting transitions occur. There is no consensus as to which analysis is correct, if the different mechanisms are additive, or if they are all different ways of calculating the same thing. No matter, the important point is that dissipation does indeed occur whenever the flux vortices are set in motion and the simple empirical form for the flux flow resistivity is useful to describe this effect.

The flux flow resistivity is the underlying dissipative mechanism that is responsible for the ac loss but it is crucial to note that dissipation only occurs when the vortices are set in motion. In the next chapter it is shown how this flux motion is caused by a changing external magnetic field or transport current. However the flux flow resistivity is not explicitly included in the ac loss calculation. The reasons why this is so should become more clear in Chapter III.

Now that the dissipative mechanism is quantified a lot of the behavior of type II superconductors can be explained. For instance, an ideal type II superconductor has a very low value of critical current, because, in the absence of pinning sites to restrain the flux motion, energy dissipation increases as the square of the current, thereby excessively heating the sample above T_c and destroying the superconductivity.

By contrast, in a nonideal type II superconductor, the number and strength of the pinning sites prevent the flux motion until very high values of current cause the Lorentz force to exceed the pinning force. Experimental verification of the flux flow was done by Van Ooijen and Van Gorp [27], who showed that the flux is actually pinned in "bundles" of many flux quanta. Flux motion is also involved in two other interesting phenomena, namely flux creep and flux jumping. These will be discussed in conjunction with the critical state model.

II.8 The Critical State

The concepts of flux pinning, flux motion and viscous damping have been used to develop the critical state model. Again let's consider a nonideal type II superconductor with pinning. In reality, not every vortex is pinned, just some of them. However, due to the repulsion between fluxons, the vortex lattice is fairly rigid, thereby effectively pinning all the vortices. Thus one can use an average pinning force per unit length of core, f_p . As long as the Lorentz force due to the transport current is less than the pinning force, i.e. $J_t \phi_0 < f_p$, the system is stable.

The critical state then is just the state where the Lorentz force is exactly equal to the pinning force and is governed by the equation:

$$J_c \phi_0 = f_p \quad (2.22)$$

where J_c is called the critical current density. If the current exceeds the critical current, flux flow and dissipation occur.

Bean [28] suggested that $J_c = \text{constant}$, whereas Kim [29] suggested that J_c vary as $1/B$, these two being the most widely used forms of the critical state model. Each form gives accurate results for different conditions of magnetic field.

When J is raised above J_c the Lorentz force exceeds the pinning force and the flux vortices are set in motion. Kim, et al. [30] and later Irie and Yamafuji [31], successfully treated this condition by proposing a force balance between the viscous force, the Lorentz force and the pinning force in the form,

$$\eta v_L = f_L - f_p = \phi_0 (J - J_c) \quad .$$

The induced electric field is

$$E = \frac{B\phi_0}{\eta} (J - J_c) \quad (2.23)$$

Since the dissipative mechanism is the same as that just discussed in the previous section, Eq. (2.23) can be rewritten in the form

$$E = \rho_f (J - J_c) = \left(\rho_n \frac{H}{H_{c2}} \right) (J - J_c) \quad . \quad (2.24)$$

This equation is very useful in computing the energy loss in a superconducting filament carrying a transport current.

Experimental evidence exists to back up Eq. (2.24) [30]. Figure 2.15a shows a typical plot of voltage along a specimen versus current. The different curves show the effect of increasing the impurities for pinning sites and thus increasing J_c . In Fig. 2.15b the effect of H in Eq. (2.24) is shown. The flux flow resistivity is plotted versus applied magnetic field at different temperatures in Fig. 2.15c. The curves are asymptotic to the line for $T = 0$ at low fields. Extrapolation of the measured resistivity data along this line is often done to predict the value of H_{c2} at $T = 0$.

Two other interesting features of the critical state model are phenomena called flux creep and flux jumping. Flux creep is caused by random jumping of flux vortices from one pinning site to another due to thermally induced vibrations. It manifests itself by slow decay of a trapped magnetic field and/or by a measurable resistive voltage. This phenomena has been described by the Anderson-Kim flux creep theory which assumes the vortices move in bundles [32,33]. This creep phenomenon is exceedingly slow resulting in decay times for persistent currents in superconducting loops of many millions of years. However this effect can lead to a potentially more dramatic effect called a flux jump.

The flux jump occurs due to a thermal instability. It is best explained by a series of steps. First assume some flux vortices are set in motion from the pinning site either by flux creep phenomena or

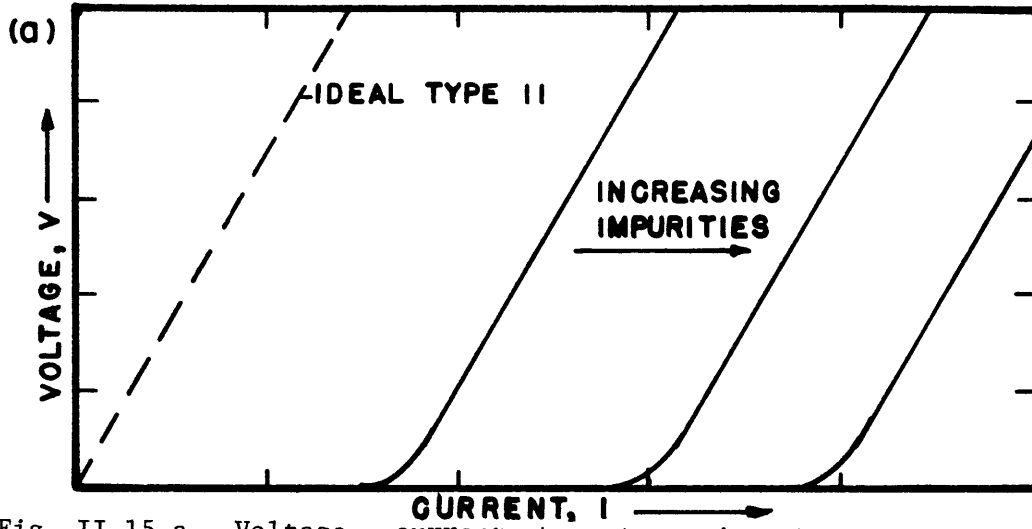


Fig. II.15.a. Voltage - current characteristics showing effect of increased impurities.

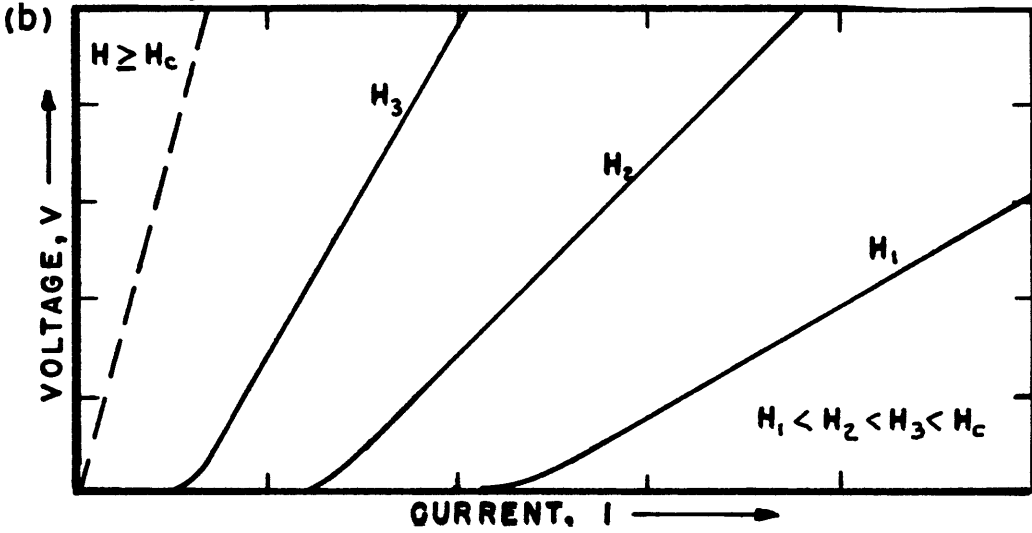


Fig. II.15.b. Effect of magnetic field on voltage - current characteristic.

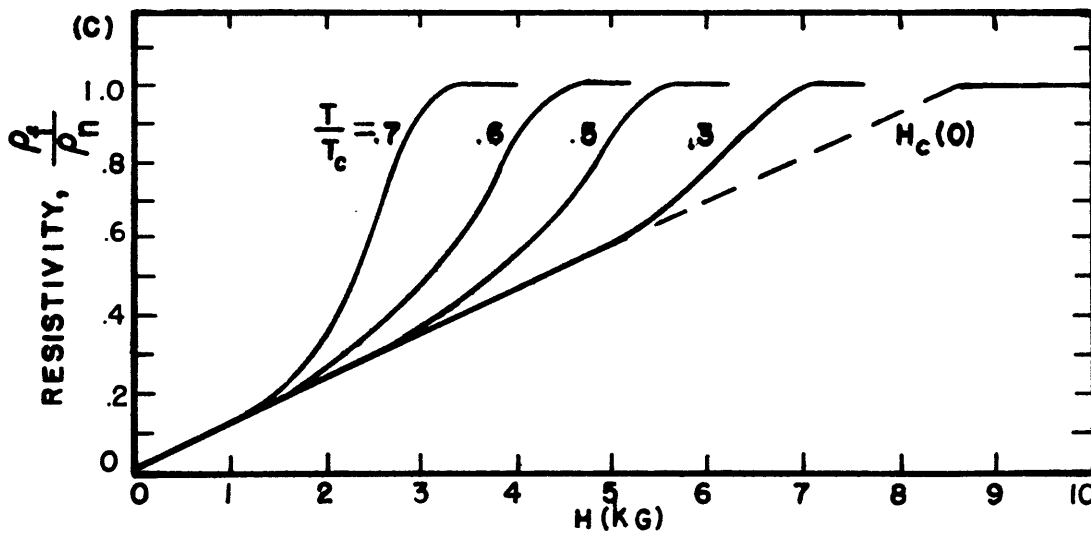


Fig. II.15.c. Flux flow resistivity versus H for different temperatures (after Kim, et. al, 1965.)

due to some other disturbance, such as a change in the external field or transport current or by an increase in temperature. The motion of the vortices dissipates energy which locally increases the temperature. Since the pinning strength is inversely proportional to temperature more vortices can be released from their pinning sites due to the lowered pinning force. This flux motion again leads to more dissipation, higher temperatures, and thus more flux motion in a cascading effect. The total effect is called a flux jump. If the effect is not damped out the result could be a catastrophic flux jump in which the temperature of the sample is rapidly increased above the critical temperature thus creating a normal region which could rapidly propagate and quench the entire winding. Flux creep does not necessarily always lead to flux jumps and flux jumps are not always catastrophic.

Once the underlying physical basis of the phenomena was understood methods of damping this instability were soon devised. These methods are described in the following section on technical superconductors.

II.9 Superconductors for Technical Applications

With the advent of the BCS and GLAG theories of superconductivity in the 1950's it quickly became apparent that the potential for creating high magnetic fields and carrying large currents depended upon the development of practical non-ideal type II superconductors. In 1961 the first high field superconducting solenoid was constructed from reacted Nb_3Sn wire [34]. The problem with Nb_3Sn however is that it is very brittle and thus rather difficult to fabricate into winding forms other than with tape conductors. Although much improvement has been made in the last 20 years

it is still somewhat restricted to very high field solenoids.

Most other early magnets were fabricated from Nb-Zr later to be supplanted by Nb-Ti which remains to date the principal superconducting material in use. The problem with the early magnets however was that their performance was usually much degraded from that expected from the short sample measured performance. The reason was primarily due to flux jumping in the single-core large diameter superconductors. The initial method of dealing with this situation was by means of adiabatic stabilization [35]. That is if the heat capacity of the superconductor was increased such that the maximum temperature reached was less than the critical temperature then the conductor would be stable to the flux jumping. This was accomplished by dividing the superconductor into very small filaments with the maximum filament size given by

$$d \leq \left[- \frac{3C}{\mu_0 J_c \frac{\partial J_c}{\partial T}} \right]^{1/2} \quad (2.25)$$

where d is the filament diameter, J_c is the critical current density and C is the specific heat of the superconductor.

However it was difficult to manufacture very small single filaments so the wires were manufactured by embedding many (on the order of 10 to 10^3) small diameter filaments in a matrix material. Not only did this alleviate the manufacturing process but it added to the stability by providing a low resistance shielding material to damp magnetic fluctuations and also by providing an increased heat capacity to the conductor. This

was called dynamic stabilization. The most common matrix material is copper although aluminium is sometimes also used. However it was soon discovered that the multifilamentary composite conductor with straight filaments acted very similar to the single core conductor because the filaments were coupled by circulating currents that returned through the matrix material. This was alleviated by twisting the filaments within the matrix [36]. One or two twists per inch is a common value for the twist pitch. Thus the twisted multifilamentary composite conductors have continued as the principal type of conductor in use.

An additional method of preventing quenching on a larger scale was due to Kantrowitz and Stekly who proposed cryostatic stabilization [37]. In this method of stabilization a large quantity of matrix material is provided as a low resistance shunt for the current should the superconductor go normal. The current will return to the superconductor (recovery) if the heat is convected to the liquid helium bath at a rate greater than the rate of heat generation by joule heating in the matrix. This usually requires matrix to superconductor ratios on the order of 10 to 20:1. This usually results in windings with very low overall current densities but is often used in very large magnets with a great amount of stored energy where a quench could be disastrous. Typical applications are bubble chamber magnets and large MHD magnets.

Besides the monolithic type wire, superconducting wires have also been manufactured in cabled or braided form. These types of wires are primarily used where ac losses may be a severe problem. Division of the conductors into very small separate individual wires helps alleviate the

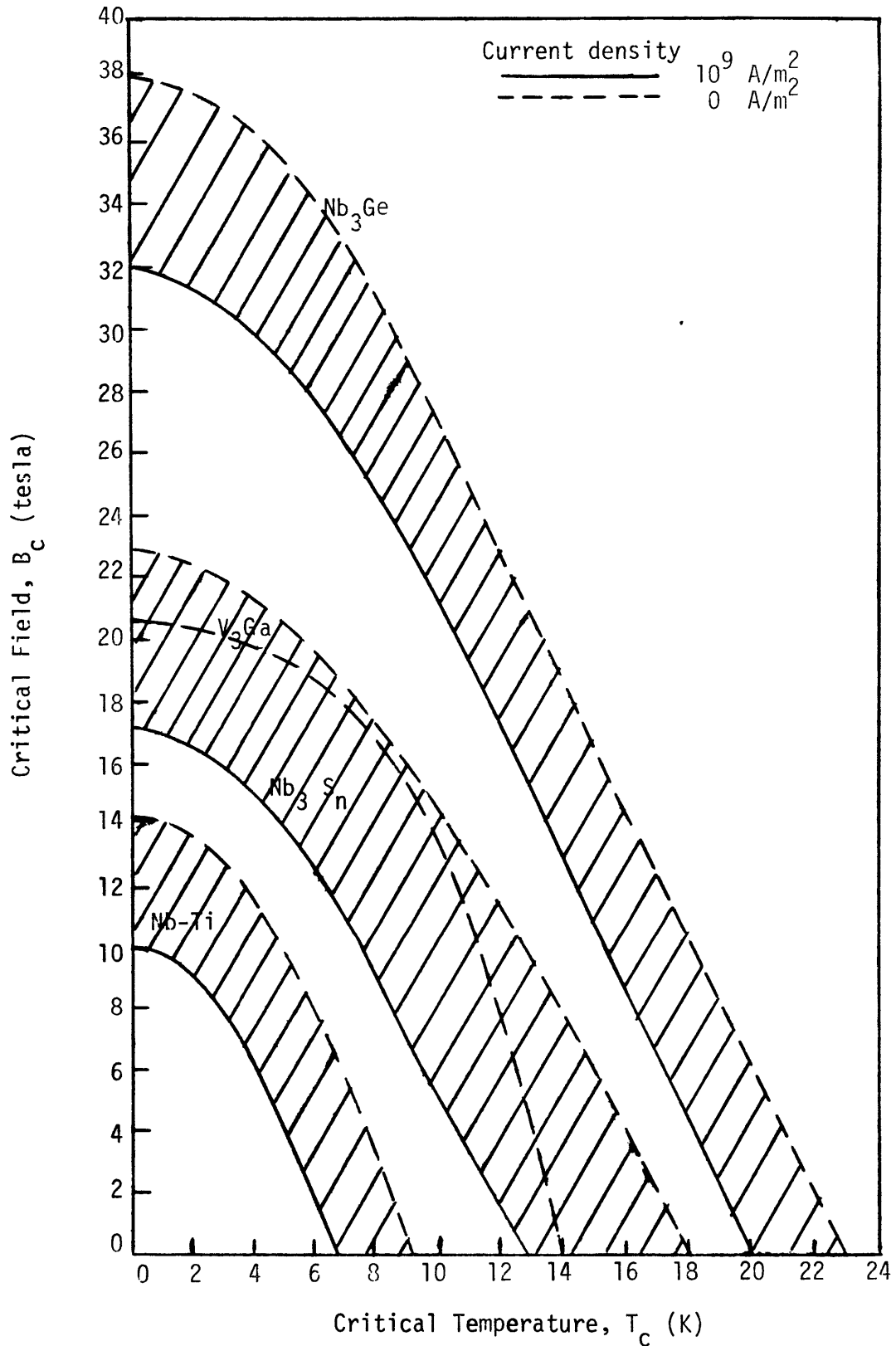


Fig. II.16. Critical field versus critical temperature for various superconductors at different current densities in the superconductor

eddy current loss problem while also diminishing the hysteresis loss in the extremely small diameter filaments. The individual conductors in the braided wires are usually insulated and twisted and transposed. Transposition is a commonly used technique for all types of electrical wire to reduce circulating current and eddy current losses. These wires are not very rigid though and usually require additional mechanical support. They are commonly found in pulsed applications such as energy storage coils or beamline dipole magnets.

Of course the most important criteria in consideration of a technical superconductor are the critical field and critical temperature characteristics of the material. As mentioned previously Nb-Ti is the most commonly used material but presently Nb₃Sn is increasing in popularity due to its higher values of critical field and critical temperature and also due to advances in manufacturing technology. In addition inter-metallic compounds such as Nb₃Ge and V₃Ga are currently under development as potential high field conductors. They are presently inhibited by manufacturing limitations, generally based upon their brittle nature. The critical field versus critical temperature are shown for these conductors in Fig. 2.16. At present a great effort is being directed by metallurgists and physicists to further development of high temperature, high field superconductors.

CHAPTER III
THEORY OF AC LOSSES IN SUPERCONDUCTORS

This chapter deals with the theory of ac losses in superconductors and specifically with a detailed mathematical model from which the losses can be quantitatively computed. Before the model is presented, however, it is extremely important to accurately define the problem and the underlying assumptions. Consideration must be given to type of conductor, type of material, conditions of magnetic field and transport current and the time dependence of the field and transport current.

The conductor that will be considered is the multifilamentary composite conductor which is comprised of many small diameter filaments of superconducting material embedded in a normal resistive matrix material. The superconductor will be a hard, type II material with many pinning sites. It was shown in Fig. II.9 that this type of conductor is in widespread use for many technical applications either in the monolithic or cabled or braided form. The superconducting material in predominant use is the alloy niobium-titanium (Nb-Ti) and increasingly the compound niobium-tin (Nb_3Sn). The model will be applicable to these and other superconducting material (e.g., V_3Ga , Nb_3Ge , etc.). However, surface loss effects will not be considered, even though this type of loss mechanism could be significant under certain conditions and particularly for materials other than Nb-Ti.

The multifilamentary composite conductor exhibits two independent loss mechanisms under the influence of a changing magnetic field. One

mechanism is an eddy current loss in the normal matrix material and the other is a hysteresis loss in the individual superconducting filaments. The relative contribution of the two-loss mechanisms to the total loss depends upon several factors. The variables which affect the ac loss are:

- 1) frequency of the alternating field or current,
- 2) amplitude of the magnetic field change
- 3) current ramping rate,
- 4) magnitude of the background field,
- 5) field orientation with respect to the conductor,
- 6) conductor properties;
 - a) twist pitch
 - b) filament size
 - c) copper to superconductor ratio
 - d) conductivity and permeability perpendicular to filaments
 - e) conductivity and permeability parallel to filaments.

The hysteresis loss and the eddy current loss are coupled by induced circulating currents which flow axially through the filaments and return through the matrix. This loss is reduced by twisting the filaments within the matrix and in the case of cables and braids by transposing the individual multifilamentary wires.

The problem of calculating the eddy current loss in the normal matrix material is significant but the underlying physical loss mechanism is clearly understood. It is just the ohmic energy dissipated by currents flowing through a normal resistive medium where the current density, J and

electric field, E are linearly related by the material conductivity, σ in the constitutive relation, $J = \sigma E$. The problem can be formidable because the calculation of J and E is complicated by the highly non-linear interaction with the array of superconducting filaments within the matrix.

The most fundamental problem at hand though is to gain an understanding of the magnetic and electric properties of the superconductor in a changing magnetic field and particularly when it is carrying a transport current. Only then can the larger problem associated with the composite be adequately analyzed. Thus the focus of this work is to develop an understanding of the loss mechanisms within an individual superconducting filament carrying a dc transport current in a changing external magnetic field. At appropriate points within the following sections comments will be made to relate the behavior of the single filament to the larger context of the multifilamentary composite conductor. The mathematical treatment will be based upon macroscopic currents and magnetic and electric fields in bulk specimens although this is consistent with the microscopic phenomena as outlined in Chapter II.

III.1 The Critical State Model Applied to AC Losses

The discussion of superconducting phenomena in Chapter II proposed that experimental evidence exists in support of the critical state model for type II superconductors. Acceptance of this model is crucial for it provides a convenient method of computing the loss in a superconductor subjected to a time varying field or transport current. That is, the hysteresis loss in a superconductor can be computed from a succession of

quasistatic time steps between equilibrium distributions of magnetic field and current within the specimen. At each equilibrium step the superconductor is in the critical state. The mechanism which allows the field and current distribution to change from one state to the next is the flux flow resistivity.

However, there is no need to determine the flux flow resistivity, ρ_f , explicitly in order to calculate the loss. It is sufficient to compute the electric field, E and the current distribution, J from the quasistatic Maxwell equations

$$\nabla \times H = J \quad \text{and} \quad \nabla \times E = - \frac{\partial B}{\partial t} \quad . \quad (3.1)$$

This condition will hold as long as $\frac{\partial B}{\partial t} \ll \frac{B_p}{\tau_m}$ where B_p is the magnetic field required to fully penetrate the filament and τ_m is the time constant for magnetic flux to diffuse through the filament. The diffusive time constant can be computed from the magnetic diffusivity which is given by

$$D_m = \frac{\rho_f}{\mu_0} \quad (3.2)$$

where ρ_f is the flux flow resistivity. The time constant then is

$$\tau_m = \frac{L^2}{D_m} = \frac{\mu_0 L^2}{\rho_f} \quad (3.3)$$

where the characteristic length, L is equal to the filament radius, $d/2$. An order-of-magnitude estimate gives values of τ_m of order 10^{-8} sec for a

typical Nb-Ti filament diameter of $50\mu\text{m}$. As long as the frequency of the external field change does not approach the gigahertz range the quasistatic model should hold. For most practical engineering applications the perturbation field frequency would realistically never exceed 10^3 hertz.

III.1.1 One-Dimensional Flux Penetration

A one-dimensional slab of non-ideal Type II superconductor is often used as a simple example to illustrate the fundamentals of the critical state model. Consider the slab of thickness d in Fig. 3.1a to be of infinite extent in the y and z directions. If a uniform external field, H_e , oriented parallel to the sides of the slab in the y direction, is increased above H_c , flux vortices will begin to penetrate the specimen. The material will be said to be in the mixed state. The flux will penetrate to the point where the pinning force will just balance the Lorentz force on the flux bundles. This condition is the critical state and the induced current density is called the critical current density, J_c . The field and current distribution will be given by solution of the Maxwell equation $\nabla \times H = J$ with the boundary condition that $H = H_e$ at the surface.

The exact form of the solution depends on whether J_c is considered to be independent of H (Bean model [38]) or J_c is considered to be inversely proportional to H (Kim model [29]). If we choose the former condition the solution is of the form

$$H = H_e + J_c(X - d/2) \quad X > 0 \quad . \quad (3.4)$$

The field penetrates to a point x_p given by

$$x_p = \frac{d}{2} - \frac{H_e}{J_c} \quad . \quad (3.5)$$

The slab is fully penetrated when $H_e = H_p$ where

$$H_p = \frac{J_c d}{2} \quad . \quad (3.6)$$

The field and current distributions that correspond to the Bean model are shown in Figs. 3.1a through 3.1c for an increasing external field and in Figs. 3.1d through 3.1g for a decreasing external field. The hysteresis inherent in the superconductor is shown by the trapped flux remaining in the slab when the external field is reduced to zero (Fig. 3.1e).

The magnetization of the slab is given by

$$M = \frac{1}{d} \int_{-\frac{d}{2}}^{\frac{d}{2}} H dx - H_e \quad (3.7)$$

and the magnetization curve for a complete cycle to the upper critical field limit of H_{c2} is shown in Fig. 3.2. The energy loss per cycle per unit volume is easily computed from the area under the magnetization curve and given by

$$W_h = \int_{\text{volume}} \left[\oint_{\text{cycle}} \mu_0 M dH \right] dv \quad . \quad (3.8)$$

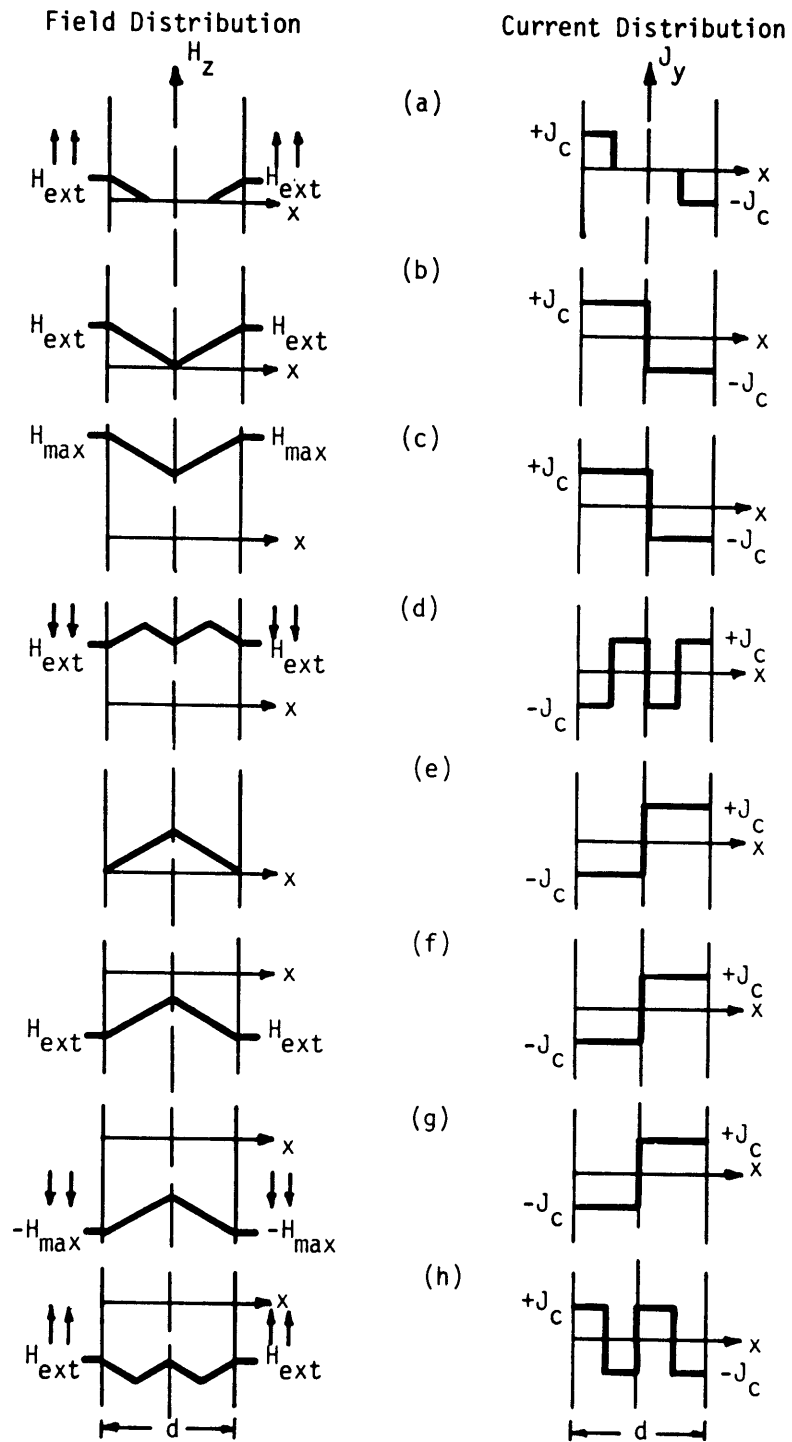


Fig. III.1. Field and current distribution in a type II superconducting slab of thickness d with external field applied parallel to the slab surfaces.

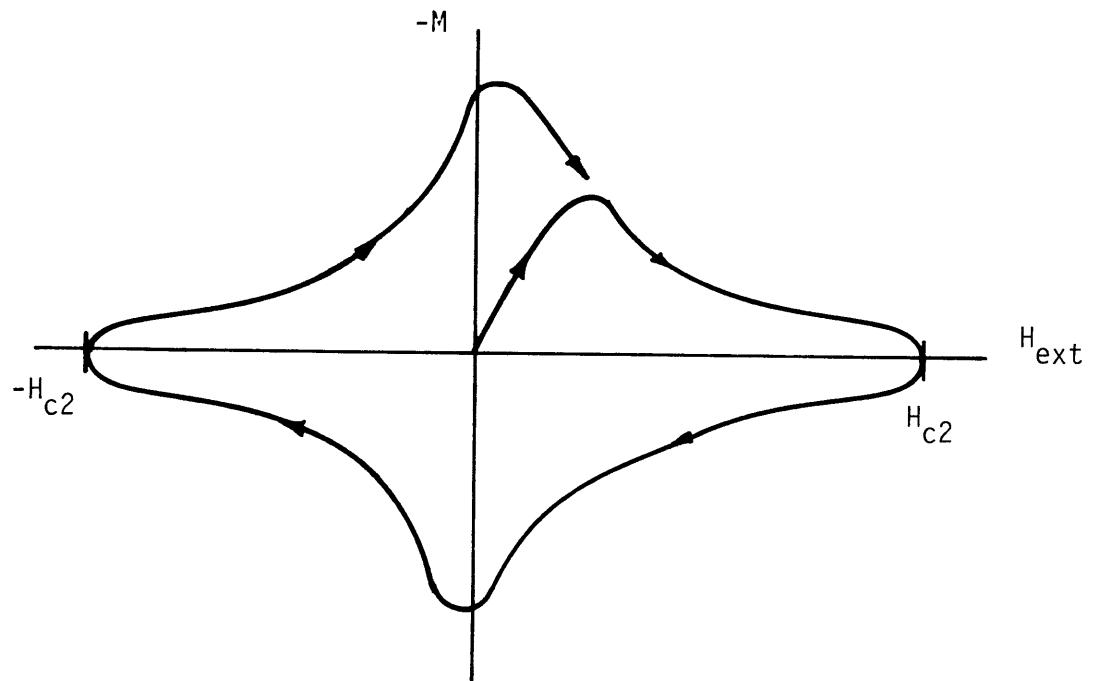


Fig. III.2. Magnetization curve for a type II superconducting slab. Negative values of M are diamagnetic states while positive magnetization indicates paramagnetism.

Carrying out the integration we get for the loss per cycle per unit volume,

$$\frac{W_h}{V} = \frac{2}{3} \mu_0 \frac{H_m^3}{H_p} \quad H_m \leq H_p \quad (3.9a)$$

and

$$\frac{W_h}{V} = 2\mu_0 H_m H_p \left(1 - \frac{2}{3} \frac{H_p}{H_m}\right) \quad H_m > H_p \quad (3.9b)$$

If $H_m \gg H_p$

$$\frac{W_h}{V} \approx 2\mu_0 H_m H_p \quad (3.9c)$$

These results were originally derived by London [39].

A similar procedure can be followed with the Kim model. In this model the functional dependence of the critical current density on the magnetic field is given by

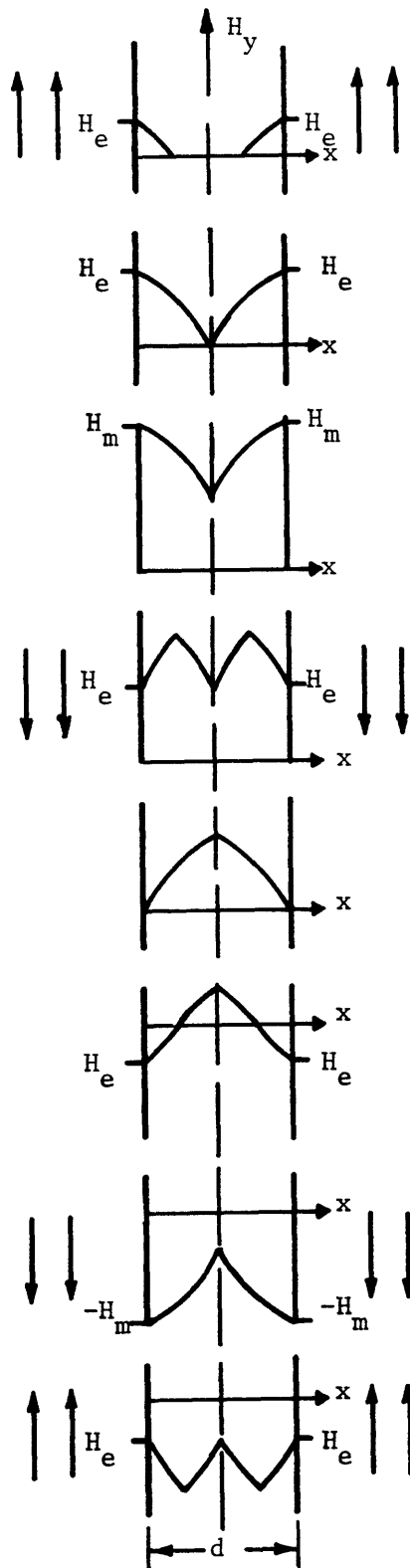
$$J_c = \frac{J_0 H_0}{H + H_0} \quad (3.10)$$

where $J_0 = J_c$ at $H = 0$ and $H_0 = H$ at $J_c = \frac{J_0}{2}$.

The field profile then as calculated from Eq. (3.1) is

$$H = H_0 \left\{ \left[\left(1 + \frac{H_e}{H_0}\right)^2 - \frac{2J_0}{H_0} \left(x - \frac{d}{2}\right) \right]^{1/2} - 1 \right\} \quad x > 0$$

Field Distribution



Current Distribution

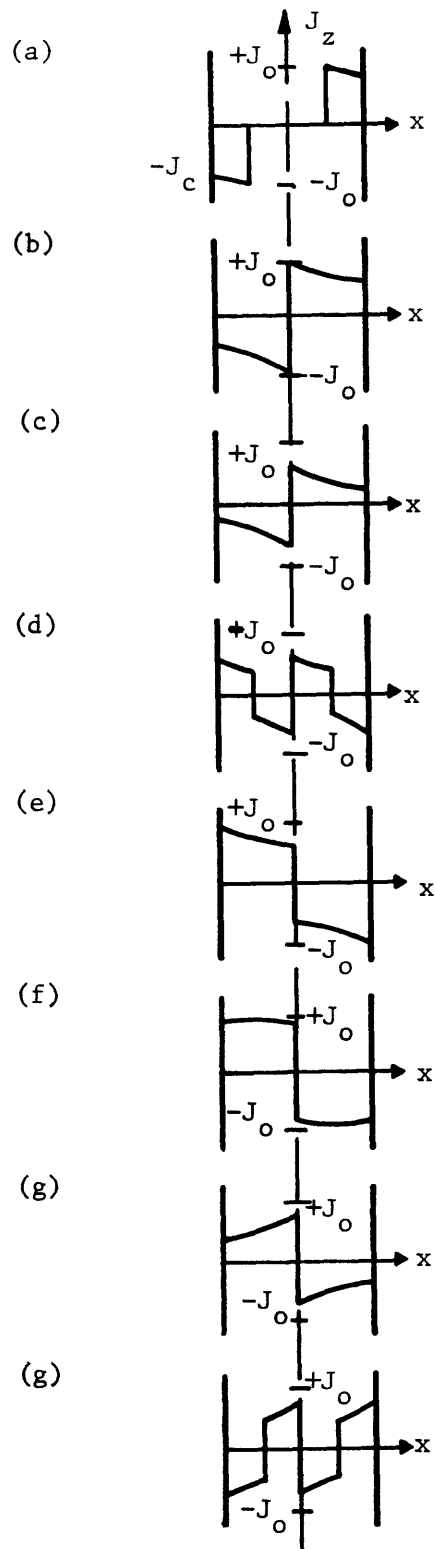


Fig. III.3. Kim model of field and current distributions in a Type II superconducting slab of thickness d with external field applied parallel to the surface.

and the field penetrates to

$$x_p = \frac{d}{2} - \frac{H_e}{H_0 J_0} \left(H_0 + \frac{H_e}{2} \right) \quad . \quad (3.11)$$

Full penetration occurs when $H_e = H_p$ where

$$H_p = H_0 \left(1 + \frac{J_0 d}{H_0} - d \right) \quad . \quad (3.12)$$

Figures 3.3a through 3.3h show the field and current distributions as given by the Kim model for various values of the external field. The hysteresis loss per cycle can be found from Eq. (3.8) for the case when H is cycled between H_m and $-H_m$,

$$\frac{W_h}{V} = \mu_0 J_0 d H_0 \ln \left(\frac{H_0 + H_m}{H_0} \right) \quad . \quad (3.13)$$

The purpose of going through this exercise is to show how the critical state model is the basis for computing the hysteresis loss in the superconducting filaments and also to introduce some of the important parameters such as the full penetration field, H_p . These simple slab models have served until recently as the basis for all ac hysteresis loss calculations.

III.1.2 One-Dimensional Effect of Transport Current

The effect of a transport current in the slab specimen can be developed by arguments consistent with the critical state model. Consider the one-dimensional slab to be in a uniform external field and

carrying a transport current I_t in the z-direction, that is a fraction of the critical current I_c such that $0 < \frac{I_t}{I_c} < 1$. The current and field distribution for the slab is shown in Fig. 3.4. Note that the current flows everywhere in the cross-section at the critical current density J_c which has been assumed a constant as per the Bean model. If the external field is cycled by an amount $\pm H_m$ about the value H_e the current and field distributions will be as shown in Fig. 3.4(a-h).

Since one can picture the central region of the slab as being occupied by the transport current the field required to fully penetrate to this region will now be less than the field required to penetrate to the center of the slab, that is the full penetration field at zero transport current, $H_p(0) = \frac{J_c d}{2}$. The full penetration field now depends upon the fraction of transport current and is given by

$$H_p\left(\frac{I_t}{I_c}\right) = H_p(0)\left(1 - \frac{I_t}{I_c}\right) \quad (3.14)$$

The magnetization and the hysteresis loss can be computed as before from Eqs. (3.7) and (3.8), respectively. The results are given below for the energy loss per unit volume per cycle;

$$H_m \leq H_p(i)$$

$$\frac{W_h(i)}{V} = \frac{2}{3} \mu_0 \frac{H_m^3}{H_p(0)} \quad (3.15a)$$

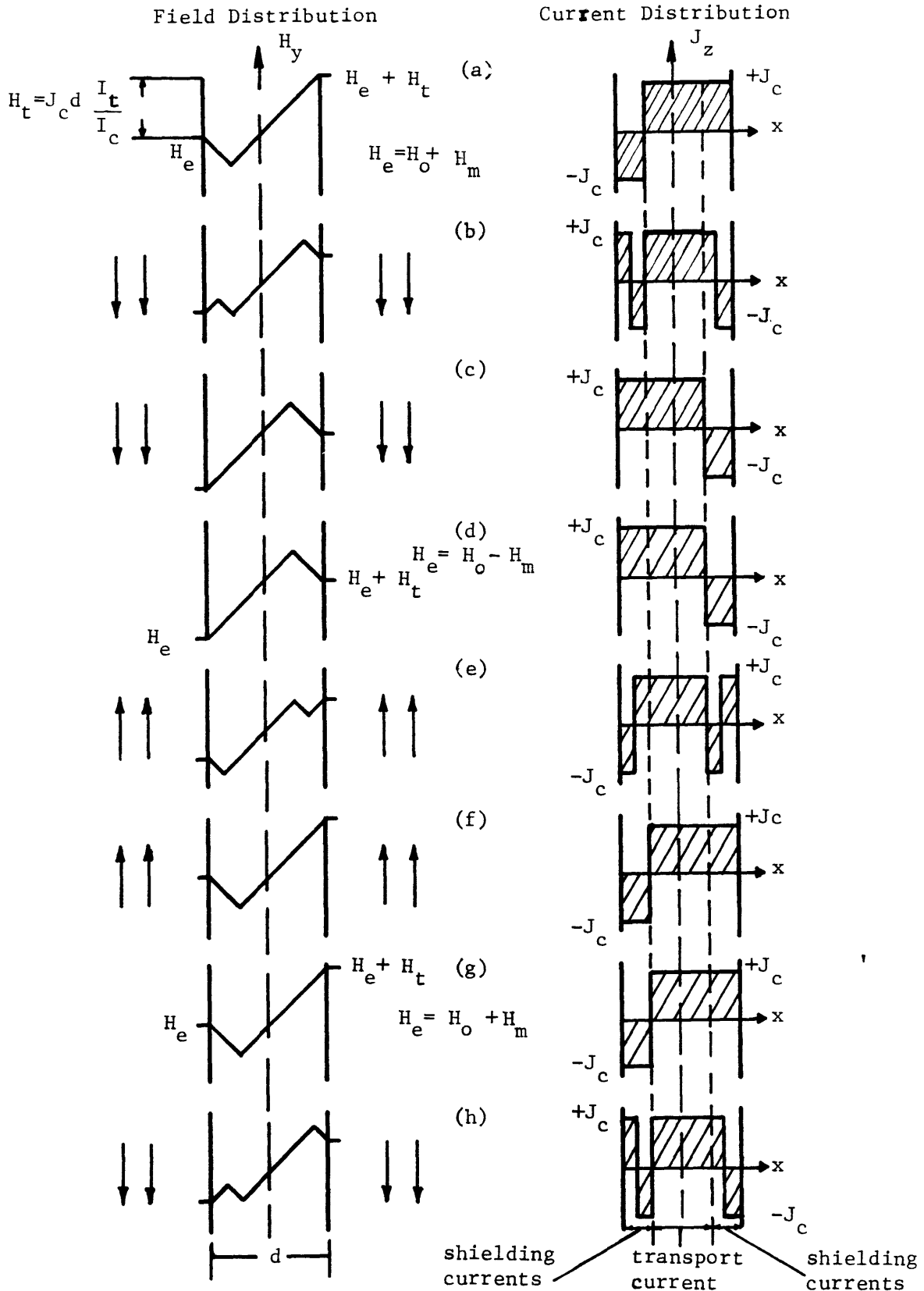


Fig. III.4. Bean model of field and current distribution in a slab carrying a transport current, $\frac{I_t}{I_c} = 0.5$

$$H_m > H_p(i)$$

$$\begin{aligned} \frac{W_h(i)}{V} &= \frac{2}{3} \mu_0 \frac{H_p^3(i)}{H_p^3(0)} + 2 \mu_0 H_p(0) H_m \left(1 - \frac{H_p(i)}{H_m}\right) (1+i^2) \\ &= \frac{2}{3} \mu_0 H_p^2(0) (1-i)^3 + 2 \mu_0 H_p(0) H_m \left[1 - \frac{H_p(i)}{H_m}\right] (1+i^2) \end{aligned} \quad (3.15b)$$

where $i = I_t/I_C$.

The loss is very similar to that given in Eq. (3.9). If $i=0$, Eq. (3.15) reduces to (3.9), the loss with zero transport current. It is interesting to note that if H_m is less than $H_p(i)$ the hysteresis loss is totally unaffected by the transport current. In a later section it will be shown that this result is valid for the two-dimensional hysteresis loss with transport current. If the specimen is carrying the maximum possible transport current ($i=1$) the loss will be twice the hysteresis loss at zero transport current, i.e.,

$$\frac{W_h(1)}{V} = \frac{2W_h(0)}{V} .$$

This condition is specific to the one-dimensional slab model.

III.2 Existing Loss Models

Much attention has been focused by many different workers since the mid-1960's toward understanding and quantifying the ac loss mechanisms in solid core and multifilamentary composite superconductors. The amount of

previous work is too great to review in detail in this section but a few general comments are in order to give the reader a perspective on how the work of this thesis complements the body of existing models.

The earliest work was aimed primarily at calculating the hysteresis loss within the superconducting materials, since multifilamentary conductors had not yet been developed. The previously referenced work by London [39] in which he computed the hysteresis loss in a slab has served in conjunction with the Bean model [38] as the basis for almost all hysteresis loss calculations to date. This has become known as the Bean-London model. Later Hancox [40] used both the Bean-London model and the Kim model to compute the loss for a slab with a changing transport current in conjunction with a changing external field. During this period of time Kim [32] and Anderson [33] were reporting on the phenomena of flux creep and flux jumping. The results of this work led to magnetic and thermal stabilization of the superconducting filaments by surrounding them with a material such as copper.

The addition of the stabilizing material solved the problem of flux jumping but introduced a new loss mechanism in the form of Joule heating by eddy currents in the matrix. Several authors treated this problem by analyzing the behavior of a twisted pair of superconducting filaments in a resistive matrix exposed to a time varying external field [41-44]. In all of these cases, the effect of transport current, if included at all, was treated by means of a one-dimensional slab model. Partial penetration of the filaments was also treated one-dimensionally.

The most comprehensive and successful ac loss model was the anisotropic continuum model developed by Carr [45-49]. Instead of treating the currents in the matrix and the filaments separately and trying to connect them through boundary conditions, Carr averaged the properties of the components and treated the wire as a highly anisotropic continuum. Thus he calculated the conductivity and magnetic permeability for directions perpendicular and parallel to the filaments, and then solved Maxwell's equations based upon these averaged material properties.

The results were very good and particularly accurate in the limiting cases. The model also includes the effect of transport current but it relies on the one-dimensional slab solutions to account for this effect. The accuracy is improved for the intermediate cases between $I_t = 0$ and $I_t = I_c$ by using an empirically derived scaling coefficient. However, the anisotropic continuum model averages the properties of the superconducting filaments and the matrix material so that the model necessarily becomes inaccurate for operating conditions which cause the local details of field and current distribution to vary sharply.

Ogasawara, et al. [50,51] have dealt specifically with the ac loss in multifilamentary composite wires carrying a dc transport current both analytically and experimentally, but they have also relied on one-dimensional slab solutions as the basis for the transport current effect. It became apparent that in order to improve the accuracy of these models it was necessary to develop two-dimensional formulations for the magnetic field and current distributions in cylindrical filaments.

As a first step in this direction several authors have computed the two-dimensional distributions of field and current in a round superconductor in a uniform external field [52 - 54]. The magnetization and hysteresis loss were calculated from these distributions and they are in good agreement with experimentally determined values. All three previous methods employed numerical techniques to generate the results, but the effect of transport current was not included in the calculations.

The focus of this thesis then was to complement this body of work by developing a two-dimensional mathematical model for the ac loss that includes the effect of transport current. The resulting mathematical formulation has been used to complete these calculations and is presented in the remaining sections of this chapter.

III.3 Mathematical Technique for Calculation of Two-Dimensional Flux Penetration

A mathematical technique is presented in this section by which the two-dimensional distributions of magnetic field and current can be computed. It is based upon a method developed by Beth [55] for calculating two-dimensional fields due to arbitrarily shaped regions of constant current density. The following derivation, which follows Beth's treatment, utilizes functions of complex variables and the application of Cauchy's integral formula. In the next section the mathematical formulation is applied to a cylindrical superconductor in a uniform external magnetic field.

The problem, simply stated, is to determine the magnetic fields inside and outside an arbitrary region, R , of constant current density, J .

Consider the two-dimensional region, R , of uniform current density $J =$ constant within the boundary and $J = 0$ outside the boundary in Fig. 3.5.

The Maxwell relations for magnetoquasistatic fields in regions of constant permeability are

$$\nabla \times \vec{H} = \vec{J} \quad \text{and} \quad \nabla \cdot \vec{H} = 0$$

which in two-dimensions can be written

$$\frac{\partial H_y}{\partial x} - \frac{\partial H_x}{\partial y} = J \quad (3.16a)$$

$$\frac{\partial H_x}{\partial x} + \frac{\partial H_y}{\partial y} = 0 \quad (3.16b)$$

First we define a field point in the complex plane $z \equiv x+iy$ and the complex field $H(x,y)$ where

$$H(x,y) \equiv H_y(x,y) + i H_x(x,y) \quad (3.17)$$

The imaginary number i is defined by $i = \sqrt{-1}$. Note that H is a complex function of position in which the real part of the function defines the y component of magnetic field and the imaginary part defines the x component of magnetic field.

We would like to find an analytic function $f(z) = u+iv$ that describes the magnetic fields within and outside the region R , such that

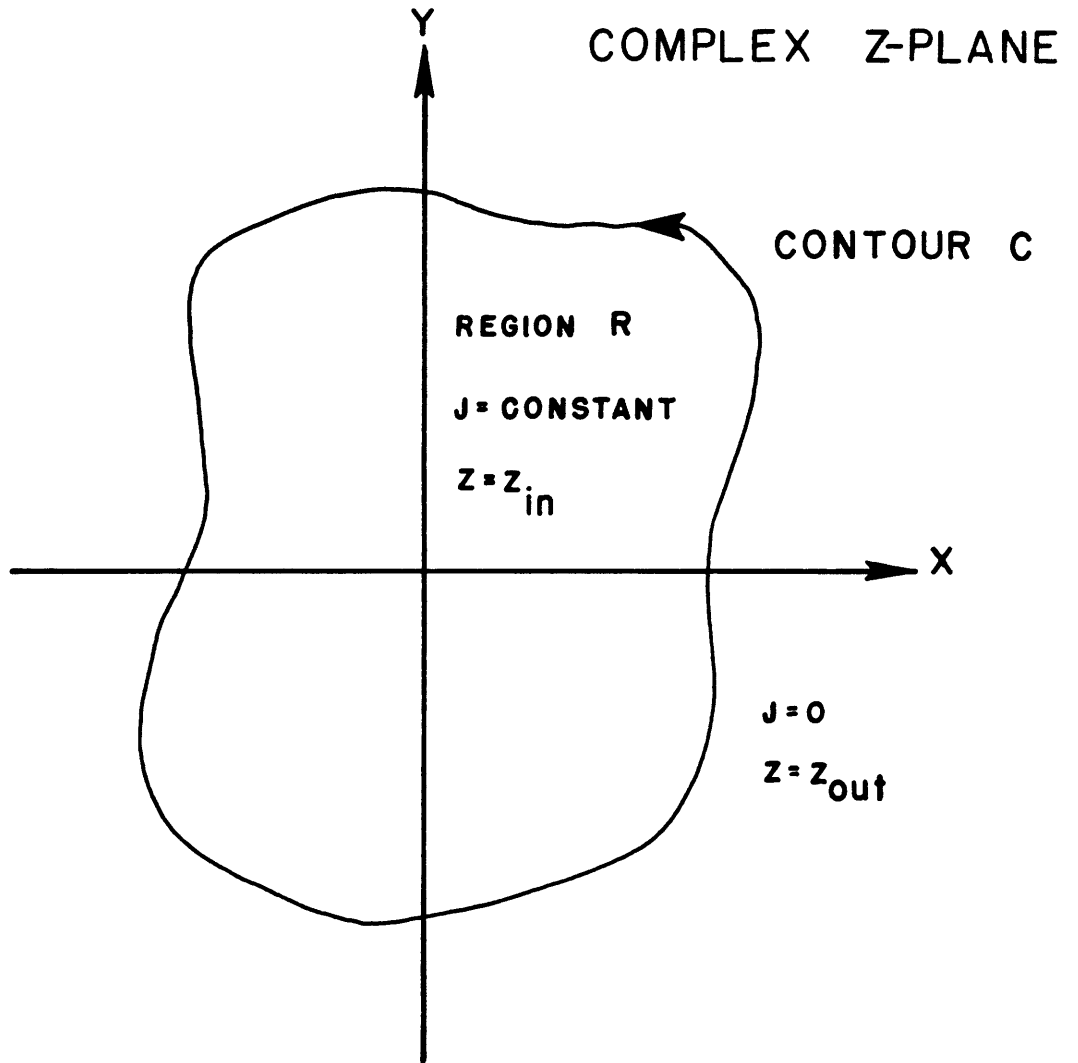


Fig. III.5. Contour C in complex Z- plane enclosing region R of constant current density J.

the Maxwell relations are satisfied. For a complex function to be analytic in R it is necessary that the function be single-valued, the first partial derivatives of u and v be continuous, and the Cauchy-Riemann equations (3.18) be satisfied within the region R .

$$\frac{\partial u}{\partial x} = \frac{\partial v}{\partial y} \quad (3.18a)$$

$$\frac{\partial u}{\partial y} = - \frac{\partial v}{\partial x} \quad (3.18b)$$

If a function is analytic it has derivatives of all orders which must be continuous and it follows that the real and imaginary parts of the analytic function are solutions of Laplace's equation

$$\frac{\partial^2 u}{\partial x^2} + \frac{\partial^2 u}{\partial y^2} = \nabla^2 u = 0 \quad (3.19a)$$

$$\frac{\partial^2 v}{\partial x^2} + \frac{\partial^2 v}{\partial y^2} = \nabla^2 v = 0 \quad (3.19b)$$

It is clear from direct substitution of Eq. (3.17) into Eqs. (3.18a) and (3.18b) that $H(x,y)$ is not an analytic function in R due to the current source J . The function $H(x,y)$ is analytic only in those regions where $J=0$.

Beth defines an analytic function $f(z)$ that is a complex combination of two real functions

$$f(z) \equiv H - \frac{1}{2} J z^* = u + iv \quad (3.20)$$

where $z^* \equiv x-iy$ is the complex conjugate of z and $u = H_y - \frac{1}{2} J \cdot x$ and $v = H_x + \frac{1}{2} J \cdot y$. Direct substitution of Eq. (3.20) into Eqs. (3.16a) and (3.16b) confirms that the Maxwell relations are satisfied which is identical with satisfying Cauchy-Riemann (3.18a and b).

The problem then is to evaluate the function $f(z)$ inside and outside the current-carrying region R thus yielding the magnetic field components H_x and H_y directly. This function can be evaluated by application of the Cauchy Integral Formula

$$f(z) = \frac{1}{2\pi i} \oint_C \frac{f(\zeta)}{\zeta-z} d\zeta \quad (3.21)$$

where ζ is a variable that denotes a point along the contour C .

We can write separate analytic functions describing the two regions, inside the contour and outside the contour, by applying the Cauchy Integral Formula to obtain

$$\text{Inside } R, \quad f_{in}(z) = \frac{1}{2\pi i} \oint_C \frac{f_{in}(\zeta)}{\zeta-z} d\zeta = \begin{cases} H_{in} - \frac{1}{2} Jz^* & \text{for } z = z_{in} \\ 0 & \text{for } z = z_{out} \end{cases} \quad (3.22a)$$

$$\text{Outside } R, \quad f_{out}(z) = -\frac{1}{2\pi i} \oint_C \frac{f_{out}(\zeta)}{\zeta-z} d\zeta = \begin{cases} 0 & \text{for } z = z_{in} \\ H_{out} & \text{for } z = z_{out} \end{cases} \quad (3.22b)$$

The symbol z_{in} denotes a field point lying inside the contour and z_{out} denotes a field point lying outside the contour. The positive direction around the contour is defined in the standard sense by the direction which encloses the area to the left. In Eq. (3.22), use has been made of the Cauchy Integral Theorem to set $f(z) = 0$ if the point z is not within the region enclosed by the contour C .

The boundary conditions require continuity of field at the boundary where $\zeta = z$, thus

$$H_{in} = H_{out}$$

and

$$f_{in}(\zeta) - f_{out}(\zeta) = -\frac{1}{2} J\zeta^* \quad (3.23)$$

Adding the two functions (Eqs. (3.22a) and (3.22b)) to form the single function $f(z)$ and using Eq. (3.23) we find

$$f(z) = f_{in}(z) + f_{out}(z) = \frac{1}{2\pi i} \int_C -\frac{1}{2} \frac{J\zeta^*}{\zeta-z} d\zeta$$

or

$$f(z) = \frac{iJ}{4\pi} \int_C \frac{\zeta^*}{\zeta-z} d\zeta = \begin{cases} H_{in} - \frac{1}{2} Jz^* & \text{for } z = z_{in} \\ H_{out} & \text{for } z = z_{out} \end{cases} \quad (3.24)$$

Thus the final result of all this mathematical manipulation is Eq. (3.24) which indicates the magnetic field can be determined everywhere if the contour integration can be performed. Note that J must be constant within the contour C . This method of computing the magnetic fields may be easier than the more traditional methods which usually require a double integration over the area of the region R . The above equation can be evaluated analytically for many regular geometric shapes.

III.4 Partial Penetration Flux Profiles

The previous mathematical formulation can be used to compute the region of flux penetration into a cylindrical non-ideal type II superconducting filament. The model is based upon the following assumptions; a) the constant background field is uniform and much greater than $H_p(0)$, b) the filament carries no transport current, and most important c) the induced currents flow at the critical current density, J_c (critical state model) which is constant and independent of H (Bean's model).

Consider the case of a cylindrical superconducting filament in a transverse uniform background field, H_e as shown in Fig. 3.6. The induced current distribution will create uniform magnetic fields in an interior region that is equal in magnitude and antiparallel to the external field such that the interior region is completely shielded. The problem is to find the shape of the induced current region and thus the limit of flux penetration that fulfills the shielding requirement.

The net magnetic field distribution is just the superposition of the external field and the field generated by the induced current distribution,

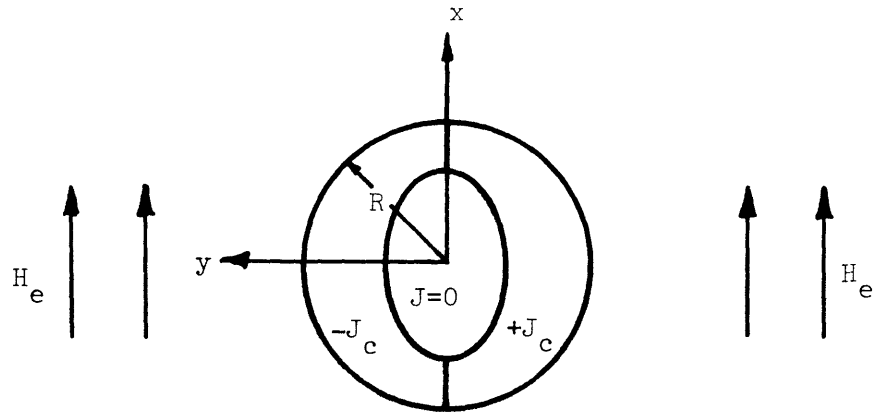


Fig. III.6. Cylindrical superconducting filament in a uniform external field showing partial penetration.

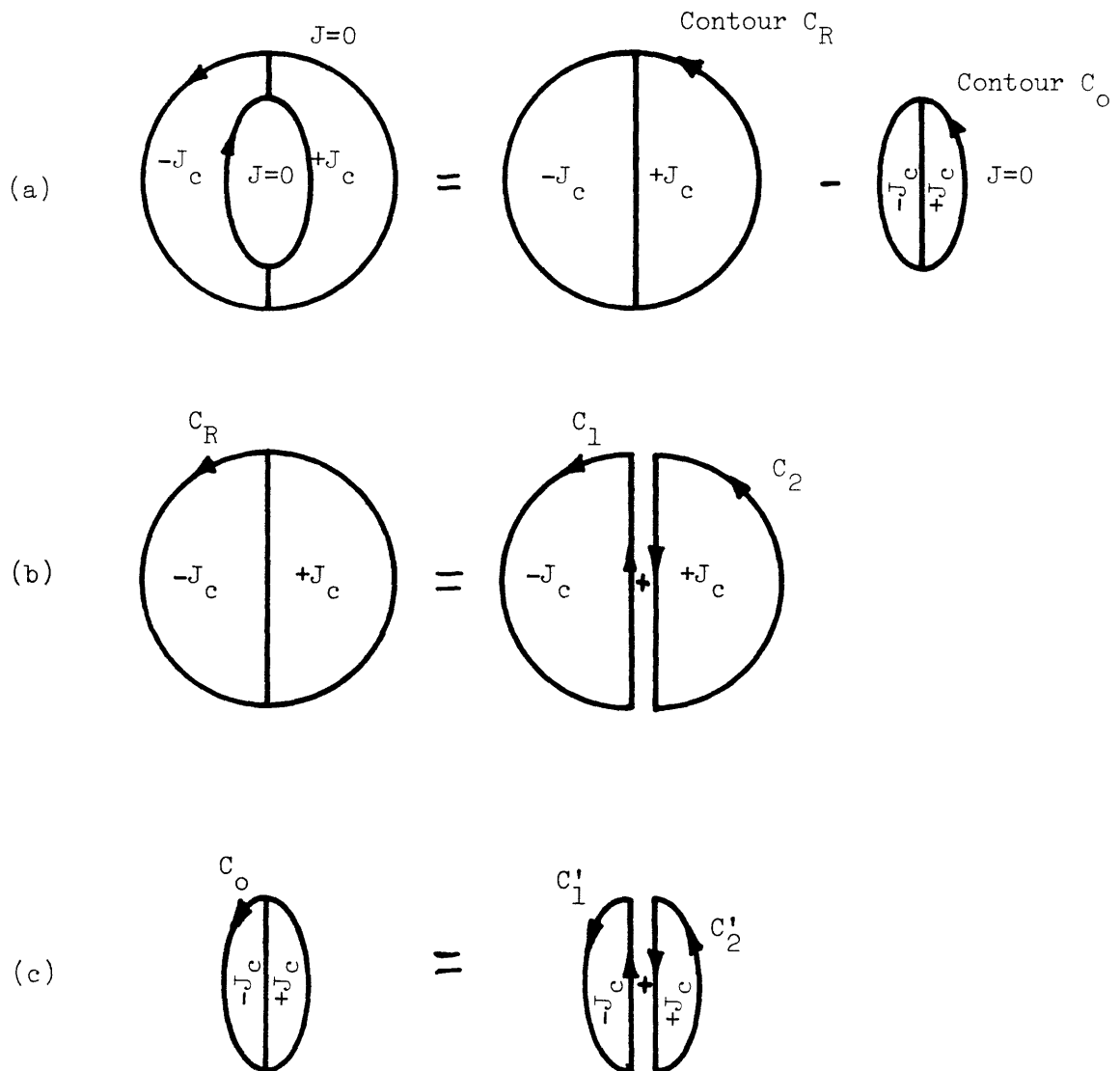


Fig. III.7. Superposition of contour to enclose regions of net positive and negative current density.

$$H(z) = iH_e + H_J(z)$$

where $H(z)$ and $H_J(z)$ are complex functions of the complex field point z . The magnetic fields in each case are computed from an analytic function $f(z)$ as determined by the methods described in the previous sections. Figure 3.2a shows how the induced current distribution can be formed by superimposing an area of $\pm J_c$ bounded by the circular contour C_R and another smaller area bounded by the contour C_0 . The contours C_R and C_0 can be further broken down into two smaller contours, $C_1 + C_2$, and $C_1 + C_2'$, shown in Figs. 3.7b and c, respectively. The total field distribution then becomes

$$H(z) = iH_e + H_R(z) - H_0(z) \quad (3.25)$$

where H , H_R , and H_0 are complex functions of x and y .

First H_R is computed from an analytic function $f_R(z)$ by Eq. (3.24)

$$\begin{aligned} f_R(z) &= \frac{iJ}{4\pi} \oint_{C_R} \frac{\zeta^*}{\zeta-z} d\zeta = -\frac{iJ_c}{4\pi} \oint_{C_1} \frac{\zeta^*}{\zeta-z} d\zeta \\ &+ \frac{iJ_c}{4\pi} \oint_{C_2} \frac{\zeta^*}{\zeta-z} d\zeta . \end{aligned} \quad (3.26)$$

The contour C_R is the outer boundary of the circular filament described by the function $\zeta = Re^{i\theta}$, and the x axis where $\zeta = x$. Carrying

out the integrations of Eq. (3.26) and solving for the magnetic field we obtain

$$H_R(z) = \frac{\delta J_c z^*}{2} + \frac{iJ_c R}{2\pi} \left(\frac{R}{z} - \frac{z}{R} \right) \ln \left(\frac{R-z}{R+z} \right) - \frac{iJ_c R}{\pi} \quad (3.27)$$

where

$$\delta = \begin{cases} -1 & \text{in regions of } -J \\ +1 & \text{in regions of } +J_c \\ 0 & \text{in regions of } J=0 \end{cases}$$

Similarly the field H_0 is computed from $f_0(z)$ by

$$\begin{aligned} f_0(z) &= \frac{iJ_c}{4\pi} \oint_{C_0} \frac{\zeta^*}{\zeta-z} d\zeta = -\frac{iJ_c}{4\pi} \oint_{C_1} \frac{\zeta^*}{\zeta-z} d\zeta \\ &+ \frac{iJ_c}{4\pi} \oint_{C_2} \frac{\zeta^*}{\zeta-z} d\zeta \end{aligned} \quad (3.28)$$

However, a problem arises with evaluating Eq. (3.28) because the exact contour C_0 which delineates the inner region of zero net flux and current is not known. In theory it can be determined by setting the net field to zero along the boundary in Eq. (3.25). After some simplification the resulting expression that governs the shape of the contour C_0 can be written

$$\oint_{C_0} \frac{\zeta^*}{\zeta-z} d\zeta = \oint_{C_1'} \frac{\zeta^*}{\zeta-z} d\zeta - \oint_{C_2'} \frac{\zeta^*}{\zeta-z} d\zeta = 4R \left(1 - \frac{2H_e}{H_p} \right) - 2R \left(\frac{R}{z} - \frac{z}{R} \right) \ln \left(\frac{R-z}{R+z} \right) \quad (3.29)$$

where $H_p = 2J_c R / \pi$ is the field required to penetrate to the center of the filament.

The exact solution of this expression for $C_0 = C_1' + C_2'$ is difficult to obtain. An approximation has been made by Kato, et al. [56] by assuming a shape for the contour. Kato chose the shape of an ellipse with semi-major axis a and semi-minor axis b . The field $H_0(z)$ is then found by substitution of $\zeta = z \cos\theta + ib \sin\theta$ into Eq. (3.28). After evaluating the integrals, he is left with an expression for $H(z)$ in terms of the two parameters a and b . These parameters are then determined by setting $H(z) = 0$ at $z = \pm a$ and $z = \pm ib$. This results in two equations which are solved simultaneously for the two unknown parameters a and b . The ellipse thus defined is not the exact contour C_0 since Eq. (3.29) is satisfied only at the four points $z = \pm a$ and $z = \pm ib$.

The technique applied in this work is similar to that taken by Kato. First it is convenient to recast Eq. (3.25) into a more complete form by substituting Eqs. (3.27) and (3.28) for $H_R(z)$ and $H_0(z)$, respectively. The resulting expression for $H(z)$ when normalized by the full penetration field H_p is

$$\begin{aligned}
\frac{H(z)}{H_p} = & i \left\{ \left(\frac{H_e}{H_p} \right) + \frac{\delta\pi}{4} \left(\frac{z^*}{R} \right) - \frac{1}{2} \left(1 - \frac{a}{R} \right) - \frac{1}{4} \left(\frac{z}{R} \right) \ln \left[\frac{(1-z)(a+z)}{(a-z)(1+z)} \right] \right. \\
& - \frac{1}{4} \left(\frac{R}{z} \right) \ln \left(\frac{1+z}{1-z} \right) - \frac{1}{4} \int_{C_1^{-a/R}}^{+a/R} \frac{\zeta^*}{\zeta-z} d(\zeta/R) \\
& \left. + \frac{1}{4} \int_{C_2^{+a/R}}^{-a/R} \frac{\zeta^*}{\zeta-z} d(\zeta/R) \right\}
\end{aligned} \tag{3.30}$$

where a is the x axis intercept of the contour and δ is as defined in Eq. (3.27). The technique for finding the solution for the magnetic fields in Eq. (3.30) is as follows:

- 1) fix the external field H_e such that $0 < H_e/H_p < 1$,
- 2) assume a function $\zeta(x,y)$ for the shape of the contour,
- 3) evaluate the right-hand side of Eq. (3.30) at m field points within and on the contour defined by ζ , and set equal to the residual R_k , $k=1, m$
- 4) evaluate $\sum_{k=1}^m (R_k)^2$
- 5) minimize $\sum_{k=1}^m (R_k)^2$ by perturbing the function $\zeta(x,y)$
- 6) the function $\zeta(x,y)$ that minimizes the sum of the squares of the residuals defines the limits of the flux penetration for a given value of H_e/H_p .
- 7) Repeat the process for a full range of H_e/H_p between 0 and 1.0.

Note that the exact contour is the one which gives $\sum_{k=1}^m (R_k)^2 \equiv 0$ for every point within and on the contour ζ .

The polynomial was chosen as the general form for the function $\zeta(x,y)$. Only even terms were used due to the symmetry about the y axis. The function ζ is given by

$$\zeta = x + i(a_0 + a_2x^2 + a_4x^4 + a_6x^6 + a_8x^8) \quad (3.31)$$

where the variable x and the coefficients of the polynomial are real numbers. The contour integrals in Eq. (3.30) were evaluated numerically by a computer program that performs complex simpson quadrature integration. The residuals were evaluated at 5 points within one quadrant of the filament as illustrated in Fig. 3.8.

The contour ζ was perturbed by changing the coefficients a_0 through a_8 in order to minimize the sum of the squares of the 5 residuals. A computer program was used to perform this minimization. It uses a finite difference Levenberg-Marquardt algorithm [57] to minimize the sum of squares of m functions in n variables. In this case the m functions are the magnetic fields given by Eq. (3.30) evaluated at 5 points for a total of $m=10$ functions since each evaluation gives an x and y component of magnetic field. The n variables are the 8 polynomial coefficients a_0 through a_8 . This type of algorithm is well-suited to this problem since the function evaluations are highly non-linear in the variables a_n . Also the functions can only be evaluated numerically so other methods that require the derivatives in analytic form could not be used. This program handles that condition by using a finite difference method. Details of the computer programs that were

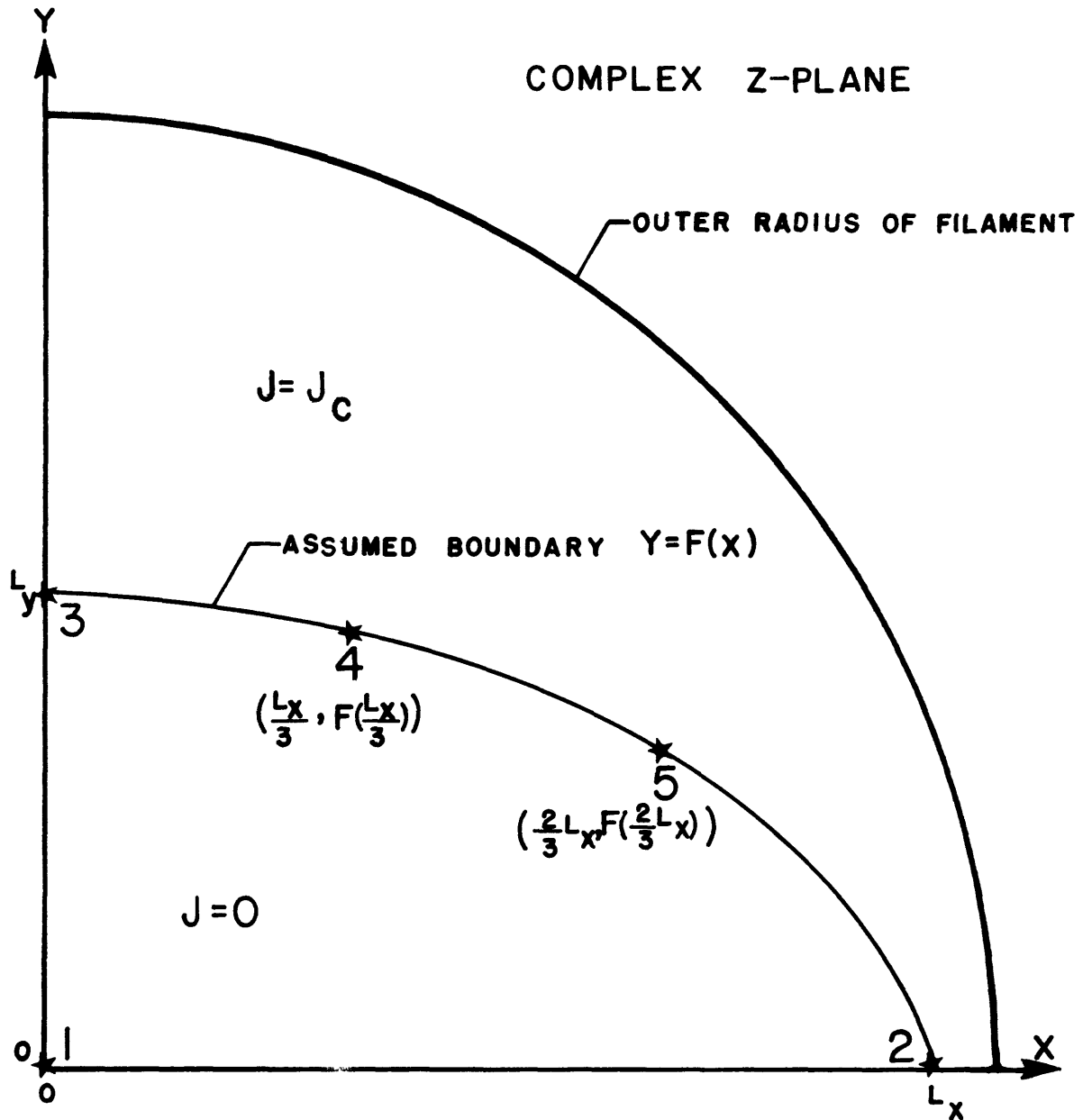


Fig. III.8. Position of field points for evaluation of residual functions. The sum of the squares of the residual fields at these points is minimized to determine the correct function $f(x)$ for a given external field, H_e/H_p .

used to find the best fit polynomial coefficients are given in Appendix B.

The results of this analysis are shown in Table 3.1 which gives the coefficients of the polynomial function that best describes the limits of shielding current distribution as a function of the normalized external field H_e/H_p . Note that for values of H_e/H_p approaching 1.0 fewer high order terms are required to describe the curve. The curves are illustrated in Fig. 3.9. The accuracy of the procedure was checked by comparing the magnitude of the residual field at various points within and on the contour with the magnitude of the uniform external field. For most cases the residual field was less than 1% of the external field especially for values of $H_e/H_p \gtrsim .3$. The accuracy was no worse than approximately 10% for the cases of small penetration, $H_e/H_p < .3$, but this is not much of a problem in the loss calculation since the total error is reduced due to the double integration of the currents over the cross-sectional area.

Recently several workers have also solved this problem through numerical techniques [52 - 54] but none have used the method of complex variables to compute the magnetic fields nor have they represented the flux penetration contours as closed-form mathematical functions.

There are two major advantages of the method presented in this work; 1) the mathematical technique of using complex variables to formulate the problem is readily adaptable to any regular geometric shape since only the contour integral around the outer boundary would be changed. Other shapes such as ellipses or rectangles are analytically tractable;

TABLE 3.1 COEFFICIENTS OF POLYNOMIAL FUNCTIONS
 THAT DEFINE FLUX PENETRATION CURVES

$\Delta H_e / H_p(0)$	a_0	a_2	a_4	a_6	a_8	x_m
.1	.8695	-.432	-.05	-.383	-.0045	1.0
.2	.760	-.492	-.209	-.0559	-.0031	1.0
.3	.640	-.467	-.180	-.010	0	.9899
.4	.529	-.450	-.095	-.038	0	.9627
.5	.423	-.427	-.050	-.026	0	.9295
.6	.328	-.420	-.001	0	0	.8828
.7	.236	-.370	-.001	0	0	.7993
.8	.150	-.315	-.01	0	0	.6850
.9	.0705	-.265	-.01	0	0	.5132
1.0	0	0	0	0	0	0

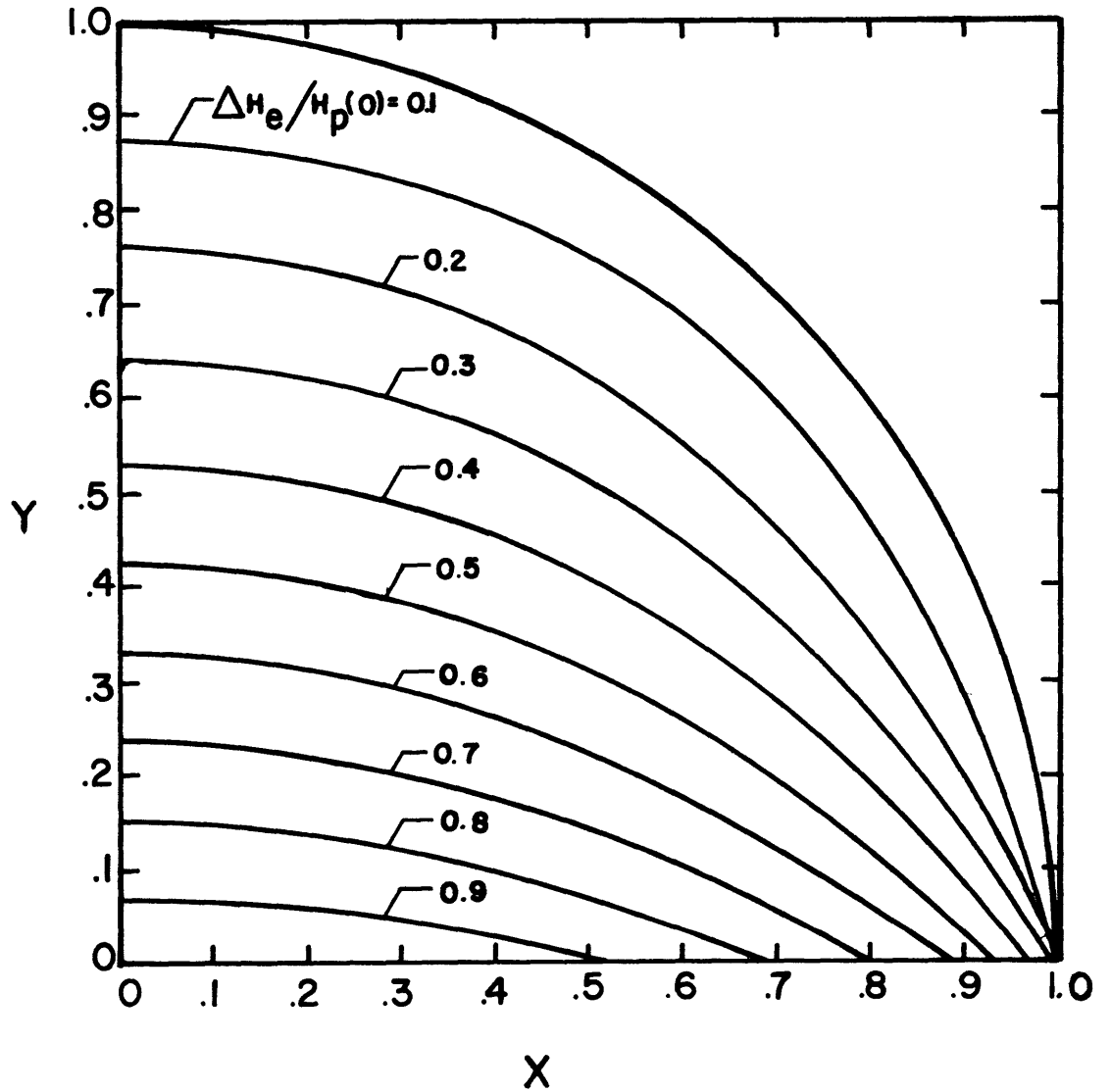


Fig. III.9. Contours of limits of flux penetration into a circular superconducting filament for different values of external field. One quadrant of the filament is shown.

2) the representation of the flux penetration curves as polynomial functions lends itself to relative analytic simplicity in further computations involving the current distributions such as the hysteresis loss calculation.

In addition this mathematical technique can be used to find solutions to other types of similar field problems involving fluid, thermal or electric fields. The results of this analysis are applied to the calculation of hysteresis losses, with and without transport current, in the following section.

III.5 Two-Dimensional AC Loss Calculation

The two-dimensional distributions of current and field that were calculated in the previous section are applied in this section to the calculations of ac loss in a cylindrical filament of non-ideal Type II superconductor carrying transport current. The development follows the example of Section III.1 where the critical state model is used as the basis for determining the current and field distributions at successive quasistatic time steps. The loss is computed for the cylindrical filament as the external field is cycled while the transport current is held constant. The current distributions of Fig. 3.9 are used in this calculation. In order to simplify the discussion of the solutions the problem has been divided into four different regimes, i.e.

- 1) no transport current, partial penetration
- 2) no transport current, full penetration
- 3) transport current, partial penetration
- 4) transport current, full penetration.

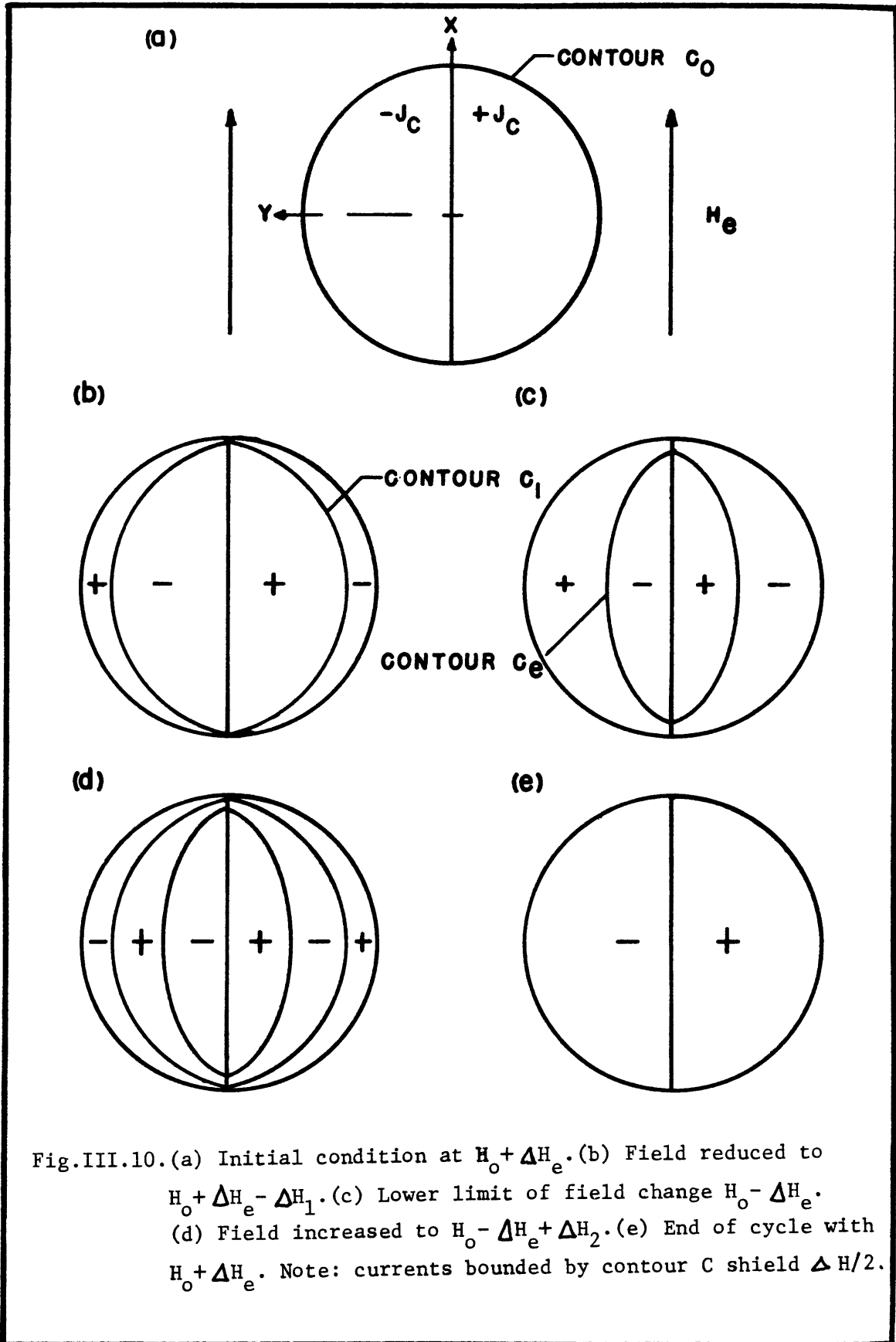
It will be shown that the expressions for the ac loss in regimes 1 through 3 are just limiting cases of the loss expression for regime 4 which is the most general situation.

III.5.1 Partial Penetration Without Transport Current

In this case we consider a circular cross-section superconducting filament situated in a uniform external field perpendicular to the longitudinal axis of the filament as shown in Fig. 3.10a. For the initial condition we assume the steady external field is much greater than the field required to fully penetrate the filament given by $H_p = J_c d / \pi$. This allows us to make two further assumptions, namely the entire conductor is in the critical state and the screening current density everywhere is J_c which is a constant as per the Bean model.

Now consider what occurs as the external field is cycled by an amount $\pm \Delta H_e$ where $\Delta H_e \leq H_p \ll H_e$. Screening currents will be induced to shield the interior region of the filament from the field change. On a macroscopic scale these will appear as regions of $+J_c$ and $-J_c$. The current distribution will create a magnetic field that exactly cancels ΔH_e everywhere within the region circumscribed by the currents as shown in Fig. 3.10b. The actual contours that define the current distribution boundaries have been found by the method of complex variables and presented in Section III.4.

The actual time dependent current and flux pattern is just a series of quasistatic steps from one critical state configuration to the next.



The mechanism that allows this sequence to develop is the flux flow resistivity which allows the flux to penetrate. As the external field is changed a current J is induced to flow which is just slightly greater than J_c , resulting in a resistivity ρ_f . The flux then penetrates into a new stable configuration.

The instantaneous energy dissipation can be computed from $J \cdot E$ integrated over the volume of the filament. The electric field can be found from the Maxwell equation

$$\nabla \times E = - \frac{\partial B}{\partial t} \quad (3.32)$$

and B is related to J by

$$\nabla \times \frac{B}{\mu_0} = J \quad (3.33)$$

The solution to the above equation is non-linear and is found from the aforementioned method of complex variables and numerical iteration.

Since B and thus E are quite complex functions of position and time it is easier to compute the average loss per cycle by integrating the area within the hysteresis loop for a complete cycle:

$$W_h = \int_{\text{cycle}} \mu_0 M(H_e) d H_e \quad (3.34)$$

The magnetization M in the above expression is found by averaging the difference between the total field and the applied field,

$$M(H_e) = \frac{1}{V} \int H \, dV - H_e \quad (3.35)$$

Equations (3.34) and (3.35) are identical to Eqs. (3.8) and (3.7), respectively.

For instance, assume the external field is cycled from $H_0 + \Delta H_e$ to $H_0 - \Delta H_e$. The current distribution, designated C_0 , would initially appear as in Fig. 3.10a, and the magnetization due to this current distribution is $M_0 = M(H_p)$. Now as the external field is lowered by an amount ΔH_1 , the current pattern would appear as in Fig. 3.10b. That is, everything within C_1 is shielded. Note however that the contour C_1 , outlines the limits of the new current distribution for a field change of $\Delta H_1/2$. This occurs because the net field within the contour C_1 , must remain constant due to the screening currents. That is for $r < C_1$, the total field is $H_0 + \Delta H_e + H(C_0)$, and this must be equated to the sum of the applied field, $H_0 + \Delta H_e - \Delta H_1$, and the field due to the new current distribution $2\Delta H_n(C_1) + \Delta H(C_0)$. This requires $\Delta H_n = \frac{1}{2} \Delta H_1$. Another way of looking at this is to note that the current density has changed by $2J_c$ thus shielding $2\Delta H$. The net magnetization then is $M_0 + 2M(\frac{1}{2} \Delta H_1)$. At the lower limit of field change the magnetization is $M_0 + 2M(\Delta H_e)$. Note that for this configuration the total external field has been decreased by $2\Delta H_e$. When the field is again increased by an amount ΔH_2 the magnetization is $M_0 + 2M(\Delta H_e) - 2M(\frac{\Delta H_2}{2})$. The complete magnetization curve can be generated in this manner. The loss then is computed by carrying out the

integral in Eq. (3.34). This is performed separately for two parts of the cycle with H_e decreasing and H_e increasing. Since the integration is over a cycle and M_0 is a constant, it doesn't contribute to the loss. For the decreasing portion of the cycle

$$\mu_0 \int M d H_e = -\mu_0 \int_0^{2\Delta H_e} 2M\left(\frac{1}{2} \Delta H_1\right) d(\Delta H_1) = -4W_0(\Delta H_e) \quad (3.36a)$$

where

$$\frac{W_0(h_0)}{V} = \int_0^{h_0} M(h)dh \quad (3.36b)$$

For the increasing portion of the cycle

$$\begin{aligned} \mu_0 \int M d H_e &= \mu_0 \int_0^{2\Delta H_e} [2M(\Delta H_e) - 2M\left(\frac{1}{2} \Delta H_2\right)]d(\Delta H_2) \\ &= 4\mu_0 M(\Delta H_e) \Delta H_e - 4\mu_0 W_0(\Delta H_e) \end{aligned} \quad (3.37)$$

Summing the two contributions, the total loss is

$$\frac{W_{p0}(\Delta H_e)}{V} = 4\mu_0 [M(\Delta H_e) \Delta H_e - 2W_0(\Delta H_e)] \quad (\Delta H_e \leq H_p) \quad (3.38)$$

The magnetization as given by Eq. (3.35) has been computed from the flux profiles given in Section III.4. Figure 3.11 shows the magnetization

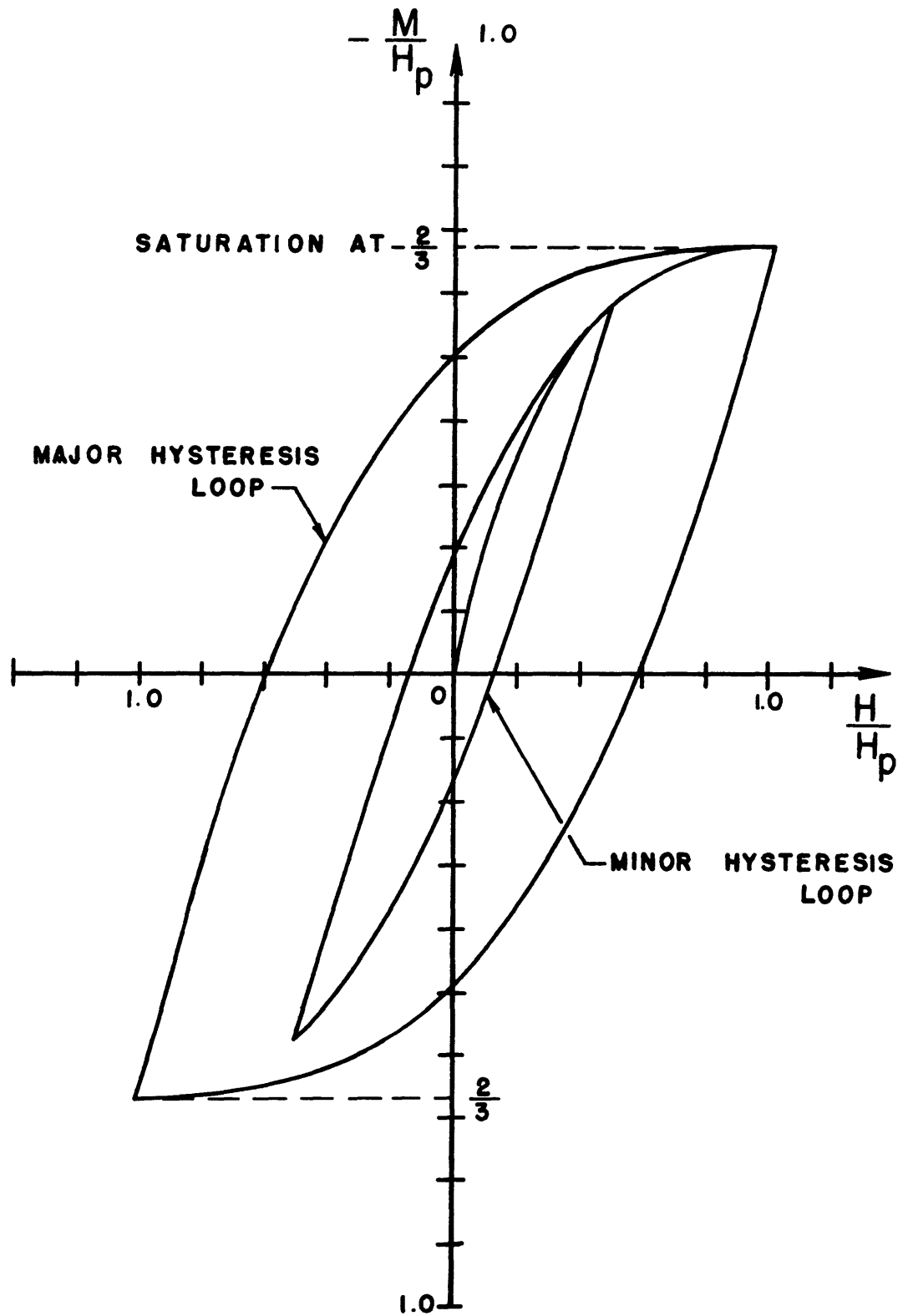


Fig. III.11. Magnetization loop for circular superconducting filament.

as a function of the external field for a cycle less than or equal to the full penetration field H_p . Pang [53] has shown that the magnetization can be expressed very accurately in the simple form

$$\frac{M}{H_p} = \frac{2}{3} \left(\frac{\Delta H_e}{H_p} \right)^3 - 2 \left(\frac{\Delta H_e}{H_p} \right)^2 + 2 \left(\frac{\Delta H_e}{H_p} \right) \quad \Delta H_e \leq H_p \quad (3.39)$$

Substituting this expression for M into Eq. (3.38) we get for the hysteresis loss per cycle per unit volume

$$\frac{W_{p0}}{V} (\Delta H_e) = \left(\frac{4\mu_0 H_p^2}{3} \right) \left[2 \left(\frac{\Delta H_e}{H_p} \right)^3 - \left(\frac{\Delta H_e}{H_p} \right)^4 \right] \quad \Delta H_e \leq H_p \quad (3.40)$$

where the external field is cycled from $H_0 + \Delta H_e$ to $H_0 - \Delta H_e$. Equation (3.40) has also been derived by Zenkevitch [54].

III.5.2 Full Penetration Without Transport Current

This is a continuation of the previous case after ΔH_e exceeds H_p . At this point the current distribution becomes a constant as long as ΔH_e continues to increase and the entire filament is in the critical state. Now as the external field is changed the current density is increased again to just over J_c and the flux flows dissipatively. The electric field now is relatively simple to compute if $\Delta H_e > H_p$ then the electric field is given by

$$E = -\mu_0 \frac{\partial(\Delta H_e)}{\partial t} y \quad (3.41)$$

The electric field is positive in the region of positive current density and negative in the region of negative current density. The line separating the regions of positive and negative current is parallel to the changing applied field and $E=0$ along this boundary (see Fig. 3.10e).

In the section of flux flow it was shown that the electric field can also be related to the current by the flux flow resistivity,

$$E = \rho_f(J - J_c) \quad , \quad J > J_c \quad . \quad (3.42)$$

Since E can be readily computed from Eq. (3.39), an order-of-magnitude estimate of $\Delta J = (J - J_c)$ can be made. This was done for typical material constants and dimensions and $\Delta J/J_c$ is approximately, 10^{-9} , a truly small value. In fact, it is so small that there would be no loss in accuracy by using J_c as the current density when computing the loss from $J \cdot E$.

The total loss over a complete cycle is the sum of the loss during the partial penetration regime plus the loss when ΔH_e exceeds H_p and is given by

$$W_{fp0} = W_{p0}(H_p) + \int_{\text{cycle}} \int_{\text{volume}} J_c \cdot E \, dV \, dt \quad (3.43a)$$

where

$$\int J_c \cdot E \, dV = -2\ell \int_{-d/2}^{+d/2} \int_0^{\sqrt{\frac{d^2}{4} - x^2}} \mu_0 J_c \cdot |\dot{H}| y \, dy \, dx = \mu_0 J_c \frac{d^3}{6} |\dot{H}| \ell \quad (3.43b)$$

and

$$\begin{aligned}
 \int_{\text{cycle}} \mu_0 J_c \ell \frac{d^3}{6} |\dot{H}| dt &= \frac{\mu_0 J_c d^3 \ell}{6} \left[- \int_{H_0 + \Delta H_e - 2H_p}^{H_0 - \Delta H_e} dH \right. \\
 &\quad \left. + \int_{H_0 - \Delta H_e + 2H_p}^{H_0 + \Delta H_e} dH \right] \tag{3.43c} \\
 &= \mu_0 J_c \frac{d^3}{6} \ell 4(\Delta H_e - H_p)
 \end{aligned}$$

In the above expression ΔH_e is the maximum value of the external magnetic field change during the cycle and $\Delta H_e > H_p$. The partial penetration loss $W_{p0}(H_e)$ is given by Eq. (3.40). The total loss per cycle per unit volume then is

$$\frac{W_{fp0}}{V\text{-cycle}} = \frac{W_{p0}(H_p)}{V} + \frac{8}{3\pi} \mu_0 J_c d \Delta H_e \left(1 - \frac{H_p}{\Delta H_e} \right)$$

or

$$\frac{W_{fp0}}{V\text{-cycle}} = \frac{4}{3} \mu_0 H_p^2 \left(\frac{\Delta H_e}{H_p} - 1 \right) \quad \Delta H_e > H_p \tag{3.44}$$

It is interesting to note that the loss per cycle for the full penetration condition is proportional to the magnitude of the field change and not the time dependence of the field change.

III.5.3 Partial Penetration with Transport Current

This case is the most interesting and also the most difficult to solve, primarily due to the addition of the net transport current. The transport current has the effect of destroying most of the symmetry of the problem by the addition of the self field of the filament. In the previous cases the net sum of the currents over the cross-section was zero whereas now they must sum to the transport current J_c . The most difficult step in the analysis, however, is determining the initial state of the superconductor. Once that condition is determined the concepts of critical state, shielding and flux flow resistivity will be the primary factors in determining the equilibrium distribution of shielding currents, transport currents and the resultant magnetic field and loss.

A start can be made by estimating the relative magnitudes of the uniform bias field, the ripple field, the full penetration field at zero transport current, and the self-field of the filament at normal operating conditions. The material properties and dimensions of the multifilamentary composite superconductor for the MIT/DOE 10 MVA generator field winding are used for this calculation. The result is

Bias Field	$\mu_0 H_0 = 4.8 \text{ T}$
Ripple Field	$\mu_0 \Delta H_e = 0.01 - 0.05 \text{ T}$
Full Penetration Field at Zero Transport Current	$\mu_0 H_p(0) = 0.045 \text{ T}$
Self Field	$\mu_0 H_t = 0.012 \text{ T}$

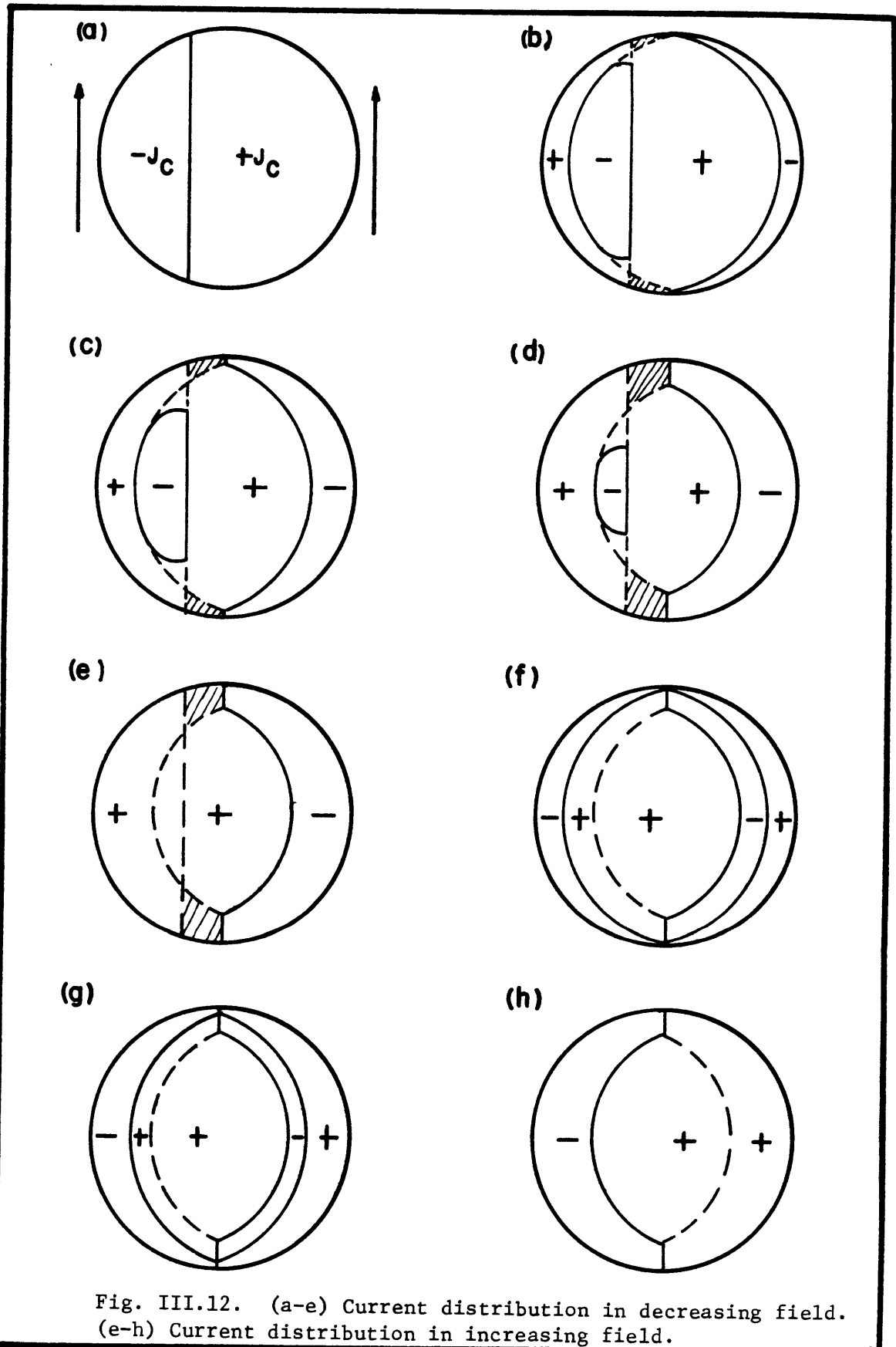
Several assumptions can be made based upon these calculations:

1) the filament is in the critical state in accordance with the Bean Model ($J_c \neq f(B)$) since $H_0 \gg \Delta H_e$; 2) the filament is full penetrated by a uniform external field long before self-field effects of the transport current become important since $H_0 \gg H_t$; 3) both partial penetration and full penetration losses must be computed since ΔH_e is of the same order of $H_p(0)$ and thus is probably larger than $H_p(I_t/I_c)$ for certain values of I_t/I_c ; 4) since the net field at the filament is amplified approximately 400 times by the other wires the external field can be assumed to be independent of the transport current, i.e., any change in the transport current distribution will be insignificant for external field changes of order ΔH_e .

The total effect of these conditions would be to assume that the filament carries a normalized transport current $i = I_t/I_c$ in a uniform background field H_0 and the filament is initially fully penetrated. The problem is to compute the loss as the external field changes from $H_0 + \Delta H_e$ to $H_0 - \Delta H_e$ and back while the transport current remains constant. This must be done for two conditions: 1) $\Delta H_e \leq H_p(i)$ and 2) $\Delta H_e > H_p(i)$. In this section we are only interested in the first condition.

The exact initial current distribution in the filament is not known. In fact, there is not any one true initial state since the current pattern is determined by the past history of current and field changes.

As an initial starting point let us assume the same current distribution as proposed by Carr for the same conditions [58]. The current distribution as shown in Fig. 3.12a has regions of positive and negative current



with the interface between the two regions forming a line parallel to the applied field. The net current is equal to the transport current and is always given by

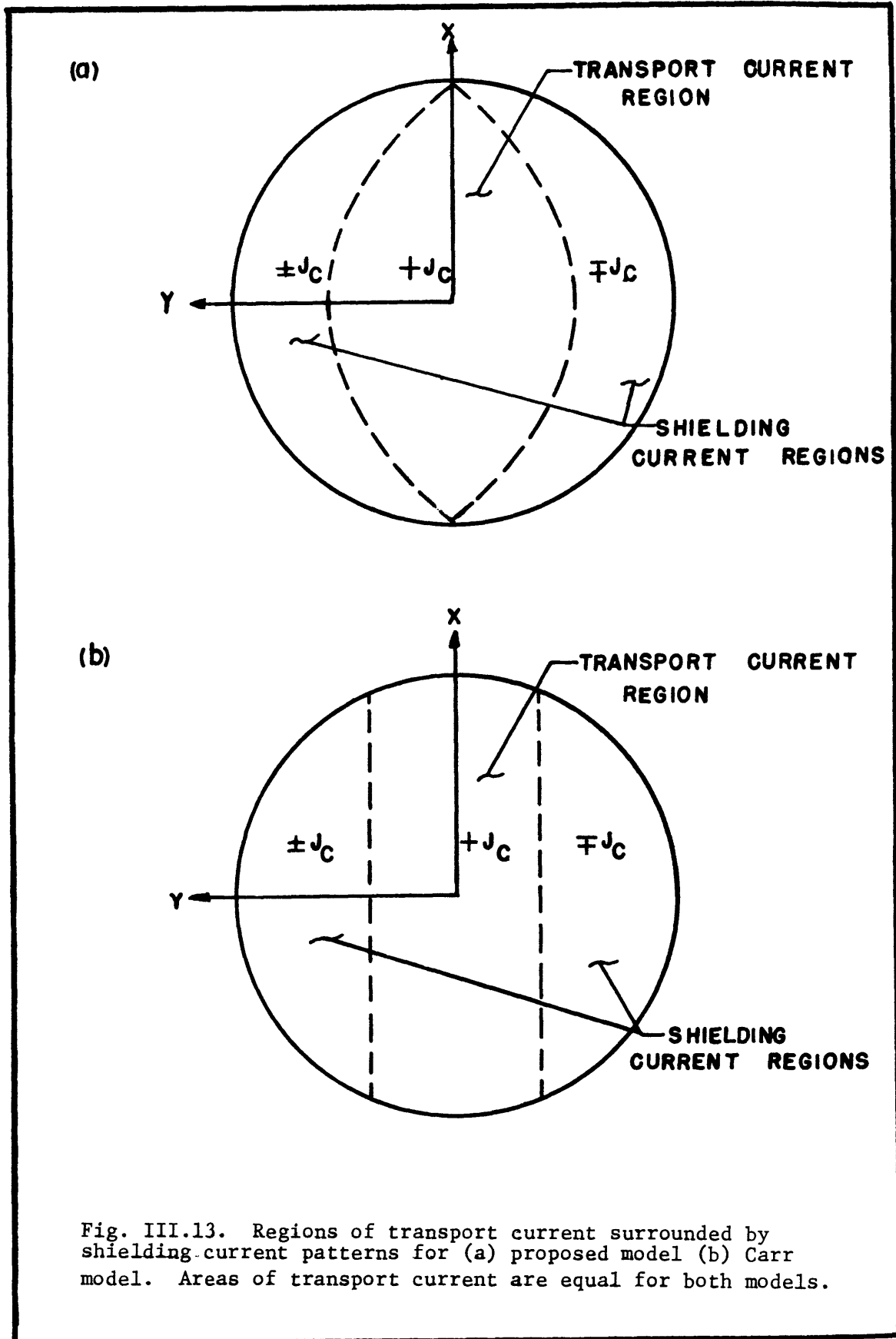
$$\frac{I_t}{I_C} = \frac{A_+ - A_-}{A_+ + A_-} \quad .$$

Now consider the general behavior as the external field is changed. Flux either enters or exits from the surface of the filament inducing currents to flow so as to maintain the flux intensity within the shielded region at the original value. The sequence of sketches in Figs. 3.12a - 3.12h are approximations of the quasistatic time dependence of the current distribution. The shielding current pattern will initially appear in an almost sinusoidal distribution with negative currents induced in the right half plane and positive currents in the left half plane, Fig. 3.12b. However, a small region of positive current on the left (shown shaded) will appear highly resistive due to the flux flow resistivity since the induced J will exceed J_C . This resistivity allows more flux to diffuse out of the negative current regions in the left plane. This unsymmetrical behavior is indicated in Figs. 3.12c and 3.12d as the external field is further decreased. The negative shielding current distribution in the right plane is relatively undisturbed. At some point the entire region of negative current in the left plane will just disappear as shown in Fig. 3.12e. The current distribution will remain constant after this point. It is very important to note that the net area of positive current has always remained constant for continuity of the transport current.

The sequence of sketches in Figs. 3.12e through 3.12h indicate the behavior as the field is increased towards the original value. Flux can now enter symmetrically from the left and right because the screening currents can flow in the proper pattern to completely shield the inner region of the filament. Again the transport current has remained constant throughout the sequence but it has been redistributed into the central region of the conductor.

Some general observations can be made about the magnetic characteristics as displayed in Fig. 3.12. First, the general behavior is for the shielding currents to flow in the outer sections of the filament while the transport current is driven towards the core. Although I have shown this as occurring in one cycle it may actually take several cycles to evolve. The equilibrium distribution of currents would appear as in Fig. 3.13a. The shielding currents will alternate sign in a region near the surface while screening the transport current in the core as long as $\Delta H_e \leq H_p(i)$. The definition of the full penetration field for transport current i , $H_p(i)$, follows in that it is just the magnitude of the external field change ΔH_e which if exceeded will no longer change the current distribution in the filament.

The curves which define the boundary between shielding currents and transport current are also known. They are just the same curves which define the field penetration profiles for the case when $i=0$. This must be true because the current distributions defined by those profiles totally shield the region within them. The distribution as proposed by Carr, cannot be an equilibrium distribution because the shielding pattern as



shown in Fig. 3.13b does not shield the internal region. That is, if the internal region is not shielded, flux must flow there, inducing currents and thereby altering the current pattern further. So far only the current distributions which have recently been computed as described in Section III.4, have been shown to fulfill the shielding requirement.

A curve $H_p(i)$ versus i has been computed from the shielding profiles which were found by procedures discussed in Section III.4. The ratio I_t/I_c is simply the fraction of the filament area bounded by the curve of the flux front. The integration for the area is trivial since the curves which define the flux fronts are generated by simple polynomials. The fraction of transport current i is given by

$$i = \frac{4}{\pi} \left(a_0 x_m + a_2 \frac{x_m^3}{3} + a_4 \frac{x_m^5}{5} + \frac{a_6 x_m^7}{7} + \frac{a_8 x_m^9}{9} \right) \quad (3.45)$$

where the coefficients a_n and the x axis intercept x_m are given in Table 3.1 for several values of $\Delta H_e/H_p$. The full penetration flux curve is shown in Fig. 3.14. It goes to zero at $i = 1.0$ because the entire filament is filled with the transport current.

The type of reasoning which led to the current distribution in Fig. 3.12 can also be applied to other ac conditions. For instance, if the external field is held constant but the transport current is changed by first increasing it to I_c lowering to $I_c - \Delta I$ and back to I_c , a series of current patterns as shown in Figs. 3.15a through 3.15f evolves. Again after several cycles the central region will be shielded as the induced current flow in the outer annular region.

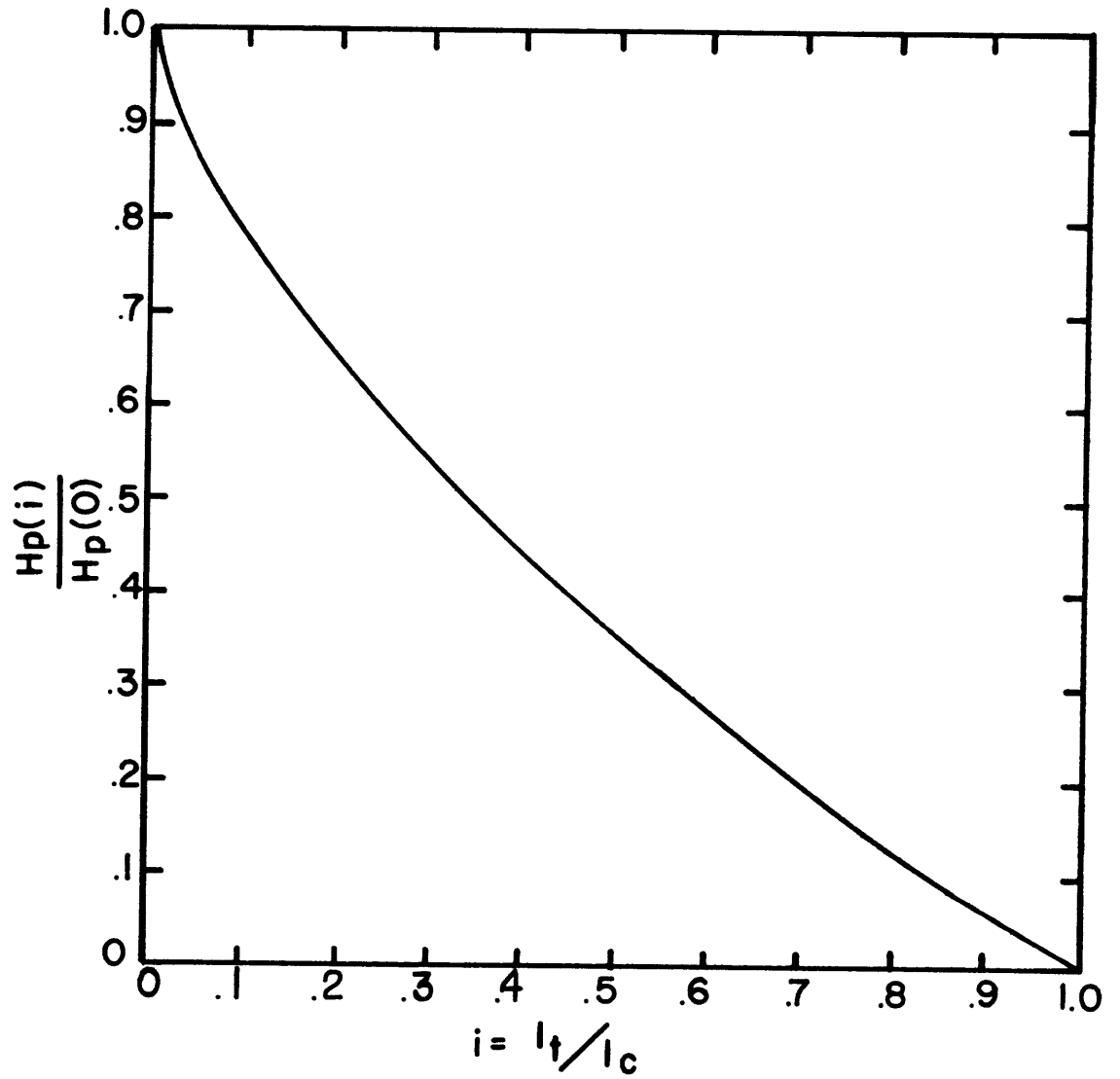


Fig. III.14. Full penetration field as a function of the transport current.

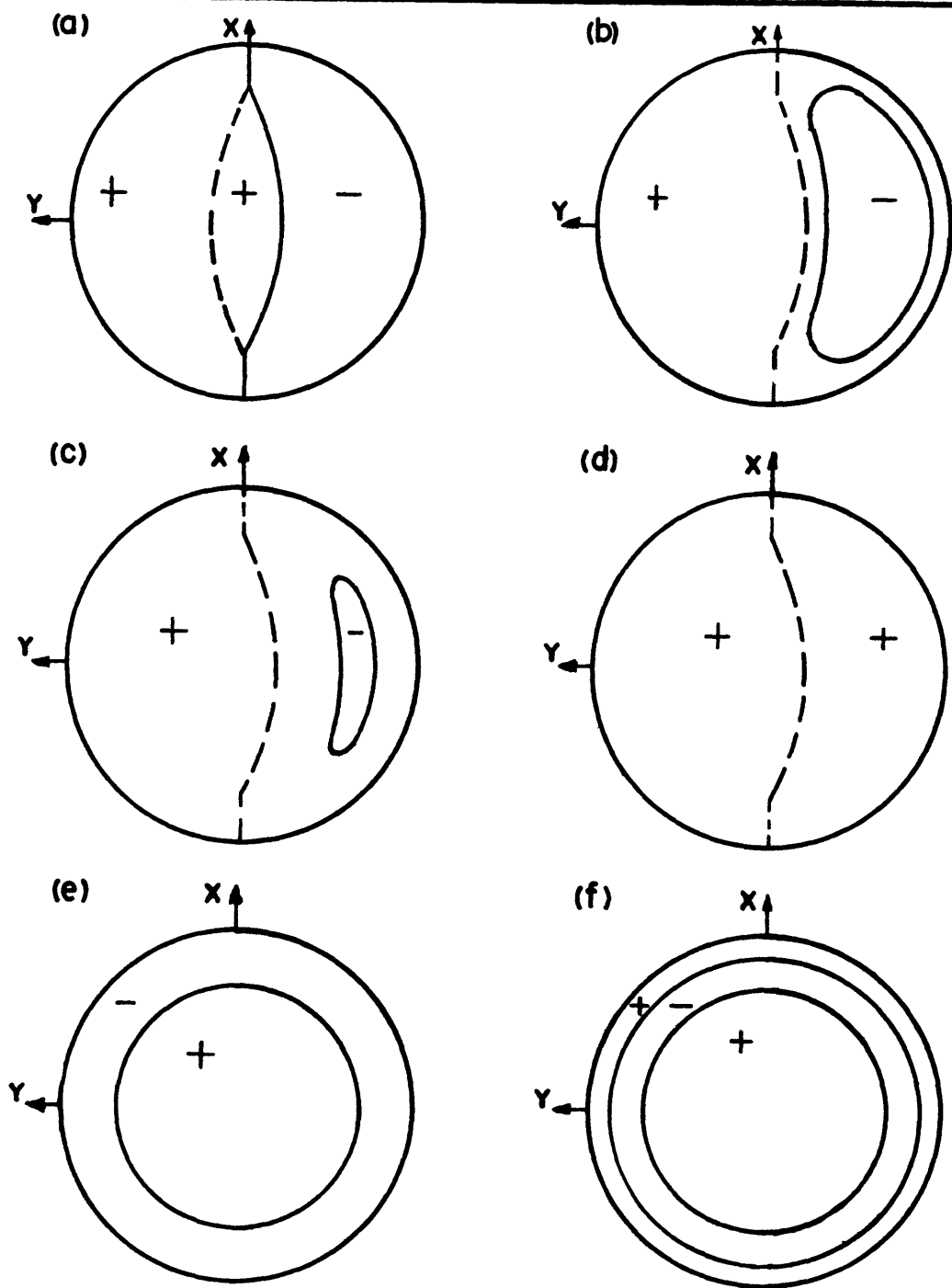


Fig.III.15. Current distributions for changing transport current in a constant uniform external field. (a-c) Increase I_t to I_c . (e) Lower current to $I_c - \Delta I_1$. (f) Increase current by $\Delta I_2 < \Delta I_1$.

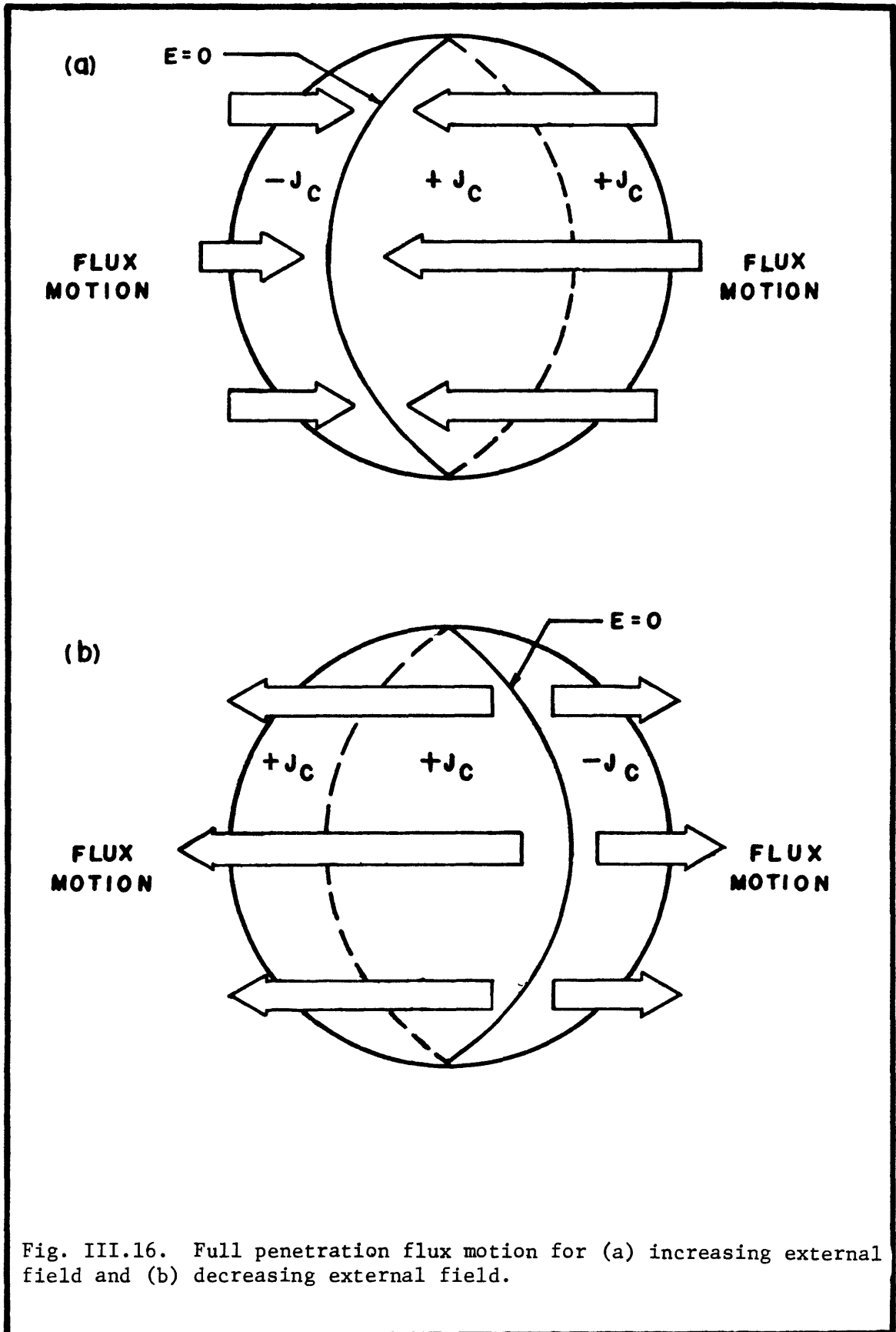
The mechanism by which these current patterns evolve quasistatically is the flux flow phenomena, just as in the zero transport current case. Therefore the losses are computed similarly to those in Section 3.5.1 (regime 1) as long as the field change is less than the full penetration field. Thus the loss per unit volume per cycle is given by Eq. (3.40) where $\Delta H_e \leq H_p(i)$

$$\frac{W_{pt}(\Delta H_e)}{V - \text{cycle}} = \left(\frac{4}{3} \mu_0 H_p^2(0) \right) \left[2 \left(\frac{\Delta H_e}{H_p(0)} \right)^3 - \left(\frac{\Delta H_e}{H_p(0)} \right)^4 \right] \quad (3.46)$$

It is interesting to note that for a given value of $\Delta H_e < H_p(0)$ the loss as a function of transport current is constant as long as $H(i) > \Delta H_e$.

III.5.4 Full Penetration with Transport Current

This case is analogous to regime 2 when ΔH_e exceeds $H_p(i)$ and the current distribution becomes fully developed. At this point the entire filament is in the critical state and any change in the external field will penetrate into the conductor dissipatively. First consider the condition for increasing H_e . The fully developed current distribution is shown in Fig. 3.16a. As H_e is increased by an amount ΔH_e greater than $H_p(i)$ flux will begin to penetrate at the surface, inducing a shielding current J that is just greater than J_c . Since the entire filament is in the critical state the Lorentz force will exceed the pinning force and flux will be driven deeper into the filament with flux in the negative current region moving to the right and flux in the positive current region moving to the left. The flux motion will only be retarded by the



viscous drag, and the electric field will be proportional to the flux flow resistivity as described previously namely,

$$E = \rho_f(J - J_c) \quad .$$

The induced current J will exceed the critical current by an amount dJ which was shown to be many orders of magnitude less than J_c ,

$$J = J_c + dJ \quad .$$

Thus the shielding field is negligible compared with ΔH_e and the rate of change of flux is uniform over the cross-section of the filament, i.e.,

$$\frac{dH}{dt} = \frac{d(H_e)}{dt} \quad .$$

Now consider what happens as the flux reaches the boundary separating regions of positive and negative current. If flux tries to move from the negative current region to the positive current region, the total induced current would be given by $J = +J_c - dJ$. The total current density would fall below J_c , the Lorentz force would drop below the pinning force and the flux motion would stop. The same reasoning holds for flux trying to cross the boundary from regions of positive current to negative current. One may ask why the total induced current does not change sign, thus allowing the flux motion to continue. The answer is that the current can't change sign because it is forced to flow

to fulfill the continuity of a net transport current. However an electric field is now required to maintain the transport current.

The total effect can be summed up as follows. The magnetic flux penetrates uniformly into the filament from both sides generating a positive electric field in regions of positive current density and a negative electric field in regions of negative current density. No flux crosses the surface separating the two regions and thus $E=0$ along this boundary. The power dissipation is given by $J_c \cdot E$ and can be separated into two contributions, one from the shielding currents and the other from the transport current. The external field source supplies the energy dissipated by the shielding currents and the current source power supply provides the energy dissipated by the transport current. At the critical current all the power is supplied by the current source.

The same arguments can be applied when the external field is decreasing. Flux leaves the specimen from both sides and always in such a fashion as to dissipate energy as shown in Fig. 3.16b. In a cyclic field the energy dissipation during the rising and falling branches of the field change are identical if the field change limits are symmetric. The energy dissipation per unit volume for the portion of the cycle when ΔH_e exceeds $H_p(i)$ is given by

$$\frac{W_{fpt}}{V - \text{cycle}} = \frac{1}{V} \int_{\text{cycle}} \int_{\text{volume}} J_c \cdot E \, dV \, dt . \quad (3.47)$$

The electric field in the above expression is given by

for $-1 < x < -x_m$ and $x_m < x < 1$

$$E = -\mu_0 |\dot{\Delta H}_e| y \cdot \frac{d}{2} \quad (3.48a)$$

and for $-x_m < x < x_m$

$$E = -\mu_0 |\dot{\Delta H}_e| \frac{d}{2} (y - f(x)) \quad (3.48b)$$

where x and y are normalized to the filament radius $R = \frac{d}{2}$, and $f(x)$ is the function defining the curve bounding the transport current region, defined by the coefficient of the polynomial given in Table 3.1.

The instantaneous power dissipation per unit length is given by Joule's energy integrated over the cross-sectional area of the filament,

$$\frac{P}{\ell} = \int J \cdot E \, dA \quad (3.49)$$

Substitution of Eq. (3.48) for E in the above expression gives,

$$\begin{aligned} \frac{P}{\ell} = \mu_0 J_c |\dot{\Delta H}_e| \frac{d^3}{8} \{ & 2 \left[\int_{x_m}^1 \int_0^{\sqrt{1-x^2}} y \, dy dx + \int_0^{x_m} \int_{f(x)}^{\sqrt{1-x^2}} (y-f(x)) dy dx \right] \\ & - 2 \left[\int_{x_m}^1 \int_{\sqrt{1-x^2}}^0 y \, dy dx + \int_0^{x_m} \int_{\sqrt{1-x^2}}^{f(x)} (y-f(x)) dy dx \right] \} \end{aligned} \quad (3.50)$$

Carrying out the integrals in Eq. (3.50) for

$$f(x) = a_0 + a_2x^2 + a_4x^4 + a_6x^6 + a_8x^8 \quad (3.51)$$

and dividing by the area of the filament we get for the power loss per unit volume,

$$\frac{P}{V} = \frac{2}{3} \mu_0 H_p |\dot{\Delta H}| \gamma(i) \quad (3.52)$$

where H_p has been substituted for $\frac{J_c d}{\pi}$.

The function $\gamma(i)$ is given by the integrals in Eq. (3.50) and for simplicity is shown plotted as a function of i in Fig. 3.17. However much more information can be learned from Eq. (3.49) if we note that a portion of the integration is over the region of the filament that carries transport current and the remainder of the integration is over the shielding current region. Then the function $\gamma(i)$ can be shown to be the sum of the two contributions, i.e.

$$\gamma(i) = \alpha(i) + \beta(i) \quad (3.53)$$

where $\alpha(i)$ is proportional to the loss in the shielding current region and $\beta(i)$ is proportional to the loss in the transport current region. The source of the power proportional to $\alpha(i)$ is the external field and the source for $\beta(i)$ is the current supply. The two functions are given by the following integrals;

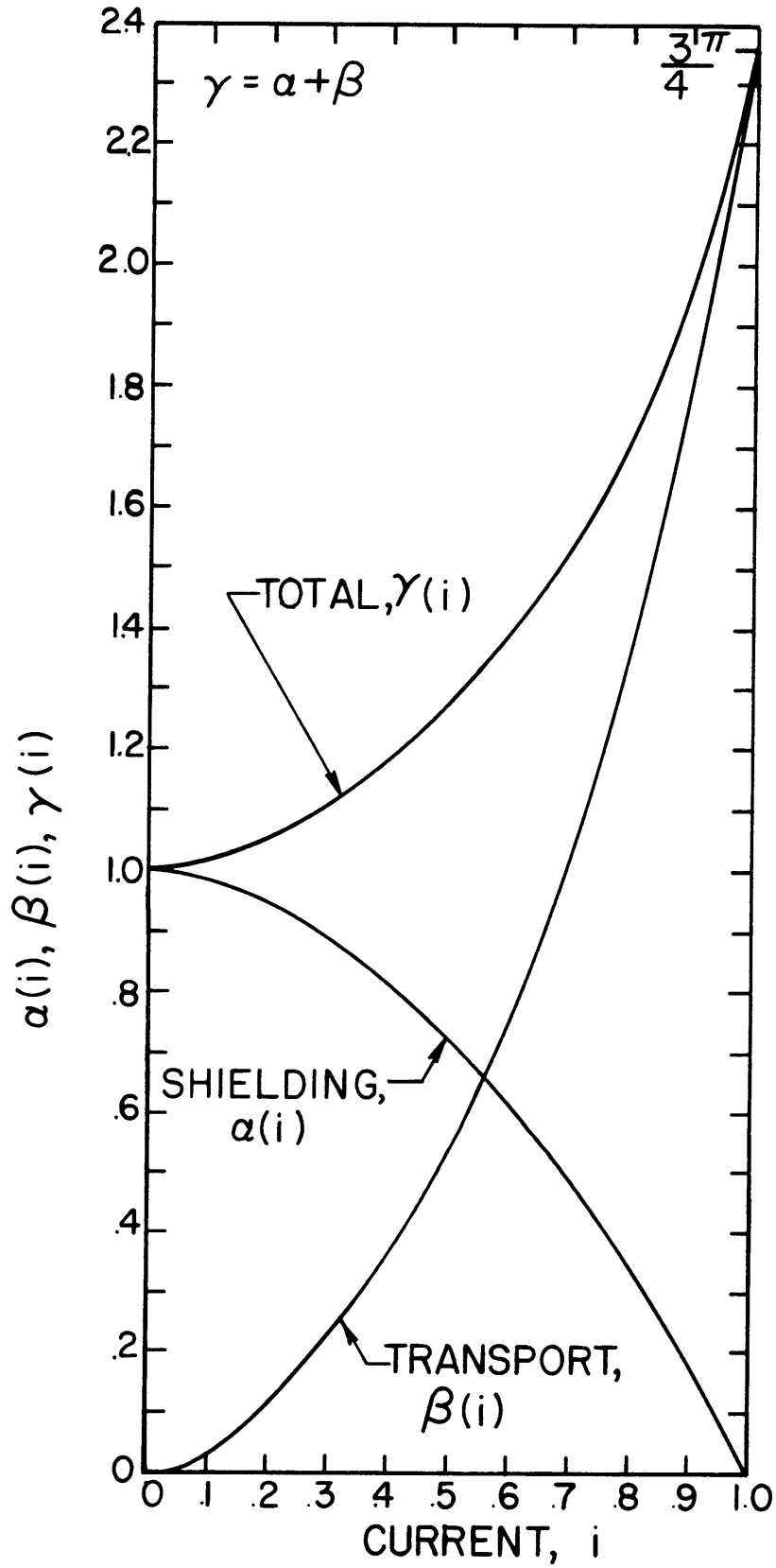


Fig. III.17 Functions α, β , and γ as a function of transport current.

$$\alpha(i) = \frac{3}{4} \left[4 \int_{x_m}^1 \int_0^{\sqrt{1-x^2}} y \, dy dx + 2 \int_0^{x_m} \int_{f(x)}^{\sqrt{1-x^2}} (y-f(x)) \, dy dx \right. \\ \left. - 2 \int_0^{x_m} \int_{\sqrt{1-x^2}}^{-f(x)} (y-f(x)) \, dy dx \right] \quad (3.54)$$

$$\beta(i) = \frac{3}{4} \left[\int_0^{x_m} \int_{-f(x)}^{f(x)} (y-f(x)) \, dy dx \right] \quad (3.55)$$

The functions $\alpha(i)$ and $\beta(i)$ have been plotted in Fig. 3.17 along with $\gamma(i)$. The shapes of the curves are not unexpected since at zero transport current it is obvious that $\beta(0) = 0$ and $\alpha(0) = 1$. As i is increased $\alpha(i)$ must decrease and $\beta(i)$ must increase since a greater area of the filament is filled with the transport current leaving less area for the shielding currents. The maximum loss occurs when the filament carries full transport current at $I_t = I_c$, and $\gamma(i) = \frac{3\pi}{4}$. Note that this result is different than that given by the slab model under similar conditions where the loss was increased by a factor of 2 over the zero transport current loss (see Section III.1.2).

Now carrying out the integration for the energy loss over a complete cycle as in regime 2 we get for the total normalized hysteresis loss per unit volume per cycle,

$$\frac{W_{fpt}}{W_0} = 2 \left(\frac{\Delta H_e}{H_p(0)} \right)^3 - \left(\frac{\Delta H_e}{H_p(0)} \right)^4 \quad \Delta H_e \leq H_p(i) \quad (3.56a)$$

$$\frac{W_{fpt}}{W_0} = 2 \left(\frac{H_p(i)}{H_p(0)} \right)^3 - \left(\frac{H_p(i)}{H_p(0)} \right)^4 + 2 \left[\left(\frac{\Delta H_e}{H_{p0}} \right) - \left(\frac{H_p(i)}{H_p(0)} \right) \right] \gamma(i) \quad (3.56b)$$

$$\Delta H_e > H_p(i)$$

where

$$W_0 = \frac{4}{3} \mu_0 H_p^2(0)$$

is the full penetration loss per unit volume per cycle at zero transport current.

The first term on the right-hand side of Eq. (3.56b) is a partial penetration loss due to shielding currents. We can now separate W_{fpt} into distinct losses due to shielding currents, W_s , and due to transport current, W_t . The result is,

$$\frac{W_{fpt}}{W_0} = \frac{W_s}{W_0} + \frac{W_t}{W_0} \quad (3.57a)$$

If $\Delta H_e > H_p(i)$

$$\frac{W_s}{W_0} = 2 \left[\left(\frac{H_p(i)}{H_p(0)} \right)^3 - \frac{1}{2} \left(\frac{H_p(i)}{H_p(0)} \right)^4 \right] + 2 \left[\left(\frac{\Delta H_e}{H_p(0)} \right) - \left(\frac{H_p(i)}{H_p(0)} \right) \right] \alpha(i) \quad (3.57b)$$

and

$$\frac{W_t}{W_0} = 2 \left[\left(\frac{\Delta H_e}{H_p(0)} \right) - \left(\frac{H_p(i)}{H_p(0)} \right) \right] \beta(i) \quad (3.57c)$$

and for $\Delta H_e \leq H_p(i)$

$$\frac{W_s}{W_0} = 2 \left[\left(\frac{\Delta H_e}{H_p(0)} \right)^3 - \frac{1}{2} \left(\frac{\Delta H_e}{H_p(0)} \right)^4 \right] \quad (3.57d)$$

$$\frac{W_t}{W_0} = 0 \quad (3.57e)$$

The shielding loss W_s/W_0 is plotted as a function of current, i , in Fig. 3.18, for different values of the maximum change in external field, $\Delta H_e/H_p(0)$. The transport current loss, W_t/W_0 is plotted similarly in Fig. 3.19 and the total loss, W_t/W_0 in Fig. 3.20. The behavior is very interesting because, for values of $\Delta H_e/H_p(0) < 1$, the shielding loss is independent of i , and the transport current loss is zero up to a certain value of i . The break point is a function of $\Delta H_e/H_p(0)$. This can be explained very simply because this portion of the

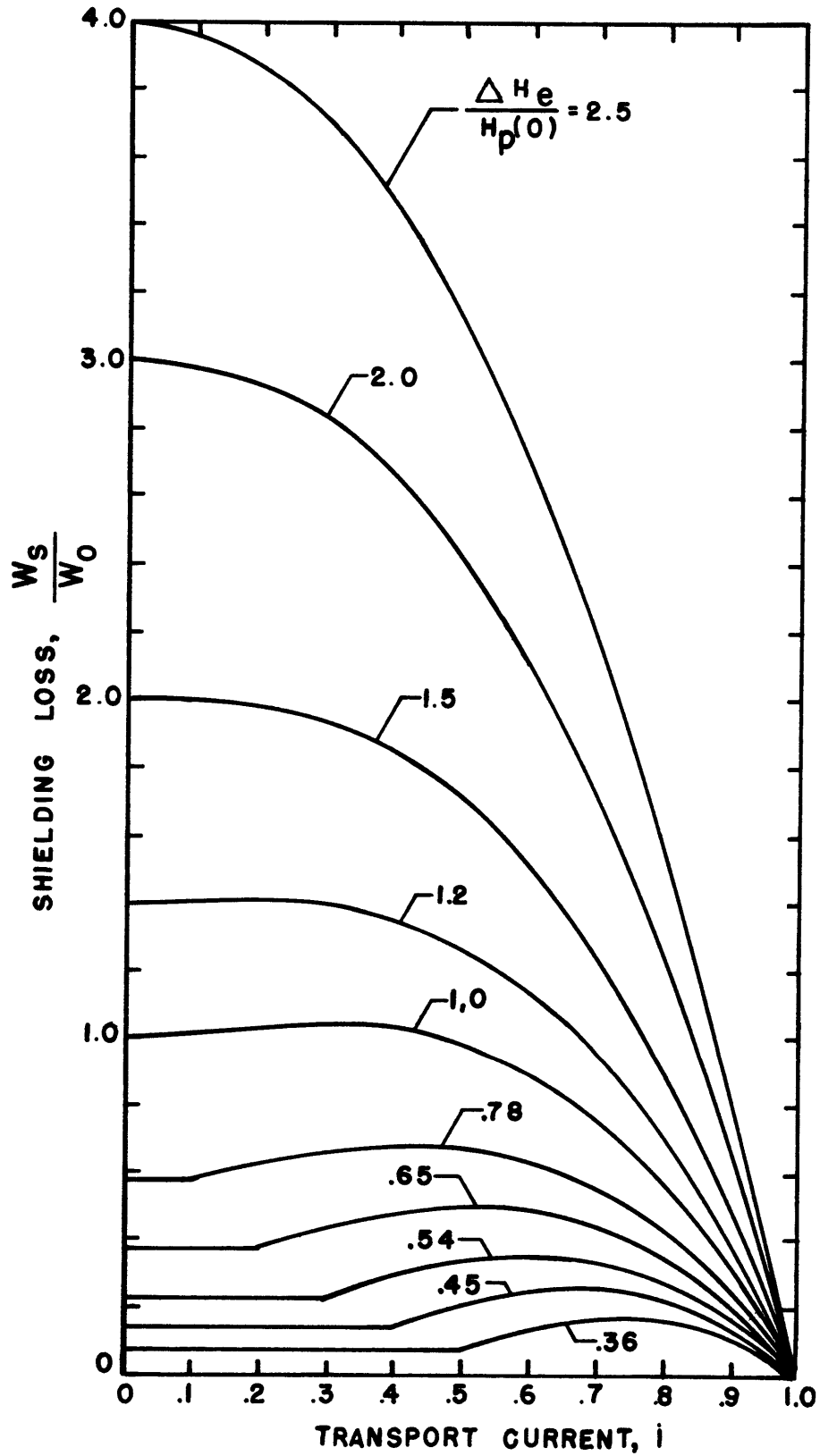


Fig. III.18. Shielding loss versus transport current for different values of external field change.

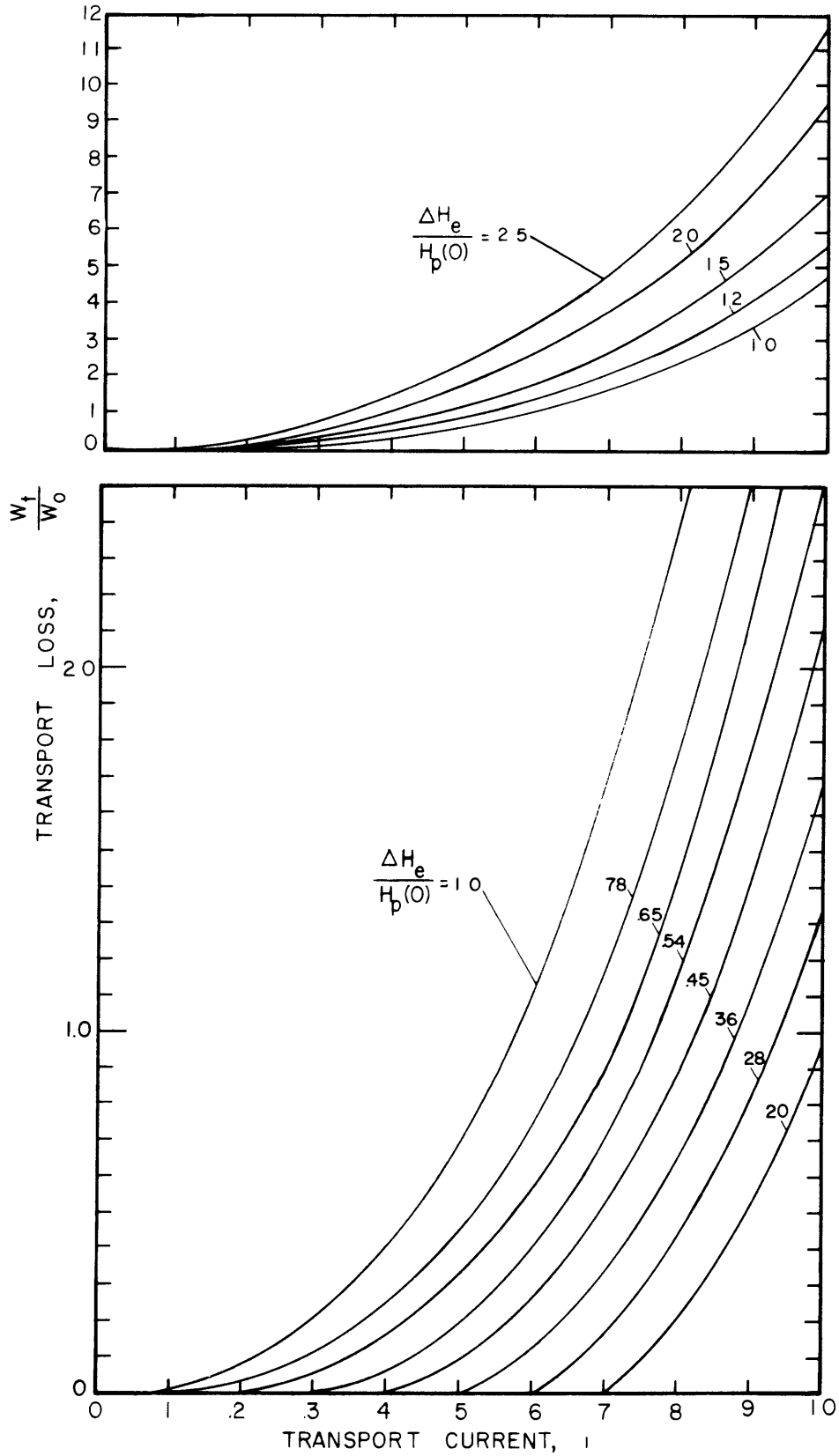


Fig. III.19 Transport loss versus transport current for different values of external field change

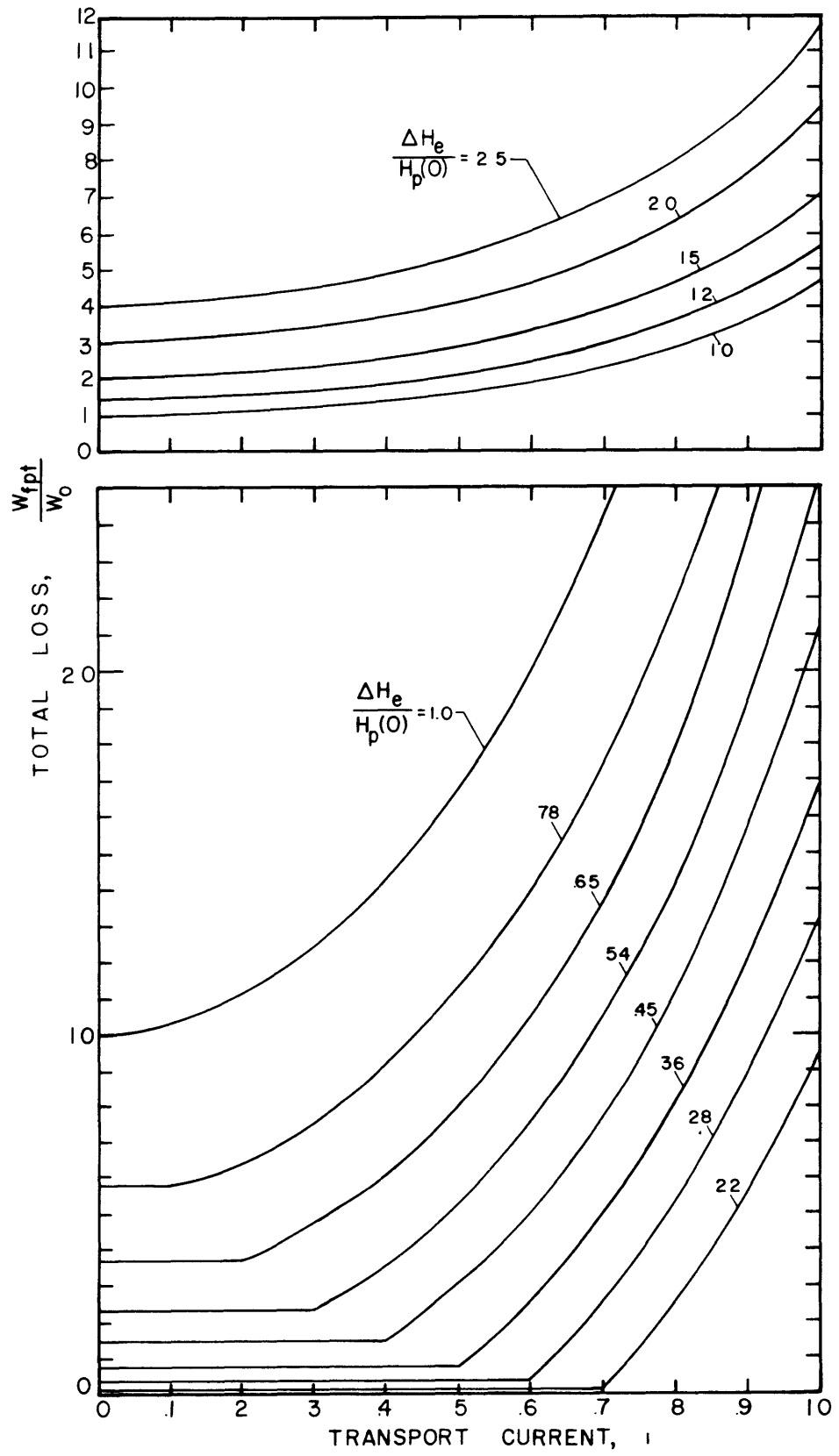


Fig. III.20 Total loss versus transport current for different values of external field change.

loss occurs only in the shielding current region as long as the field change $\Delta H_e < H_p(i)$, that is the field sweep does not penetrate as the transport current region in the central core of the filament. This type of behavior can be similarly deduced from the one-dimensional slab model as mentioned earlier in Section III.1.2. If $\Delta H_e > H_p(0)$ then the field sweep will always interact with the transport current for a portion of the cycle as long as $i \neq 0$.

The first term on the right side of Eq. (3.59b) is the magnetization loss and the second term is the loss that occurs when the filament is saturated. If $\Delta H_e \gg H_p(0)$ then the magnetization loss becomes negligible and Eq. (3.57a) reduces to

$$\frac{W_{fpt}}{W_o} \approx 2 \left(\frac{\Delta H_e}{H_p(0)} \right) (\alpha(i) + \beta(i)) = \frac{2\Delta H_e}{H_p(0)} \gamma(i) \quad . \quad (3.58)$$

Equation (3.58) is a well known result except in past work the transport current effect has been given as $\gamma(i) = 1 + i^2$ which was derived from the slab model. The correct function for $\gamma(i)$ is that plotted in Fig. 3.17. The remainder of this chapter will be concerned with reconciling the two-dimensional loss analysis for a single filament with the loss in a multifilamentary composite conductor.

III.6 Application to Multifilamentary Conductors and Experimental Evidence

The preceding analysis has dealt solely with the loss in an individual superconducting filament acting independently of any other

conductor. In practice, though, the most common type of conductor is the multifilamentary composite conductor. The analysis for this type of conductor becomes somewhat more difficult due to the interaction amongst the other superconducting filaments by coupling currents that flow through the matrix material. However, some of the essential features of the behavior of the composite conductor are qualitatively understood.

One of the most important questions that must be addressed concerns the current distribution in the composite conductor carrying a transport current. Upon initial charge of the current up to the operating level the current distribution will be non-uniform across the cross-section. The exact pattern will be determined by the geometric arrangement of the transition connections from the current supply to the composite conductor and by the magnitude and orientation of the background field. Once the external field is cycled, however, this current pattern is changed. One effect of the changing field is to redistribute the current uniformly across the composite leading to all the filaments carrying the same amount of transport current [42,59]. This effect has also been proven experimentally [60,61].

At very low frequencies the eddy current loss solely in the matrix should be negligible and so should any matrix loss due to coupling between the filaments. Thus each filament should act independently from the surrounding filaments and matrix material allowing the results of the previous section to be applied directly to each filament. The total loss for the composite will just be the loss per filament multiplied by the

number of filaments in the conductor. In the case of a pure superconducting filament the characteristic time is proportional to the time for flux to diffuse through the filament due to the flux flow resistivity and is given by Eq. (3.3). It was shown to be extremely small, usually much faster than the time scale of the field change.

In a composite conductor, however, the characteristic time is given by the time required for decay of the coupling currents in the matrix. This time, τ_0 , is given by [62]

$$\tau_0 = \frac{\mu_0}{\rho_m} \left(\frac{\ell_t}{2\pi} \right)^2 \quad (3.59)$$

where ℓ_t is the twist pitch of the filaments and ρ_m is the matrix resistivity. This resistivity is usually much less than the flux flow resistivity and, except for extremely small twist lengths, τ_0 will usually be much greater than τ_m . Very often the frequency of the external field change is of the same order as $1/\tau_0$. When this occurs the filaments no longer act individually and the currents in the entire composite become important.

At this point the composite begins to behave as a solid uniform conductor. An important parameter to describe this behavior though is no longer given by $\Delta H_e/H_p(i)$ since this new frequency limit must be accounted for. Ogasawara and coworkers [50,51] have shown that the important dimensionless parameter for this case is β , given by

$$\beta = \frac{\tau_0 \dot{H}_e}{H_p} \quad (3.60)$$

where \dot{H}_e is the time rate of change of the external magnetic field and H_p is the field required to fully penetrate the composite conductor. The time constant τ_0 is given by Eq. (3.59). Their analysis was based upon a composite conductor but used the slab model as the basis for the quantitative calculations. The qualitative behavior, however, is very similar to the two-dimensional loss behavior developed in this work, and many analogies can be drawn. The primary difference lies in the difference in the form of the functions for $\alpha(i)$, $\beta(i)$, and $\gamma(i)$. Although they don't compute these explicitly, they do compute separate equivalent losses for the shielding current loss, transport current loss, and the total loss based upon the slab model. In addition a full set of experimental data is given that qualitatively supports the analysis. The variation of the losses as a function of transport current, i , given in Figs. III.18 to III.20 bears a remarkable similarity to the data given in the work by Ogasawara. The forms differ somewhat, once $\Delta H_e/H_p(0) \geq 1$ or in his case once $\beta \geq 1$. In the case of a single filament the losses continue to increase with ΔH_e . In the case of the composite the losses saturate, i.e. all begin to fall on the same line once $\beta > 1$. The reason for this is because β depends upon frequency and once $\beta = 1$ the losses become independent of frequency because the composite acts like a single core conductor. Since the experimental data was taken by keeping ΔH_e constant and increasing the frequency the losses must become constant.

Some other experimental loss measurements with transport current are given by Carr [63], but these are not as complete as those given by Ogasawara. However, they do exhibit similar behavior. Unfortunately

very little experimental data of losses with transport current is published in the literature. The reason for this is twofold; highly accurate two-dimensional loss models for conductors with transport current did not exist, and the measurements are difficult to make with a high level of accuracy.

The experimental evidence that does exist is consistent with the loss analysis of this thesis. There is also a good probability that this analysis for a filament can be successfully extended to a composite conductor. A full set of experiments designed specifically to test the theoretical model is required.

CHAPTER IV

APPLICATION OF LOSS THEORY TO A SUPERCONDUCTING GENERATOR

An experimental electrical generator with a superconducting field winding has been designed and is presently under construction at M.I.T. as part of a U.S. Department of Energy research program to develop advanced concepts in superconducting generators for use in large central power generating stations [12,64,65]. The prototype machine is a two pole, 3600 rpm synchronous generator with a 10 MVA rating at 13.8 kV and a power factor of 0.85.

Details of the superconducting field winding design of this machine are given in this chapter and the ac loss analysis as developed in the previous chapter is applied to the superconducting winding. A thermal analysis examines the steady state and transient operating characteristics of the winding due to the ac loss and other heat inputs.

IV.1 Superconducting Field Winding Design for a 10 MVA Generator

The field winding is composed of a unique arrangement of fourteen individual saddle-shaped modules supported at discrete locations by a series of stainless steel yokes [66,67]. Figure 4.1 shows a cross-section of the generator rotor indicating the modules of the field winding located between the inner and outer support tubes. The structural yokes are individually pinned to these support tubes (Fig. 4.2) so that each module acts independent of the other modules in the winding under the influence of the steady state and transient electromechanical loading. The yokes follow the saddle shape around the end turns.

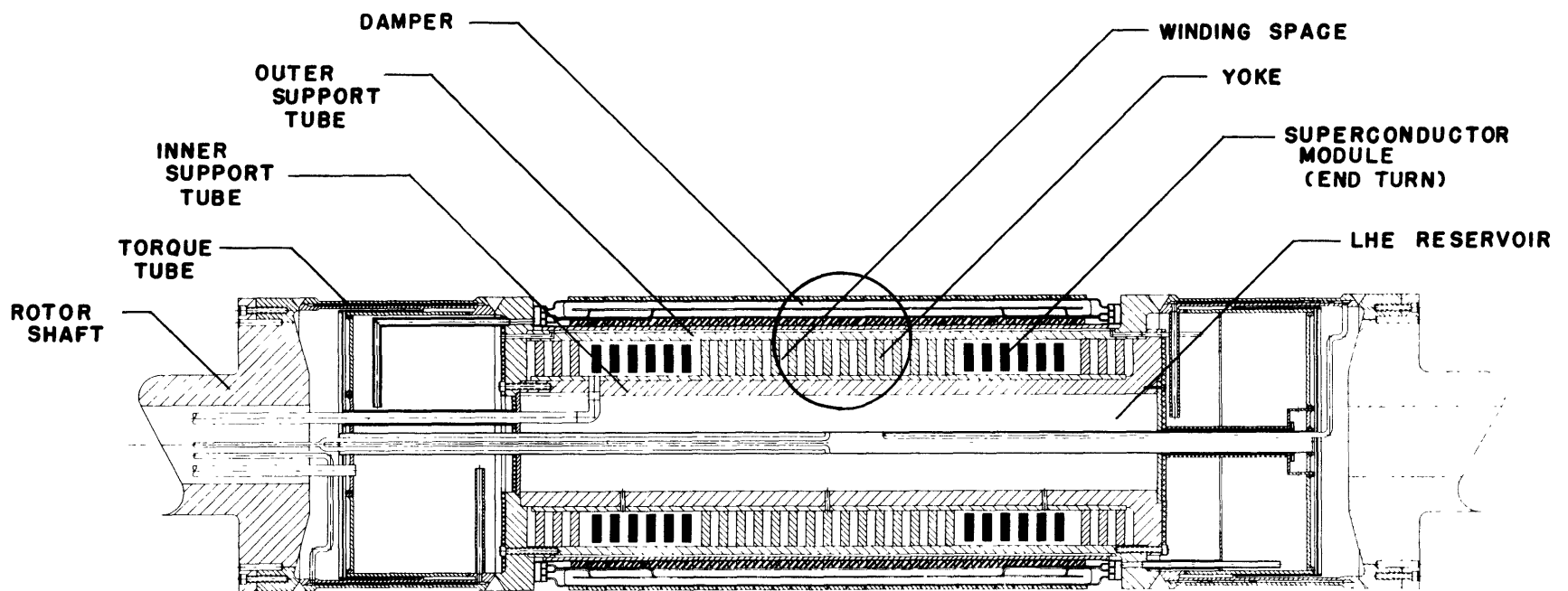


Figure IV.1 Cross-Section of the MIT 10 MVA Rotor

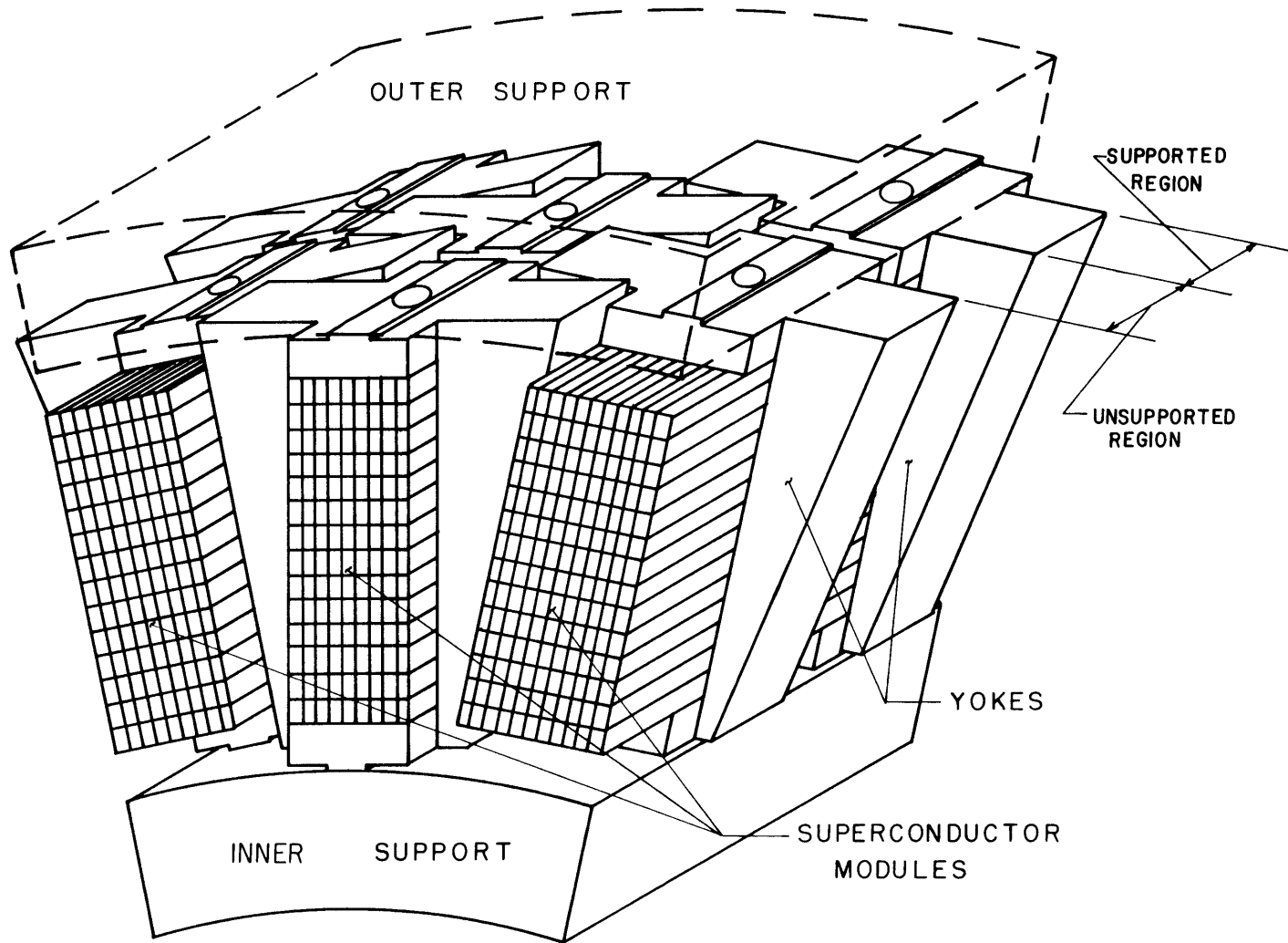


Figure IV.2 View of Field Winding in the Straight Section

Each module is composed of several layers of conductor, the number of layers per module varying from 4 near the pole face to 10 at the rotor midplane. Table 4.1 contains the characteristics of the field winding geometry. The conductors have been distributed in this fashion in order to: 1) minimize the third harmonic induced currents in the delta connected armature; 2) reduce the peak mechanical stress in the winding and structure; and 3) to minimize the peak magnetic field in the winding.

The conductors are bonded turn to turn within a layer, only in the region directly surrounded by the yokes. The layers are not bonded together but are separated by double layers of teflon so that there is no inter-layer accumulation of shear stress. This type of construction allows for a large fraction (50%) of the conductor surface area to be in direct contact with the liquid helium at the uninsulated portion of the conductors spanning the unsupported distance between yokes. Details of the winding insulation and fabrication techniques are given in Chapter V. A schematic representation of the yoke and module arrangement is shown in Fig. 4.3.

The actual conductor that is used in the field winding was chosen through an iterative process in which the number of turns was traded off against the operating current to determine the conductor size. The copper to superconductor ratio, filament diameter and number of filaments were varied in order to minimize the ac loss. The base conductor is a multifilamentary, monolithic composite of niobium-titanium alloy superconductor in a copper matrix. A monolithic conductor was chosen for ease of winding into the saddle-shaped modules and for its structural

TABLE 4.1 CHARACTERISTICS OF THE FIELD WINDING MODULES

Module Number	Angle From Pole (degrees)	Total Module Axial Length (mm)	Module Width (mm)	Number of Turns Width by Height
1	16	440	7.9	4 x 14
2	25	506	11.6	6 x 14
3	35	576	11.6	6 x 14
4	46	654	15.2	8 x 14
5	58	738	15.2	8 x 14
6	70	830	18.9	10 x 14
7	84	924	18.9	10 x 14
			Total Turns (2 coils)	1456

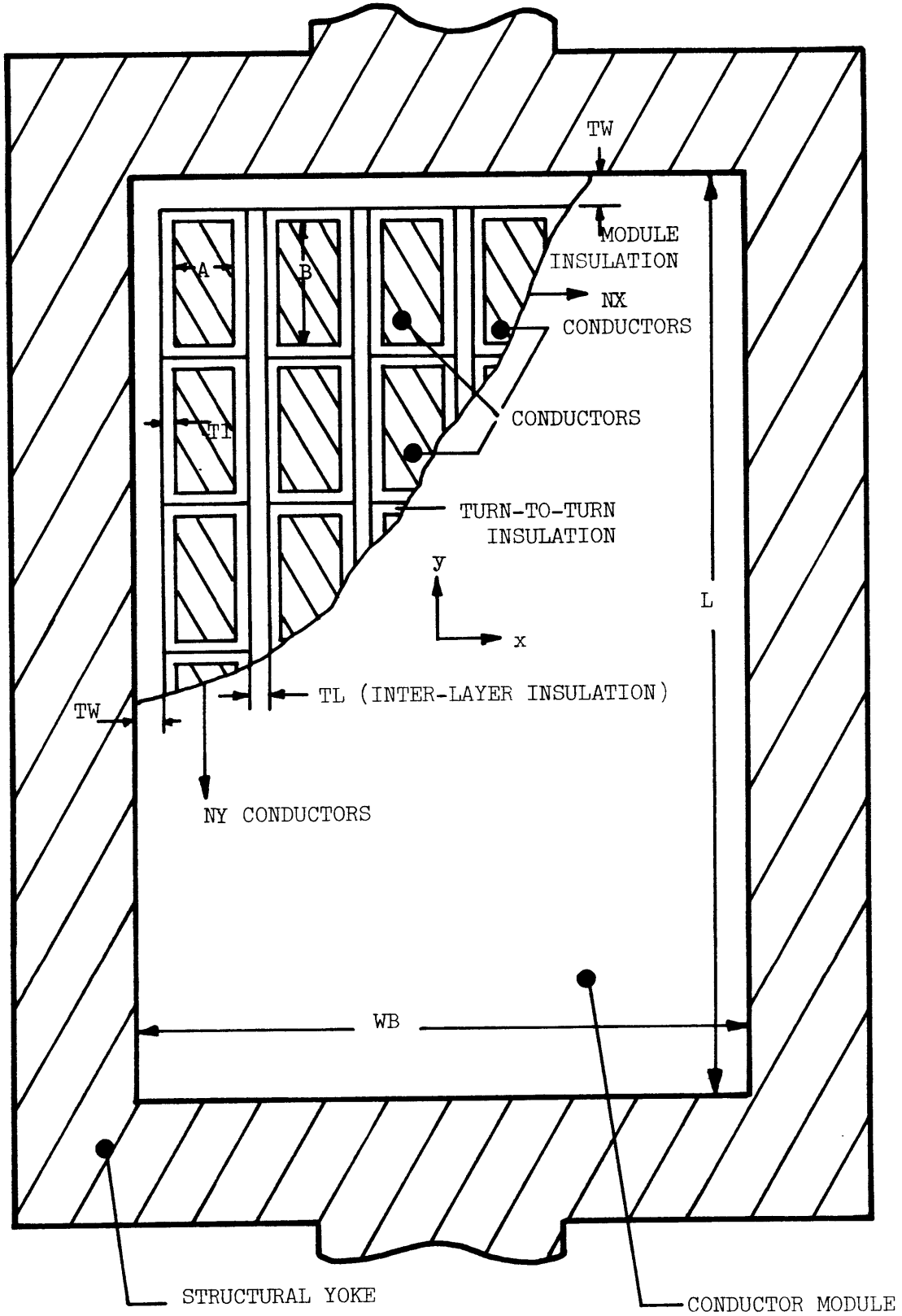


Fig. IV.3. Schematic Representation of Yoke Structure and Conductor Module

Niobium-titanium was chosen for the superconductor material due to its proven performance in many applications, its well documented properties and its wide availability.

Various conductors were analyzed ranging from 13,700 turns carrying 100 A to 137 turns carrying 10,000 A. Each gave the required number of ampere-turns, 1.37×10^6 . The low current conductors are undesirable primarily due to the complexity of winding a large number of very small conductors. The high current conductors are undesirable due to the large liquid helium boiloff in the conductor leads and problems associated with carrying large current across slip rings. A nominal operating current of 1000 A gave a reasonable compromise on lead boiloff, conductor size and ease of winding. Table 4.2 contains the conductor dimensions and operating characteristics.

Other quantities that were considered in specifying the conductor described in Table 4.2 are the copper to superconductor ratio, aspect ratio, filament size and number of filaments. The following paragraphs describe the criteria used to define these parameters.

A small aspect ratio was desired for two reasons: 1) a highly aspected conductor presents mechanical difficulties when trying to form it into a saddle-shaped winding; and 2) a large demagnetizing coefficient reduces the critical current of the conductor at the segments of the wire which are exposed to a magnetic field which is perpendicular to the large dimension. Too small an aspect ratio is not desired either since a square (1:1) conductor tends to twist when bent about two axes. This would be a problem in the end turn region. A round conductor is

TABLE 4.2 CONDUCTOR DIMENSIONS AND OPERATING CHARACTERISTICS

<u>CONDUCTOR</u>	
Matrix	Copper
Superconductor	Nb-Ti
Dimensions (mm)	2.72 x 1.49
Matrix-Superconductor Ratio	1.7:1
Twist Pitch (mm)	25.4
Filament Diameter (μm)	63
Number of Filaments	480
Volume Fraction of Superconductor	0.37
Total Length (m)	2530
Total Volume (m^3)	1.02×10^{-2}
<u>OPERATING CHARACTERISTICS</u>	
Current (A)	939
Peak Field (T)	4.8
Conductor Current Density (A/m^2)	2.32×10^8
Overall Current Density (A/m^2)	1.31×10^8
Ampere Turns (A)	1.37×10^6
Critical Current Density in Superconductor at 4.8T and 4.2K (A/m^2)	17.0×10^8
Critical Current at 7.2T and 4.2K (along magnet line) (A/m^2)	1410
Peak Discharge Ramp Rate (T/s)	.48
Peak Transient Field Rate (T/s)	.20

unsatisfactory since it reduces the packing fraction by a factor of $\pi/4$ when wound into parallel layers. Thus the value of 1.83 evolved as a suitable compromise consistent with the module fabrication.

A small copper to superconductor ratio was chosen to help provide a relatively high current density field winding to insure a large power density rating for the generator. Conductors with a large copper to superconductor ratio tend to provide quench protection since the extra copper acts as a thermal damper through increased heat capacity during thermal transients. The use of an extreme amount of copper results in a conductor which is said to be cryostable since the heat transfer to the surrounding liquid helium is greater than the resistive heat generation in a normal zone [37]. Thus a normal zone will collapse rather than propagate. This stability insurance comes at a cost of a greatly reduced current density, a price that is economically unfeasible for commercial power generators.

This field winding has been designed to avoid a quench under all but the most severe operating conditions. If a quench should occur a detector will sense this condition and rapidly extract current back through the exciter to protect the field winding [68,69,70].

It is desirable to have small filaments for stability against flux jumps and for reduced hysteresis loss. Flux jump stability was previously discussed in Chapter II. The maximum filament diameter based upon this criterion is approximately 120 μm . In Chapter III it was shown that the hysteresis loss is proportional to the filament diameter squared so the loss can be made quite small by reducing the filament size for

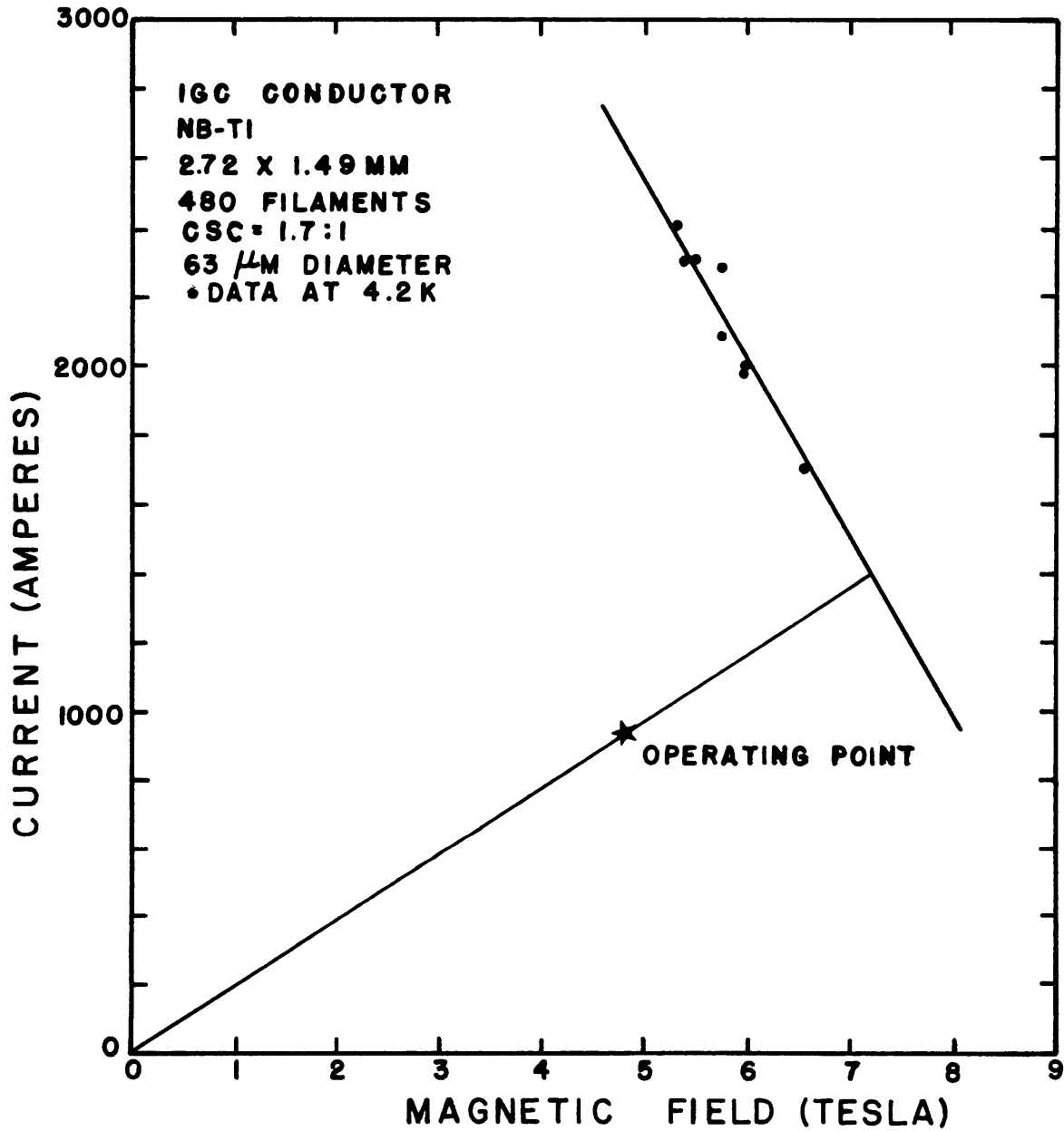


Fig. IV.4. Short sample data for 10 MVA generator superconducting wire.

this reason also. Of course the minimum size is limited by conductor fabrication considerations since very small filaments are more likely to break under strain while being drawn down and twisted.

The conductor specified in Table 4.2 meets all of the above requirements. It was manufactured by Intermagnetics General Corporation. Short samples from the ends of the conductor reels were tested at the Francis Bitter National Magnet Laboratory to determine the critical current versus magnetic field characteristics at a temperature of 4.2 k. The results of the test are shown in Fig. 4.4.

The remaining two sections contain an ac loss analysis to predict the level of energy dissipation within the conductors and a thermal analysis to calculate the temperature rise within the winding.

IV.2 AC Loss Calculation

The energy dissipated in the conductors due to alternating fields must be calculated to determine the effect of this heat generated within the winding space. The primary source of the alternating field is the transient armature current which occurs during fault conditions on the electrical system external to the machine. These fault currents generate a transient magnetic field which is shielded from the field winding by induced currents in the damper winding and copper can shield on the rotor. Since the damper and copper can are not perfect shields some of this alternating magnetic field leaks through to the field winding although it is highly attenuated. The worst condition occurs when there is a three phase short circuit directly across the armature terminals. In actual operation this condition is highly improbable.

A computer model that performs a dynamic simulation of fault transients on the generator, including three-dimensional field effects, has been developed at the M.I.T. Electric Power Systems Engineering Laboratory [71]. This program has been used to compute the rate of field change, dB/dt , at various points within the field winding during a three phase terminal fault from rated load. Although the field change for this condition is truly a transient effect it will be treated as a steady state sinusoidal variation so that the total dissipation will be overestimated. In addition, the peak loss rate will be assumed to be acting over the entire winding volume. These assumptions will give a very conservative estimate for the ac loss.

The loss calculation is divided into hysteresis and eddy current losses. The hysteresis loss is computed from the results of Chapter III. The eddy current loss is computed from Carr's anisotropic continuum model [45]. The total loss then is just the linear sum of the eddy current and hysteresis loss as long as the two mechanisms are not coupled. This will be shown to be the case from a discussion of the anisotropic continuum model.

IV.2.1 Eddy Current Loss

Carr defines eddy current losses for three different ranges of excitation frequency. In the low frequency range the eddy current flow is dominated by the composite matrix resistance given by

$$\sigma_{\perp} = \sigma_m \left(\frac{1-\lambda}{1+\lambda} \right) \quad (4.1)$$

if the filaments are insulated from the matrix and by

$$\sigma_{\perp} = \sigma_m \left(\frac{1+\lambda}{1-\lambda} \right) \quad (4.2)$$

if the filaments are in good contact with the matrix. In Eqs. (4.1) and (4.2) σ_m is the electrical conductivity of the matrix material and λ is the volume fraction of superconductor. Equation (4.1) usually applies for copper matrices because the matrix resistivity is much lower than the interface resistance between matrix and filament. The inverse is usually true for relatively high resistance matrix materials such as cupro-nickel. In the low frequency range the induced currents are determined from the time rate of change of the external field while the reaction fields of the eddy currents are neglected. The hysteresis loss and the eddy current loss are independent since the eddy currents do not shield the filaments from the external field. Hysteresis loss usually dominates.

In the intermediate frequency range the eddy current loss and the hysteresis loss become coupled, because twisted pairs of filaments carry circulating currents induced by the changing field. The closed loop currents link the filament pairs through the matrix material.

In the high frequency range the filaments are shielded from the external field by induced eddy currents that flow primarily in the matrix. Thus the hysteresis loss is small and the eddy current loss predominates. The three frequency ranges are given by;

$$\text{low frequency} \quad f \ll \left(\frac{4\pi}{L^2 \mu_0 \mu_r \sigma_{\perp}} \right) \quad , \quad (4.3a)$$

intermediate frequency

$$\left(\frac{4\pi}{L^2 \mu_0 \mu_r \sigma_{\perp}} \right) \ll f \ll \left(\frac{1}{2\pi R_0^2 \mu_0 \mu_r \sigma_{\perp}} \right) , \quad (4.3b)$$

high frequency

$$f \gg \left(\frac{1}{2\pi R_0^2 \mu_0 \mu_r \sigma_{\perp}} \right) , \quad (4.3c)$$

where L is the twist pitch, R_0 is the outer radius of the filament bundle, σ_{\perp} is as defined in Eq. (4.1) or (4.2), and the relative permeability is given by

$$\mu_r = \frac{1-\lambda}{1+\lambda} . \quad (4.4)$$

If an equivalent radius is used for the design conductor ($R_0 = 1.136$ mm) the two cutoff frequencies are $f_{low} = 26.4$ hz and $f_{high} = 167$ hz.

The frequency of transient field change at the field winding for the three phase fault is less than or equal to 2 hz which is in the low frequency range. Then the expression for the eddy current loss per unit volume in the low frequency range is appropriate;

$$\frac{P_e}{V} = \frac{1}{8} \sigma_{\perp} R_0^2 (\mu_0 H_m 2\pi f)^2 \left(\frac{2\mu_r}{1+\mu_r} \right)^2 \left[1 + 4 \left(\frac{L}{2\pi R_0} \right)^2 \right] . \quad (4.5)$$

IV.2.2 Hysteresis Loss

The results of Section III.5 are applied here to the calculation of the hysteresis loss. In the low frequency regime each filament in the composite is exposed to the full external field change. Also it is

assumed that the transport current is uniformly distributed among all the filaments so that every filament carries the same fraction of critical current as the whole composite conductor (see Section III.6). Then it is sufficient to compute the hysteresis loss in a single filament and multiply this value by the number of filaments to get the total hysteresis loss for the composite.

Based upon these assumptions several basic parameters must be computed including, the fraction of transport current to critical current i , the full penetration field at zero transport current $\mu_0 H_p(0)$, and the field to penetrate at current i , $\mu_0 H_p(i)$. These parameters are then used in the expression for hysteresis loss derived in Section III.5. The appropriate equations for the total hysteresis loss per unit volume per cycle are repeated here for convenience;

$$\Delta H_e \leq H_p(i)$$

$$W_{fpt} = W_o \left[2 \left(\frac{\Delta H_e}{H_p(0)} \right)^3 - \left(\frac{\Delta H_e}{H_p(0)} \right)^4 \right] ,$$

$$\Delta H_e > H_p(i)$$

$$W_{fpt} = W_o \left\{ \left[2 \left(\frac{H_p(i)}{H_p(0)} \right)^3 - \left(\frac{H_p(i)}{H_p(0)} \right)^4 \right] + 2 \frac{\Delta H_e}{H_p(0)} \left[1 - \left(\frac{H_p(i)}{\Delta H_e} \right) \right] \gamma(i) \right\} ,$$

where $W_o = \frac{4}{3} \mu_0 H_p^2(0)$. The instantaneous power dissipation is the loss per cycle multiplied by the frequency, f .

Equations (4.5) and (3.56) have been used to compute the losses at several different positions within the field winding during a three phase fault. The results for two points with the greatest loss are shown in Table 4.3. The total loss in watts assumes the loss rate is uniform over the entire winding, and is given by

$$P_{\text{total}} = \left(\frac{P_e}{V} + \lambda \frac{P_h}{V} \right) \cdot V \quad (4.6)$$

where λ is the volume fraction of superconductor in the composite and V is the total volume of conductor in the winding.

The results are interesting because they point out the significance of dB/dt on the loss rate. The eddy current loss is greater at position 1 than at position 2 because the frequency is greater at that point. However the hysteresis loss at position 2 is greater than at position 1 because the magnitude of the field change, $\mu_0 \Delta H_e$, is greater, that is, the hysteresis loss depends on the magnitude of the field change, not the time rate of change of the field. However the total loss at position 1 is greater than at position 2 since the difference in the hysteresis loss is not sufficient to balance the difference in the eddy current loss. These results are used in the analysis of the next section to determine their effect on the thermal performance of the field winding.

IV.3 Thermal Analysis

The thermal analysis consists of determining the origin, magnitude, and time dependence of the heat inputs to the winding space and then developing an appropriate heat transfer model to predict the spatial varia-

TABLE 4.3 AC LOSS PARAMETERS AND RESULTS

<u>PARAMETER</u>	<u>POSITION 1*</u>	<u>POSITION 2**</u>
I_t (A)	939	939
$\mu_0 H_e$ (T)	3.15	1.93
$i = I_t / I_c$ at $\mu_0 H_e$	0.26	0.22
$\mu_0 H_p(0)$ (T)	0.06	0.072
$\mu_0 H_p(i)$ (T)	0.035	0.046
$\mu_0 \Delta H_e$ (T)	0.02	0.047
f (hz)	1.7	0.37
dB/dt (T/S)	0.20	0.11
<u>LOSS</u>		
P_e / V (w/m^3)	169	50.2
P_e (w)	1.72	0.51
W_h / v -cycle (J/m^3 -cycle)	236	1743
P_h / v (w/m^3)	401	645
λP_h (w)	1.51	2.43
P_{total} (w)	3.23	2.94

* Position 1 at outer radius of module #1 in end turn region
($r = .144$ m, $\theta = 0^\circ$, $z = .220$ m).

** Position 2 at outer radius of module #7 at center of straight section
($r = .144$ m, $\theta = 84^\circ$, $z = 0.0$ m).

tion and time dependence of the conductor temperature. This analysis also determines the cryogenic refrigeration requirements. Four primary sources of heat input to the winding space have been identified;

- 1) internal heat generation in conductors due to ac losses,
- 2) internal heat generation in conductors due to joule heating in segments of conductor that have gone normal;
- 3) conduction into the winding space due to heating in rotor structural members and electromagnetic shields,
- 4) frictional heating due to relative motion between conductor layers or between conductors and structure.

The effect of the first two heat sources are analyzed with one-dimensional and two-dimensional steady state heat transfer models. The third heat source is treated by a lumped, transient adiabatic heating model. The frictional heating source is analyzed by a local transient heating model.

IV.3.1 One-dimensional Steady State Heat Transfer Model

The individual conductors are bonded and surrounded with insulation and structure only in the locations of the yokes. Elsewhere they are in good contact with the liquid helium bath. Thus it is reasonable to assume that there is very little heat transfer transverse to the conductor axis through the insulation into the other conductors and the yoke walls, and that the primary heat removal occurs in the uncovered portion of the conductors by convection directly into the liquid helium. The one-dimensional model for this condition is shown in Fig. 4.5a where the conductor acts like a partially insulated fin with internal heat genera-

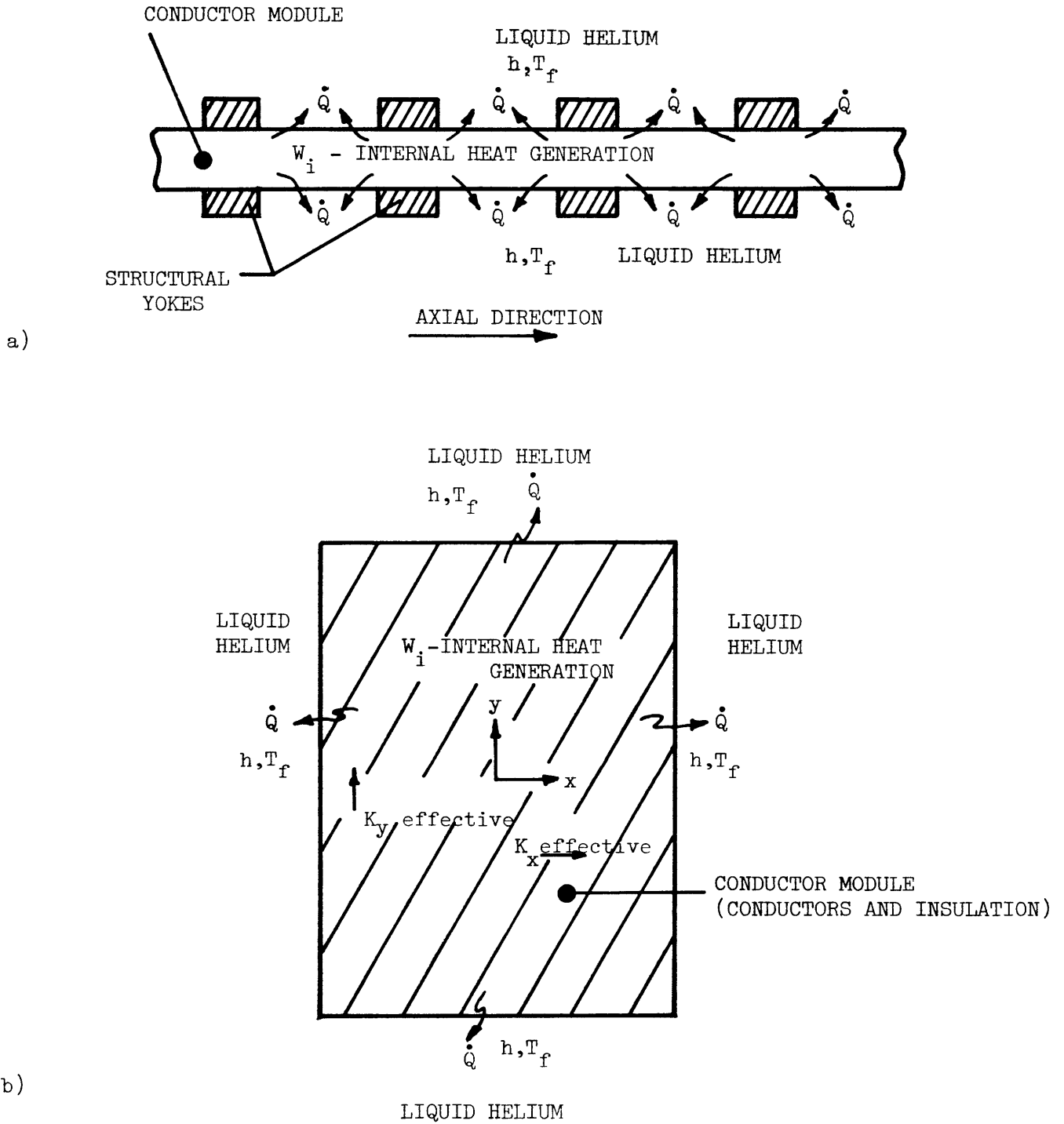


Fig. IV.5. a) One-Dimensional Heat Transfer Model;
 b) Two-Dimensional Heat Transfer Model.

tion. Details of the mathematical heat transfer analysis are given in Appendix C.

The maximum temperature rise in the conductor above the fluid temperature occurs at the location directly under the center of the yoke and is given by

$$\Delta T_{\max} = \frac{W_i}{k \beta^2} \left\{ 1 + \left(\frac{f \beta L_2}{2} \right)^2 + (f \beta L_2) \left[\frac{1 + e^{-2\beta L_2(1-f)}}{1 - e^{-2\beta L_2(1-f)}} \right] \right\} \quad (4.7)$$

where W_i = uniform internal heat generation per unit volume (W/m^3)
 k = axial thermal conductivity of the conductor ($W/m-k$)
 β = hP/kA = fin coefficient (m^{-1})
 h = convective heat transfer coefficient (W/m^2k)
 P = cooled perimeter of conductor (m)
 A = cross-sectional area of conductor (m^2)
 L_2 = half the distance between yokes (m)
 f = fraction of cooled conductor surface area.

Typical values of these parameters and the calculated temperature rise are given in Table 4.4.

IV.3.2 Two-dimensional Steady State Heat Transfer Model

In the previous one-dimensional heat transfer model the temperature gradient transverse to the conductor cross section was neglected. In order to justify this assumption a two-dimensional heat transfer model was developed to determine the ΔT across the conductor. Figure 4.5b shows the configuration of the heat transfer model. It was assumed there is a uniform internal heat generation with heat removal at all four surfaces by convection to the liquid helium. Effective thermal

TABLE 4.4 HEAT TRANSFER MODEL PARAMETERS
AND MAXIMUM TEMPERATURE RISE

Heat Transfer Parameters

One-Dimensional Model

W_i (w/m ³)	317
k (w/m-K)	157
h (w/m ² -K)	5.0×10^3
β (m ⁻¹)	257
P (m)	8.42×10^{-3}
A (m ²)	4.05×10^{-6}
L_2 (m)	9.52×10^{-3}
f	0.5
$\Delta T_{1\max}$	1×10^{-4}

Two-Dimensional Model

w_i (w/m ³)	317
k (w/m ² K)	115
h (w/m-K)	5.0×10^3
B_i	.032
γ	1.826
$\Delta T_{2\max}$	1.5×10^{-6}

conductivities in two directions were calculated to account for the composite nature of the conductor.

The effective thermal conductivity can be easily computed by noting that the thermal conduction problem is just a potential field problem similar to the electric field problem for currents in a resistive composite conductor. In both cases the "conductivity" is determined by constitutive relationships, namely,

$$\text{heat conduction: } \frac{\dot{Q}}{A} = k \frac{dT}{dx} \quad (4.8a)$$

$$\text{electric fields: } J = \sigma E \quad , \quad (4.8b)$$

where by analogy,

$$J \rightarrow \dot{Q}/A \quad \text{Flux per unit area}$$

$$E \rightarrow \frac{dT}{dx} \quad \text{Potential gradient}$$

$$\sigma \rightarrow k \quad \text{Conductivity} \quad .$$

Since the thermal conductivity of the superconducting filaments is much less than the thermal conductivity of the copper matrix the heat flux will tend to flow around the filaments giving an expression for the thermal conductivity which is similar to that for electrical conductivity in Eq. (4.1),

$$k_x = k_y = k_m \left(\frac{1-\lambda}{1+\lambda} \right) \quad (4.9)$$

where k_m is the thermal conductivity of the matrix material. Equation (4.9) breaks down for values of λ approaching 1 because at that limit k is just the thermal conductivity of the filament material. However,

Eq. (4.9) is relatively accurate for $\lambda = .37$ as per the design conductor.

The maximum temperature occurs in the center of the conductor. An expression for the temperature rise above the fluid temperature has been derived from the heat conduction equation and is presented in detail in Appendix C. This ΔT is given by

$$\Delta T_{2\max} = \frac{t^2 W_i}{4k} \left\{ \frac{1}{B_i} + \frac{1}{2} - \frac{1}{4} \sum_{m=1}^{\infty} \frac{\sin(\alpha_m)}{\alpha_m^2 [2\alpha_m + \sin(2\alpha_m)] \left[\left(\frac{\alpha_m}{B_i} \right) \sinh(\gamma \alpha_m) + \cosh(\gamma \alpha_m) \right]} \right\} \quad (4.10)$$

where

t = conductor thickness (m)

L = conductor width (m)

k = $k_x = k_y$ = thermal conductivity (W/m-k) (Eq. 4.9)

h = $h_x = h_y$ = convective heat transfer coefficient (W/m²-k)

W_i = uniform internal heat generation per unit volume (W/m³)

B_i = $ht/2k$ = Biot Number

γ = L/t = conductor aspect ratio

α_m = the eigenvalues given by the positive roots of

$$\alpha_m \tan(\alpha_m) = B_i \quad m = 1, 2, 3, \dots$$

The maximum temperature for various values of internal heat generation are tabulated in Table 4.4.

IV.3.3 Adiabatic Heating Model

This simple model is used to compute the maximum bulk temperature of the winding space (including conductor, structure, and liquid helium) due to transient heating from all sources during a three phase fault. It assumes the heating occurs in a time much shorter than that required to remove the heat from the winding space by convection and boiling of the liquid helium at the centerline of the rotor.

The governing equation is derived from the first law of thermodynamics which equates the total energy input to the winding volume with the increase in internal energy of the components within the winding volume,

$$\Delta Q = \Delta E = \int_{T_0}^{T_{Amax}} [(mC_p)_{\text{conductor}} + (mC_p)_{\text{structure}} + (mC_p)_{\text{helium}}]dT \quad (4.11)$$

where

ΔE = total energy input to winding volume (J)

m = mass of component (kg)

C_p = specific heat of component (J/kg-K)

T_0 = initial bulk temperature (K)

T_{Amax} = final bulk temperature (K) .

The final bulk temperature, T_{Amax} , is the unknown to be determined. Fortunately Eq. (4.11) can be easily simplified by noting that the specific heat of liquid helium is several orders of magnitude greater

than the specific heat of either the conductor or structure. Although the total mass of liquid helium is much less than the amount of either conductor or structure the product of $m \cdot C_p$ for liquid helium still dominates which results in Eq. (4.11) being reduced to

$$\Delta E \approx \int_{T_0}^{T_{Amax}} (mC_p)_{\text{conductor}} dT. \quad (4.12)$$

The sources of energy input to the winding space during a transient are primarily internal heat generation within the conductors due to ac loss and heat conduction from the copper can shield. The copper can shield must dissipate some energy while shielding the field winding from transient magnetic fields and some fraction of this energy which is not removed by the liquid helium in the shield cooling circuit leaks into the winding space. The magnitude of this energy leak into the winding space has been estimated by Schwoerer [72] to be approximately 110 joules.

The ac loss contribution was estimated previously and listed in Table 4.3. The energy deposition is just the heating rate times the duration of the heating which was assumed to be six seconds, for a total ac loss energy of approximately 19.4 joules.

Since the specific heat of liquid helium is relatively constant over a small temperature range near 4.2K, Eq. (4.12) can be solved for the temperature rise ΔT_{Amax} given by

$$\Delta T_{Amax} = \frac{\Delta E}{mC_p}. \quad (4.13)$$

The amount of liquid helium in the winding space has been estimated at 0.75 liter. Evaluation of Eq. (4.13) gives an adiabatic temperature rise of 0.3 K. This value is compared with the temperature rise computed by other models in Table 4.5.

IV.3.4 Frictional Heating

This section is included for completeness to estimate the maximum local transient temperature rise due to relative motion between separate layers of conductor or between a layer of conductor and the yoke sidewall. Only the results are given of a complete heat transfer analysis developed by Tepper [66] for this condition.

The worst case that can be expected to occur, although highly unlikely, would be for the layers of conductor to suddenly slide relative to each from their unenergized equilibrium position to their fully energized deformed equilibrium position. This could occur only if the slip planes located between the conductor layers do not perform as expected and thus the static coefficient of friction is great enough to support a shear stress just until the winding is fully energized. At this point it would suddenly move to the new loaded equilibrium condition. In order to put an upper bound on the energy released it is assumed that the motion occurs instantaneously. This assumption, although unphysical, is useful if the characteristic time for motion to occur is much less than the thermal response time of the conductor and insulation system. It results in an infinite temperature at the sliding surface interface but the actual temperature at the conductor is attenuated by the intervening layers of insulation. All cooling takes place at a position axially dis-

TABLE 4.5 SUMMARY OF HEAT TRANSFER ANALYSES

One-Dimensional Model	$\Delta T_{1\max}$	=	1×10^{-4} K
Two-Dimensional Model	$\Delta T_{2\max}$	=	1.5×10^{-6} K
Adiabatic Heating Model	$\Delta T_{A\max}$	=	0.3 K
Frictional Heating Model	$\Delta T_{f\max}$	=	0.51 K

Maximum Operating Temperatures*

Steady state heating due to 3 phase fault		4.2 K
Adiabatic heating	} transient	4.5 K
Frictional heating		
		4.71 K

*Bulk fluid temperature assumed to be 4.2 K. If this temperature is greater or less than this value the operating temperature is changed by the same amount.

placed from the frictional heat generation area at the uninsulated conductor length between the yokes.

The results of Tepper's analysis have been applied to the field winding design and indicate a maximum temperature rise in the conductor of $\Delta T_{fmax} = 0.51$ K for this frictional heating condition. This is a very conservative worst case estimate but it indicates that this could be the most significant source of conductor heating as shown in the summary of the heat transfer analysis results in Table 4.5. In practice it is generally suspected that some form of frictional heating due to relative conductor motion may be the cause of some magnets quenching and training.

However, the thermal analyses for this field winding indicate there will be no sources of heating during all expected operating conditions that would increase the superconductor temperature locally above the critical temperature. If a quench is initiated for any reason the field winding will be totally protected by extraction of the energy through the exciter circuit.

CHAPTER V
EXPERIMENTAL COIL

The field winding and support structure of the 10 MVA generator represents an entirely new concept in superconducting coil design. The yoke and module winding arrangement with built-in slip planes is a new and untried approach to solving the field, force and stress distribution problems inherent in this high current density winding. Therefore, a small superconducting test coil was fabricated to evaluate the feasibility of such a design and to develop the tooling and winding techniques necessary to construct the field winding modules. Although no ac loss experiments were performed on this coil the steady state electrical, thermal, and structural characteristics were tested.

The test coil was wound with a conductor similar to that which is to be used in the field winding. Although this coil was wound in a solenoidal shape to fit the testing facilities, the cross-section of the winding and size of the structural yokes are identical to field winding module 2. This module was chosen to be simulated because it will encounter the highest net force and stress levels in the field winding.

This section includes a discussion of the details of the coil fabrication, assembly to the structure and test holder and also the characteristics of the coil as determined in the test facility.

The test coil was wound as a solenoid in order to fit easily into the large cylindrical test dewars available at the Francis Bitter National Magnet Laboratory (FBNML). The purpose of using these facilities was to

test the coil under full operating conditions by providing a uniform background field with a water-cooled, copper disc Bitter coil. Thus the overall coil dimensions were largely determined by the maximum size dewar and Bitter coil available. This was a Janus dewar sitting in the bore of the 10A (9-3/4 inch clear bore) magnet. The inner diameter of this dewar is 8-5/8" (21.91 cm). The cross-sectional dimension of the module is fixed by the field winding design and the coil O.D. was made as large as possible considering the clearances required to fit the dewar I.D. Figure V.1 shows a schematic of the coil and structure cross-section indicating the final dimensions.

The conductor that was used in the test coil is a monolithic multifilamentary composite made up of a copper matrix and 517 filaments of Nb-Ti superconductor. Each filament has a diameter of 63 μm and the copper to superconductor ratio is 1.5:1. The conductor dimensions are 2.72 \times 1.49 mm (.107 \times .059 inch).

The winding has a unique design because it is supported by a series of individual yokes surrounding the conductors in discrete locations around the module. The module which was simulated is made up of 6 layers of conductor with 14 turns per layer. The turns in each layer were bonded together and insulated from one another by pieces of pre-impregnated, B-stage, woven fiberglass-epoxy tape. This insulation was not continuous but placed only under the locations of the yokes, thus leaving the uninsulated portion of every conductor exposed to liquid helium in the areas between yokes. The resultant winding is well ventilated.

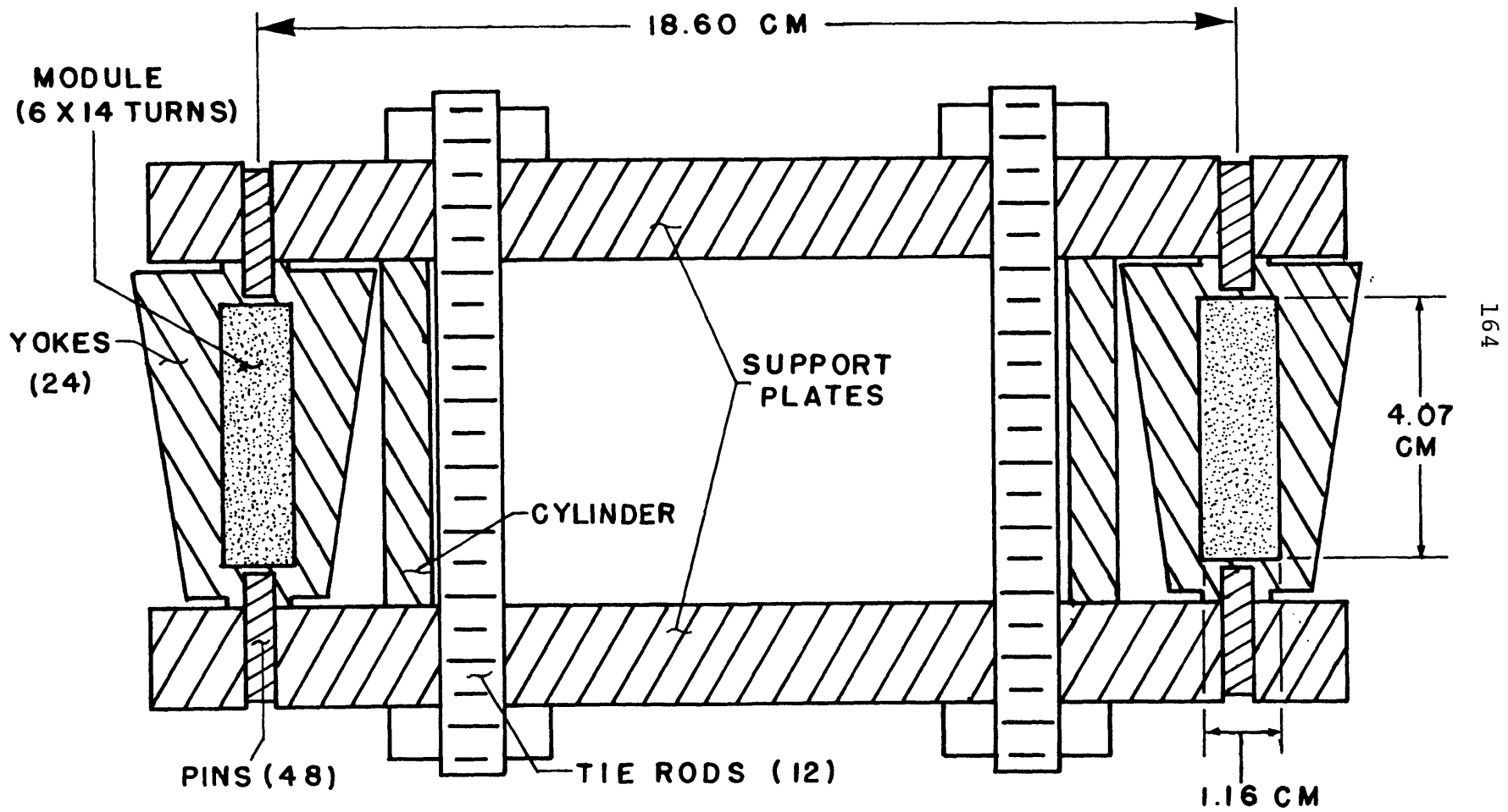


Fig. V.1. Test coil and structure cross section

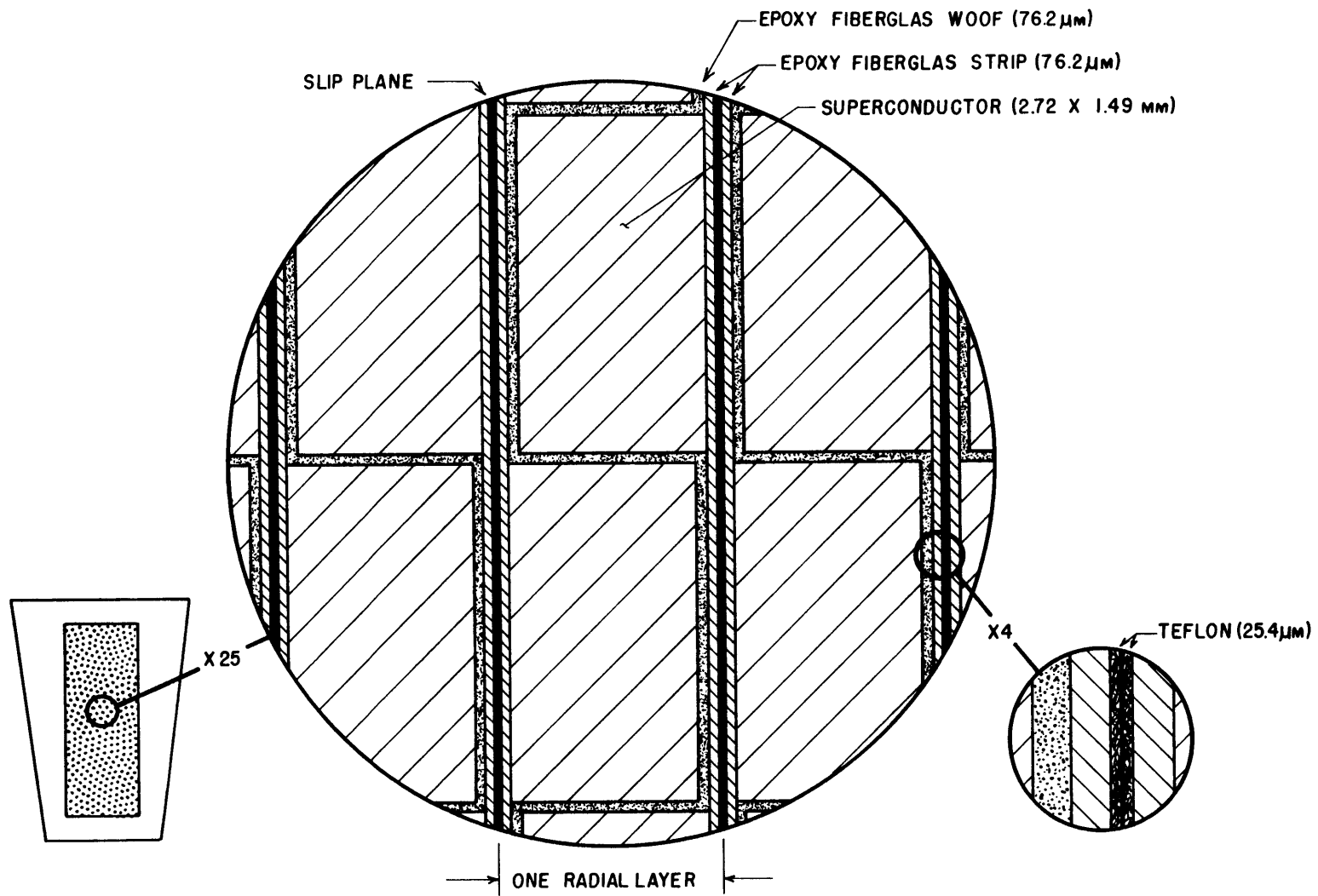


Fig. V.2. Detail of the inter-module construction

Another unique feature of this winding is that adjacent layers of conductors are not bonded together, but separated by two layers of insulation with a very low coefficient of friction, in this case Teflon. These layers of insulation are referred to as slip planes since they allow a minimum amount of shear stress to be carried across the interface. The details of the winding and insulation pattern are indicated in Fig. V.2. Further discussion of the details of the interactions within the modules due to electromagnetic and centrifugal loading can be found in the Ph.D. thesis by K.A. Tepper [66].

V.1 Winding Fabrication

Basic tooling was devised to construct such a winding, in this case a small solenoid. However this tooling had to be adaptable to winding the saddle-shaped field winding modules. The use of radial layers in the saddle-shaped modules precluded winding with pre-tension to hold the conductors in place. Therefore a winding jig was developed to hold the conductors with a series of individual linear action clamps, each positioned at the discrete location of each yoke. The clamp chosen for this application was the commonly available De Sta Co. model 610 toggle clamp. Figure V.3 shows the mandrel on which the coil was wound. The top and bottom flanges are separable from the cylinder and a clamp is provided to hold a length of conductor inside the cylinder to form a current lead. The complete winding jig is shown in Fig. V.4. It consists of the mandrel, which is held to a cylindrical table by six bolts, and 24 toggle clamps which are also bolted to the table. The toggle clamps are shown in various positions from fully extended to fully retracted. Attached to

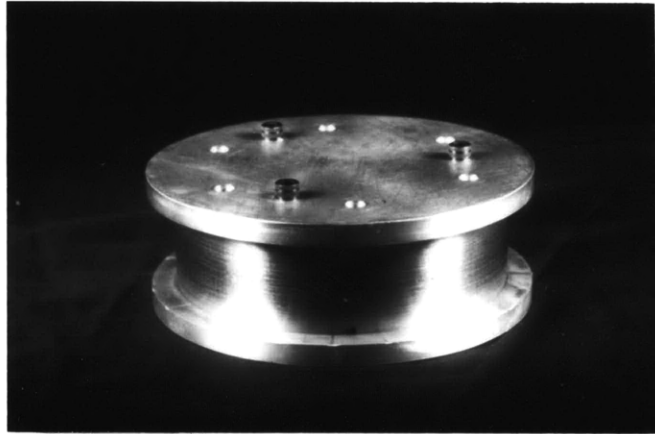


Fig. V.3. Winding mandrel

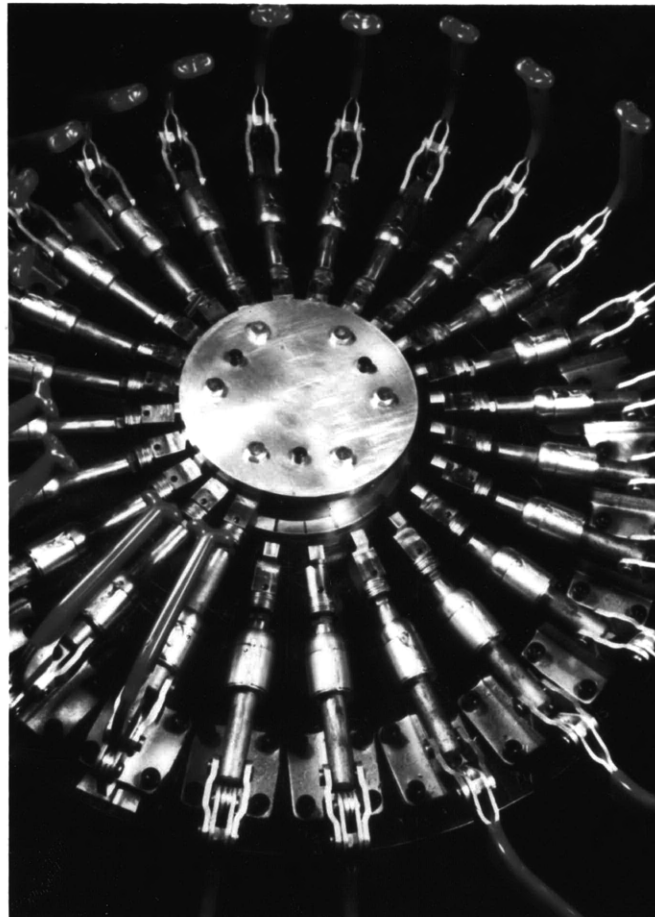


Fig. V.4. Winding jig showing the mandrel and 24 clamps mounted to the base table

the end of each clamp is a machined metal block (the pusher) which provides a uniform contact surface to force and hold the conductors in the proper radial position. These pushers are held by socket head set screws on a stud threaded into the toggle clamp. In addition, six metal spacer pieces, 0.072 inches thick, are positioned between the pusher and the clamp. Each spacer is the thickness of one layer of conductor plus insulation. These spacer pieces are removed as each layer is wound to give positive placement of the face of the pusher when the clamp is fully extended and locked. The toggle clamp provides whatever force is necessary to push the conductors into the desired position.

The following paragraphs and figures describe the winding sequence. Initially the conductor was wrapped on a spool which was suspended directly over the winding table. The spool rotates so that the wire can be pulled down and in addition the spool can swivel in a plane parallel to the table to relieve any twisting. The end of the wire was fed through a hole in the cylinder and clamped inside the mandrel. This is indicated in Fig. V.5 which shows the wire extending from the mandrel up to the spool overhead. The clamps are all retracted and three have the pusher pieces removed to show how the spacers are removed.

Before any turns were wound, the mandrel surface was covered with a sheet of Teflon .001 inch thick. Then strips of the pre-impregnated fiberglass tape .375 inches wide by .003 inches thick were fastened to the mandrel by adhesive tape to the top and bottom mandrel flanges. These were located directly in front of the clamps. A second set of fiberglass tape was located in the same position but fastened only to the bottom flange. These were used to weave between succeeding turns.

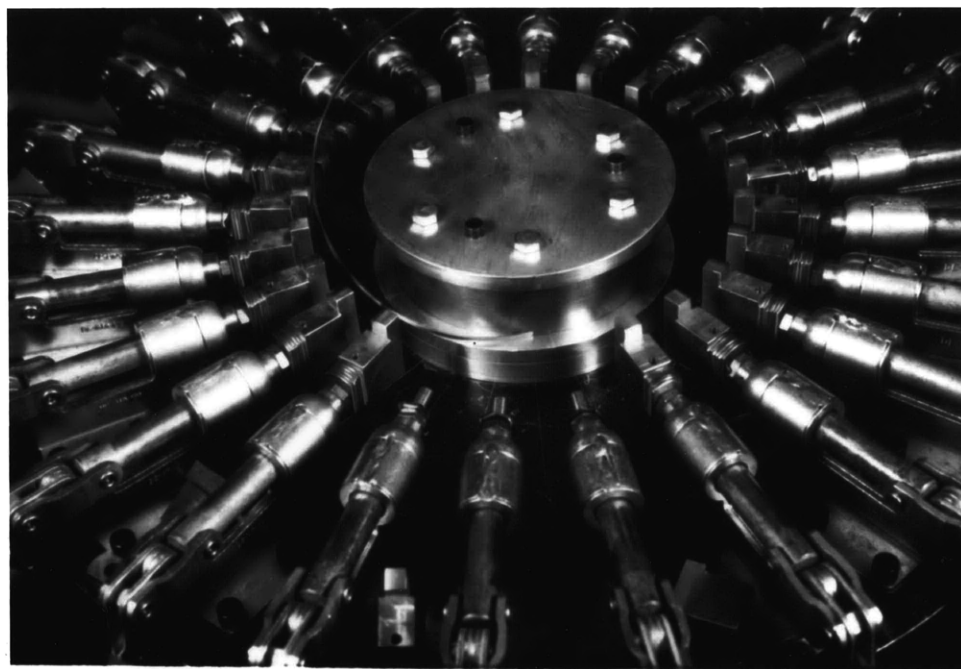


Fig. V.5. Conductor started in winding mandrel and leading to spool overhead. Note pusher pieces and spacers.

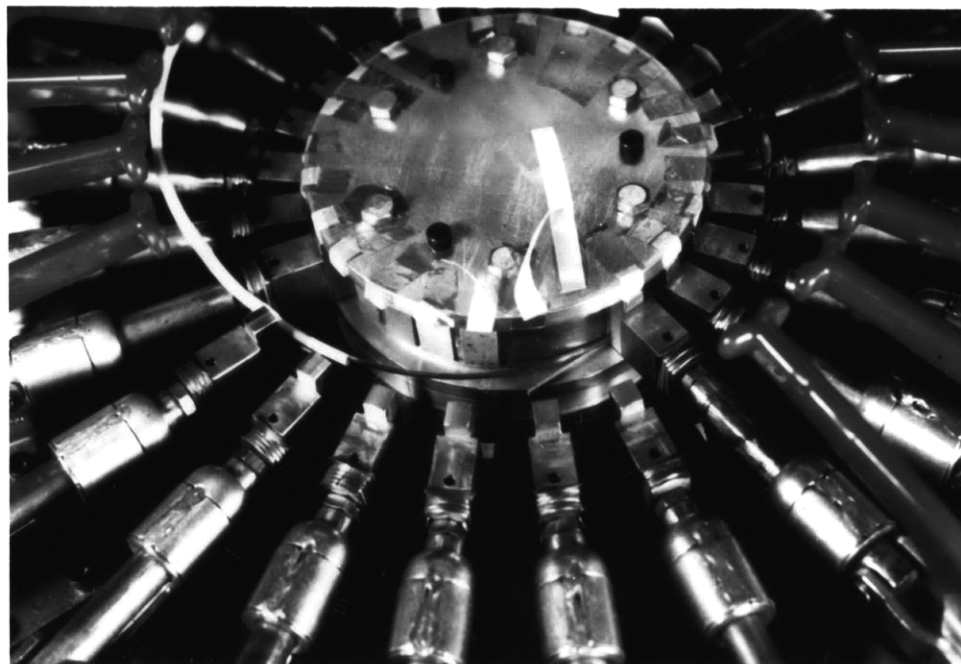


Fig. V.6. Completion of first turn showing phenolic transition piece and phenolic positioning pieces.

Winding began by extending the clamps in a clockwise sequence which forced the conductor to lie snug against the mandrel surface. Before each clamp was extended a phenolic spacer was positioned between the conductor and the mandrel top flange to keep the conductor in the proper vertical position. There were 13 sets of these phenolic spacers for the 14 turns per layer with one spacer used under each clamp. A minimum of six clamps were kept retracted to allow space for the conductor to lead up to the spool without kinking. The spool was swivelled through one revolution for each turn and the conductor was pulled down as required.

At the end of the first turn a tapered phenolic piece was wound in to serve as a transition ramp to the second turn. Figure V.6 is a photograph of the winding jig showing the completed first turn of the first layer, the phenolic vertical spacers, and the phenolic transition piece. From this point on, one clamp at the leading edge is retracted as a clamp is extended at the trailing edge. The second set of fiberglass insulation strips are positioned either all in front of or all behind the conductor as each turn is applied.

The series of Figs. V.7 through V.9 show the sequence of construction of the first layer. The second turn is just being wound in Fig. V.7 while Fig. V.8 shows the layer half completed up to turn 7. The latter figure begins to reveal the pattern of the insulation that was threaded between turns. This insulation provided all of the .003 inch turn-to-turn separation. Figure V.9 shows completion of the first layer. As the last turn was applied two more phenolic pieces were placed in the winding. One piece filled the transition space between turns 13 and 14

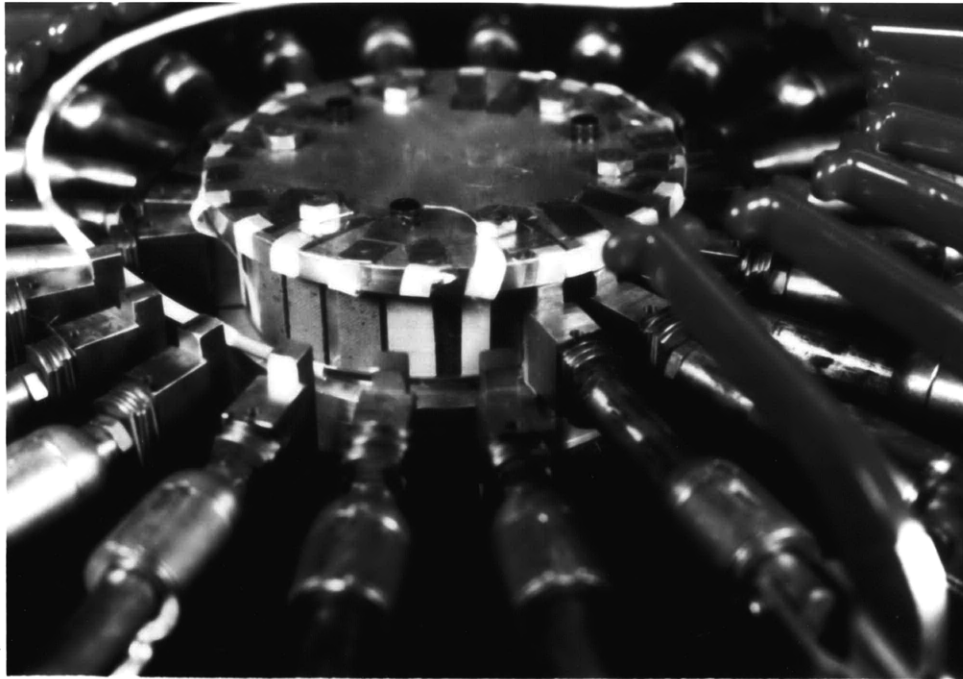


Fig. V.7. Beginning of winding of second turn

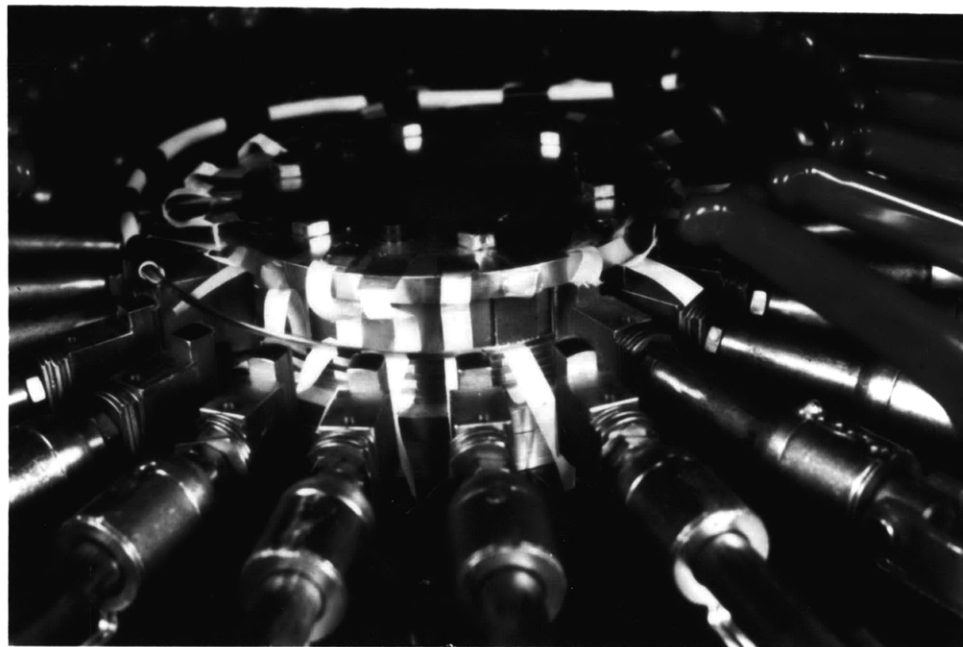


Fig. V.8. First layer half complete up to turn seven. Note interweaving of fiber-glass tape.

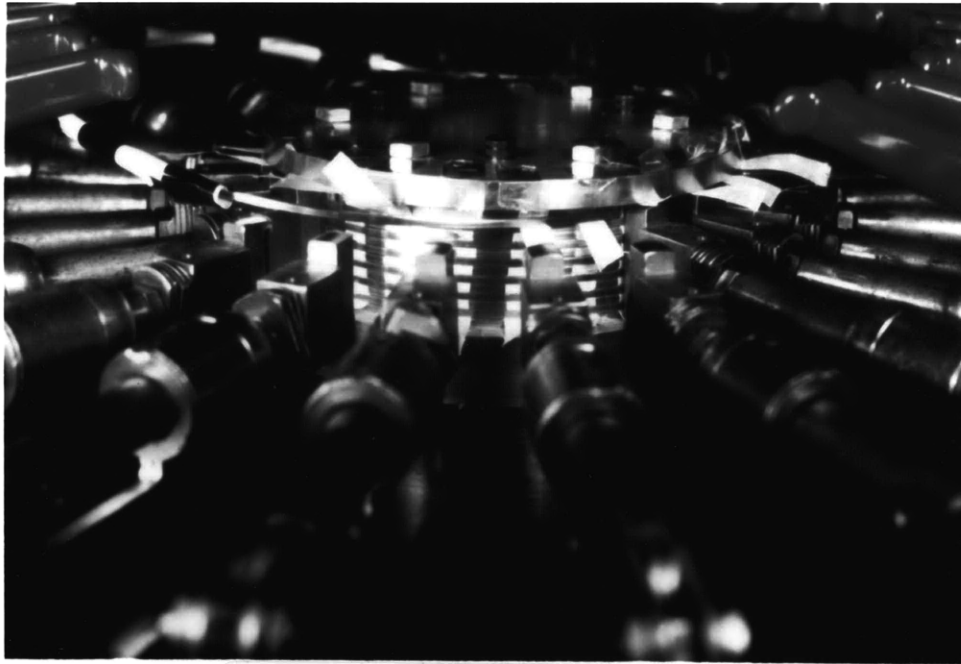


Fig. V.9. First layer complete and ready for short testing

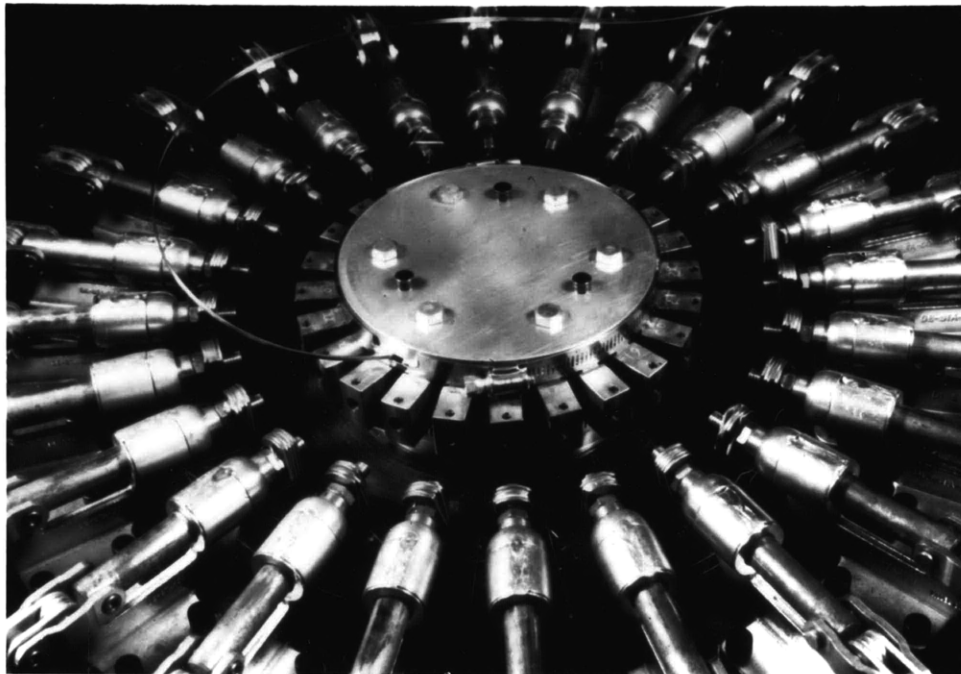


Fig. V.10. First layer is prepared for removal from winding jig and curing in the oven.

and the other was tapered radially outward to bring the last turn of layer one out to become the first turn of layer two. To complete the layer a third set of pieces B-staged of fiberglass tape followed by two pieces of Teflon, each .001 inches thick, were placed between the coil and the pusher pieces. This third set of fiberglass-epoxy tapes served in conjunction with the other two sets to bond all the turns of the layer together while the Teflon insulation formed the slip plane.

At this point all the clamps were pushed in and the layer was tested for turn-to-turn shorts and shorts to ground. This was accomplished by energizing the coil at a very low current level with a current source and then measuring the turn-to-turn voltage drop and the voltage to ground. The resistance of each turn was thus measured and compared with the calculated value of 3.5Ω . Any shorts that were found were then isolated and removed by insertion of additional insulation as required.

When the layer was shown to be free of any shorts it was prepared for curing. All of the clamps were pushed in and the pusher pieces were held tight against the coil by metal straps (Band-Its) (Fig. V.10). The set screws holding the pusher pieces to the clamps were loosened and all of the clamps retracted. A third metal strap was then tightened around the central circumference of the pushers. At this point two thermocouples were affixed to the conductor surface, one to measure and record the conductor temperature and the second as the input sensor to the temperature controller of the oven which was used to cure the layer. The whole winding mandrel was removed from the winding table and placed in the oven. An opening in the oven door was provided so the conductor could lead



Fig. V.11. Winding mandrel top and bottom flanges have had slots machined for better placement of the insulating strips.

directly up to the spool. The layer was cured at 150°C for 4 hours, beginning with the time the conductor temperature first reached 150°C. The curing process will be slightly different in the production of the field winding modules since it is more practical to cure each layer in place on the winding mandrel by building an oven to fit over the winding jig.

At the end of the curing process the mandrel was removed from the oven, all the metal straps and pushers were removed and the layer checked again for shorts. The mandrel was reattached to the winding table and the pushers reattached to the clamps after one metal spacer was removed from each clamp. This set the position of the clamps for winding the next layer. The entire winding process was repeated for the next layer beginning with the placement of the fiberglass-epoxy tape pieces. The winding procedure for the remaining layers was identical to that just described except that alternate layers were wound from the top down. Each layer was cured individually.

One refinement to the mandrel was made after the first layer was wound, because there was a problem of binding of the pusher pieces on the insulation as they moved into the mandrel between the flanges. Material was machined away in these areas to allow the insulation to be held down so that it didn't interfere with the motion of the clamps. This change can be seen in Fig. V.11 which clearly shows the top and bottom flanges with material machined away, allowing the insulation to be held vertical.

The completed coil can be seen in Fig. V.12, still mounted on the cylindrical mandrel. A top view of the coil is shown in Fig. V.13 which

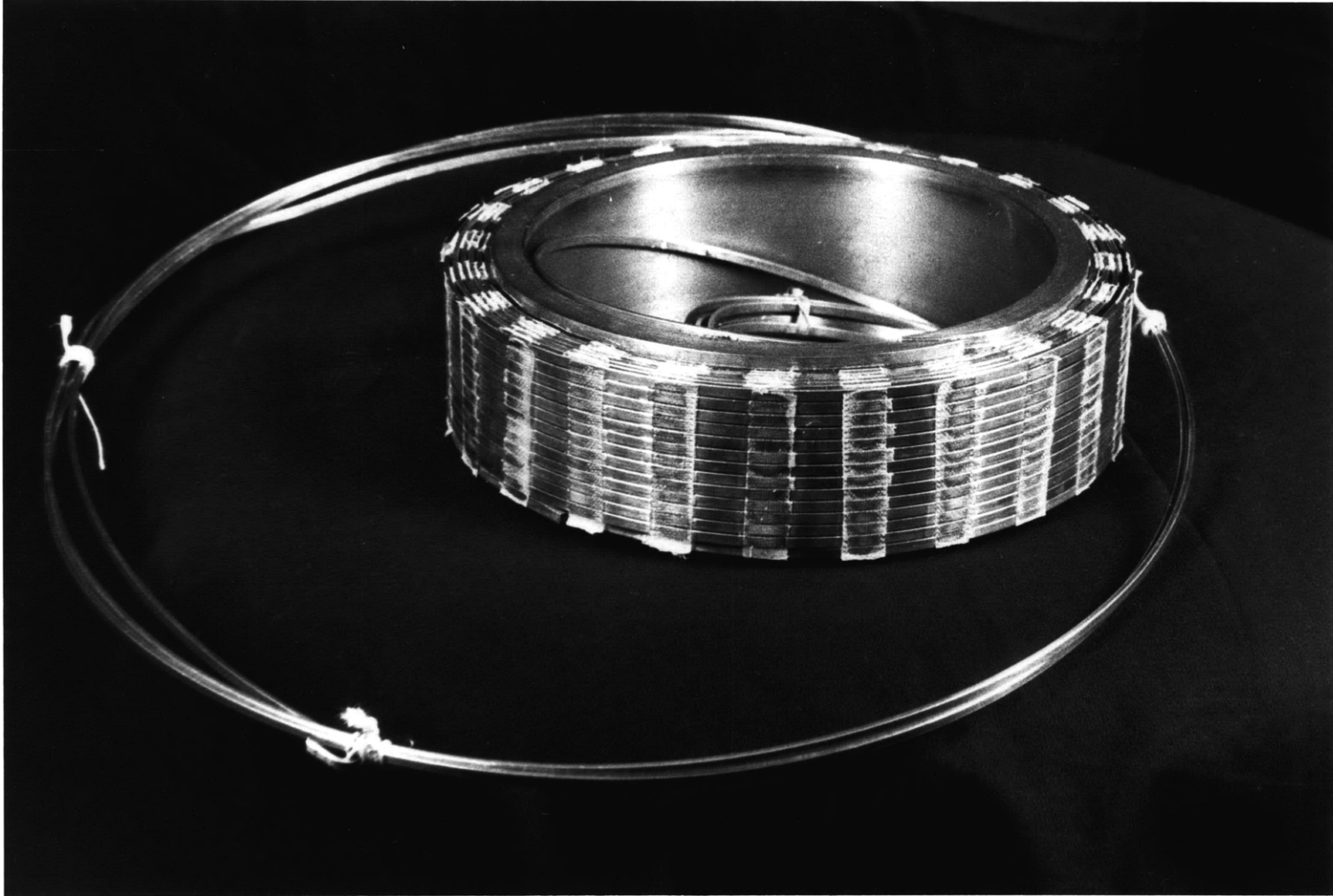


Fig. V.12. Completed coil showing all six cured layers, still mounted on the winding mandrel.



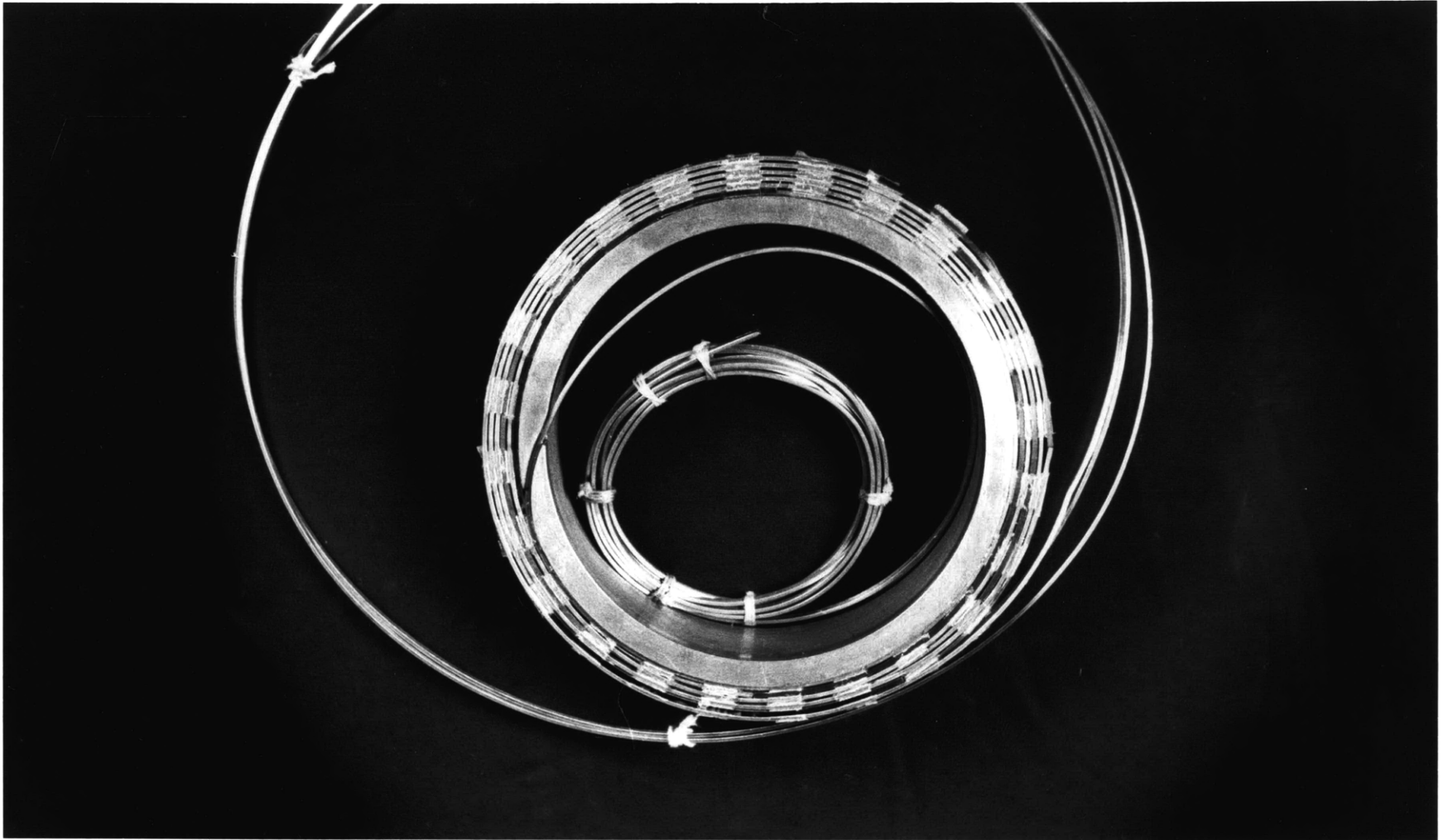


Fig. V.13. Top view of the coil. The large cooling channels between the layers are clearly visible.

clearly shows the cooling channels between layers. Some of the phenolic transition pieces are also visible.

V.2 Assembly to Structure

Once the coil was completed it was removed from the mandrel, the inner layer of Teflon permitting it to slide easily. Assembly of the yokes on the coil was begun with a trial fit-up. Each yoke was individually fit to the coil by filling the clearance between the yoke walls and the conductors with several turns of woven fiberglass-epoxy tape to serve as ground insulation. The average number of wraps of tape was three. In addition, two turns of .001 inch thick Teflon were wrapped over the ground insulation to form a final slip plane at the yoke walls. This also permitted a small amount of motion of the yokes on the coil to facilitate alignment of the yokes and the retaining pins. Several yokes were hand filed where necessary to allow the conductor ends to lead out of the inner and outer layers with a minimum amount of bending. Figure V.14 shows the coil loosely fitted into the yokes and temporarily seated on the bottom structural plate.

A Minco thermofoil heater was inserted between the coil and one of the yokes at the inner radius of the winding. The purpose of the heater was to simulate heating along this surface due to friction and to empirically determine the energy level and pulse rate required to quench the winding.

With all 24 yokes fitted to the coil over the ground insulation welding of the yoke caps to the yoke bottoms was begun. First the yokes were loosely pinned to the top and bottom structural plates. This was

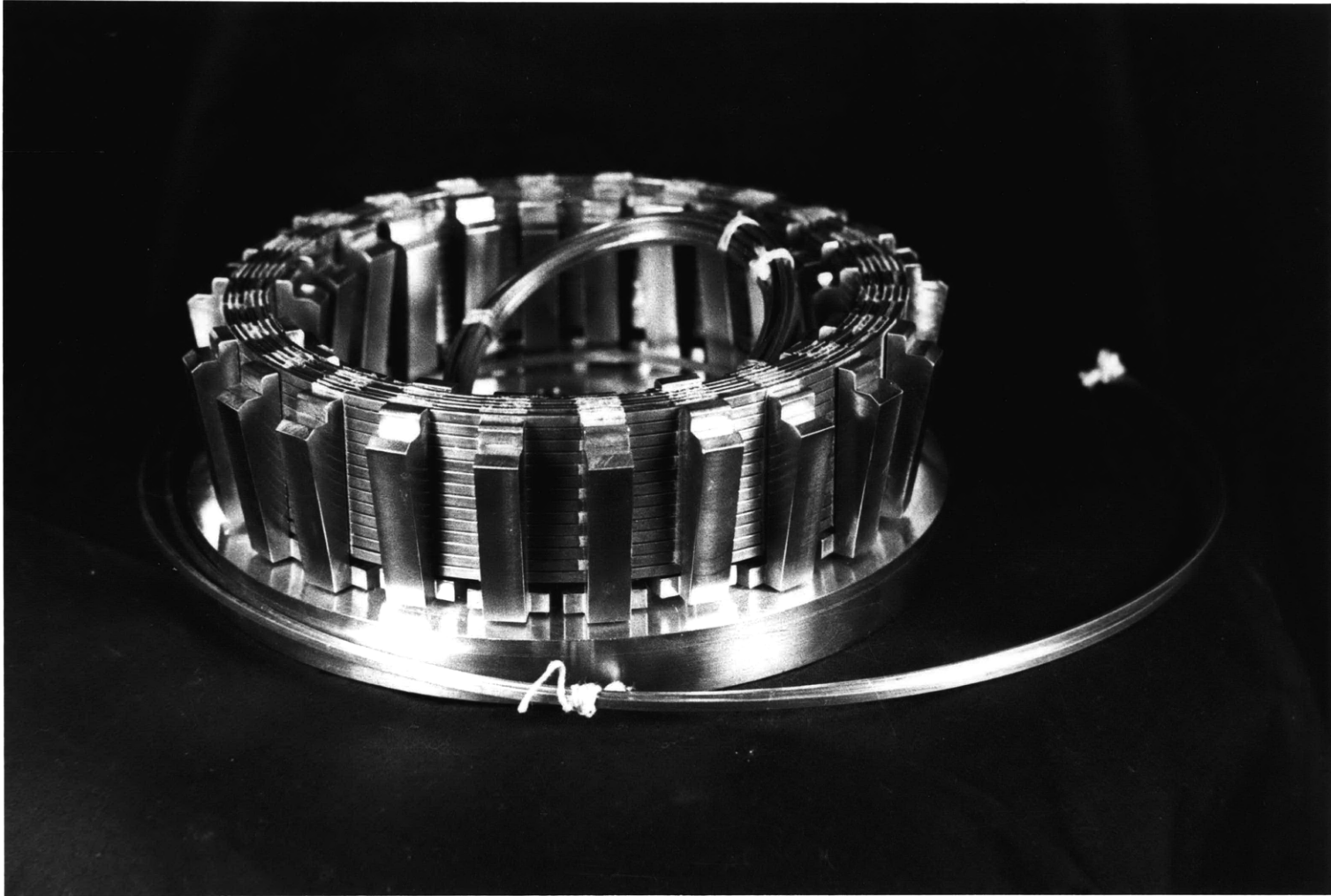


Fig. V.14. Yokes loosely fitted to the coil and resting on one of the support plates.

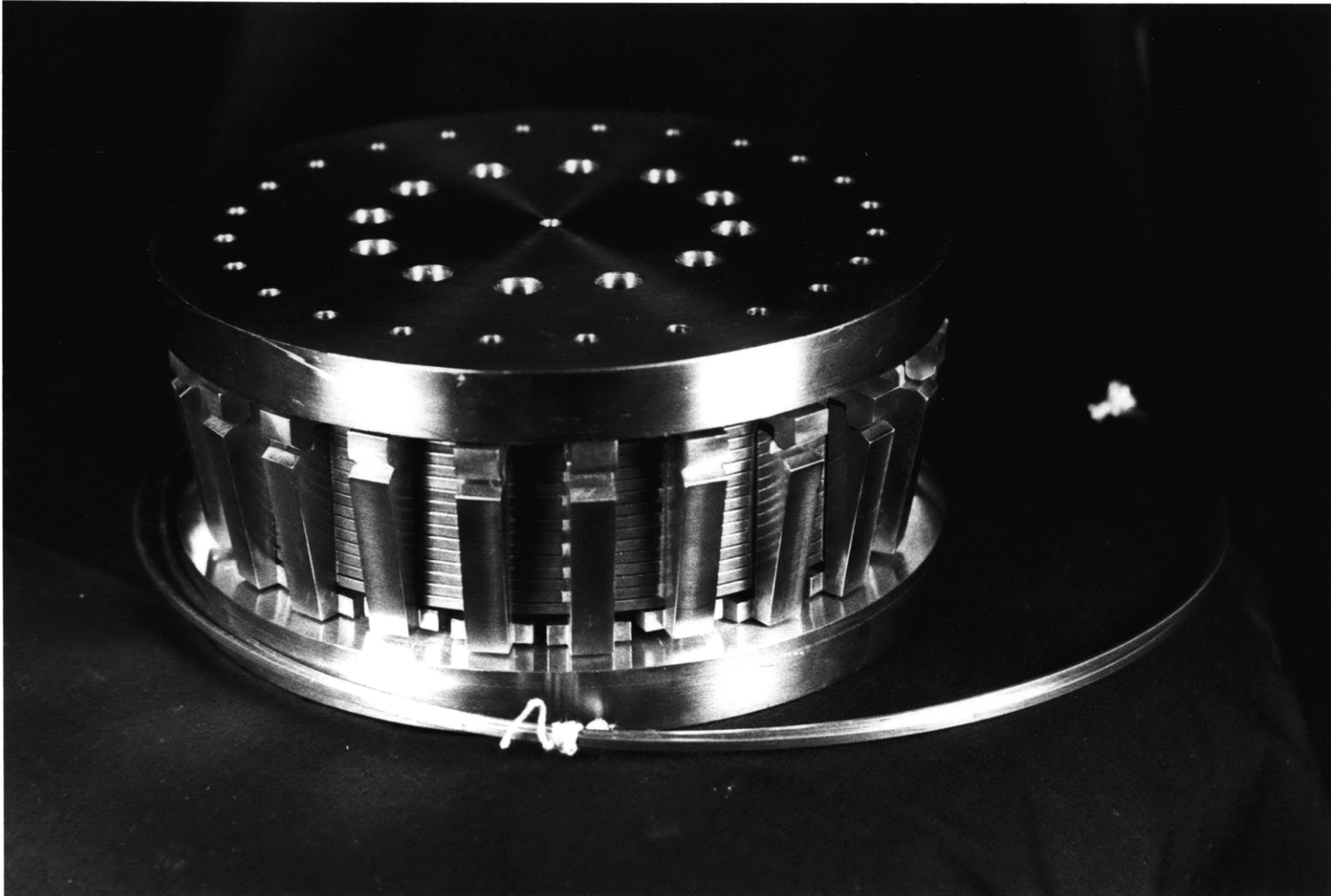


Fig. V. 15. The coil is loosely fitted to the structure and prepared for welding. Note the weld preparations between the yoke bottoms and yoke tops.

done to align the yoke caps to the bottoms and to align the coil within the yokes. Figure V.15 shows the structure loosely fitted to the coil. At this time all the caps were tack welded at the outer weld preparation. The plates were then removed and final welding was begun. Figure V.16 shows the copper chill and clamping arrangement that was used during the welding process to prevent overheating of the insulation and conductors. The C-clamp served to align and seat the top and bottom yoke pieces. The copper chill was water-cooled to remove heat from the welded areas. The vise-grip clamps were used to ensure surface contact for good conduction heat transfer between the yoke walls and the chills. The chill was designed to allow each yoke to be welded in place on the coil. All the inner joints were welded first followed by welding of the outer joints.

Provisions were then made to allow the inner lead to pass through one of the support plates by designing a copper bushing surrounded by a thin cylinder of G-10. The inner lead was bent to pass through the hole in the plate, a second length of superconductor soldered in parallel with it and then the doubled lead was soldered to the copper bushing, and inserted in the plate. The doubled lead and copper bushing were used to decrease the current density to avoid any normal transitions in this region.

Final assembly of the structure was completed in two steps. First the yokes were pinned to the two inconenl plates by pressing the pins through the plates until they just contacted the bottom of the blind holes in the yokes. An arbor press and guides were used for this purpose.

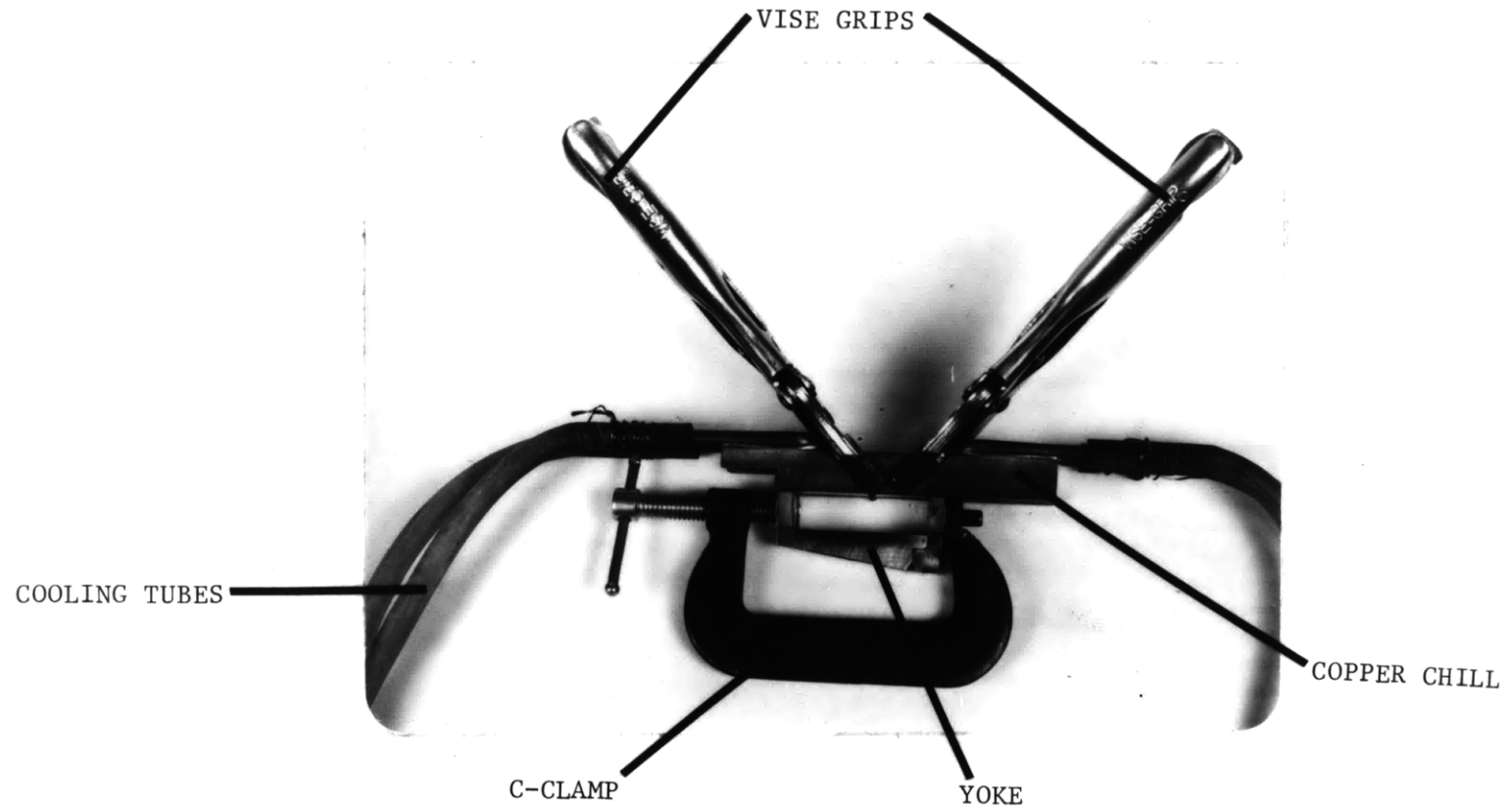


Fig. V.16. Welding clamp and chill arrangement.

An inconel cylinder was located between the plates within the coil to act as a spring of known spring constant for pre-stressing the yokes. This simulated the stress due to the interference fit between the inner and outer support tubes of the generator rotor. The second step of the assembly procedure was to torque the twelve tie bolts to establish the desired amount of pre-stress. When this was completed the entire coil and structure was put in the oven to cure the ground wrap insulation.

V.3 Test Configuration

The magnet was set up to be tested at the Francis Bitter National Magnet Laboratory. It was placed in a dewar which had an internal diameter of 8.375 inches and an inside height of 87.5 inches. The magnet was suspended near the bottom of the dewar by three 3/8 inch stainless steel rods from a 1 inch thick phenolic top flange. Vapor-cooled current leads rated at 2000A were connected to the coil terminals by 1.5 inch diameter braided copper conductor. The overall configuration is shown in Fig. V.17. The upper half of the dewar was filled with styrofoam to reduce the heat leak due to convection and radiation. The intermediate phenolic plates provided lateral support. The details of the copper lead to superconducting wire interface can be seen in Fig. V.18. It shows the inner and outer coil leads, each made of doubled superconductor, soldered into semi-circular copper blocks. These blocks were screwed into a G-10 plate which insulated the leads from the structure. This arrangement provided a smooth transition of current from the normal copper into the superconductor with the transition region always covered by liquid helium.

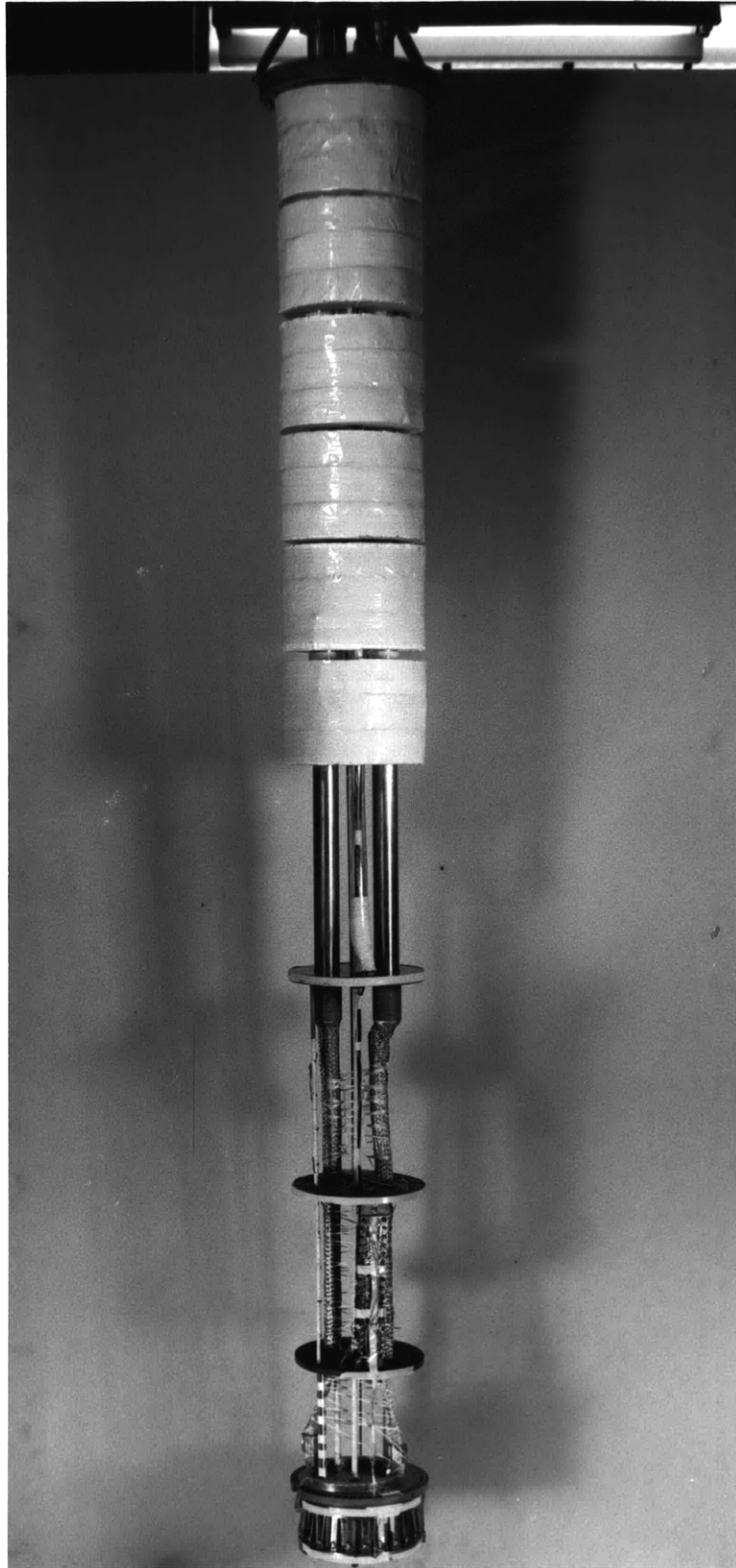


Fig. V.17. Coil and structure attached to current leads and holder and ready for insertion in test dewar.

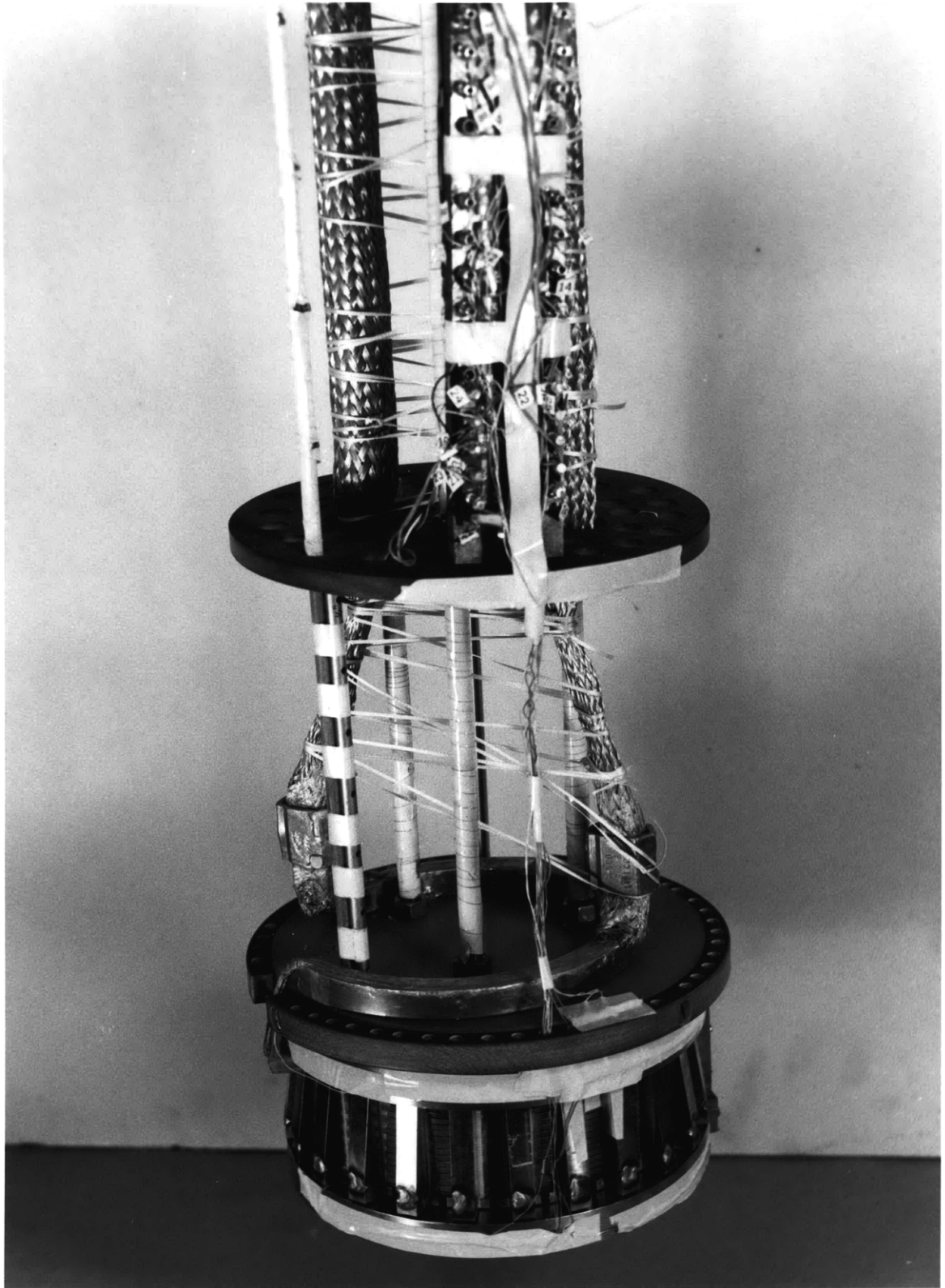


Fig. V.18. Arrangement of current leads and normal to superconducting transition in copper blocks. Instrumentation connecting strip is at top of picture.

The coil was instrumented with a heater and 10 voltage taps. The connecting strip for the instrumentation leads can be seen in Fig. V.19. Voltage taps were placed on the top, bottom, and center turns of the innermost layer and the outermost layer. These were affixed by threading copper screws through a G-10 mounting block and soldering a lead wire to each. The three taps on the outer layer can be clearly seen in Fig. V.20. The stainless steel tube on the right of the picture is the liquid helium fill tube. The picture in Fig. V.21 shows the outer superconducting current lead exiting the coil and the transition to the copper block. The outer welds on the yokes are clearly visible in these last two pictures.

The magnet was suspended inside the dewar which was supported on top of the Bitter coil by a ring stand (Fig. V.22). The test coil was concentric with the Bitter coil and axial alignment of the coil centers was effected by adjustment of the ring stand. When energized the Bitter coil magnetic field was directed upward and the test coil was energized to create a magnetic field downward. The resulting Lorentz forces put the test coil in radial compression, thus making it stable to radial motions. The center of the test coil was adjusted to be approximately 1/4" below the center of the Bitter coil when cold. The axial forces were thus directed downward putting the support rods in tension and the dewar in compression.

V.4 Test Results

Experimental runs are scheduled at FBNML in 3 hours and 15 minute shifts. This is the amount of time that power is provided for the Bitter

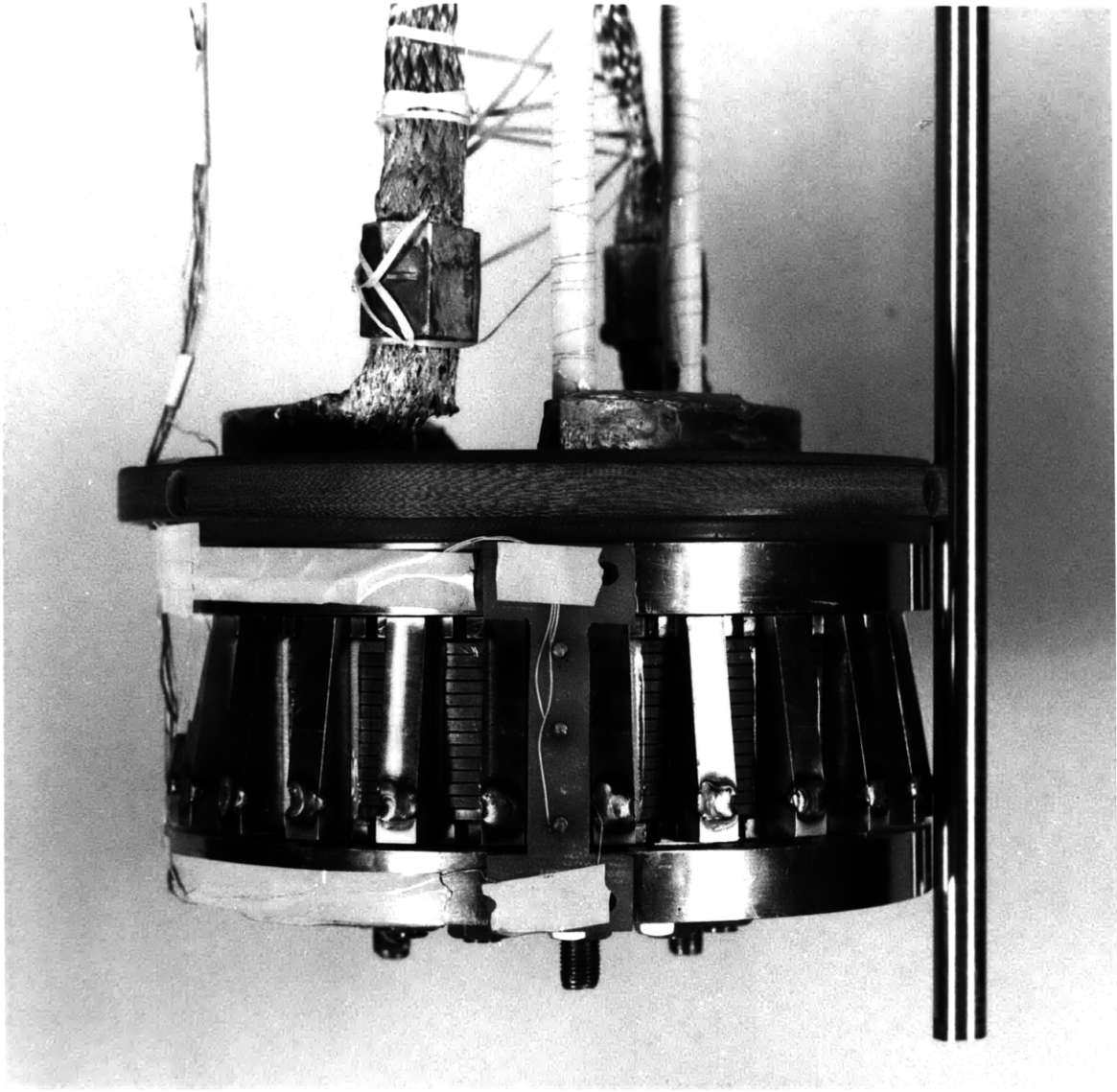


Fig. V.19. Close up of coil showing voltage taps in center of picture.

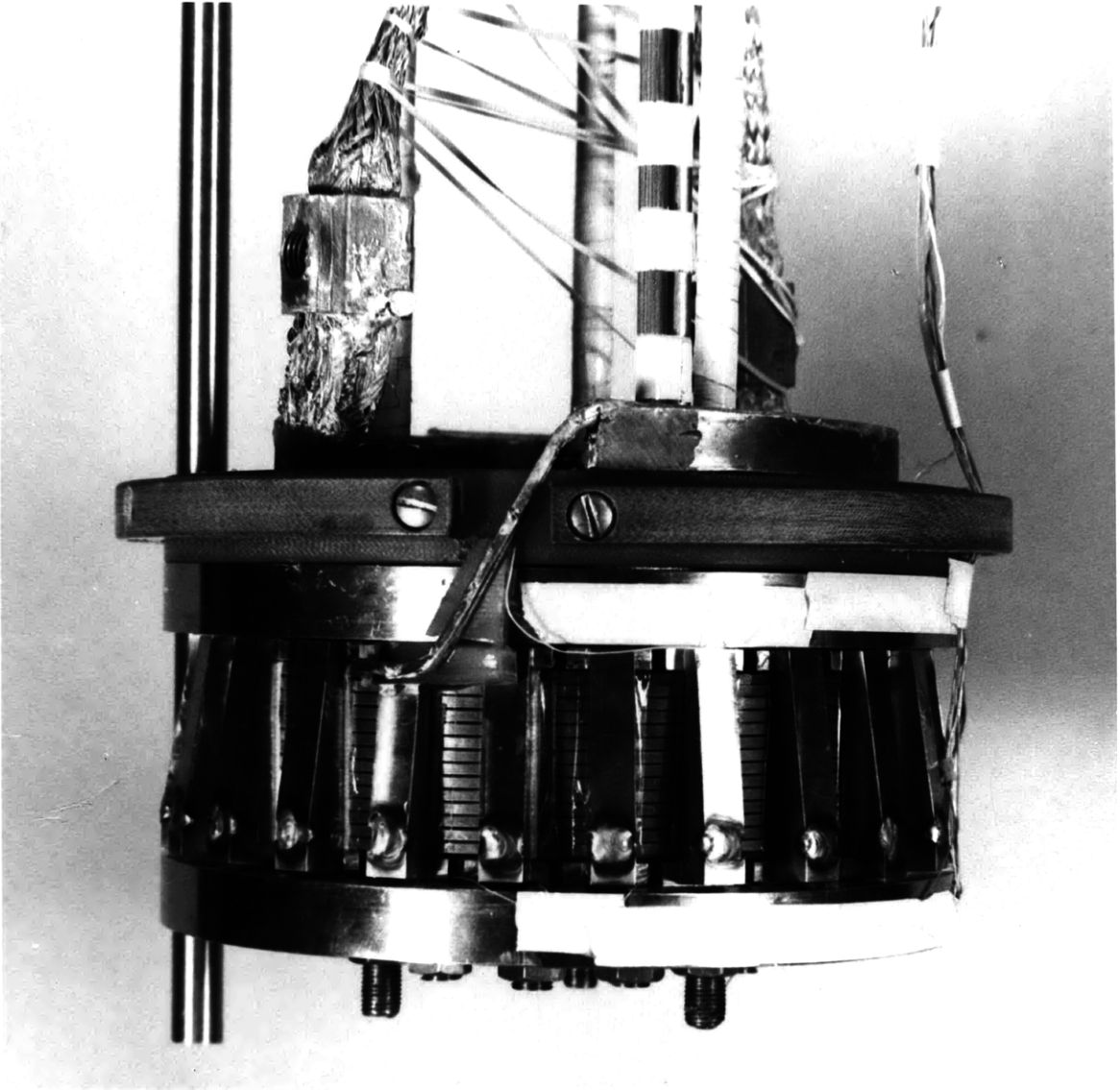


Fig. V.20. Superconducting current lead transition to copper block. The conductor is doubled in this region to insure a low current density.

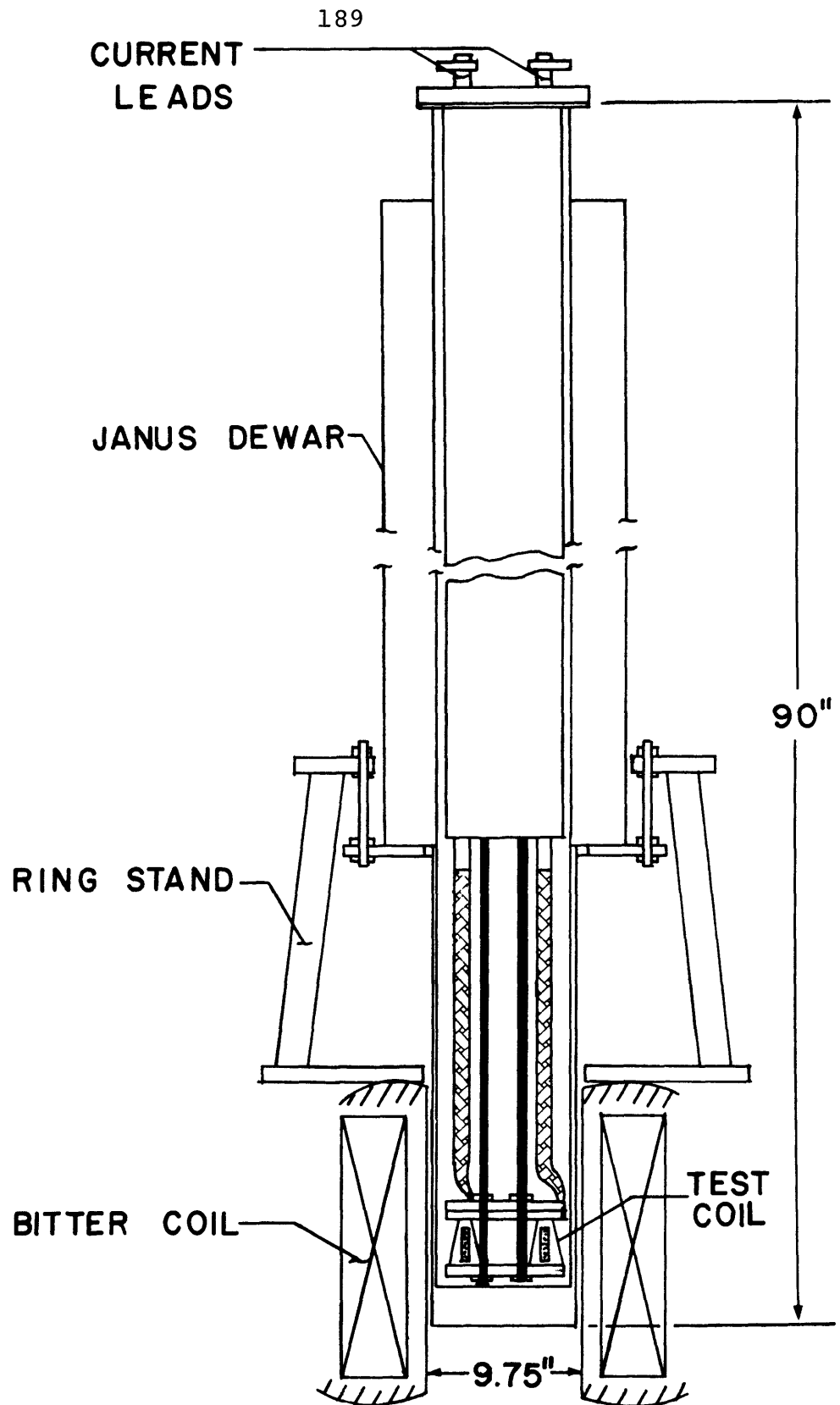


Fig. V.21. Schematic of set up to test the model coil at FBNML.

magnet. The coil was first tested on June 19, 1980. Two out of a maximum of four generators were scheduled for this run since it was decided to test the coil at a low field level the first time. During the magnet cooldown a small current was put through the coil and the voltage taps monitored on an Autodata 9 Digital Voltmeter. Thus the coil resistance was continuously monitored until it went superconducting. All the instrumentation leads worked well and no unusual phenomena were detected.

The voltage across the coil was monitored on two channels of a Nicolet Digital Storage Oscilloscope. This device samples at a very high rate and storage on a magnetic disc can be triggered by setting a trigger voltage level. This was used to detect any measurable voltage drop in the coil which would indicate a resistive zone and probable quench. A record of voltage across the superconducting leads versus current was measured on an x-y plotter.

The Bitter coil current was set at 16,000A which corresponded to a central field of 3.04T. The test coil was very slowly energized over a period of several minutes by a power supply rated to 10,000A. At a value of 710A a significant voltage was measured on the Nicolet and the power supply circuit breakers were opened. The coil was protected by a 70 mA shunt resistor mounted as a short across the current leads on top of the dewar. The transient did not appear to be a quench so the coil was re-energized. Again at 725A a similar transient was measured, but this time it was obvious that the voltage was due to gross coil motion as the dewar was levitated out of the Bitter coil bore. The desired axial alignment of the coils had not been attained so the axial forces moved the coil

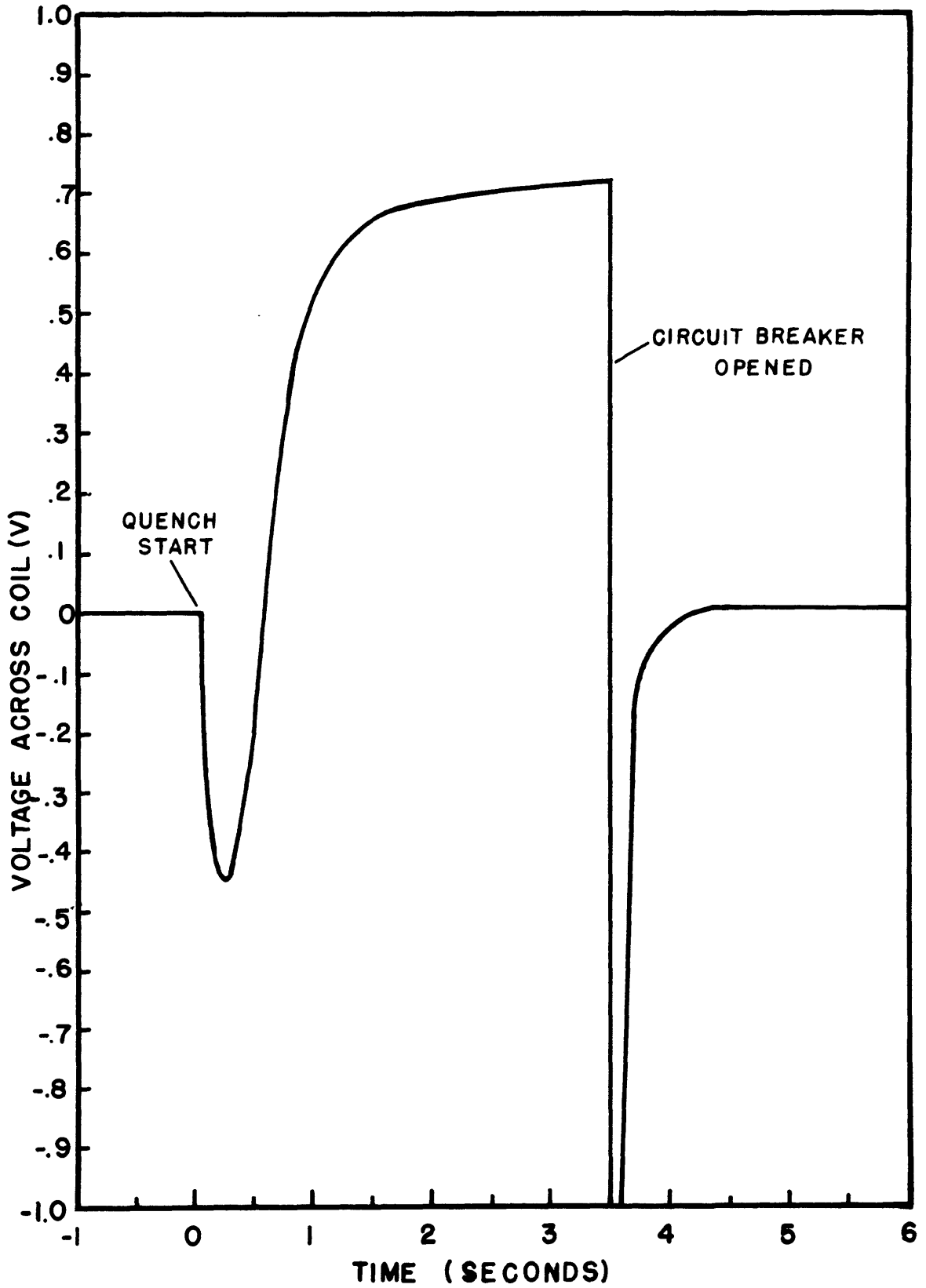


Fig. V.22. Trace of voltage across coil terminals versus time during heater induced quench.

vertically upward instead of downward from the high field region.

After readjustment of the axial position the coil was quickly and uneventfully energized to the rated operating current of 940A. At this point the shift ended.

The coil was tested again on July 7, 1980. All four generators were available to power the Bitter coil for this test run. The instrumentation was the same as that used in the previous test with the addition of a 4 channel Biomation 1015 waveform recorder. The Bitter coil current was set at 24,446A which corresponds to a center field of 4.547T and a peak field at the test coil windings of 4.82T. The test coil current was raised to a level of 940A and maintained there without incident. The peak field was calculated to be 4.98T. There were no signs of magnet training.

A series of quench tests were then run by pulsing the coil heater and monitoring the voltage taps. Attempts were made to quench the coil at reduced current with .2 watt power lasting for 5 ms with no success. The pulse width and height were increased several times without any further results. The operating current was increased to 940A and the pulse width limit of 98.3 msec reached, still with no effect. Finally the heater was energized continuously and the voltage across it increased gradually to 29 volts when a normal region was started in the coil. This test was repeated twice more with quenching occurring at the same point each time. A typical trace of voltage across the coil versus time is shown in Fig. V.23. The steady-state power level in the heater was measured at 10 watts. A plot of the current versus field operating

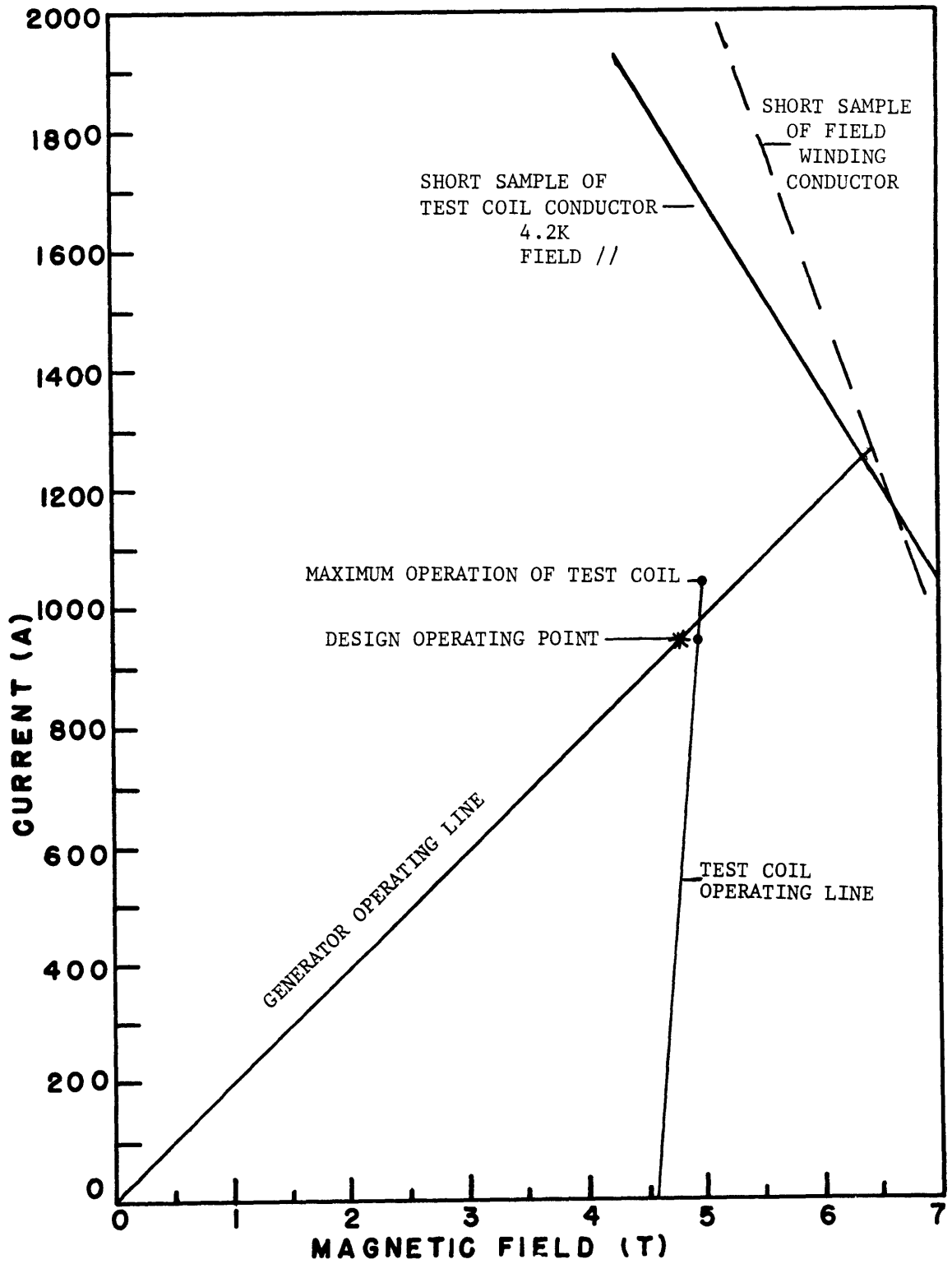


Fig. V.23. Operating characteristics of test coil and generator field winding.

conditions and the short sample characteristics are shown in Fig. V.24.

The coil suffered no damage whatsoever. This is partly due to the nature of the power supply which maintains a nearly constant voltage output and the shunt protection resistor which shares a significant portion of the current when the test coil develops a resistive zone.

Additional tests included over-energizing the coil to 1040A at a peak field of 5.0T and rapid charge and discharge of the coil at a rate of 21 A/sec. The coil performed perfectly during all these tests and showed absolutely no signs of training. The relatively large power dissipation required to initiate a quench and the recovery aided by the protective circuit indicate good turn-to-turn cooling. The overall excellent performance of the test coil gives confidence in the yoke-module design for the 10 MVA generator field winding.

CHAPTER VI

CONCLUSIONS

The conclusions to be drawn from the work performed in this thesis can be divided into three distinct categories concerning the theoretical ac loss analysis, the ac loss and heat transfer calculations for the 10 MVA generator field winding, and the construction and operation of the test coil.

In regard to the theoretical ac loss analysis (Chapter III) it can be concluded that:

- 1) the mathematical technique of using complex variables is a convenient method by which to formulate field problems with distributed sources, and it is specifically useful for finding the unknown boundary flux penetration in a superconductor;

- 2) the aforementioned mathematical technique can be used to find the flux penetration into non-circular superconductors with no greater difficulty than that encountered in the circular geometry;

- 3) this same technique can be used in many other similar field problems with distributed sources; these may be found in heat transfer problems with internal heat generation, electric field problems with distributed charge sources, or in fluid problems with vorticity;

- 4) the current distributions computed for the zero transport current case can be used when the filament does carry a transport current if the external field has been cycled a few times while holding the transport current constant. The number of cycles required to establish

the new distribution is unknown but a logical estimate can be made in the range of 2-4 cycles. The transport current occupies the inner core of the filament while surrounded by shielding currents;

5) Once the current distribution is established the external field required to fully penetrate the filament is established as a function of the transport current (Fig. 3.13);

6) the losses are readily computed for two regimes when $\Delta H_e \leq H_p(i)$ and when $\Delta H_e > H_p(i)$. In addition the loss is readily divided into two components; a loss in the shielding current region provided by the external field source and; a loss in the transport current region provided by the current power source (Figs. 3.16 through 3.19);

7) the non-dimensional form of the loss expressions (Eqs. 3.56 to 3.57) are valid for all circular superconducting filaments of any size.

The ac loss analysis of Chapter III has been successfully applied to the field winding design for a 10 MVA experimental generator. The computed losses are very small and indicate the field winding is well shielded from alternating fields during a fault by the damper winding and copper can shield. The worst heating of the conductors could possibly be caused by frictional heating due to relative conductor motion but all analyses indicate the maximum temperature in the winding should never exceed the critical temperature. Thus the field winding should not quench under any foreseen operating condition. Even if a quench did occur it would not be catastrophic since the winding is protected with a quench detector and energy removal scheme.

The experimental coil described in Chapter V was useful in developing the tooling and winding techniques required to wind the prototype generator field winding modules. The successful operation of the test coil indicates a great likelihood of success with the actual generator field winding. The yoke and module type winding and structure configuration with the built-in slip planes can be scaled up without difficulty to larger generator ratings such as the proposed 2000 MVA central power station design. In addition this yoke-module design could be applied to any other type of large scale superconducting winding where the accumulation of stress due to Lorentz forces would present problems. A typical application may be in large MHD magnets.

Further work needs to be done in experimentally verifying the theoretical ac loss model. The model needs to be clearly incorporated into the loss models for composite conductors where the interaction of the matrix currents with the superconducting filaments complicates the current distribution.

The work of this thesis indicates that the 10 MVA experimental generator can be built and operated successfully and thus an optimistic outlook for large scale application of this technology is warranted. An improvement has been made to the theory of ac losses in superconductors carrying transport current which should allow for minimization of ac losses for optimum magnet system design and performance.

APPENDIX A. SUMMARY OF IMPORTANT LOSS FORMULA

The loss formula which were developed in Chapter III for round superconducting filaments are summarized here for convenience. All losses are given as a normalized loss per unit volume per cycle. They are presented for the four categories of Section III.5 as follows:

A.1 Partial Penetration Without Transport Current

$$\frac{\Delta H_e}{H_p(0)} \leq 1 \quad , \quad i = 0$$

$$\frac{W_{p0}}{W_0} = 2 \left(\frac{\Delta H_e}{H_p(0)} \right)^3 - \left(\frac{\Delta H_e}{H_p(0)} \right)^4$$

A.2 Full Penetration Without Transport Current

$$\frac{\Delta H_e}{H_p(0)} > 1 \quad , \quad i = 0$$

$$\frac{W_{fp0}}{W_0} = 2 \left(\frac{\Delta H_e}{H_p(0)} \right) - 1$$

A.3 Partial Penetration with Transport Current

$$\frac{\Delta H_e}{H_p(i)} \leq 1 \quad , \quad 0 \leq i \leq 1$$

$$\frac{W_{pt}}{W_0} = 2 \left(\frac{\Delta H_e}{H_p(0)} \right)^3 - \left(\frac{\Delta H_e}{H_p(0)} \right)^4$$

A.4 Full Penetration with Transport Current

$$\frac{\Delta H_e}{H_p(i)} > 1 \quad , \quad 0 \leq i \leq 1$$

$$\begin{aligned} \frac{W_{fpt}}{W_0} = & \left[2 \left(\frac{H_p(i)}{H_p(0)} \right)^3 - \left(\frac{H_p(i)}{H_p(0)} \right)^4 \right] + 2 \left[\left(\frac{\Delta H_e}{H_p(0)} \right) \right. \\ & \left. - \left(\frac{H_p(i)}{H_p(0)} \right) \right] \gamma(i) \end{aligned}$$

W_{fpt}/W_0 is the total loss. It can be further broken down into a shielding current loss, W_s/W_0 and a transport current loss, W_t/W_0 .

$$\frac{W_{fpt}}{W_0} = \frac{W_s}{W_0} + \frac{W_t}{W_0}$$

where

$$\begin{aligned} \frac{W_s}{W_0} = & \left[2 \left(\frac{H_p(i)}{H_p(0)} \right)^3 - \left(\frac{H_p(i)}{H_p(0)} \right)^4 \right] + 2 \left[\left(\frac{\Delta H_e}{H_p(0)} \right) \right. \\ & \left. - \left(\frac{H_p(i)}{H_p(0)} \right) \right] \alpha(i) \end{aligned}$$

and

$$\frac{W_t}{W_0} = 2 \left[\left(\frac{\Delta H_e}{H_p(0)} \right) - \left(\frac{H_p(i)}{H_p(0)} \right) \right] \beta(i) \quad .$$

If $\Delta H_e \gg H_p(0)$

$$\frac{W_{fpt}}{W_0} \approx 2 \left(\frac{\Delta H_e}{H_p(0)} \right) [\alpha(i) + \beta(i)] = 2 \left(\frac{\Delta H_e}{H_p(0)} \right) \gamma(i)$$

Note (1): These losses are for a constant transport current, $i = I_t/I_c$ and for an alternating external field, H_e , given by

$$H_e = H_0 \pm \Delta H_e$$

where H_0 is the uniform background field.

$$H_0 \gg H_p(0)$$

$$H_p(0) = \frac{J_c d}{\pi}$$

$$W_0 = \frac{4}{3} \mu_0 H_p^2(0)$$

Note (2): The partial penetration field as a function of transport current, $H_p(i)$, is given in Fig. III.14.

Note (3): $\gamma(i) = \alpha(i) + \beta(i)$

The coefficients $\alpha(i)$, $\beta(i)$, and $\gamma(i)$ are given in Fig. III.17. The losses W_s/W_0 , W_t/W_0 , and W_{fpt}/W_0 are given in Figs. III.18, III.19, and III.20, respectively.

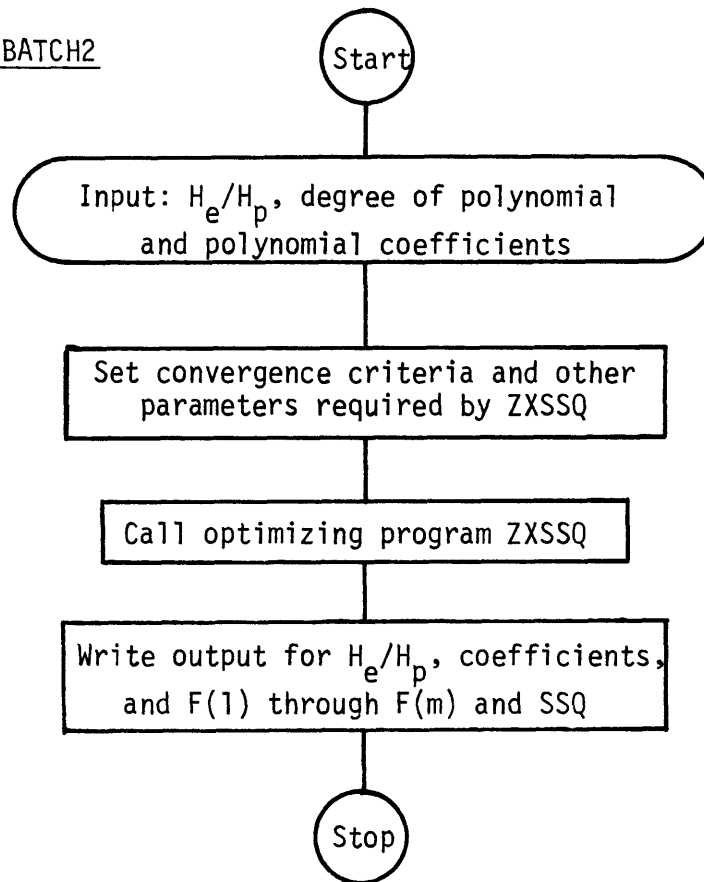
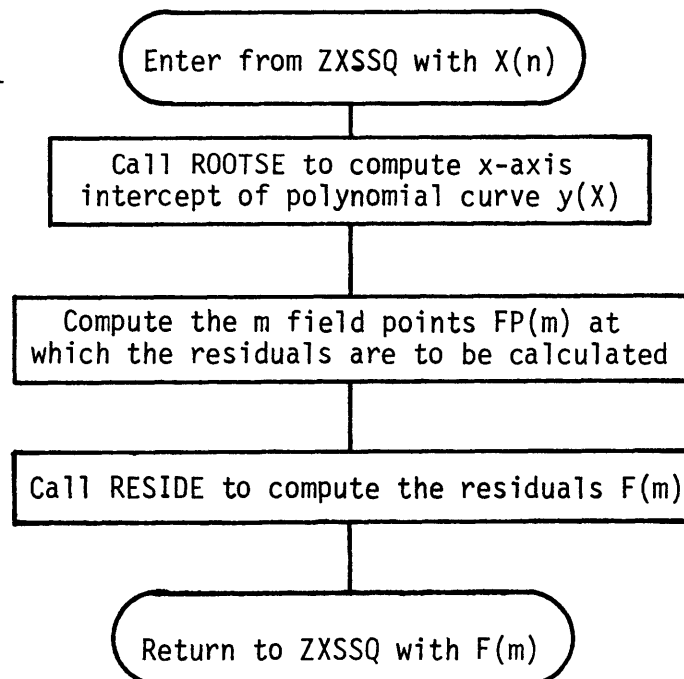
APPENDIX B - COMPUTER PROGRAMS

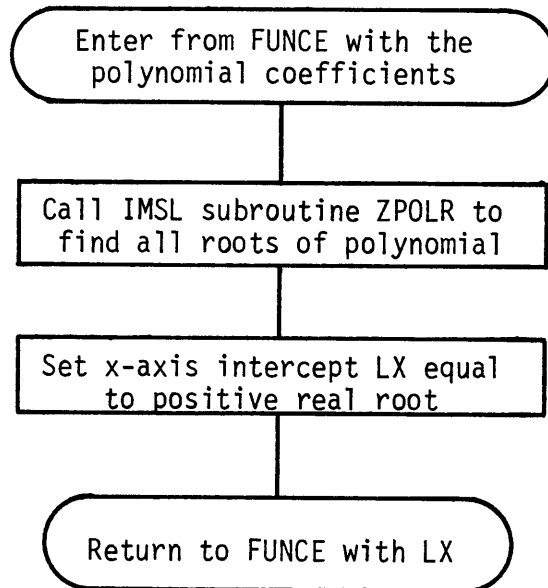
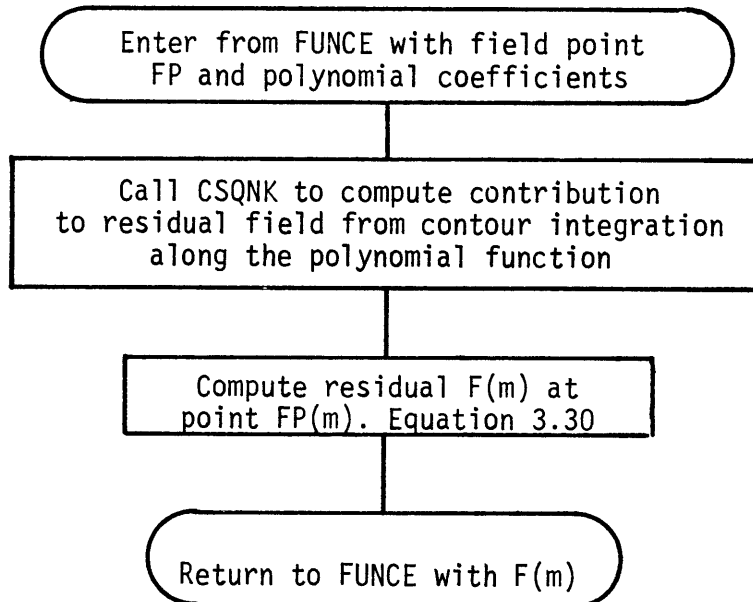
The curves that represent the limits of flux penetration into a circular superconducting filament as described in Chapter III were calculated from a computer program. The main program called EBATCH2 is very simple to use. The primary inputs are the normalized external field H_e/H_p and the initial guess at the polynomial coefficients a_0 through a_8 . This program calls subroutine ZXSSQ which is a program in the International Mathematical and Statistical Library which is widely available on many computer systems. Since the computer programs in this library are proprietary a fortran source listing is not available.

The program ZXSSQ finds the minimum of the sum of squares of M functions in N variables using a finite difference Levenberg-Marquardt Algorithm. The primary input to this program are the initial coefficient parameters $X(N)$ and a subroutine which calculates the residual vector $F(M)$. This user supplied subroutine is called FUNCE. The program FUNCE computes the residuals by means of a subroutine called RESIDE which requires subroutine CSQNK to perform the complex simpson quadrature integration along a contour in Eq. (3.30). The program CSQNK is available in the M.I.T. Information Processing Center Mathlib subroutine library. The program ZXSSQ iterates on the vector $X(N)$ until the residual sum of squares, SSQ, is minimized. SSQ is given by

$$SSQ = F^2(1) + F^2(2) + \dots + F^2(M) \quad .$$

Following is a simplified flowchart of the computer programs and a fortran listing of programs EBATCH2, FUNCE, ROOTSE, RESIDE, and CSQNK.

MAIN PROGRAM- EBATCH2SUBROUTINE FUNCE

SUBROUTINE-ROOTSESUBROUTINE-RESIDE

```

C*****EBA00010
C*   THIS PROGRAM COMPUTES THE OPTIMUM COEFFICIENTS OF A POLY- *EBA00020
C*   NOMIAL CURVE THAT APPROXIMATES THE FLUX PENETRATION IN A ROUND *EBA00030
C*   SUPERCONDUCTOR. IT USES THE IMSL SUBROUTINE ZXSSQ WHICH GIVES *EBA00040
C*   THE SUM OF SQUARES OF M FUNCTIONS IN N VARIABLES USING A *EBA00050
C*   FINITE DIFFERENCE LEVENBERG-MARQUARDT ALGORITHM. THE PROGRAM *EBA00060
C*   ALSO MAKES USE OF THE IMSL SUBROUTINE ZPOLR TO FIND THE ROOTS OF *EBA00070
C*   A REAL POLYNOMIAL. THE M FUNCTIONS ARE THE RESIDUALS OF THE *EBA00080
C*   MAGNETIC FIELD AT M FIELD POINTS. THE N VARIABLES ARE THE N *EBA00090
C*   COEFFICIENTS OF THE POLYNOMIAL. *EBA00100
C*****EBA00110
C*   EBA00120
C*   EBA00130
REAL*4   HEA,X(6)/6*0.0/,F(10),PARM(4),XJAC(10,5),XJTJ(15) EBA00140
REAL*4   WORK(60),EPS,DELTA,SGN EBA00150
INTEGER*4 I,NDEG,M,N,IXJAX,NSIG,MAXFN,IOPT,INFER,IER,K,IRUN EBA00160
EXTERNAL FUNCE EBA00170
COMMON /FUNC1/HEA,NDEG EBA00180
C*   EBA00190
C*   EBA00200
C*   INPUT VARIABLES EBA00210
READ(5,*)IRUN EBA00220
DO 20 J=1,IRUN EBA00230
READ(5,*)HEA,NDEG EBA00240
N=NDEG+1 EBA00250
READ(5,*)(X(I),I=1,N) EBA00260
C***** SET CONVERGENCE AND OTHER PARAMETERS FOR CALLING ZXSSQ EBA00270
C**   SET M, NUMBER OF RESIDUAL (FIELD) POINTS EBA00280
M=10 EBA00290
C**   SET FIRST CONVERGENCE CRITERION EBA00300
NSIG=4 EBA00310
C**   SET SECOND CONVERGENCE CRITERION EBA00320
EPS=0.0001 EBA00330
C**   SET THIRD CONVERGENCE CRITERION EBA00340
DELTA=0.0001 EBA00350
C**   SET MAXIMUM NUMBER OF FUNCTION EVALUATIONS EBA00360
MAXFN=500 EBA00370
C**   SET OPTIONS PARAMETER EBA00380
IOPT=0 EBA00390
C**   PARM(I) NOT REQUIRED UNLESS IOPT=2 EBA00400
C**   SET IXJAC=M EBA00410
IXJAC=M EBA00420
C**   NOW CALL THE OPTIMIZING FUNCTION ZXSSQ EBA00430
PRINT 1100 EBA00440
CALL ZXSSQ(FUNCE,M,N,NSIG,EPS,DELTA,MAXFN,IOPT,PARM, EBA00450
1 X,SSQ,F,XJAC,IXJAC,XJTJ,WORK,INFER,IER) EBA00460
PRINT 1200 EBA00470
C**   NOW PRINT THE OUTPUT EBA00480
WRITE(6,300) HEA EBA00490
PRINT 400 EBA00500
WRITE(6,500) X(5),X(4),X(3),X(2),X(1) EBA00510
WRITE(6,600) SSQ EBA00520
WRITE(6,700) (F(I),I=1,M) EBA00530
DO 10 K=1,5 EBA00540
WRITE(6,800) K,WORK(K) EBA00550

```

```
10 CONTINUE                                     EBA00560
   WRITE(6,900) INFER                           EBA00570
   WRITE(6,1000) IER                            EBA00580
20 CONTINUE                                     EBA00590
C***** FORMAT STATEMENTS *****             EBA00600
300 FORMAT(15X,'OTUPUT FOR CASE HE/HA=',F7.4,/) EBA00610
400 FORMAT(5X,'COEFFICIENTS OF THE POLYNOMIAL',/) EBA00620
500 FORMAT(' A0=',F10.5,' A2=',F10.5,' A4=',F10.5,' A6=',F10.5, EBA00630
      1 ' A8=',F10.5)                          EBA00640
600 FORMAT(' RESIDUAL SUM OF SQUARES=',F10.6) EBA00650
700 FORMAT(' RESIDUALS OF FIELDS=',10F10.6) EBA00660
800 FORMAT(' WORK(',I1,')=',F10.6)           EBA00670
900 FORMAT(' CONVERGENCE CRITERION,INFER=',I1) EBA00680
1000 FORMAT(' ERROR CODE=',I3)              EBA00690
1100 FORMAT(' NOW ZXSSQ IS BEING CALLED*****') EBA00700
1200 FORMAT(' RETURN FROM ZXSSQ AND READY TO PRINT OUTPUT') EBA00710
      STOP                                     EBA00720
      END                                       EBA00730
```

```

SUBROUTINE FUNCE(X,M,N,F)
C*****
C* THIS IS THE SUBROUTINE FUNC WHICH IS USED BY THE IMSL ROUTINE
C* ZXSSQ TO COMPUTE THE RESIDUALS OF M FUNCTIONS
C*****
C**
C**
COMMON /FUNC1/HEA,NDEG
REAL*4 HEA,X(6),F(10),LX,LY,A0,A2,A4,A6,A8,XV,Y,Q(9)
INTEGER*4 M,N,NDEG,II,ND
COMPLEX*8 FP(5),ZP,R
Y(XV)=A0+A2*XV**2+A4*XV**4+A6*XV**6+A8*XV**8
A0=X(5)
A2=X(4)
A4=X(3)
A6=X(2)
A8=X(1)
Q(9)=X(5)
Q(8)=0.0
Q(7)=X(4)
Q(6)=0.0
Q(5)=X(3)
Q(4)=0.0
Q(3)=X(2)
Q(2)=0.0
Q(1)=X(1)
ND=NDEG+4
C** COMPUTE THE MAXIMUM VALUE OF X (LX)
PRINT 100
WRITE(6,*)(X(I),I=1,N)
CALL ROOTSE(Q,ND,LX)
C** COMPUTE THE POINTS AT WHICH THE RESIDUALS ARE TO BE EVALUATED
LY=X(5)
FP(1)=CMPLX(.0001,.0001)
FP(2)=CMPLX(.99*LX,.5*Y(.99*LX))
FP(3)=CMPLX(.0001,LY-.001)
FP(4)=CMPLX(LX/3.0,Y(LX/3.0)-.001)
FP(5)=CMPLX(2.0*LX/3.0,Y(2.0*LX/3.0)-.001)
C**
DO 10 II=1,5
ZP=FP(II)
C** CALL THE SUBROUTINE RESID TO COMPUTE THE VECTOR F OF THE RESIDUALS
C** AT EACH OF THE M POINTS
CALL RESIDE(HEA,ZP,LX,X,R)
III=II+5
F(II)=REAL(R)
F(III)=AIMAG(R)
WRITE(6,200) II,F(II),III,F(III)
10 CONTINUE
100 FORMAT(' ***IN SUBROUTINE FUNC***',/)
RETURN
200 FORMAT(' F(',I1,')=',F10.6,' F(',I1,')=',F10.6,/)
END

```

```
      SUBROUTINE ROOTSE(Q,NDEG,LX)
C*****
C*      THIS PROGRAM, ROOTS, COMPUTES THE REAL *
C*      ROOTS OF A POLYNOMIAL BY USE OF THE IMSL *
C*      SUBROUTINE ZPOLR(A,NDEG,Z,IER). *
C*****
C**
C**      REAL*4 Q(9),ZR(8),LX,ZI(8)
      INTEGER*4 NDEG,IER,N
      COMPLEX*8 Z(8)
      CALL ZPOLR(Q,NDEG,Z,IER)
      DO 10 N=1,NDEG
      ZR(N)=REAL(Z(N))
      ZI(N)=AIMAG(Z(N))
      IF(ZI(N).EQ.0.0.AND.ZR(N).GT.0.0) LX=ZR(N)
10  CONTINUE
      IF(IER.NE.0) PRINT 100
100  FORMAT(' *****WARNING=ERROR IN ROOTS SUBROUTINE!!!*****')
      RETURN
      END
      R0000010
      R0000020
      R0000030
      R0000040
      R0000050
      R0000060
      R0000070
      R0000080
      R0000090
      R0000100
      R0000110
      R0000120
      R0000130
      R0000140
      R0000150
      R0000160
      R0000170
      R0000180
      R0000190
      R0000200
      R0000210
```

```

SUBROUTINE RESIDE(HEA,ZP,A,X,R) RES00010
C***** RES00020
C* THIS PROGRAM TAKES AS INPUT THE COEFFICIENTS OF A POLYNOMIAL THAT RES00030
C* APPROXIMATES THE EXACT CONTOUR OF FIELD PENETRATION IN A SUPER- RES00040
C* CONDUCTOR. IT INTEGRATES A COMPLEX FUNCTION ALONG THIS CONTOUR RES00050
C* USING A FUNCTION SUBPROGRAM CSQNK FOUND IN THE IPS MATHLIB LIB- RES00060
C* RARY. A RESIDUAL OF A FUNCTION IS RETURNED AT SPECIFIED FIELD RES00070
C* POINTS WITHIN THE CONTOUR. DEVIATION OF THE RESIDUAL FROM ZERO RES00080
C* INDICATES RELATIVE INACCURACY OF THE CONTOUR RES00090
C***** RES00100
C* RES00110
REAL*4 A,B,HEA,A0,A2,A4,A6,A8,DUMI,X(6) RES00120
COMPLEX*8 W,CSQNK,TOL,FIFTH,RETERR,CURVE1,CURVE2,FUN,R,Z,ZP RES00130
COMPLEX*8 JLOG,W1,DUM,ARG,ZCON,FUDGE,ZPP RES00140
INTEGER*4 NO RES00150
EXTERNAL CURVE1,CURVE2,FUN RES00160
COMMON /POLY/A0,A2,A4,A6,A8 RES00170
COMMON /POINT/ZPP RES00180
C** RES00190
ZPP=ZP RES00200
AB=X(1) RES00210
A6=X(2) RES00220
A4=X(3) RES00230
A2=X(4) RES00240
A0=X(5) RES00250
TOL=CMPLX(.0001,.0001) RES00260
B=-A RES00270
W=CSQNK(B,A,TOL,FIFTH,RETERR,NO,CURVE1,FUN) RES00280
W1=CSQNK(A,B,TOL,FIFTH,RETERR,NO,CURVE2,FUN) RES00290
C** RES00300
R=HEA-1./2.*(1.-A)-ZP/4.*JLOG((1.-ZP)*(A+ZP)/((A-ZP)
1 *(1.+ZP)))-1./(4.*ZP)*JLOG((1.+ZP)/(1.-ZP))-1./8.*(W-W1) RES00310
RES00320
C** RES00330
FUDGE=W-W1 RES00340
RETURN RES00350
END RES00360
C*** RES00370
FUNCTION SUBPROGRAMS RES00370
COMPLEX FUNCTION JLOG*8(ARG) RES00380
REAL*4 DUMI RES00390
COMPLEX*8 ARG,DUM RES00400
DUM=CLOG(ARG) RES00410
DUMI=A IMAG(ARG) RES00420
IF(DUMI.LT.0.0) DUM=CMPLX(REAL(DUM),AIMAG(DUM)+2.*3.141592654) RES00430
JLOG=DUM RES00440
RETURN RES00450
END RES00460
C** RES00470
COMPLEX FUNCTION CURVE1*8(T,DZDT) RES00480
REAL*4 T RES00490
COMPLEX*8 DZDT RES00500
COMMON /POLY/A0,A2,A4,A6,A8 RES00510
CURVE1=CMPLX(T,A0+A2*T**2+A4*T**4+A6*T**6+A8*T**8) RES00520
DZDT=CMPLX(1.,2.*A2*T+4.*A4*T**3+6.*A6*T**5+8.*A8*T**7) RES00530
RETURN RES00540
END RES00550

```



```
C**          RES00560
COMPLEX FUNCTION CURVE2*8(T,DZDT)          RES00570
REAL*4 T          RES00580
COMPLEX*8 DZDT          RES00590
COMMON /POLY/A0,A2,A4,A6,A8          RES00600
CURVE2=CMPLX(T,-(A0+A2*T**2+A4*T**4+A6*T**6+A8*T**8))          RES00610
DZDT=CMPLX(1.,-(2.*A2*T+4.*A4*T**3+6.*A6*T**5+8.*T**7))          RES00620
RETURN          RES00630
END          RES00640
C**          RES00650
C**          RES00660
COMPLEX FUNCTION FUN*8(Z)          RES00670
COMPLEX*8 Z,ZPP,ZCON          RES00680
COMMON /POINT/ZPP          RES00690
ZCON=CONJG(Z)          RES00700
FUN=ZCON/(Z-ZPP)          RES00710
RETURN          RES00720
END          RES00730
```

```

      COMPLEX FUNCTION CSQNK(A,BIG,ERROR,FIFTH,RUM,NO,CURVE,FUN)      00000010
C 'CSQNK' STANDS FOR * COMPLEX SIMPSON QUADRATURE USED ADAPTIVELY,    00000020
C   NOISE KILLED*                                                    00000030
C                                                                      00000040
C   CALLING PROGRAM REQUIRES                                         00000050
C EXTERNAL CURVE,FUN                                                 00000060
C 'CURVE' IS THE PARAMETRIC EQUATION OF THE CONTOUR Z = G(T),       00000070
C   IT ALSO RETURNS DZ/DT.                                           00000080
C 'FUN' IS THE FUNCTION TO BE INTEGRATED F(Z)                        00000090
C                                                                      00000100
C INPUT                                                                00000110
C                                                                      00000120
C   A   LOWER LIMIT OF INTEGRATION (VALUE OF THE REAL PARAMETER T)  00000130
C   B   UPPER LIMIT OF INTEGRATION                                    00000140
C   ERROR THE REQUIRED TOLERANCE (REAL AND IMAGINARY PARTS)(ABSOLUTE 00000150
C        ERROR)                                                       00000160
C                                                                      00000170
C   OUTPUT                                                            00000180
C                                                                      00000190
C   CSQNK THE FIFTH ORDER (COMPLEX) RESULT = THIRD + FIFTH          00000200
C   FIFTH THE FIFTH ORDER (COMPLEX) ADJUSTMENT TERM                 00000210
C   RUM   THE CLAIMED TOLERANCE (REAL AND IMAGINARY PARTS)(ADJUSTED 00000220
C        FOR ROUND-OFF ERROR)                                          00000230
C   NO    THE NUMBER OF FUNCTION EVALUATIONS REQUIRED                 00000240
C                                                                      00000250
C   NOTES ON USE. (1) DISCONTINUOUS FUNCTIONS                        00000260
C                                                                      00000270
C   THIS ROUTINE IS BASED ON DEGREE 3 AND DEGREE 5 LOCAL POLYNOMIAL  00000280
C   APPROXIMATION. CONSEQUENTLY IT SHOULD NOT BE USED WITH FUNCTIONS 00000290
C   WHICH HAVE DISCONTINUITIES IN THE FOURTH OR LOWER DERIVATIVES  WITHIN 00000300
C   THE INTERVAL OF INTEGRATION. IF THERE ARE SUCH DISCONTINUITIES, THIS 00000310
C   ROUTINE WILL TAKE THIS TO BE EVIDENCE OF ROUND OFF ERROR IN FUNCTION 00000320
C   VALUES AND WILL ADJUST THE TOLERANCE.                           00000330
C   IF THE LOCATIONS OF SUCH DISCONTINUITIES ARE KNOWN, THE ROUTINE MAY 00000340
C   BE USED SEPARATELY FOR EACH INTERVAL BETWEEN CONSECUTIVE DISCONTI-  00000350
C   NUITIES. WHILE, LIKE ALL SUCH ROUTINES, IT DISLIKES DISCONTINUITIES, 00000360
C   IT CAN HANDLE THEM IF THEY ARE LOCATED AT THE END POINTS OF THE    00000370
C   INTEGRATION INTERVAL.                                             00000380
C                                                                      00000390
C   NOTES ON USE. (2) FUNCTIONS WITH HIGH-FREQUENCY OSCILLATIONS.   00000400
C                                                                      00000410
C   THE ROUTINE WILL RETURN UNRELIABLE RESULTS FOR FUNCTIONS LIKE G(X) 00000420
C   TIMES COS(100*X). IF THE HIGHEST PERIOD LIKELY TO BE ENCOUNTERED IS 00000430
C   KNOWN, THE INTERVAL SHOULD BE SUB-DIVIDED IN SUCH A WAY THAT,      00000440
C   (ONE) THERE ARE NOT MORE THAN THREE PERIODS PER INTERVAL, AND      00000450
C   (TWO) THE PERIOD *P* DIVIDED BY THE SUB-INTERVAL *(B-A)* IS NOT A  00000460
C   SIMPLE FRACTION *N/M* WITH N OR M LESS THAN 9.                    00000470
C                                                                      00000480
C   NOTES ON USE. (3) INTERVAL SUB-DIVISION                           00000490
C                                                                      00000500
C   THE FAILURES DESCRIBED ABOVE ARE GENERALLY WORSE FOR *CSQNK* THAN FOR 00000510
C   OTHER ROUTINES BECAUSE *CSQNK* TAKES THE INCONVENIENT BEHAVIOR AS AN 00000520
C   INDICATION OF ROUND OFF ERROR. IN GENERAL SUB-DIVISION OF THE      00000530
C   INTERVAL IS ADVOCATED. ESSENTIALLY THE USER CARRIES OUT, UNDER    00000540
C   DRIVING PROGRAM CONTROL, A SEQUENCE OF CALCULATIONS WHICH SHOULD HAVE 00000550

```

```
C BEEN CARRIED OUT IN THE SUBROUTINE IN ANY CASE. IN THIS WAY HE 00000560
C PREVENTS CHANCE LOW ORDER FALSE CONVERGENCE AT VIRTUALLY NO ADDI- 00000570
C TIONAL COST. NOTE THAT THE SUM OF PARAMETERS *ERROR* FOR THE 00000580
C SUB-INTERVALS SHOULD CORRESPOND TO THE VALUE REQUIRED FOR THE WHOLE 00000590
C INTERVAL. 00000600
C 00000610
C NIM NUMBERING SYSTEM AND LOGIC 00000620
C 00000630
C THE INTERVAL (A,B) IS DEFINED NIM = 1, LEVEL = 0. 00000640
C THE INTERVAL NIM = N, LEVEL = L IS BISECTED, IF NECESSARY, INTO 00000650
C TWO INTERVALS, NIM = 2*N AND NIM = 2*N + 1, BOTH AT LEVEL = L + 1. 00000660
C IF INTERVAL NIM = N, LEVEL = L DOES NOT CONVERGE, THE NEXT INTERVAL 00000670
C CONSIDERED IS NIM = 2*N, LEVEL = L + 1. 00000680
C IF INTERVAL NIM=N,LEVEL=L DOES CONVERGE, THE NEXT INTERVAL CONSIDERED 00000690
C IS NIM = M(R) + 1, LEVEL = L-R, WHERE M(R) IS THE FIRST 00000700
C EVEN MEMBER OF THE SEQUENCE M(0) = N, M(S+1) = (M(S)-1)/2. IF THIS 00000710
C GIVES LEVEL = 0, THE CALCULATION IS COMPLETE. 00000720
C 00000730
C SCALING TO AVOID EXCESSIVE DIVISION BY TWO. 00000740
C 00000750
C THE INTERVAL(X1,X5) IF OF LENGTH H = X5-X1. THE POINTS X1,X2,X3,X4,X5 00000760
C ARE THE POINTS OF QUARTERSECTION OF THIS INTERVAL AND FX1,FX2,FX3, 00000770
C FX4,FX5 ARE THE CORRESPONDING FUNCTION VALUES. 00000780
C EST IS APPROXIMATION TO (6.0/H)* INTEGRAL(X1,X5). 00000790
C (EST1+EST2) IS APPROXIMATION TO (12.0/H) * INTEGRAL(X1,X5). 00000800
C SUM IS APPROXIMATION TO (12.0) * INTEGRAL(A,X1). 00000810
C 00000820
C STORAGE 00000830
C 00000840
C X3ST(L) = 0.5*(X5ST(L) + X1). THUS X3ST(L) COULD BE RECALCULATED 00000850
C AT EACH STAGE TO AVOID STORAGE. ESTST(L) IS SAME IN THIS RESPECT. 00000860
C THE RESULTS OF ABOVE RECALCULATION ARE IDENTICAL MACHINE NUMBERS. 00000870
C X5ST(L) = X1 + (B-A)*(2**(-L)). THIS COULD ALSO BE RECALCULATED. BUT 00000880
C IN THIS CASE CALCULATION IS EXCESSIVE AND THERE IS A POSSIBILITY OF 00000890
C ROUND OFF ERROR ARISING BECAUSE THE SAME POINT IS BEING CALCULATED 00000900
C IN TWO OR MORE DIFFERENT WAYS. 00000910
C 00000920
C AVOIDANCE OF ROUND OFF ERROR TROUBLE 00000930
C 00000940
C IF INTERVAL DOES NOT CONVERGE, FOLLOWING INTERVAL SHOULD HAVE ADIFF 00000950
C (ADIFFI) VALUE APPROXIMATELY EQUAL TO (1/16) TIME PREVIOUS ADIFF 00000960
C (ADIFFI) VALUE, CALLED ADIFF1 (ADIFI1) IN THE CODE. THERE IS A 00000970
C THEOREM WHICH STATES THAT, UNLESS THE FOURTH DERIVATIVE OF FUN(X) 00000980
C VANISHES IN THE PREVIOUS INTERVAL, ADIFF (ADIFFI) IS LESS THAN OR 00000990
C EQUAL TO ADIFF1 (ADIFI1). IF THIS DOES NOT HAPPEN, IT IS TAKEN TO BE 00001000
C AN INDICATION OF POSSIBLE ROUND OFF LEVEL. IN THIS CASE, UNLESS LEV 00001010
C IS LESS THAN FIVE, THE CURRENT TOLERANCE LEVEL, CEPS (CEPSI), IS 00001020
C APPROPRIATELY ADJUSTED. HOWEVER CEPS (CEPSI) IS RESET AS AND WHEN IT 00001030
C APPEARS THAT IT SHOULD BE ADJUSTED EITHER UP OR DOWN. IT IS REDUCED 00001040
C IF CONVERGENCE OCCURS WITH A NON-ZERO ADIFF STRICTLY LESS THAN 00001050
C 0.25*CEPS (0.25*CEPSI). AN INVOLVED SECTION OF CODING GUARDS TO SOME 00001060
C EXTENT AGAINST AN UNREALISTIC VALUE ARISING AS A RESULT OF A ZERO IN 00001070
C THE FOURTH DERIVATIVE. A FACTOR EFACT (EFACTI) IS CALCULATED WHICH 00001080
C ADJUSTS THE CLAIMED TOLERANCE TO TAKE INTO ACCOUNT THESE ALTERATIONS 00001090
C IN THE TOLERANCE LEVEL. THE ROUTINE ENTERS THESE INVOLVED SECTIONS 00001100
```

```

C OF CODING ONLY IF ROUND-OFF ERROR APPEARS TO BE PRESENT. IN A NORMAL00001110
C (ROUND OFF ERROR FREE) RUN, THESE SECTIONS ARE SKIPPED AT A COST OF A00001120
C SINGLE COMPARISON PER ITERATION (TWO FUNCTION EVALUATIONS). 00001130
C 00001140
C ARBITRARY CONSTANTS 00001150
C 00001160
C THE FOLLOWING CONSTANTS HAVE BEEN ASSIGNED IN THE LIGHT OF EXPERIENCE00001170
C WITH NO THEORETICAL JUSTIFICATION. 00001180
C (1) NO CONVERGENCE IS ALLOWED AT LEVEL = **ZERO**. THIS MEANS THAT 00001190
C THE ROUTINE IS CONSTRAINED TO BASE THE RESULT ON AT LEAST 9 FUNCTION 00001200
C VALUES. 00001210
C (2) NO UPWARD ADJUSTMENT OF THE TOLERANCE LEVEL IS CONSIDERED AT 00001220
C LEVEL LOWER THAN LEVEL = **FIVE**. THE POINT SPACING IS THEN 00001230
C (BIG-A)/128.0. 00001240
C (3) PHYSICAL LIMIT. HIGHEST LEVEL ALLOWED IS LEVEL = **THIRTY**. HERE00001250
C CONVERGENCE IS ASSIGNED WHETHER OR NOT THE INTERVAL HAS CONVERGED. 00001260
C THE POINT SPACING IS THEN ABOUT (BIG-A)*2.0*10**-10. 00001270
C (4) UPWARD ADJUSTMENT OF TOLERANCE LEVEL IS LIMITED IN GENERAL TO 00001280
C A FACTOR **2.0** OR LESS. 00001290
C (5) DOWNWARD ADJUSTMENT OF TOLERANCE LEVEL IS INHIBITED IN GENERAL 00001300
C UNLESS BY A FACTOR GREATER THAN **4.0**. 00001310
C 00001320
C SOME NOTATION 00001330
C 00001340
C SUM AND SIM ARE RUNNING SUMS, INCREASED AT STAGE EIGHT. THEY ARE 00001350
C RESPECTIVELY 12.0 * (THIRD ORDER APPROXIMATION TO THE INTEGRAL) 00001360
C AND -180.0 * (FIFTH ORDER ADJUSTMENT TO THE INTEGRAL). 00001370
C CEPSF (CEPSFI) IS THE REQUIRED (SCALED) TOLERANCE. 00001380
C CEPS (CEPSI) IS THE RUNNING VALUE OF THE ADJUSTED TOLERANCE. 00001390
C QCEPS = 0.25*CEPS QCEPSI = 0.25*CEPSI 00001400
C LEVTAG (LEVTDI) = -1 OR 0,2,3 INDICATES WHETHER TOLERANCE IS NOT OR 00001410
C IS CURRENTLY ADJUSTED. (SEE COMMENT IN STAGE SEVEN.) 00001420
C EFAC (EFACI) IS RUNNING SUM CORRESPONDING TO 180.0 * RUM 00001430
C FACERR (FACERI) = 15.0 OR 1.0 DEPENDING ON WHETHER TOLERANCE IS OR IS 00001440
C NOT CURRENTLY ADJUSTED. IF IT IS, THERE IS NO JUSTIFICATION FOR 00001450
C THE FIFTH ORDER ADJUSTMENT AND ACCURACY IS NOT EXPECTED TO BE 00001460
C (1/15) TIMES THE DIFFERENCE OF APPROXIMATIONS. FACERR (FACERI) = 00001470
C 15.0 REMOVES THE BUILT IN 15. FACTOR FOR CALCULATION OF EFAC 00001480
C (EFACI). 00001490
C EPMACH - THE MACHINE ACCURACY PARAMETER. THE ROUND-OFF ERROR GUARD 00001500
C DOES NOT REQUIRE THIS NUMBER. IT IS MACHINE INDEPENDENT. THIS IS 00001510
C ONLY USED TO HELP IN AN INITIAL GUESS IN STAGE TWO IF THE VALUE OF 00001520
C ERROR HAPPENS TO BE ZERO. ANY NON-ZERO NUMBER MAY BE USED INSTEAD, 00001530
C WITH VERY SMALL PENALTY IN NUMBER OF FUNCTION EVALUATIONS IF A 00001540
C COMPLETELY UNREASONABLE NUMBER IS USED. 00001550
C DIMENSION X3ST(30),X5ST(30),PREDIF(30),PREDFI(30) 00001570
C COMPLEX FX1,FX2,FX3,FX4,FX5,EST,EST1,EST2,DIFF,THIRD,FIFTH 00001580
C COMPLEX FUN,CURVE,W,DZDT,RUM,ERROR,CMPLX 00001590
C COMPLEX FX3ST(30),FX5ST(30),ESTST(30) 00001600
C COMPLEX*16 SUM.SIM 00001610
C INTEGER SW1,SW2 00001620
C COMMON /TOL/CEPSF,CEPSFI,FX1,FX3,FX5,EPMACH,CEPS,CEPSI,LEVTDI, 00001630
1 LEVTGI,FACERR,FACERI,QCEPS,QCEPSI 00001640
COMMON /RND/LEV,X1,XZERO 00001650
EPMACH = 0.0000000000075 00001660

```

```

C      **** STAGE ONE ****                00001670
C INITIALIZE ALL QUANTITIES REQUIRED FOR CENTRAL CALCULATION (STAGE3). 00001680
SUM = 0.0                                00001690
SIM = 0.0                                00001700
CEPSF=180.0*REAL(ERROR)/(BIG-A)          00001710
CEPSFI=180.0*AIMAG(ERROR)/(BIG-A)        00001720
CEPS = CEPSF                              00001730
CEPSI=CEPSFI                              00001740
ADIFF = 0.0                               00001750
ADIFFI=0.                                 00001760
LEVTAG = -1                               00001770
LEVIGI=-1                                 00001780
FACERR = 1.0                              00001790
FACERI=1.0                                00001800
XZERO = A                                 00001810
EFACT = 0.0                               00001820
EFACTI=0.                                 00001830
NIM = 1                                   00001840
LEV = 0                                   00001850
C FIRST INTERVAL                          00001860
X1 = A                                    00001870
X5 = BIG                                  00001880
X3 = 0.5*(A+BIG)                          00001890
W=CURVE(X1,DZDT)                           00001900
FX1=FUN(W)*DZDT                            00001910
W=CURVE(X3,DZDT)                           00001920
FX3=FUN(W)*DZDT                            00001930
W=CURVE(X5,DZDT)                           00001940
FX5=FUN(W)*DZDT                            00001950
NO = 3                                      00001960
EST=FX1+FX5+(4.0,0.0)*FX3                  00001970
C      **** STAGE TWO ****                00001980
C SET STARTING VALUES FOR TOLERANCES IN THE CASE THAT CEPSF OR CEPSFI=0 00001990
CALL SETTOL                                00002000
C INITIALIZING COMPLETE                    00002010
C      **** STAGE THREE ****              00002020
C CENTRAL CALCULATION.                     00002030
C      REQUIRES X1,X3,X5,FX1,FX3,FX5,EST,ADIFF. 00002040
300 CONTINUE                               00002050
X2 = 0.5*(X1 + X3)                         00002060
X4 = 0.5*(X3 + X5)                         00002070
W=CURVE(X2,DZDT)                           00002080
FX2=FUN(W)*DZDT                            00002090
W=CURVE(X4,DZDT)                           00002100
FX4=FUN(W)*DZDT                            00002110
NO = NO + 2                                00002120
EST1=FX1+(4.0,0.0)*FX2+FX3                 00002130
EST2=FX3+(4.0,0.0)*FX4+FX5                 00002140
ADIFF1 = ADIFF                             00002150
ADIFFI1=ADIFFI                             00002160
DIFF = EST + EST - EST1 - EST2             00002170
IF(LEV - 30) 305,800,800                   00002180
305 ADIFF=ABS(REAL(DIFF))                   00002190
ADIFFI=ABS(AIMAG(DIFF))                    00002200
CRIT = ADIFF - CEPS                        00002210

```

```
      CRITI=ADIFFI-CEPSI                                00002220
C      **** STAGE FOUR ****                            00002230
      SW1=0                                              00002240
      IF (CRIT) 310,310,400                              00002250
400    CALL ROUND(ADIFF,ADIFF1,EFACT,FACERR,CEPS,LEVTAG,QCEPS,&309,&310) 00002260
309    SW1=1                                              00002270
310    IF (CRITI) 311,311,401                            00002280
311    IF (LEV) 312,401,312                              00002290
312    IF (SW1) 700,700,500                              00002300
401    CALL ROUND(ADIFFI,ADIFI1,EFACTI,FACERI,CEPSI,LEVTGI,QCEPSI,&500,
      1&499)                                              00002310
499    IF (SW1) 800,800,500                              00002320
C      END OF CENTRAL LOOP                              00002330
C      SUBROUTINE ROUND IS CALLED IN CASE OF NO NATURAL CONVERGENCE 00002340
C      NEXT STAGE IS STAGE SEVEN IN CASE OF NATURAL CONVERGENCE 00002350
C      **** STAGE FIVE ****                              00002360
C      NO ACTUAL CONVERGENCE.                            00002370
C      STORE RIGHT HAND ELEMENTS                        00002380
500    CONTINUE                                          00002390
      NIM = 2*NIM                                        00002400
      LEV = LEV + 1                                      00002410
      ESTST(LEV) = EST2                                  00002420
      X3ST(LEV) = X4                                    00002430
      X5ST(LEV) = X5                                    00002440
      FX3ST(LEV) = FX4                                  00002450
      FX5ST(LEV) = FX5                                  00002460
      PREDIF(LEV) = ADIFF                               00002470
      PREDFI(LEV)=ADIFFI                                00002480
C      **** STAGE SIX ****                              00002490
C      SET UP QUANTITIES FOR CENTRAL CALCULATION.        00002500
C      READY TO GO AHEAD AT LEVEL LOWER WITH LEFT HAND ELEMENTS 00002510
C      X1 AND FX1 ARE THE SAME AS BEFORE                00002520
      X5 = X3                                            00002530
      X3 = X2                                            00002540
      FX5 = FX3                                          00002550
      FX3 = FX2                                          00002560
      EST = EST1                                         00002570
      GO TO 300                                          00002580
C      **** STAGE SEVEN *****                          00002590
700    CONTINUE                                          00002600
C      CHECK THAT IT WAS NOT LEVEL ZERO INTERVAL. IF SO ASSIGN NON CONVERGEN 00002610
      IF(LEV) 400, 400, 705                              00002620
705    SW2=0                                              00002630
      CALL CHECK(LEVTAG,CEPS,CEPST,CRIT,ADIFF,ADIFF1,QCEPS,EFACT,FACERR,
      1CEPSF,&715,&710)                                  00002640
710    SW2=1                                              00002650
      QCEPS=0.25*CEPS                                    00002660
715    CALL CHECK(LEVTGI,CEPSI,CEPSTI,CRITI,ADIFFI,ADIFI1,QCEPSI,EFACTI,
      1FACERI,CEPSFI,&725,&720)                          00002670
720    QCEPSI=0.25*CEPSI                                00002680
      GO TO 500                                          00002690
725    IF (SW2) 800,800,500                              00002700
C      **** STAGE EIGHT ****                            00002710
C      ACTUAL CONVERGENCE IN PREVIOUS INTERVAL. INCREMENTS ADDED INTO 00002720
C      RUNNING SUMS                                     00002730
```

```

C ADD INTO SUM AND SIM                                00002770
800 CONTINUE                                          00002780
    SUM = SUM + (EST1+EST2)*(X5-X1)                   00002790
    IF(LEVTAG)804,810,810                             00002800
  804 IF(LEVTGI)805,810,810                           00002810
C WE ADD INTO SIM ONLY IF WE ARE CLEAR OF ROUND OFF LEVEL. 00002820
  805 SIM=SIM+DIFF*(X5-X1)                            00002830
810 CONTINUE                                          00002840
C **** STAGE NINE ****                                00002850
C SORT OUT WHICH LEVEL TO GO TO. THIS INVOLVES NIM NUMBERING SYSTEM 00002860
C DESCRIBED BEFORE STAGE ONE.                        00002870
905 NUM = NIM/2                                       00002880
    NOM = NIM - 2*NUM                                 00002890
    IF(NOM) 910, 915, 910                             00002900
910 NIM = NUM                                          00002910
    LEV = LEV - 1                                     00002920
    GO TO 905                                          00002930
915 NIM = NIM + 1                                     00002940
C NEW LEVEL IS SET. IF LEV = 0 WE HAVE FINISHED        00002950
    IF(LEV) 1100, 1100, 1000                          00002960
C **** STAGE TEN ****                                00002970
C SET UP QUANTITIES FOR CENTRAL CALCULATION.          00002980
1000 CONTINUE                                         00002990
    X1 = X5                                           00003000
    FX1 = FX5                                         00003010
    X3 = X3ST(LEV)                                    00003020
    X5 = X5ST(LEV)                                    00003030
    FX3 = FX3ST(LEV)                                  00003040
    FX5 = FX5ST(LEV)                                  00003050
    EST = ESTST(LEV)                                  00003060
    ADIFF = PREDIF(LEV)                               00003070
    ADIFFI=PREDFI(LEV)                                00003080
    GO TO 300                                          00003090
C **** STAGE ELEVEN ****                              00003100
C CALCULATION NOW COMPLETE. FINALIZE.                 00003110
1100 CONTINUE                                         00003120
    EFACT = EFACT + CEPS *(BIG-XZERO)*FACERR          00003130
    EFACTI=EFACTI+CEPSI*(BIG-XZERO)*FACERI            00003140
    RUM=CMPLX(EFACT/180.0,EFACTI/180.0)              00003150
    THIRD=SUM/(12.0,0.0)                              00003160
    FIFTH=-SIM/(180.0,0.0)                            00003170
    CSQNK=THIRD+FIFTH                                 00003180
    RETURN                                            00003190
C END OF CSQNK                                        00003200
    END                                              00003210
    SUBROUTINE SETTOL                                00003220
C SET STARTING VALUES FOR THE TOLERANCES WHEN CEPSF OR CEPSFI = 0. 00003230
    COMMON /TOL/CEPSF,CEPSFI,FX1,FX3,FX5,EPMACH,CEPS,CEPSI,LEVTAG, 00003240
    1LEVTGI,FACERR,FACERI,QCEPS,QCEPSI              00003250
    COMPLEX FX1,FX3,FX5                              00003260
C SET STARTING VALUES FOR THE TOLERANCES IN THE CASE THAT CEPSF=0. 00003270
    IF (CEPSF) 240,205,240                            00003280
  205 LEVTAG=0                                         00003290
    FACERR=15.0                                       00003300
C SET REAL TOLERANCE                                 00003310

```

```
      IF (REAL(FX1)) 210,215,210      00003320
210  CEPS= EPMACH*ABS(REAL(FX1))      00003330
      GO TO 240                        00003340
215  LEVTAG=3                          00003350
      IF (REAL(FX3)) 220,225,220      00003360
220  CEPS= EPMACH*ABS(REAL(FX3))      00003370
      GO TO 240                        00003380
225  IF (REAL(FX5)) 230,235,230      00003390
230  CEPS= EPMACH*ABS(REAL(FX5))      00003100
      GO TO 240                        00003410
235  CEPS= EPMACH                      00003420
C SET IMAGINARY TOLERANCE            00003430
240  IF (CEPSFI) 295,275,295          00003440
275  LEVTGI=0                          00003450
      FACERI=15.                      00003460
      IF (AIMAG(FX1)) 245,250,245     00003470
245  CEPSI= EPMACH*ABS(AIMAG(FX1))    00003480
      GO TO 295                        00003490
250  LEVTGI=3                          00003500
      IF (AIMAG(FX3)) 255,260,255     00003510
255  CEPSI= EPMACH*ABS(AIMAG(FX3))    00003520
      GO TO 295                        00003530
260  IF (AIMAG(FX5)) 265,270,265     00003540
265  CEPSI= EPMACH*ABS(AIMAG(FX5))    00003550
      GO TO 295                        00003560
270  CEPSI= EPMACH                     00003570
295  QCEPS=0.25*CEPS                  00003580
      QCEPSI=0.25*CEPSI               00003590
      RETURN                           00003600
      END                              00003610
      SUBROUTINE ROUND(ADIFF,ADIFF1,EFACT,FACERR,CEPS,LEVTAG,QCEPS,*,*) 00003620
C NO NATURAL CONVERGENCE. A COMPLEX SEQUENCE OF INSTRUCTIONS 00003630
C FOLLOWS WHICH ASSIGNS CONVERGENCE AND / OR ALTERS TOLERANCE 00003640
C LEVEL IN UPWARD DIRECTION IF THERE ARE INDICATIONS OF ROUND OFF 00003650
C ERROR. 00003660
      COMMON /RND/LEV,X1,XZERO 00003670
      IF(ADIFF1 - ADIFF) 410, 410, 500 00003680
C IN A NORMAL RUN WITH NO ROUND OFF ERROR PROBLEM, ADIFF1 IS GREATER TH 00003690
C ADIFF AND THE REST OF STAGE FOUR IS OMITTED. 00003700
410  IF(LEV - 5) 500, 415, 415 00003710
415  EFACT = EFACT + CEPS *(X1 - XZERO)*FACERR 00003720
      XZERO = X1 00003730
      FACERR = 15.0 00003740
C THE REST OF STAGE FOUR DEALS WITH UPWARD ADJUSTMENT OF TOLERANCE (CEP 00003750
C BECAUSE OF SUSPECTED ROUND OFF ERROR TROUBLE. 00003760
      IF(ADIFF-2.0*CEPS) 420, 420, 425 00003770
C SMALL JUMP IN CEPS. ASSIGN CONVERGENCE 00003780
420  CEPS = ADIFF 00003790
      LEVTAG = 0 00003800
      QCEPS=0.25*CEPS 00003810
      RETURN 2 00003820
425  IF(ADIFF1 - ADIFF) 435, 430, 435 00003830
C LARGE JUMP IN CEPS 00003840
430  CEPS = ADIFF 00003850
      GO TO 445 00003860
```



```
C FACTOR TWO JUMP IN CEPS                                00003870
435 CEPS = 2.0*CEPS                                       00003880
    IF(LEVTAG - 3) 440, 445, 445                          00003890
440 LEVTAG = 2                                             00003900
445 QCEPS = 0.25*CEPS                                     00003910
500 RETURN 1                                              00003920
    END                                                    00003930
    SUBROUTINE CHECK(LEVTAG,CEPS,CEPST,CRIT,ADIFF,ADIFF1,QCEPS,EFACT, 00003940
    1FACERR,CEPSF,*,*)                                    00003950
C NATURAL CONVERGENCE IN PREVIOUS INTERVAL. THE FOLLOWING COMPLEX SEQUE 00003960
C CHECKS PRIMARILY THAT TOLERANCE LEVEL IS NOT TOO HIGH. UNDER CERTAIN 00003970
C CIRCUMSTANCES NON CONVERGENCE IS ASSIGNED AND / OR TOLERANCE LEVEL 00003980
C IS RE-SET.                                              00003990
    COMMON /RND/LEV,X1,XZERO                               00004000
C LEVTAG = -1 CEPS = CEPSF, ITS ORIGINAL VALUE.          00004010
C LEVTAG = 0 CEPS IS GREATER THAN CEPSF. REGULAR SITUATION. 00004020
C LEVTAG = 2 CEPS IF GREATER THAN CEPSF. CEPS PREVIOUSLY ASKED FOR A B 00004030
C JUMP, BUT DID NOT GET ONE.                              00004040
C LEVTAG = 3 CEPS IS GREATER THAN CEPSF. CEPS PREVIOUSLY HAD A BIG JUM 00004050
705 IF(LEVTAG) 800, 710, 710                              00004060
C IN A NORMAL RUN WITH NO ROUND OFF ERROR PROBLEM, LEVTAG = -1 AND THE 00004070
C REAT OF STAGE SEVEN IS OMITTED.                        00004080
710 CEPST = 15.0*CEPS                                     00004090
C CEPST HERE IS FACERR*CURRENT VALUE OF CEPS             00004100
    IF(CRIT) 715, 800, 800                                 00004110
715 IF(LEVTAG-2) 720, 740, 750                            00004120
C LEVTAG = 0                                              00004130
720 IF(ADIFF) 800, 800, 725                                00004140
725 IF(ADIFF - QCEPS) 730, 800, 800                      00004150
730 IF(ADIFF - CEPSF) 770, 770, 735                      00004160
735 LEVTAG = 0                                             00004170
    CEPS = ADIFF                                           00004180
    EFACT = EFACT + CEPST * (X1 - XZERO)                  00004190
    XZERO = X1                                             00004200
    RETURN 2                                               00004210
C LEVTAG = 2                                             00004220
740 LEVTAG = 0                                             00004230
    IF(ADIFF)765, 765, 725                                  00004240
C LEVTAG = 3                                             00004250
750 LEVTAG = 0                                             00004260
    IF(ADIFF) 775, 775, 730                                00004270
765 CEPS = ADIFF1                                         00004280
    GO TO 775                                              00004290
770 LEVTAG = -1                                           00004300
    FACERR = 1.0                                           00004310
    CEPS = CEPSF                                           00004320
775 EFACT = EFACT + CEPST*(X1 - XZERO)                   00004330
    XZERO = X1                                             00004340
780 CONTINUE                                              00004350
    QCEPS = 0.25*CEPS                                     00004360
800 RETURN 1                                              00004370
    END                                                    00004380
```

APPENDIX C - HEAT TRANSFER MODELS

Details of the heat transfer solutions for the field winding conductors are given in this section. The object of the analysis is to determine the maximum steady-state temperature within a conductor due to internal heat generation from the combined eddy current and hysteresis ac loss. A one-dimensional solution is given for temperature gradients along the conductor axis and a two-dimensional solution is given for temperature gradients across the conductor cross-section.

C.1 One-Dimensional Model

The yoke-module winding configuration can be thermally modelled as a one-dimensional fin with internal heat generation. The schematic representation of the field winding in Fig. IV.5.a can be thermally modelled as shown in Fig. C.1. Assume a one-dimensional temperature dependence in the x-direction. The solution is divided into two regions. In region 1 it is assumed the conductor is well insulated and since, by symmetry, there can be no temperature gradient at $x=0$ all of the internal heat generated must leave the region at $X=L_1$, in the steady-state. In region 2 the heat flux into the section at $X=L_1$, plus the heat generated internally leaves the conductor along its length by convection to the liquid helium bath. Again symmetry requires there be no heat flux at $X=L_2$. Solutions for the two regions are written independently and joined by boundary conditions at the common boundary. Let

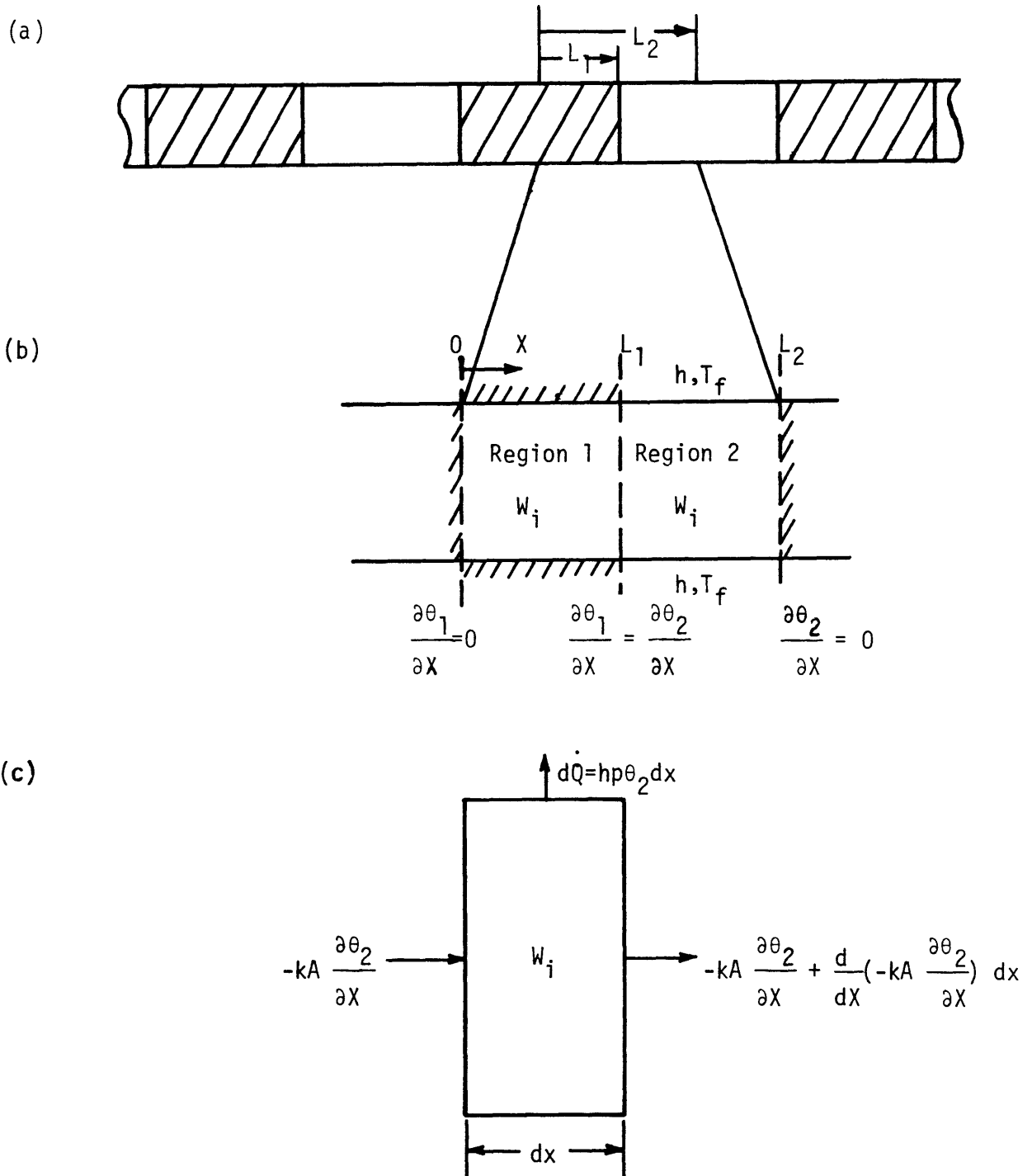


Fig. C.1 One-dimensional heat transfer model; a) schematic of conductor; b) boundary conditions; c) differential element of region 2.

$$\begin{aligned}\theta_1 &= T_1 - T_f \\ \theta_2 &= T_2 - T_f\end{aligned}\tag{C.1}$$

and $k_1 = k_2 = k$

where T_f is the temperature of the fluid bath, and k is the thermal conductivity of the conductor in the axial direction.

The governing equation for region 1 is

$$\frac{\partial^2 \theta_1}{\partial x^2} = \frac{-w_i}{k} \quad .\tag{C.2}$$

The general solution has the form

$$\theta_1 = \frac{-w_i x^2}{2k} + c_1 x + c_2 \quad .\tag{C.3}$$

The governing equation for region 2 can be determined by writing the steady-state energy balance for the differential element of Fig. C.1.c. The resulting simplified equation is given by

$$\frac{\partial^2 \theta_2}{\partial x^2} - \left(\frac{hp}{kA} \right) \theta_2 = \frac{-w_i}{k}\tag{C.4}$$

where $hp\theta_2 dx$ has been substituted for $d\dot{Q}$ and P and A are the wetted perimeter and cross-sectional area respectively. The combined homogeneous and particular solutions to Eq. (C.4) are

$$\theta_2 = \frac{w_i}{k \beta^2} + C_3 e^{\beta x} + C_4 e^{-\beta x} \quad (C.5)$$

where $\beta = \sqrt{hp/kA}$ is the fin coefficient.

The constant coefficients C_1 through C_4 are found from simultaneous solution of the boundary conditions;

$$\begin{aligned} x = 0 & \quad , \quad \frac{\partial \theta_1}{\partial x} = 0 \\ x = L_1 & \quad , \quad \frac{\partial \theta_1}{\partial x} = \frac{\partial \theta_2}{\partial x} \\ x = L_1 & \quad , \quad \theta_1 = \theta_2 \\ x = L_2 & \quad , \quad \frac{\partial \theta_2}{\partial x} = 0 \end{aligned} \quad (C.6)$$

Substitution of Eqns. (C.3) and (C.5) into Eqns. (C.6) and solving for the maximum temperature at $x=0$ results in

$$\theta_{\max} = \frac{w_i}{k \beta^2} \left\{ 1 + \left(\frac{f\beta L_2}{2} \right)^2 + (f\beta L_2) \left[\frac{1 + e^{-2\beta L_2(1-f)}}{1 - e^{-2\beta L_2(1-f)}} \right] \right\} \quad (C.7)$$

where $f = L_1/L_2$ and $\theta_{\max} = T_0 - T_f$. The temperature T_0 is the maximum temperature.

C.2 Two-Dimensional Model

The previous section neglected temperature gradients across the conductor transverse to the axial direction. In order to justify this assumption a thermal model is given to determine the transverse temperature

gradient in a conductor. The solution for steady heat flow in a rectangle with internal heat generation and convective cooling on all surfaces can be found in the literature but it is developed here for completeness [73].

The governing equation for the configuration of Fig. C.2 is given by

$$\frac{\partial^2 \theta}{\partial x^2} + \frac{\partial^2 \theta}{\partial y^2} = -\frac{w_i}{k} \quad . \quad (C.8)$$

The homogeneous solution is given by

$$\theta_h = (C_1 \sin \alpha x + C_2 \cos \alpha x)(C_3 \sinh \alpha y + C_4 \cosh \alpha y) \quad (C.9)$$

and a particular solution is given by

$$\theta_p = -\frac{w_i}{2k} x^2 + w_i \frac{th}{2} + \frac{w_i t^2}{8k} \quad . \quad (C.10)$$

The total solution is given by the sum of Eqns. (C.9) and (C.10).

Noting the symmetry about $x=0$, $y=0$, the boundary conditions are;

$$x = 0 \quad , \quad \frac{\partial \theta}{\partial x} = 0 \quad (C.11a)$$

$$x = \frac{t}{2} \quad , \quad -k \frac{\partial \theta}{\partial x} = h\theta \quad (C.11b)$$

$$y = 0 \quad , \quad \frac{\partial \theta}{\partial y} = 0 \quad (C.11c)$$

$$y = \frac{w}{2} \quad , \quad -k \frac{\partial \theta}{\partial y} = h\theta \quad . \quad (C.11.d)$$

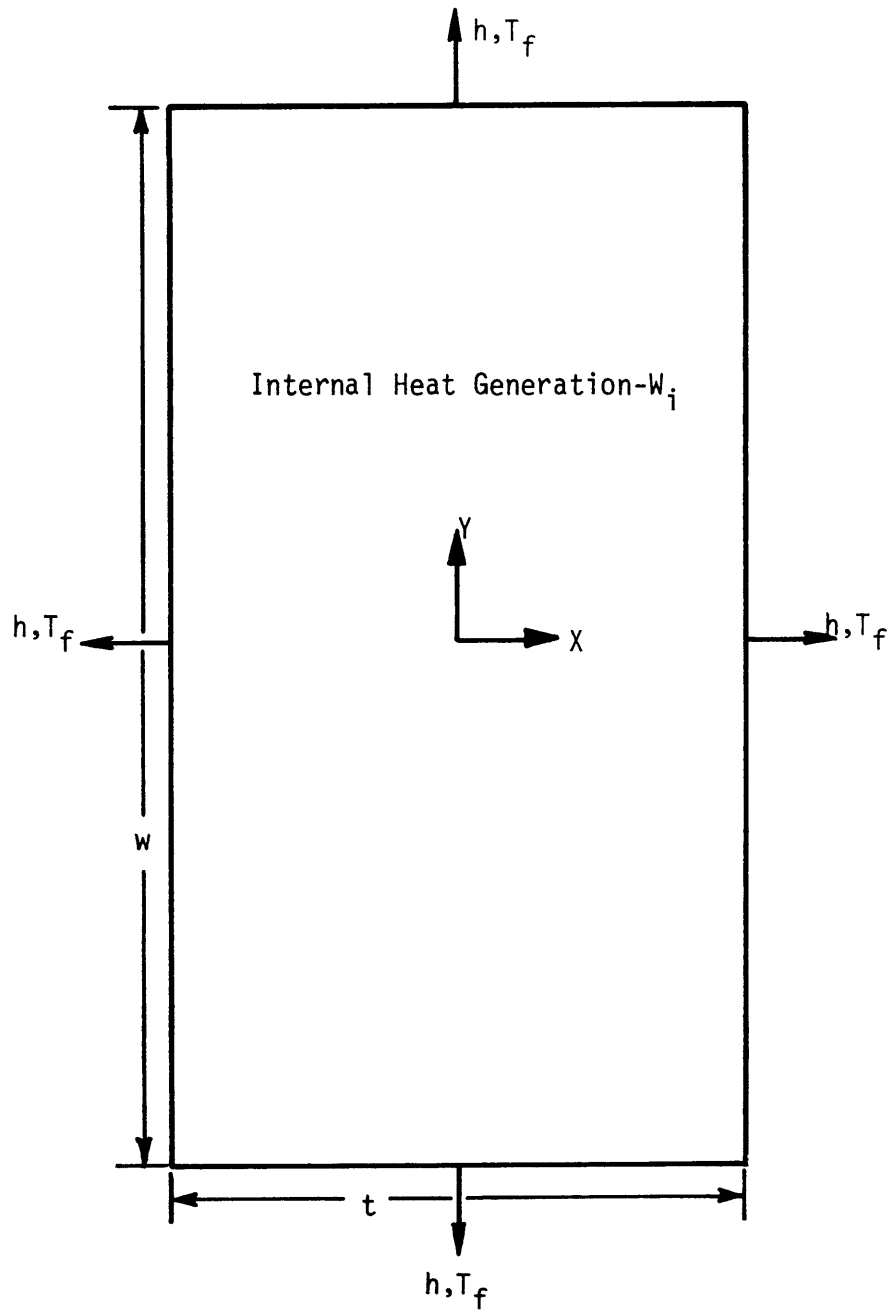


Fig. C.2 Two-dimensional heat transfer model.

Substituting Eqns. (C.9) and (C.10) into Eqns. (C.11a,b) and (C.11.c) and solving for the unknown constants results in

$$\theta = \frac{w_i}{2k} \left(\frac{t^2}{4} - x^2 \right) + \frac{w_i t}{2h} + \sum_{m=1}^{\infty} A_m \cos(\alpha_n x) \cosh(\alpha_n y) \quad (C.12)$$

where α_n are the eigenvalues given by the positive roots of

$$\left(\alpha_n \frac{t}{2} \right) \tan\left(\alpha_n \frac{t}{2}\right) = \left(\frac{ht}{2k} \right) \quad . \quad (C.13)$$

The coefficients A_n are determined from the last boundary condition, Eq. (C.11.d). The result is

$$A_n = -\frac{4w_i}{k} \frac{\sin\left(\alpha_n \frac{t}{2}\right)}{\alpha_n^2 [t\alpha_n + \sin(t\alpha_n)] \left[\left(\frac{\alpha_n k}{h} \right) \sinh\left(\frac{w}{2} \alpha_n\right) + \cosh\left(\frac{w}{2} \alpha_n\right) \right]} \quad . \quad (C.14)$$

The maximum temperature occurs at $x=0, y=0$ and is given by

$$\theta_{\max} = \frac{t^2 w_i}{4k} \left\{ \frac{1}{B_i} + \frac{1}{2} - \frac{1}{4} \sum_{m=1}^{\infty} \frac{\sin(\alpha_m)}{\alpha_m^2 [2\alpha_m + \sin(2\alpha_m)] \left[\left(\frac{\alpha_m}{B_i} \right) \sinh(\gamma \alpha_m) + \cosh(\gamma \alpha_m) \right]} \right\} \quad (C.15)$$

where $B_i = \frac{ht}{2k}$ is the Biot number, $\gamma = \frac{w}{t}$ and α_m is the non-dimensional form of α_n given by

$$\alpha_m \tan \alpha_m = B_i \quad m = 1, 2, 3, \dots \quad .$$

BIBLIOGRAPHY

1. Tinkham, M., Introduction to Superconductivity, McGraw-Hill, New York, 1975.
2. Rose-Innes, A.C., and Rhoderick, E.H., Introduction to Superconductivity, Pergamon Press, Oxford, 1969.
3. Williams, J.E.C., Superconductivity and Its Applications, Pion Limited, London, 1970.
4. Kittel, C., Introduction to Solid State Physics, Chapter 12, John Wiley and Sons, New York, 1976.
5. Huebener, R.P., Magnetic Flux Structures in Superconductors, Springer-Verlag, Berlin, 1979.
6. Saint-James, D., Sarma, G., and Thomas, E.S., Type II Superconductivity, Pergamon Press, Oxford, 1969.
7. Brechna, H., Superconducting Magnet Systems, Springer-Verlag, Berlin, 1973.
8. London, F., Superfluids, Volume 1, John Wiley and Sons, New York, 1950.

REFERENCES

1. Birmingham, B.W. and Smith, C.N., Cryogenics, 16, (1976), 59.
2. Schwartz, B.B. and Foner, S., Physics Today, Vol. 30, No. 7, (1977)
3. Geballe, T.H., and Hulm, J.K., Scientific American, Vol. 243, No. 5 (1980), 138.
4. Stekly, Z.J.J., and Woodson, H.H., IEEE Trans. on Aerospace, Vol. A5-2, (1964), 826.
5. Woodson, H.H., Stekly, Z.J.J., and Halas, E., IEEE Trans. Power Apparatus and Systems, Vol. PAS-85, No. 3, (1966).
6. Thullen, P., "Analysis of the Application of Superconductivity to Commercial Electric Power Generation," ScD., June 1969 (M.I.T. Thesis).
7. Thullen, P. and Smith, J.L., Jr., Advances in Cryogenic Engineering, Vol. 15, Plenum Press, (1970), 132.
8. Kirtley, J.L., Jr., Smith, J.L., Jr., Thullen, P., and Woodson, H.H., Proc. IEEE, Vol. 61, No. 1, (1973), 112.
9. "Superconductors in Large Synchronous Machines", EPRI 92, Final Report, June 1975; prepared by M.I.T., printed by Electric Power Research Institute.
10. Bejan, A., Keim, T.A., Smith, J.L., Jr., Kirtley, J.L., Jr., Thullen, P., and Wilson, G.L., Advances in Cryogenic Engineering, Vol. 19, Plenum Press, (1974), 53.
11. Kingsley, C., Wilson, G.L., Kirtley, J.L., Jr., Keim, T.A., Smith, J.L., Jr., and Thullen, P., IEEE Paper PG 75645-2, presented at 1975 Joint Power Generation Conference, Portland, Oregon, Sept. 29, 1975.
12. "Demonstration of an Advanced Superconducting Generator", Interim Reports 1 through 13, MIT Cryogenic Engineering Laboratory and Electric Power Systems Engineering Laboratory, EX-76-A-01-2295, T.O. #11, IR1-IR13.
13. Bardeen, J., Cooper, L.N., and Schrieffer, J.R., Phys. Rev., 108, (1957), 1175.
14. Ginzburg, V.L., and Landau, L.D., Zh. Eksperim. i Teor. Fiz., 20, (1950), 1064.

15. Gorkov, L.P., Soviet Physics-JETP, 9, (1959), 1364.
16. Abrikosov, A.A., Zh. Eksperim. i Teor. Fiz., 32, (1957), 1442,
Soviet Physics-JETP, 5, (1957), 1174.
17. Meissner, W., and Ochsenfeld, R., Naturwissenschaften, 21, (1933), 787.
18. Gorter, C.J., and Casimir, H.B.G., Physica, 1, (1934), 306.
19. London, F. and London, H., Proc. Royal Society, A149, London, (1935), 71.
20. Pippard, A.B., Proc. Royal Society, A216, London, (1953), 547.
21. Kim, Y.B., Hempstead, C.F., and Strnad, A.R., Physical Review Letters,
12, 145, (1964), and Physical Review, 139, A1163, (1965).
22. Bardeen, J. and Stephen, M.J., Physical Review, 140, A1197, (1965).
23. Schmid, A., Phys. Kondensierten Materie, 5, 302 (1966).
24. Caroli, C. and Maki, K., Physical Review, 159, 306 and 316, (1967);
164, 541, (1967); 169, 381 (1968).
25. Hu, C.R. and Thompson, R.S., Physical Review, B6, 110 (1972).
26. Chen, J.R., Physical Review Letters, 20, 735 (1968).
27. Van Oijen, and van Gorp, Philips Research Report, Number 21,
(1966) 343.
28. Bean, C.P., Physical Review Letters, Vol. 8, 250 (1962).
29. Kim, Y.B., Hempstead, C.F., and Strnad, A.R., Physical Review, Vol. 131,
2486 (1963).
30. Kim, Y.B., Hempstead, C.F., and Strnad, A.R., Physical Review, Vol. 139,
No. 4A, A1163 (1965).
31. Irie, F., and Yamafuji, K., Journal of the Physical Society of Japan,
Vol. 23, No. 2, 255, (1967).
32. Anderson, P.W., Physical Review Letters, Vol. 9, 309 (1962).
33. Anderson, P.W., and Kim, Y.B., Rev. Mod. Physics, Vol. 36, 39 (1964).
34. Kunzler, J.E., Buehler, E., Hsu, F.S.L., and Weinick, J.H., Physical
Review Letters, Vol. 6, 89 (1961).
35. Hancox, R., IEEE Trans. on Magnetics, MAG-45, 486, (1968).

36. Smith, P.F., Wilson, M.N., Walters, C.R., and Lewin, J.C., Proc. Summer Study on Superconducting Devices (Brookhaven National Lab.), 967 (1965).
37. Kantorowitz, A.R. and Stekly, Z.J.J., Applied Physics Letters, Vol. 6, 56, (1965).
38. Bean, C.P., Review of Modern Physics, Vol. 36, 31 (1964).
39. London, H., Physics Letters, Vol. 6, No. 2, 162 (1963).
40. Hancox, R., Proc. IEEE, Vol. 113, No. 7, 1221 (1966).
41. Morgan, G.H., Journal of Applied Physics, Vol. 41, No. 9, 3673, (1970).
42. Wilson, M.N., Proc. 1972 Applied Superconductivity Conference, IEEE-72 CH 0682-5-TABSC, 385, (1973).
43. Ries, G., IEEE Trans on Magnetics, Vol. MAG-13, No. 1, 524 (1977).
44. Kwasnitza, K., Brown Boveri Review, p. 105, February 1977.
45. Carr, W.J., Jr., Journal of Applied Physics, Vol. 45, 929 (1974).
46. Carr, W.J., Jr., Physical Review B, Vol. 11, No. 4, 1547 (1975).
47. Walker, M.S., Murphy, J.R., and Carr, W.J., Jr., IEEE Trans. on Magnetics, Vol. MAG-11, No. 2, 309, (1975).
48. Murphy, J.H., Walker, M.S., and Carr, W.J., Jr., IEEE Trans. on Magnetics, Vol. MAG-11, No. 2, 313 (1975).
49. Murphy, J.H., Walker, M.S., and Carr, W.J., Jr., IEEE Trans. On Magnetics, Vol. MAG-10, No. 3, 868 (1974).
50. Ogasawara, T., Takahashi, Y., Kanbara, K., Kubota, Y., Yasohama, Y., and Yasukochi, K., Cryogenics, Vol. 20, 216 (1980).
51. Ogasawara, T., Takahashi, Y., Kanbara, K., Kubota, Y., Yasohama, K., Yasukochi, K., Cryogenics, Vol. 21, No. 2, 65, (1981)
52. Ashkin, M., Journal of Applied Physics, Vol. 50, No. 11, 7060 (1979).
53. Pang, C.Y., McLaren, P.G., Campbell, A.M., Proceedings of the 1980 International Cryogenic Engineering Conference, Genova, Italy (1980).
54. Zenkevitch, V.B., Romanyuk, A.S., Zheltov, V.V., Cryogenics, Vol. 20, No. 12, 703 (1980).
55. Beth, R.A., Journal of Applied Physics, Vol. 38, No. 12, (1967).

56. Kato, Y., Hanawaka, M., and Yamafuji, K., Japanese Journal of Applied Physics, Vol. 15, No. 4, (1976).
57. Brown, K.M., and Dennis, J.E., Numerische Mathematik, Vol. 18, 289, (1972).
58. Carr, W.J., Jr., IEEE Trans. on Magnetics, Vol. MAG-15, No. 1, (1979).
59. Duchateau, J.L., and Turck, B., Cryogenics, Vol. 14, 545 (1974).
60. Ogasawara, T., Yasukochi, K., Sagama, S., Proceedings of the Sixth International Conference on Magnet Technology, Bratislava, 728, (1977).
61. Ogasawara, T., Yasukochi, K., Takahashi, Y., Yasohama, K., and Kubota, Y., IEEE Trans. on Magnetics, Vol. MAG-15, 236 (1978).
62. Soubeyrand, J.P., and Truck, B., IEEE Trans. on Magnetics, Vol. MAG-15, 248 (1978).
63. Carr, W.J., Jr., Murphy, J.H., and Wagner, G.R., Advances in Cryogenic Engineering, Vol. 24, Plenum Press, 415 (1978).
64. Smith, J.L., Jr., Wilson, G.L., and Kirtley, J.L., Jr., IEEE Trans. on Magnetics, Vol. MAG-15, No. 1, 727, (1979).
65. Ula, A.H.M.S., Kirtley, J.L., Jr., and Smith, J.L., Jr., Proceedings of the International Conference on Electric Machines, Sept. 15-17, 1980, Athens, Greece.
66. Tepper, K.A., Minervini, J.V., and Smith, J.L., Jr., Advances in Cryogenic Engineering, Vol. 25, Plenum Press, 137 (1980).
67. Tepper, K.A., "Mechanical Design of the Rotor of a Fault-Worthy, 10MVA Superconducting Generator", Ph.D. Thesis, M.I.T., Dept. of Mechanical Engineering (1980).
68. "Demonstration of an Advanced Superconducting Generator", M.I.T. Cryogenic Engineering Laboratory and Electric Power Systems Engineering Laboratory, E(49-18)-2295, T.O. #11, IR-5, pp 178-183.
69. "Demonstration of an Advanced Superconducting Generator", M.I.T. Cryogenic Engineering Laboratory and Electric Power Systems Engineering Laboratory, E(49-18)-2295, T.O.11, IR-6, pp. 102-118.
70. "Demonstration of an Advanced Superconducting Generator", M.I.T. Cryogenic Engineering Laboratory and Electric Power Systems Engineering Laboratory, EX-76-A-01-2295, T.O. #11, IR-8, pp. 157-163.
71. Umans, S.D., Roener, P.B., Mallick, J.A., and Wilson, G.L., IEEE Trans. on Power Apparatus and Systems, PAS, Vol. 98, No. 6, Nov-Dec (1979).

72. Schwoerer, J.A., "Thermal Analysis of a Cryogenic Cooling Scheme for a Fault-Worthy Superconducting Generator, S.M. Thesis, M.I.T., Dept. of Mechanical Engineering (1978).
73. Carslaw, H.S., and Jaeger, J.C., Conduction of Heat in Solids, Oxford University Press, London, 1959.

BIOGRAPHICAL NOTE

Joseph V. Minervini was born in Jersey City, New Jersey on December 3, 1948. His family moved to Hallandale, Florida in 1956 where he attended elementary and high schools. In 1966 he was appointed by his Congressman as a Cadet/Midshipman to the U.S. Merchant Marine Academy at Kings Point, New York. His sophomore year was spent at sea aboard several freighters. He made voyages for Lykes Bros. Steamship Lines to North Europe and the Mediterranean and voyages for Delta Steamship Lines to West Africa, South America and the Caribbean. He graduated in 1970 receiving the B.S. degree, a U.S. Coast Guard License as Third Assistant Engineer of Steam and Motor Vessels of Any Horsepower, and a commission as an Ensign in the Naval Reserve. From 1970 to 1972 he was employed by Humble Oil and Refining Co., Marine Department, as an operating engineer on tankers carrying oil products from U.S. Gulf Coast Refineries to East Coast ports. In 1972 he entered M.I.T. and worked as a Research Assistant in the Cryogenic Engineering Laboratory receiving the Master's degree in Mechanical Engineering in 1974. From 1974 to 1976 he was employed by Magnetic Corporation of America, in Waltham, Mass., as a Research Engineer where his work involved analysis and design of superconducting and conventional magnets, and magnet systems. He re-entered M.I.T. in the Fall of 1976 for completion of his graduate studies again working as a Research Assistant in the Cryogenic Laboratory. He is an associate member of the American Society of Mechanical Engineers and his publications include:

"Two Dimensional Analysis of AC Loss in Superconductors Carrying Transport Current," to be presented at the 1981 International Cryogenic Materials Conference, August 10-14, San Diego, CA.

"Model Test Coil for a 10MVA Superconducting Generator Field Winding" with K.A. Tepper and J.L. Smith, Jr., IEEE Transactions on Magnetics, Volume MAG-17, No. 1, January 1981.

"Superconducting Field Winding for a 10MVA Generator" with K.A. Tepper and J.L. Smith, Jr., Advances in Cryogenic Engineering, Volume 24, New York: Plenum Press, 1980.

"Shape Effect of the Matrix on the Capture Cross Section of Particles in High Gradient Magnetic Separation," with Z.J.J. Stekly, IEEE Transactions on Magnetics, Volume MAG-12, September 1976.

"Multipole, Superconducting Electric Motors for Ship Propulsion," with P. Thullen and T.A. Keim, IEEE Transactions on Magnetics, Volume MAG-11, No. 2, March 1975.